Conception et fabrication d'un magnétomètre à jauge de contrainte

Dirk Ettelt

UNIVERSITÉ DE GRENOBLE

THÈSE

Pour obtenir le grade de

DOCTEUR DE L'UNIVERSITÉ DE GRENOBLE

Spécialité : **Nano Electronique et Nano Technologies**

Arrêté ministériel : 7 août 2006

Présentée par

Dirk ETTELT

Thèse dirigée par **Jérôme DELAMARE** et
codirigée par **Arnaud WALTHER**

préparée au sein du **CEA-Leti**
dans **l'École Doctorale « Electronique, Electrotechnique, Automatique et Traitement du Signal »**

Conception et fabrication d'un magnétomètre à jauge de contrainte

Thèse soutenue publiquement le **13 juin 2012**,
devant le jury composé de :

Dr Alain BOSSEBOEUF
Directeur de recherche IEF Paris Sud, Président
Dr David P. ARNOLD
Professeur University of Florida, Rapporteur
Dr Pavel KEJIK
Chercheur EPFL, Rapporteur
Dr Skandar BASROUR
Professeur Université Joseph Fourier, Membre
Dr Paul FARBER
Senior Manager Robert Bosch GmbH, Membre
Dr Arnaud WALTHER
Chercheur CEA-Leti, Membre
Dr Jérôme DELAMARE
Professeur INP Grenoble, Membre

Résumé

Ce travail de thèse est consacré à la conception, la réalisation technologique et la caractérisation fonctionnelle d'un nouveau type de capteur de champ magnétique MEMS 3D. Différent de l'approche classique utilisée pour des magnétomètres MEMS 3D, le capteur conçu dans le cadre de cette thèse n'a pas comme base le principe de la force de Lorentz, mais se sert des avantages qu'offrent les matériaux magnétiques intégrés dans des systèmes MEMS. Le matériau magnétique subit un moment lorsqu'il est soumis à un champ magnétique environnant. Le principe de détection du signal est basé sur la piézorésistivité et utilise des jauges en silicium mono-crystallin avec une section nanométrique. Le concept technologique convient également pour la fabrication de capteurs inertiels et est donc une approche prometteuse pour la fabrication des centrales de mesure inertielle (IMUs).

La conception est principalement basée sur un modèle de bruit. En dehors de la considération des limitations technologiques, des aspects mécaniques, magnétiques et thermiques sont également pris en compte. Deux pistes ont été étudiées pour l'intégration du matériau magnétique. Une première option consiste dans l'intégration d'aimants terres-rares comme SmCo et NdFeB. Une deuxième option a pour objet l'intégration des multi-couches antiferromagnétiques et ferromagnétiques, couplées par le couplage d'échange. La réalisation technologique bien exigeante des ces deux approches sera présentée avec une concentration particulière sur les propriétés magnétiques des matériaux utilisés. Une autre partie sera consacrée à la caractérisation des contraintes mécaniques dans des couches minces qui peuvent devenir problématiques pour les micro-systèmes conçus dans le cadre de ce travail.

Au final, la fabrication du capteur ainsi que des caractérisations fondamentales seront présentées afin d'établir une preuve expérimentale pour le concept du capteur.

Conception and fabrication of a strain-gauge magnetometer

by Dirk Ettelt

A thesis submitted in partial satisfaction of the requirements for the degree of

Doctor of Philosophy

in Nano Electronics and Nano Technologies
at the University of Grenoble

submission date: April 14th, 2012

Thesis directed by *Jérôme Delamare* and co-directed by *Arnaud Walther*

Abstract

This PhD thesis deals with the design, the technological implementation, and functional characterizations of a new type of monolothic 3D MEMS magnetometer. Other than for the classical approach used for 3D MEMS magnetometers, the sensor developed in this work is not based on the principle of Lorentz force, but takes advantage of magnetic material which is integrated into the MEMS device and experiences a torque when surrounded by a magnetic field. Signal detection is based on piezoresistive detection using gauges of monocrystalline silicon with nanometric section. The technological concept is also suitable for the fabrication of inertial sensors and thus a very promising approach for fabrication of inertial measurement units (IMUs).

Sensor design mainly relies on a noise model. Besides technological limitations, mechanical, magnetic and thermal aspects are also taken into account. Two different methods for integration of magnetic material were explored. A first option consists in the integration of rare-earth magnets like SmCo and NdFeB, a second option is about the integration of exchange-bias coupled antiferromagnetic and ferromagnetic multilayers. The technologically challenging implentation of both approaches will be discussed with a special focus on magnetic properties of the used materials. A further part will be dedicated to the characterization of mechanical stress in thin layers, which may become problematic for the microsystems conceived in this work.

Finally, sensor fabrication and fundamental characterizations will be presented as experimental proof of concept for the sensor.

Contents

Acknowledgements

At the very beginning, I would like to express my acknowledgements towards many people I have had the pleasure to work with during my PhD thesis and/or who have contributed by different manners to the successful termination of what I am going to present in this manuscript.

D'abord, j'aimerais remercier *Jérôme Delamare* d'avoir pris en main la direction de ma thèse. Jérôme, je me sens vraiment privilégié d'avoir pu être sous ta surveillance scientifique. Merci pour tes encouragements, tes remarques et pour toutes les discussions constructives que nous avons eues. Et bien sûr je n'oublierai jamais les moments que nous avons passés en avion au-dessus de Belledonne. C'était vraiment génial.

Je tiens également à remercier *Arnaud Walther* de m'avoir encadré au cours de ma thèse au sein du Leti. Un grand merci à toi Arnaud pour ton engagement dans mon encadrement, pour ton travail de relecture de mon manuscrit, pour tous tes conseils et pour ta disponibilité.

Merci à *Philippe Robert* de m'avoir acceuilli dans son laboratoire et pour son soutien, notamment pour mes départs en conférence.

Je voudrais ensuite remercier toute l'équipe "M&NEMS" qui a rendu possible le fait que j'aie maintenant les résultats à présenter que le lecteur pourra trouver en parcourant ce manuscrit. En premier lieu je remercie *Patrice Rey* pour sa disponibilité, d'avoir répondu à chacune de mes questions et pour son indulgence quand je ne savais pas bien m'exprimer en français... Mais ma reconnaissance s'adresse bien sûr aussi envers les autres membres de l'équipe : *Mylène Savoye, Caroline Coutier, Pierre Meininger, Marie-Hélène Vaudaine, Brigitte Desloges, Fanny Delaguillaumie* et *Guillaume Jourdan*.

Merci à *Mathilde Cartier* pour son aide énorme dans la réalisation des couches magnétiques minces, pour son travail de relecture et pour toutes ses remarques constructives. Merci aussi à *Bernard Viala* pour toutes les discussions riches en matière sur le magnétisme des couches AF/F.

Je remercie *Marcel Audoin* et *Romain Anciant* pour leur aide dans la mise au point des procédés de caractérisation.

Merci à *Laurent Truong* d'avoir effectué toute la série de gravures Si qui était vraiment longue.

I would like to thank *Nora Dempsey* and *Youpeng Zhang* for all the friendly exchanges we have had about hard magnetic films and the nice collaboration. It was a pleasure to work together with you.

Je remercie *Guillaume Dodane* et *Lucas Dudon* pour leur implication dans les travaux de caractérisation des magnétomètres.

Je voudrais ensuite remercier mes collègues de bureau, *Antoine Niel*, *Eric Sage*, *Yannick Deimerly*, *Paul Ivaldi*, *Simeon Nachev* et *Henri Blanc* pour l'ambiance sympa dans notre

bureau.

Merci beaucoup à tous mes amis de Grenoble et de Bourgoin-Jallieu, pour leur amitié et pour tous les moments que nous avons pu passer ensemble. Vous avez tous une très grande valeur pour moi.

Ich danke meinen Eltern, meinen Brüdern und Schwestern dafür, dass sie innerlich mit mir waren, auch wenn wir geographisch weit voneinander entfernt sind. Es ist einfach wertvoll zu wissen, seine ganze Familie hinter sich sich haben und von ihr geliebt zu sein.

Je remercie également ma belle-famille pour tout leur soutien et pour leur amour.

Vielen Dank, meine geliebte *Elise*, für die Liebe und Zuneigung, die wir beide als Ehepaar miteinander teilen. Ohne dich wäre ich hier nie angekommen!

Über alles danke ich meinem Gott und Vater für seine Leitung und für die Kraft, die ich immer durch Glauben schöpfen konnte und jeden Tag neu erfahren habe.

Chapter 1

General introduction

1.1 Context of this work

1.1.1 A growing market for electronic compass applications

Many of today's every day life applications use magnetic field sensors. Most representative examples are found in the automotive- and wireless communication industry. According to iSupply [1], the market for magnetic sensors and switches was 880M$ in 2008 with growing tendency and growing market share in the domain of wireless communication applications (fig. 1.1(a)). A very promising domain is the growing market share of costumer electronics (smartphones, gaming etc.). This includes electronic compass applications in particular (fig. 1.1(b)), in which three major competing technologies are used:

- Hall effect magnetometers. For example, Apple is currently using AKM's 3D magnetometer technology for iPhone. Market share of Hall sensors was 85% in 2008.
- AMR magnetometers. They occupied 13% of the magnetic sensor market in 2008. A representative manufacturer is Honeywell.
- GMR magnetometers. With 2%, they took the smallest amount of the magnetometer market in 2008. A representative GMR sensor manufacturer is Yamaha.

The reason for the predominance of Hall sensors in the market is their low price and mature fabrication technology, even though AMR and GMR sensors are generally more precise than Hall sensors. Amongst others, these different sensor types are presented in more detail in section 1.2.

The emerging domain of MEMS[1] magnetic sensors is very promising to give access to new concepts for magnetic field sensing. Microfabrication allows building of sensors with very small size in the range below $1mm^2$ and low power consumption by maintaining high sensing performances. The present work adresses these aspects by development of a new MEMS 3D magnetometer, by demonstration of its technological feasibility as well as the validation of the sensor concept. In contrast to the commonly used Lorentz force principle for resonant MEMS magnetometers, the presented sensor uses integrated magnetic material for low power consumption and piezoresistive strain-gauges of nanometric scale for high sensitivity.

[1] Micro-Electro-Mechanical Systems

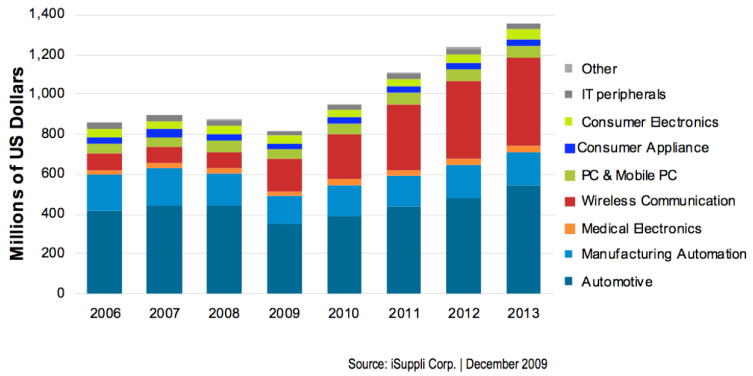

(a)

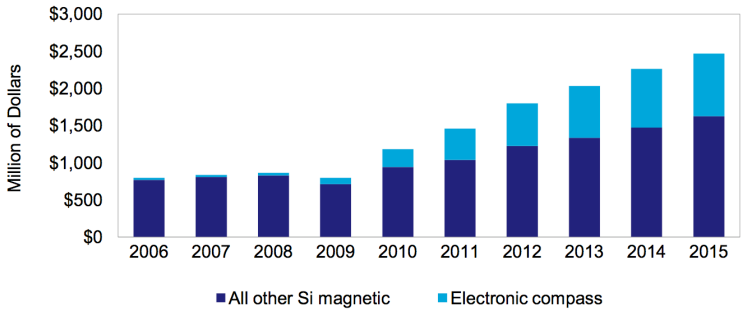

(b)

Fig. 1.1: Market evolution for magnetic sensors: (a) Market for magnetic sensors and switches [1]; (b) Evolution of the market for electronic compasses [2].

1.1.2 The "Capucine" project

The present document was composed during the work for my PhD thesis, entitled "Conception and fabrication of a strain-gauge magnetometer", which started in October 2009 and was carried out in the MEMS sensor Laboratory (LCMC) at CEA Leti-Minatec in Grenoble, France. The framework at the initial stage of this work was the "Capucine" project[2] (duration of 15 months). It aimed to demonstrate the feasibility of a fully integrated 6 axis sensor, including a 3D accelerometer and a 3D magnetometer, using piezoresistive strain-gauges of nanometric dimensions for signal aquisition. The basic technological concept is called "M&NEMS" and is also suitable for the fabrication of gyroscopes. Another aim was to show the concept to be competetive with existing MEMS sensor technologies, concerning size reduction, measurement performance and power consumption. Target applications are medical/healthcare, sports and mobile phones. Partners of this project were

- Leti (CEA-Grenoble) for sensor design and technological realization
- Néel laboratory (Grenoble) for integration of magnetic material into MEMS

[2]This project was supported by the French National Research Agency (ANR), grant No. ANR-09-NIRT-001.

- IM2NP (Marseille) for development of the associated ASIC[3]
- Movea (Grenoble) as industrial partner which develops solutions for motion recognition, and
- SPEC (CEA-Saclay) for modelization of magnetic layers.

1.1.3 Target of this work and organization of the manuscript

The major target of this work consists in the proof of concept of a new MEMS magnetic field sensor. This sensor should mainly exhibit following properties:

- chip-integrated 3-axis magnetic field sensing
- high sensitivity at reduced sensor size
- power consumption below state-of-the art 3D MEMS Lorentz force magnetometers
- high resolution for applications in the range of earth's magnetic field
- technological compatibility with the fabrication process used for inertial sensors for capability to build single-chip inertial measurement units (IMUs) within a single process.

This work is subdivided into six chapters.

- This first chapter introduces the reader into the context of this thesis by presenting an overview over the current state of the art and by mentioning particular advantages of the MEMS scale as a major motivation to realize the 3D magnetic field sensor presented in this work.
- The second chapter discusses the subject of magnetometer design, including the technological concept, the establishment of basic design rules, the discussion of effects to be considered for design, and a presentation of the designed magnetometers and their expected performances.
- Chapter three discusses the development of magnetic materials for integration into the magnetometer, by invesigation of two possible approaches using rare-earth magnets and exchange-bias-coupled ferromagnetic- and antiferromagnetic multilayers. It also includes the validation of steps which were crucial for the 3D magnetometer application.
- Chapter four presents fabrication results, including the discussion of effects which are related to residual stress in used materials.
- A validation of the 3D magnetometer concept is given in chapter five by presentation of characterization results.
- Chapter six is a general conclusion of this work.

[3]Application Specific Integrated Circuit

1.2 State of the art of magnetic field sensors

1.2.1 General overview over magnetic field sensors

Magnetic field sensors are used since over 2000 years. Their earliest and most known use was related to compass and navigation applications. Today, their use has expanded to a larger application range. Common applications of magnetic field sensors are proximity sensing, speed- and distance measurement, navigation compassing and current sensing. Magnetic field sensors perform measurements without physical contact and are thus suitable for use in rough industrial environment. If the earth's magnetic field in the range of 30µT to 60µT is taken as a reference, today's typical applications may be classified into three categories [3, 4]:

- High-sensitivity sensors for field gradient measurement in the range below earth's magnetic field (e.g. brain function mapping, magnetic anomaly detection).
- Medium sensitivity sensors applied to measure perturbations in the range of earth's magnetic field (e.g. navigation applications)
- Low-sensitivity sensors for application in fields greater than the earth's magnetic field (e.g. current measurement, non-contact switching)

Depending on the required sensitivity range, different types of sensors are used. Fig. 1.2 shows a comparison of different types of magnetic field sensors and their typically associated measurement range.

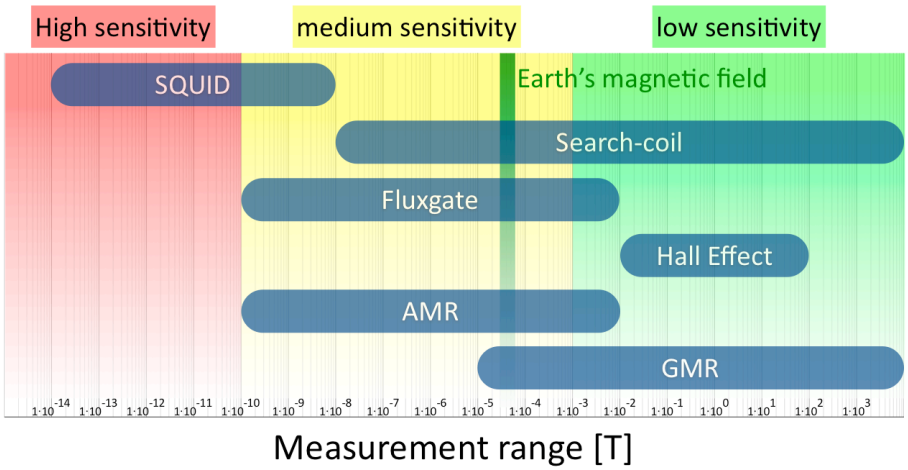

Fig. 1.2: Comparison of different magnetic field sensors and their measurement ranges, inspired by [4].

In this section, some important types of magnetic field sensors will be briefly presented. After this global overview, a more specific focus will be laid on the state of the art concerning magnetometers fabricated by MEMS technologies.

Magnetometers for high sensitivity applications

Magnetometers for high sensitivity show field resolutions down to 1pT. In general, they exhibit high complexity and are not miniaturizable.

SQUID The most sensitive magnetic field sensor is a SQUID (Superconducting Quantum Interference Device) and is applicable in measurement ranges of 10fT up to 10nT. Its measurement principle consists in cooling a superconducting ring down to its superconducting state, so that an ambient flux density induces a current in the ring which, in theory, is ceaseless as it is not derogated by any electrical resistance. In 1962, Brian D. Josephson predicted the effect of two superconductors which are connected by "weak links" [5]. Such a "weak link" can be realized by a thin insulating layer and allows the current in the superconducting ring to flow. The induced ring current pulsates with a frequency that depends on the magnitude of the magnetic flux and is read out by a dedicated radio-frequency circuit.

Magnetometers for medium sensitivity applications

Fluxgate magnetometers Fluxgate magnetometers were first used in the early 1930's. Today, they are often used in space applications and geophysics [6]. In the case of a fluxgate magnetometer (fig. 1.3), a ferromagnetic core is periodically driven into its saturation by a primary drive coil with drive signal $V(t)$. A second coil senses the flux density of the core and the external flux density. The external field makes the output of the pickup coil to become assymetric so that the external flux density can be measured by extracting the second harmonic of the sensed signal.

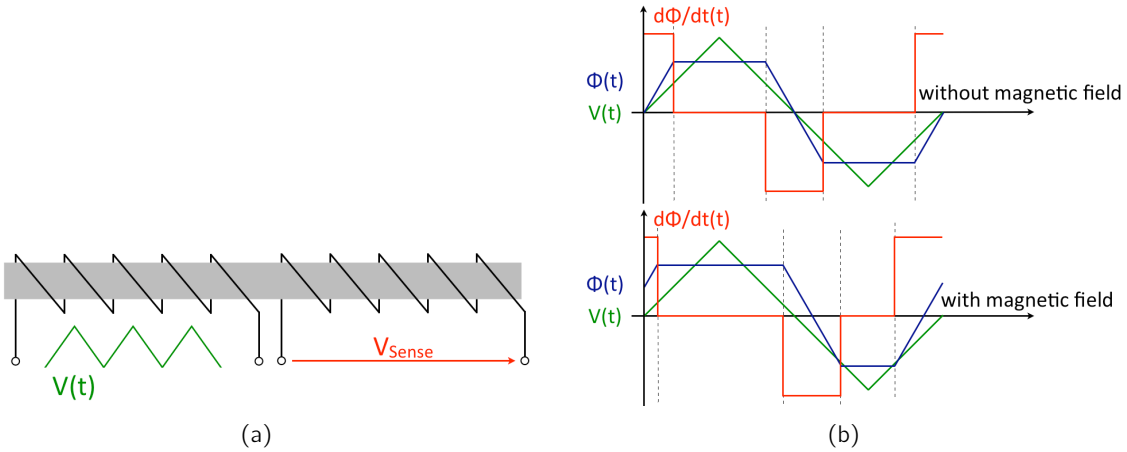

Fig. 1.3: Principle of a fluxgate magnetometer: (a) A ferromagnetic core is alternatively driven in- and out of saturation by a primary drive coil. Changes in flux density are then sensed by the secondary coil; (b) Scheme of the induction signal with and without external magnetic field.

Anisotropic Magnetoresistive (AMR) sensors The Anisotropic Magnetoresistive effect is a property known from ferromagnetic materials. A well-known example for today's commonly used materials in AMR sensors is Permalloy, an alloy of Nickel and Iron. This material can be pre-magnetized in a way that it exhibits an easy axis defined by its magnetization $\vec{M}$, which coincides with the geometric long axis of the Permalloy resistor. If a current crosses the Permalloy resistor at an angle θ with respect to the magnetization direction (fig. 1.4), the resistor exhibits a resistance depending on the angle θ. When the resistor's magnetization is tilted by an external magnetic field, the resistance is changed because electrons with different

spins are diffused in a different manner.

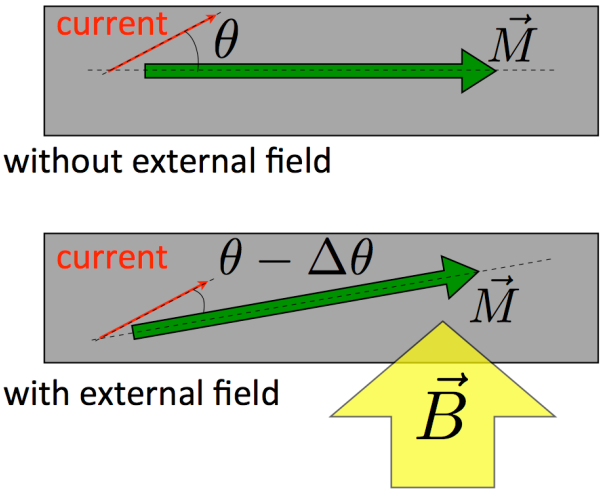

Fig. 1.4: Principle of an AMR device: An external magnetic field tilts the magnetization, so that the electrical resistance is modified with a changing angle θ between current and magnetization direction.

Resistance reaches its maximum value if the current direction is parallel to magnetization and tends towards a minimum for increasing angles up to 90° (fig. 1.5(a)). For an angle θ situated in the region about 45°, the resistance change shows linear dependency on the angle. Therefore, AMR devices are usually conceived for Barber Pole biasing (fig. 1.5(b)), where shorting bars are disposed at an angle of 45° with respect to the magnetization direction[4]. By this way, the current's flow direction is also constrained to form an angle of 45° with the magnetization direction. For signal readout, several individual AMR resistors are usually connected in a Wheatstone bridge configuration.

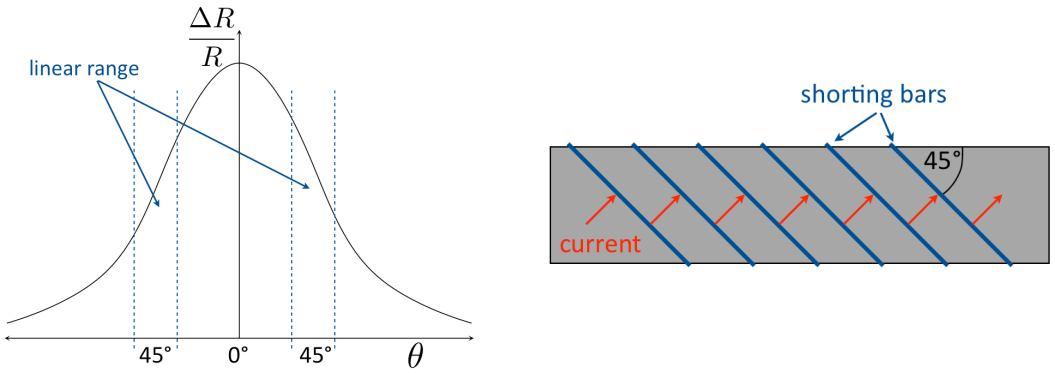

(a) (b)

Fig. 1.5: Linearity of an AMR resistor: (a) Linear behaviour in the region of about $\theta = 45°$; (b) Individual AMR resistor conceived for Barber Pole biasing with shorting bars.

AMR sensors have been miniaturized and are used in commercial applications. An example

[4]Barber Pole configuration also allows recognition of the magnetic field direction.

for a commercial three-axis AMR sensor is given by the Honeywell HMC1043, where three independent AMR bridges are assembled to a 3 axis magnetometer [7]. The fully packaged sensor exhibits a size of $3\times3mm^2$, has a resolution of $1.7nT/\sqrt{Hz}$ and a power consumption of about 30mW. In 3D AMR sensors, it is disadvantageous to use 3 seperate AMR bridges because of possible disposition errors between the individually mounted AMR bridges. Also the required volume for packaging and assembling costs are significant. Nevertheless, this concept is still used in commercial applications.

In 2008, da Silva *et al.* published a concept for an out-of plane AMR sensor [8]. They etched trenches into the $< 100 >$ Silicon plane by anisotropic KOH etching. By this way, the $< 111 >$ plane in Silicon is exposed, which has a known angle of 54.7° with respect to the $< 100 >$ plane (fig. 1.6). They deposited 35nm thick $Ni_{80}Fe_{20}$ layers as ferromagnetic material on the exposed $< 111 >$ plane. Due to their inclination, the sensors are sensitive to the out-of-plane field component. Da Silva presented a 3D magnetometer configuration for detection of one in-plane and one out-of-plane field component with a resolution of $20nT/\sqrt{Hz}$ and a power consumption of about 20mW. The system's size was $100\times100\mu m^2$.

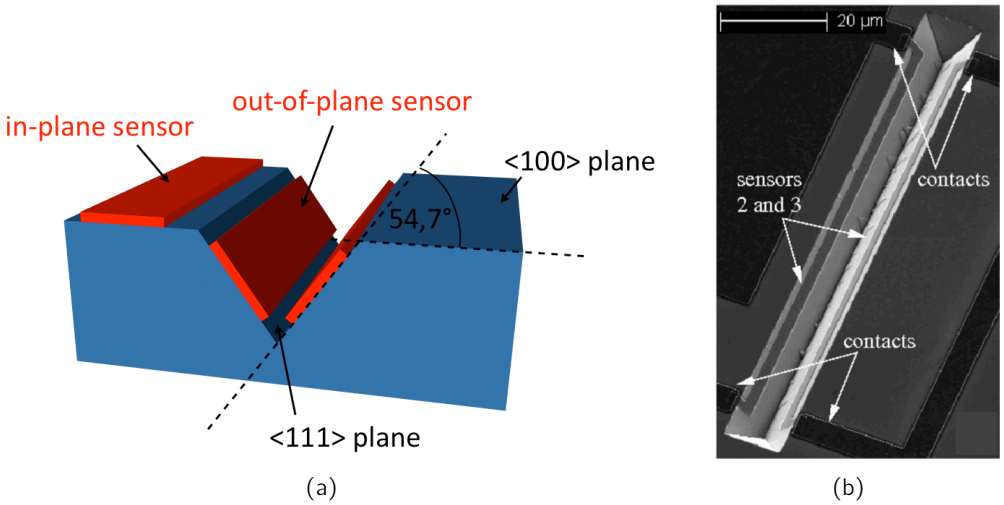

(a) (b)

Fig. 1.6: Z-sensitive AMR sensor: (a) Principle of an out-of-plane AMR sensor: Trenches etched by anisotropic KOH etching into the $< 100 >$ plane of a Silicon substrate fix the out-of-plane sensors at an angle of 54.7° with respect to the substrate. So, the sensor is sensitive to the magnetic field component vertical to the $< 100 >$ Silicon plane; (b) SEM photograph of the technological realization of da Silva *et al.* [8].

Magnetometers for low sensitivity applications

Search-coil magnetometer An example for a medium-low sensitivity range magnetometer is the search-coil device which is based on Faraday's law of induction (fig. 1.7). Its lower sensitivity limit goes down to the range of 100pT, whereas no upper limit does exist. A disadvantage of a search-coil magnetometer is that it requires a varying magnetic field for its working principle. Thus, it is not suitable for DC and low-frequency measurement.

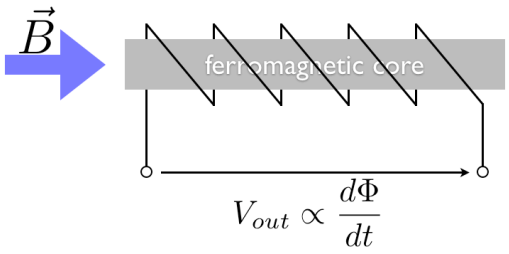

Fig. 1.7: Principle of a search-coil magnetometer

Magnetoresistors Besides Giant Magnetoresistivity (GMR), the Lorentz force $\vec{F}_L$ is one of the most common principles used for low-sensitivity applications. It is generated in presence of a magnetic field $\vec{B}$ and is perpendicular to the direction of a moving charge q with velocity $\vec{v}$:

$$\vec{F}_L = q(\vec{v} \times \vec{B}). \tag{1.1}$$

One type of magnetic field sensor using this principle is the magnetoresistor. Magnetoresistors are often made of semiconducting materials with high carrier mobilities such as InSb or InAs. If a magnetoresistor bar with length l and width w is flown through by a current i according to fig. 1.8, the moving charges are deflected in a way that the path on which the current travels becomes longer. As a result, an increased bar resistance is measured. The modified bar resistance resistance depends on the magnetic field as described by eqn. 1.2:

$$R_B = R_0 \frac{\rho_B}{\rho_0} \left(1 + m(\mu B)^2\right). \tag{1.2}$$

R_B is the resistance for the bar under a magnetic field B, R_0 is the bar resistance at zero field, ρ_B and ρ_0 are the respective resistivities, m is the geometric form factor given by l/w, and μ the carrier mobility. Relative increases of resistance up to several hundred percent are achievable thanks to the disposition of so-called shorting lines, which generate an equipotential across the bar and so force the carriers to move on a longer way [4]. A great disadvantage of this sensor is its non-linear dependence on the magnetic field B.

Giant Magnetoresistivity (GMR) devices Giant Magnetoresistivity (GMR) was first discovered in 1988 by Baibich *et al.* for coupled Fe and Cr thin layers, where they found a resistivity variation of approximately 200% [9]. This phenomenon is related to a spin-dependent transmission of conduction electrodes between two ferromagnetic layers with same or opposite magnetization orientations. Both ferromagnetic layers are seperated by a thin non-magnetic conducting layer. Referring to fig. 1.9(a), both ferromagnetic layers are magnetized in opposite direction in their initial state, so their spins are also orientated in opposite directions at the border line between them. Due to the initial spin of conduction electrons, they are scattered in this configuration of opposite magnetized layers, leading to a high resistance. If an external magnetic field overcomes the initial magnetization of the ferromagnetic layers

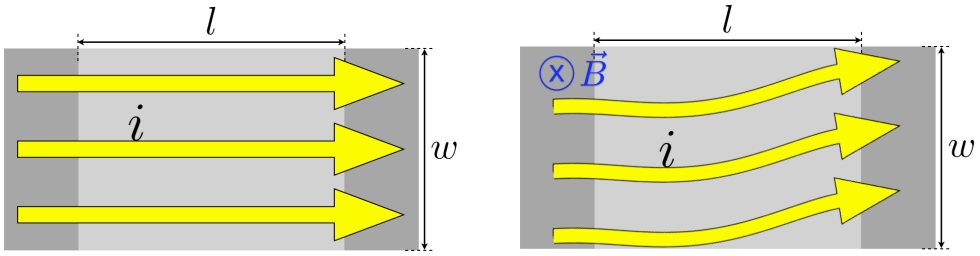

(a) (b)

Fig. 1.8: Principle of a magnetoresistor: (b) Device without an external magnetic field: the resistance is minimum; (b) Device with an external magnetic field, where the current direction is deviated and resistance increases.

(fig. 1.9(b)), they are magnetized in the same direction, so that they exhibit equal spin configuration. This is very advantageous for conduction electrons to flow through the resistor with less scattering, leading to a low resistance.

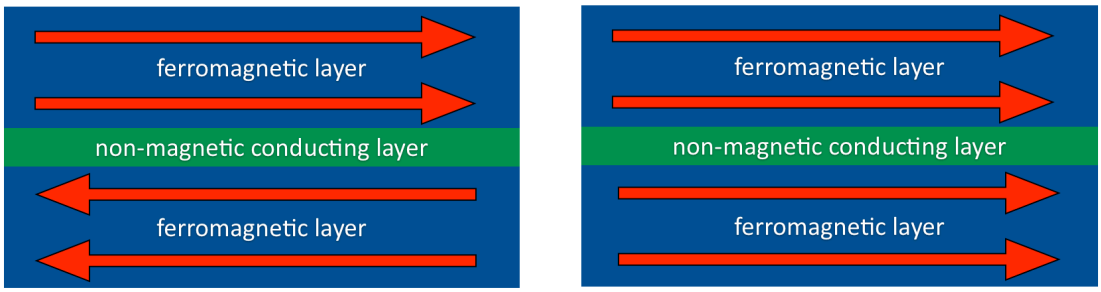

→High resistance (a) →Low resistance (b)

Fig. 1.9: Principle of Giant Magnetoresistivity: (a) adjacent ferromagnetic layers are separated by thin non-magnetic, electrically conducting layers and exhibit opposite magnetization directions in their initial state; (b) in presence of an external magnetic field, magnetizations in the ferromagnetic layers align into the same direction, which leads to a reduction of electrical resistance.

Hall Effect magnetic field sensors Another measurement principle similar to the one of magnetoresistors is the Hall Effect. Hall Effect devices make use of the Lorentz force in conductors and are often realized in n-type Silicon. As principally shown in fig. 1.10, carriers are deviated under a perpendicular magnetic field, so that the carrier density is increased at one side and reduced at the other side of the bar, which results in a voltage perpendicular to the current direction. The so-called Hall voltage V_{Hall} is given by

$$V_{\text{Hall}} = R_H \frac{iB}{d}, \tag{1.3}$$

where R_H is the Hall constant which depends on the carrier concentration, i the current flowing through the probe, B the magnetic field and d the probe thickness. V_{Hall} increases

linear with the external magnetic field up to the magnitude of several Teslas.

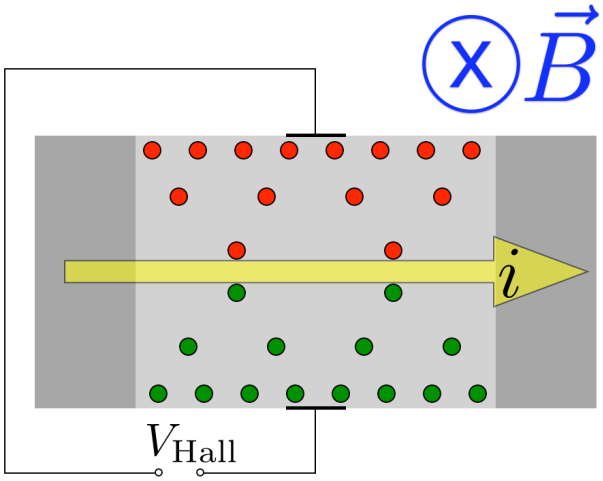

Fig. 1.10: Principle of the Hall effect: Charge carriers cumulate at both opposite sides of the Hall device in presence of a perpendicular magnetic field, so that a Hall voltage V_{Hall} is generated.

There are solutions to miniaturize Hall sensors. In 2001, Roumenin *et al.* published their realization of a fully integrated 3 axis magnetic sensor with means of IC technology [10]. Under normal operation conditions (room temperature, no further amplification), the sensor consumes about 30mW of power, and its dimensions are 250×220×100µm^3. As the sensor's resolution was not sufficient for compassing application, ferrite flux concentrators had to be added and the device had to be cooled down to 77K in order to achieve sufficiently high resolution for sensing of earth's magnetic field. This results in a total sensor length of 70mm and more complex measurement setup, which does not satisfy the requirements for miniaturization in the sense of MEMS technology. A similar solution was presented by Schott and Popovic of the EPFL Institute of Switzerland [11], where miniaturizations down to an active area of 50µm^2 were achieved. An illustration of the sensor is given in fig. 1.11.

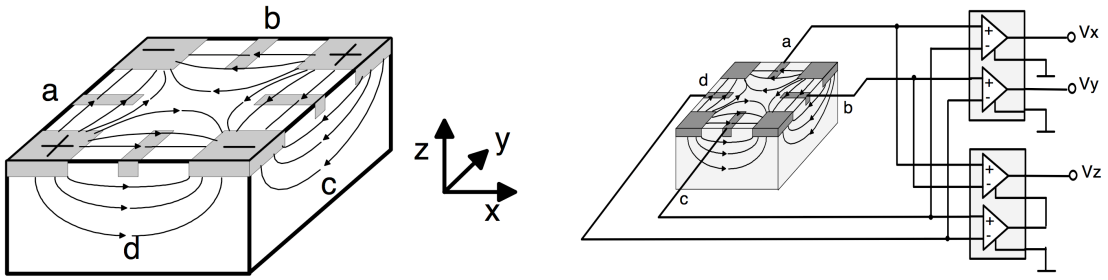

(a) (b)

Fig. 1.11: Principle of a 3D Hall according to Schott and Popovic [11]: (a) The 3D sensor is a low doped Silicon block with 8 ohmic contacts at its surface. Current is injected in the four corners and sensing is achieved by the contacts a,b,c and d; (b) Simultaneous sensing of the three magnetic field components.

1.2.2 Magnetic field sensors in MEMS technology

Parallel to the miniaturization of several sensors, the motivation to build miniaturized magnetic field sensors has been driven in the last years by the need for devices of higher integration density, less energy consumption and lower costs. Main targets are amongst others their integration into portable devices such as mobile phones (e.g. for navigation) and their use in medical and healthcare applications (e.g. for motion tracking). For example, Hall sensors and AMR have been recently used for cellphone applications[5]. Nevertheless, Hall sensors usually require flux concentrators in order to increase sensitivity. AMR sensors need to be degaussed regularly, where much current is needed for. MEMS technology offers new possibilities for fabrication of smaller and cheaper sensors with increased measurement performance and less power consumption. The relevance of scaling effects for magnetic interactions in MEMS devices will be mentioned in 1.3. A major challenge consists in the monolithic integration of vector magnetometers, i.e., a magnetic field sensor that measures the magnitude of all three spatial field components, which is generally difficult for sensors based on Hall-effect, AMR, GMR and the fluxgate principle. In the case where different types of sensors need to be cointegrated within a single microfabrication process (e.g. for realization of IMU[6] devices), above-mentioned magnetometers are not compatible with the fabrication of other types of sensors.

Solutions for miniaturized magnetometers based on Hall Effect and AMR were presented above. For MEMS-based magnetometers, Lorentz Force has often been the fundamental tranduction principle. As an overview, this section presents some examples of recent technological achievements in the domain of MEMS magnetic field sensors based on Lorentz force.

Lorentz force MEMS magnetometers

Lorentz force is the most frequently used principle for magnetic field detection in MEMS devices. In general, an oscillator is flown through by an AC current, so that the Lorentz force on the conductor resulting from an external magnetic field leads it to oscillate. Early realizations were presented by Kádár *et al*. and Eyre *et al*. in 1998, who both used torsional resonators (fig. 1.12(a)). Eyre *et al*. achieved a resolution of $25\text{nT}/\sqrt{\text{Hz}}$ with a power consumption of 4.5mW [14]. Two years later, Emmerich and Schöfthaler presented another resonant structure using capacitive sensing (fig. 1.12(b)) and reached a resolution of about $70\text{nT}/\sqrt{\text{Hz}}$ [13], which is close to the results obtained by Izham *et al*. in 2003 [15]. Active sensor areas were situated in the order of 1mm side length in the above-mentioned cases. In 2003, Beroulle *et al*. presented a U-shaped resonant cantilever using piezoresistive strain gauges for signal detection [16], as presented in fig. 1.13. According to Dumas *et al*. [17], this sensor exhibits a total surface of 10.6mm^2, a resolution of about $110\text{nT}/\sqrt{\text{Hz}}$ and a power consumption of 56mW. A fully-integrated 3 axis magnetometer was for the first time presented in 2008 by Kyyränäinen *et al*. in 2008 [18]. They used 500nm thick Mo coils on their structures and capacitive sensing (fig. 1.14). Power consumption for a single structure was 300µW. For detection of the in-plane field component, a resolution of $10\text{nT}/\sqrt{\text{Hz}}$ was achieved and $70\text{nT}/\sqrt{\text{Hz}}$ for the out-of-plane field component, respectively. Another example

[5] For example, ST uses Honeywell's AMR technology for smartphones.

[6] These are inertial measurement units which typically use inertial sensors combined with magnetometers for position tracking applications.

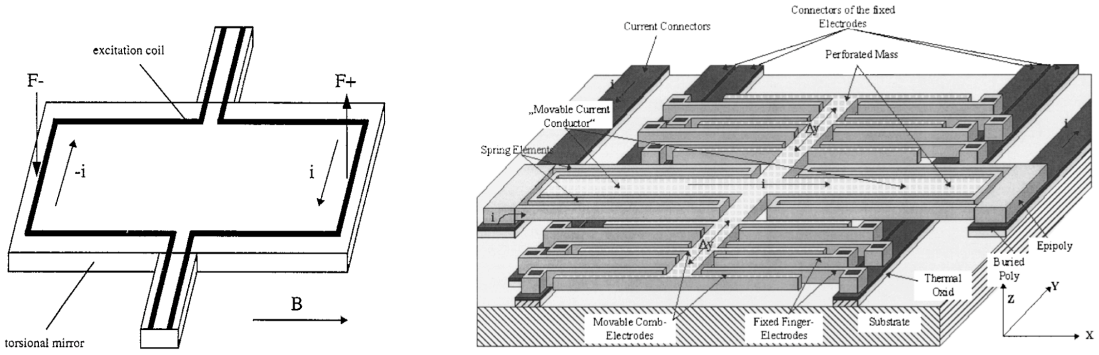

(a) (b)

Fig. 1.12: Title/description: (a) Principle of a torsional resonator as presented by Kádár *et al.* in 1998 [12]; (b) Resonator presented as presented by Emmerich and Schöfthaler in 2000 [13].

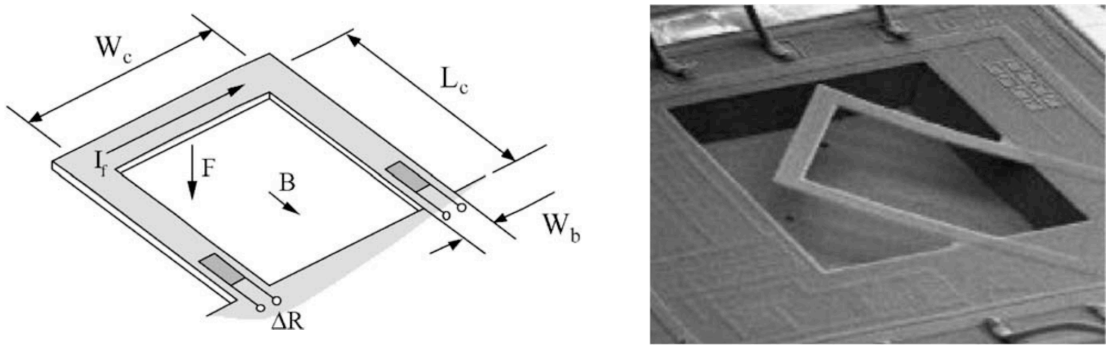

(a) (b)

Fig. 1.13: U-shaped cantilever as presented by Beroulle *et al.* and Dumas *et al.* [16, 17]: (a) Functional principle; (b) Technological realization.

for a fully integrated 3D magnetometer was presented in 2011 by Thompson *et al.* [19], where they achieved a resolution of $\sim$300nT/$\sqrt{\text{Hz}}$ for sensing of the X-axis and $\sim$140nT/$\sqrt{\text{Hz}}$ for z-axis. In contrast to the solution of Kyyränäinen *et al.*, a power of only 300µW was required for the complete 3D sensor. It should be noted that resonant MEMS magnetometers generally require vacuum packaging in order to obtain high quality factors for improved sensitivity, which sets technological constraints.

Target of this work

The target of this work is to develop a new concept for a 3D MEMS magnetometer which is technologically compatible with the fabrication of accelerometers and gyroscopes, and which is competitive with Lorentz force MEMS magnetometers and known commercial 3D MEMS sensors in terms of measurement performances, sensor size and power consumption. For this purpose, the use of integrated permanent magnets instead of electrical currents is a very promising approach. Fig. 1.15 illustrates how the 3D MEMS magnetometer developped in this work is positioned towards known 3D MEMS magnetometers in terms of performances

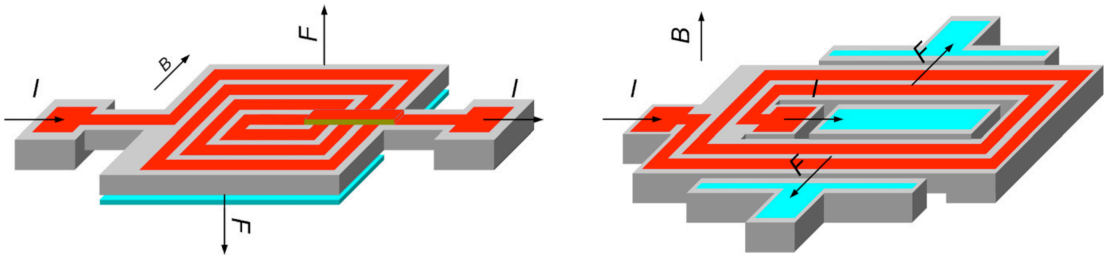

(a) (b)

Fig. 1.14: 3 axis magnetometer as presented by Kyynäräinen *et al.* [18], using capacitive sensing: (a) structure for measurement of the in-plane field component; (b) structure for measurement of the out-of-plane field component.

and power consumption.

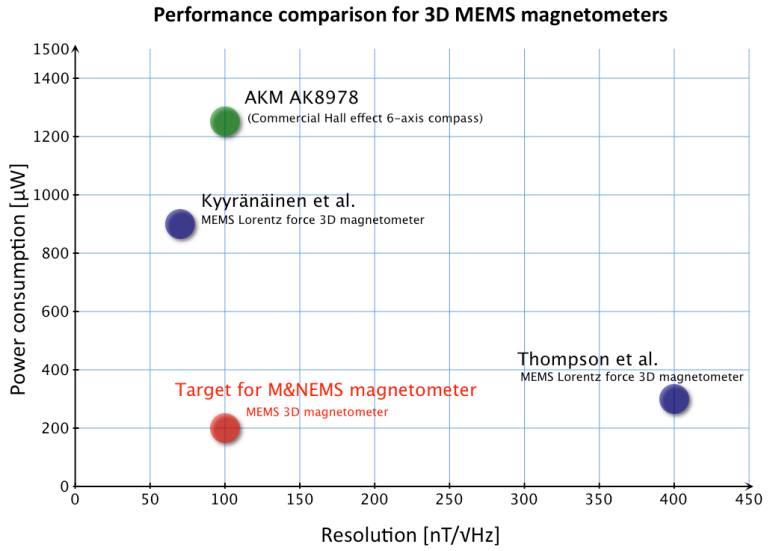

Fig. 1.15: Comparison of sensor performances for state-of-the-art 3D MEMS magnetic field sensors. The AKM AK8978 6-axis compass integrates a 3-axis magnetometer and a 3-axis accelerometer.

1.3 Consideration of scaling effects for MEMS magnetometers

1.3.1 General considerations

It is known that changes in dimensions of a system affect the manifestation of physically observable parameters like temperature, mechanical properties, sensitivity to forces (inertial, electrostatic, magnetic, etc.) [20]. For a classical example, consider the effect of an acceleration on a cube with volume l^3. The force F due to an acceleration a is known as

$$F = ma, \tag{1.4}$$

if m is the mass of the cube. By assuming a density ρ, we get

$$F = l^3 \rho a. \tag{1.5}$$

If the cube is now shrinked in size by reducing its side length l, the acceleration force scales down with l^3. Scaling-related effects are of great importance in MEMS design. On the one hand, many advantages are given by devices of small dimensions, e.g., it is possible to attain higher frequencies for oscillators. On the other hand, undesirable effects appear as well. For instance, surface-to-volume ratio increases for shrinked sizes, which makes the respective object becoming more susceptible to noise which is related to the thermal environment.

1.3.2 Relevance of MEMS scale for electromagnetic interactions

In this section, the relevance of scaling laws for electromagnetic interactions will be briefly discussed with special focus on torques on a permanent magnet in a magnetic field and torques on a current loop in a magnetic field. The pertinence of downscaling of magnetic microsystems was already shown by Cugat *et al.* in 2003 [21]. They alluded that magnetic interactions between permanent magnets take benefit of a scale reduction, while interaction forces decrease in case of current-current or current magnet-interactions.

Magnetic field generated by a magnet

The magnetic field in a point P situated at a distance $|\vec{r}|$ from a permanent magnet can be expressed as

$$\vec{H}(P) = \vec{\nabla} U(P), \tag{1.6}$$

where $U(P)$ is the scalar potential in point P. We express it as

$$U(P) = \frac{V}{4\pi\mu_0} \frac{\vec{M} \cdot \vec{r}}{|\vec{r}|^3}, \tag{1.7}$$

where V is the magnet's volume and $\vec{M}$ the magnetization of the permanent magnet. If the magnet's dimensions are reduced by a factor k and its magnetization remains unchanged, we obtain the corresponding scalar potential $U_k(P_k)$:

$$U_k(P_k) = \frac{V_k}{4\pi\mu_0} \frac{\vec{M} \cdot \vec{r}_k}{|\vec{r}_k|^3} = \frac{1}{k} U(P), \tag{1.8}$$

where $V_k = V/k^3$ and $\vec{r}_k = \frac{1}{k}\vec{r}$. If the magnetic field is scaled down by the factor k, it keeps its relative geometry and magnitude, so that $\vec{\nabla}(k) \propto k$. Thus, we obtain for the scaled magnetic field $\vec{H}_k(P_k)$:

$$\vec{H}_k(P_k) = \vec{H}(P). \tag{1.9}$$

Torque on a magnet in a magnetic field

In presence of a magnetic field $\vec{B}$, a permanent magnet with volume V experiences the torque

$$\vec{\Gamma} = V\vec{M} \wedge \vec{B}. \tag{1.10}$$

If the magnet is scaled down by a factor k while magnetization and external field do not change, we get:

$$\vec{\Gamma}_k = \frac{1}{k^3}\vec{\Gamma}, \tag{1.11}$$

so the torque in relation to the modified volume remains unchanged:

$$\frac{\Gamma(k)}{V(k)} = \text{const.} \tag{1.12}$$

Magnetic field generated by a conductor

We consider now the magnetic field generated by an electric conductor which is flown through by a current density $j = i/A$, where A is the conductor's section. According to the law of Biot-Savart, the magnetic field $\vec{H}(P)$ in a point P situated at distance $|\vec{r}|$ from the conductor is then expressed as:

$$\vec{H}(P) = \frac{jA}{4\pi}\frac{d\vec{l}\wedge\vec{r}}{|\vec{r}|^3}. \tag{1.13}$$

If the dimensions of the conductor are reduced by a factor k and current density remains constant, we get

$$\vec{H}_k(P_k) = \frac{jA_k}{4\pi}\frac{d\vec{l}_k\wedge\vec{r}_k}{|\vec{r}_k|^3} = \frac{1}{k}\vec{H}(P), \tag{1.14}$$

where $A_k = \frac{1}{k^2}A$, $d\vec{l}_k = \frac{1}{k}d\vec{l}$ and $\vec{r}_k = \frac{1}{k}\vec{r}$.

Torque on a current loop in a magnetic field

To evaluate the torque generated on a current loop in an external magnetic field $\vec{B}$, we consider a closed current loop with current density $j = i/A$ and loop area $\vec{S}$. The torque exerted on it is

$$\vec{\Gamma} = jA\vec{S}\wedge\vec{B}. \tag{1.15}$$

By reducing the size by k, the torque is modified as

$$\vec{\Gamma}_k = jA_k\vec{S}_k\wedge\vec{B} = \frac{1}{k^4}\vec{\Gamma}, \tag{1.16}$$

where $A_k = A/k^2$ and $\vec{S}_k = \frac{1}{k^2}\vec{S}$. Relative to volume reduction, the torque decreases with $1/k$:

$$\frac{\Gamma(k)}{V(k)} \propto \frac{1}{k}. \tag{1.17}$$

Discussion

As seen from eqn. 1.9, the magnetic field of a permanent magnet remains unchanged after scaling. The interaction force between two magnets which are reduced in size by a factor k is hence increasing linearly with k, as this force is proportional to $\nabla\vec{H}$. For the same reason, interaction forces between conductors and magnets remain unchanged when the system is shrinked, as magnetic fields generated by conductors decrease linearly with k, according to eqn. 1.14. In terms of magnetometer sensitivity, it can be concluded from eqns. 1.12 and

1.17 that use of permanent magnets is more advantageous than use of electrical conductors for the M&NEMS magnetometer concept which implies interactions at the MEMS scale. However, the performance loss in case of electrically generated fields can be compensated by higher current densities, which is emphazised in the PhD thesis of H. Rostaing [22]. Nevertheless, higher current densities lead to higher power consumption in a MEMS system, while permanent magnets do not require any power supply. The integration of permanent magnets in microsystems is thus a very promising approach for MEMS systems involving electromagnetic interactions, while low power consumption is required.

1.3.3 Relevance of MEMS scale for combined use of magnetometers and inertial sensors

A further advantage of the MEMS scale is related to the potential use of a MEMS magnetometer (with integrated magnetic material) in combination with inertial sensors (accelerometers and gyroscopes) for the realization of Inertial Measurement Units (IMUs). These sensors ideally integrate a 3D magnetometer together with a 3D accelerometer and a 3D angular rate sensor. It is already a great advantage of the M&NEMS concept that it is suitable for the fabrication of all three sensor types. Furthermore, another advantage consists in the fact that the output signal of all three sensor types is situated in the same order of magnitude, if the case of typical applications for IMU devices such as motion tracking is considered. This can be demonstrated by a brief analytical example, where we compare the orders of magnitude between moments which are generated by acceleration forces and by Coriolis forces with magnetic moments. For this purpose, a homogeneous silicon sphere with radius $|\vec{r}|$ and mass density ρ_{Si} is considered to be uniformly covered by magnetic material of thickness t, which is representative for the case of the magnetometer presented in this work.

Moments generated by acceleration

In the case of an accelerometer, the force generated by an acceleration $\vec{a}$ is $\vec{F_a} = m_S\vec{a}$. However, no moment is generated if the sphere's rotation axis is situated in its center of mass. Therefore, the rotation axis has to be situated at a lever arm distance l away from the sphere's center of mass. Here, the lever arm is considered to be of the same size range as the sphere and is fixed to $l = r$ for simplification. The resulting moment generated by the acceleration force is then expressed as

$$\vec{\Gamma_a} = l\vec{F_a} = \frac{4}{3}\pi\rho_{Si}r^4\vec{a}\wedge\vec{r_e}, \tag{1.18}$$

where $\vec{r_e}$ is a vector with length 1 and collinear with $\vec{r}$.

Moments generated by Coriolis force

In case of gyroscopes, a moment is generated by Coriolis force

$$\vec{F_c} = 2m\vec{v}\wedge\vec{\Omega} \tag{1.19}$$

which acts at a lever arm distance with respect to a rotation axis, as it is the case for accelerometers. Here, $\vec{v}$ is the scale-independent sphere velocity and $\vec{\Omega}$ the yaw rate of

the gyroscope. Again, the lever arm is fixed to length r, so that the resulting moment is expressed as

$$\vec{\Gamma}_c = \frac{8}{3}\pi\rho_{Si}r^4\vec{r}_e \wedge (\vec{v} \wedge \vec{\Omega}). \tag{1.20}$$

Comparison with moments generated by magnetic fields

The magnetic moment can be derived from eqn. 1.10 as

$$\vec{\Gamma}_m = 4\pi r^2 t\vec{M} \wedge \vec{B}, \tag{1.21}$$

where t is the thickness of magnetic material which coveres the sphere. For simplification, the different moments are considered to be maximized by setting $\vec{a} \perp \vec{r}$, $(\vec{v} \wedge \vec{\Omega}) \perp \vec{r}$, and $\vec{M} \perp \vec{B}$, respectively. With eqns. 1.18 and 1.21, the ratio between moments induced by acceleration forces and magnetic fields is then given by

$$\frac{\Gamma_a}{\Gamma_m} = \frac{r^2\rho_{Si}a}{3tMB}. \tag{1.22}$$

In analogy, the ratio between moments generated by Coriolis forces and magnetic fields is derived from eqns. 1.20 and 1.21 as

$$\frac{\Gamma_c}{\Gamma_m} = \frac{2r^2\rho_{Si}v\Omega}{3tMB}. \tag{1.23}$$

Parameters for evaluation were set to values which typically occur in case of navigation- and motion tracking applications and are listed in table 1.1 There is an optimum sphere size,

Symbol	Value	Description
ρ	2329 kg/m^3	Silicon mass density
Ω	π rad/s	Gyroscope angular rate
f_d	20 kHz	Gyroscope drive frequency
$\hat{x}$	1 µm	Gyroscope displacement amplitude
a	1 m/s^2	Acceleration
$\mu_0 M$	0.7 T	In-plane magnetization of NdFeB
B	10 µT	External magnetic field
t	1 µm	Thickness of integrated magnetic material

Table 1.1: Assumptions for comparison of moments.

expressed in terms of r, where moments generated by acceleration forces, Coriolis forces and magnetic fields are all situated in the same range. For the studied case, it is found that

$$r(\Gamma_a/\Gamma_m = 1) = \sqrt{\frac{3tMB}{\rho_{Si}a}} \approx 85\mu m \tag{1.24}$$

and

$$r(\Gamma_c/\Gamma_m = 1) = \sqrt{\frac{3tMB}{2\rho_{Si}v\Omega}} \approx 95\mu m. \tag{1.25}$$

This leads to the conclusion that MEMS scale becomes very important for IMU sensors which are based on the concept of M&NEMS technology, as the output signals are all of the same order of magnitude. For comparison, we can consider the case of a centrimetric scale ($r = 1$cm). In this case, the ratios defined in eqns. 1.22 and 1.23 are $\sim 10^4$.

Impact of angular accelerations in case of the magnetometer application

Finally, we can also estimate the impact of angular accelerations on a sphere which is able to rotate around an axis which coincides with its center of mass. This case is representative for the M&NEMS magnetometer application, as presented in chapter 2. For an angular acceleration $\frac{d\vec{\omega}}{dt}$, the sphere experiences the moment $\vec{\Gamma}_{ang}$, given by

$$\vec{\Gamma}_{ang} = J_S \frac{d\vec{\omega}}{dt}, \tag{1.26}$$

where J_S is the sphere's mass moment of inertia. The moment then becomes

$$\vec{\Gamma}_{ang} = \frac{8}{15}\pi\rho_{Si}\frac{d\vec{\omega}}{dt}r^5. \tag{1.27}$$

Comparison of a moment induced by angular acceleration with a moment generated by a magnetic field yields then

$$\frac{\Gamma_{ang}}{\Gamma_m} = \frac{2\rho_{Si}\frac{\partial\omega}{\partial t}r^3}{15tMB}. \tag{1.28}$$

Assuming $r = 100$µm for the micrometric scale and $\frac{\partial\omega}{\partial t} = \pi$ rad/s^2, it is found that sensitivity to angular accelerations is $\sim 10^4$ times smaller than sensitivity to magnetic fields, so that the parasitic influence of angular accelerations can be neglected for this type of application at the MEMS scale. In contrast to this, the impact of angular accelerations would be ~ 100 times larger than the intrinsic signal induced by the magnetic field in case of a centrimetric scale, where $r = 1$cm.

Discussion

We conclude that typical dimensions of MEMS devices (where r is in the range of a hundred µm in length) are very advantageous to cointegrate accelerometers, gyroscopes and magnetometers which use permanent magnets. Physical parameters to be measured are sensed without differences in sensitivity and measurement of the magnetic field is not obstructed by the influence of angular accelerations. However, linear accelerations have to be considered during design of the sensor, which will discussed in chapter 2.

Chapter 2

Sensor design

This chapter focuses on the design of a magnetometer based on the principle of magnetic torque created by an external magnetic field on a permanent magnet, which uses piezoresistive strain gauges as sensitive elements. The functional principle of the magnetic field sensor will be explained by description of the signal transduction chain with basic analytical modeling. This model, reaching from the measured magnetic field until the sensor's final output, allows to define design rules for the magnetometer. As the transduction chain comprizes different components of the sensor, there are several elements to design in order to maximize the sensor's performances. Basically, the sensor consists of three uncorrelated mechanical elements to design:

- a piezoresistive strain gauge
- a hinge to suspend a silicon mass
- a MEMS structure (silicon mass), containing magnetic material.

FEM modeling with COMSOL software was used in order to complement the analytical description of the sensor. For design issues, it is crucial to focus on characteristic sensor performances like sensitivity, resolution and accuracy. Sensitivity is defined as the ratio between the sensor's output and input signal, resolution determines the minimum detectable physical variable, accuracy the preciseness to measure a physical variable with drifts depending on time, on space, on temperature and so on. Given that the fabrication technique allows microscale integration of several sensor elements, it is intended to achieve the fabrication of a 3D magnetic sensor for compass application. This requires consideration of other aspects like interference of magnetic fields from nearby placed micro-magnets as well as geometrical and technological constraints for the structures to be designed.

After a brief introduction into the technological approach and a presentation of the magnetometer's working principle, an analytical description of the model for sensor performances will be introduced by a noise model. This enables to define important design criteria. A particular regard will be given to geometrical and mechanical aspects, including technological constraints for the former mentioned sensor elements. Finally, the designed sensors will be presented.

2.1 M&NEMS as technological approach for a 3D MEMS magnetometer

Sensor design and fabrication in this work is based on the "M&NEMS" principle, which has been presented as a new approach to low-cost inertial sensors in 2009 [23]. This concept merges the advantages of both, MEMS and NEMS technology. Parallel to its use for magnetometers, it is also used for accelerometers and gyroscopes. As a particularity, piezoresistive strain gauges are fabricated in nanoscale dimensions and are connected to the MEMS part of the sensor which is fabricated at microscale dimensions (fig. 2.1). A deformation of the MEMS structure induces mechanical stress in the nano-gauges. If scaling laws are considered for a shrinked gauge section, the relative change in resistance $\frac{\Delta R}{R} \propto \frac{1}{L^2}$, while L is a typical length unit to be scaled. If L is shrinked, this leads to amplification of mechanical stress on a small gauge section and thus to higher sensitivity. A major advantage of the M&NEMS concept consists in the fact that high sensitivity can be achieved without any need for increased MEMS structure size. A further advantage of M&NEMS technology is that it is also appropriate for fabrication of 3D magnetometers, which is generally difficult for Hall effect-, AMR-, GMR-, and fluxgate magnetometers. Furthermore, M&NEMS technology is also suitable for cointegration of multiple sensor types, particularly accelerometers and gyroscopes, in one single monolithic fabrication process, because the technological concept is applicable to other inertial sensors. This enables to realize highly integrated and low-cost IMUs (Inertial Measurement Units).

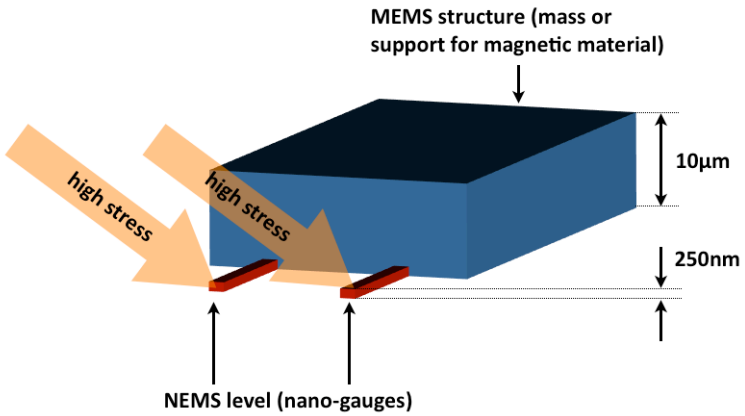

Fig. 2.1: M&NEMS concept: a relatively thick (10µm) MEMS structure is connected to a piezoresistive strain-gauge with nanometric section. A displacement of the MEMS structure deforms the nano-gauges and induces high mechanical stresses.

The simplified fabrication process of the M&NEMS magnetometer is shown in fig. 2.2. Silicon nano-gauges are etched within a thin monocrystalline silicon top layer of a SOI substrate and protected by an SiO_2 layer. A monocrystalline silicon layer with typical thickness of 10µm is then deposited by epitaxy, which is followed by integration of the magnetic material. MEMS structures are dry etched by DRIE[1] and finally released by a hydrofluoric acid etching step.

[1]Deep Reactive Ion Etching

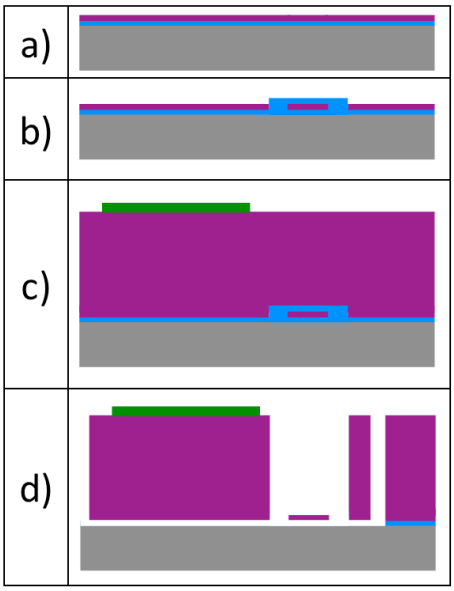

Fig. 2.2: Simplified process flow of the M&NEMS magnetometer: a) Start of the process on a SOI substrate; b) etching of nano-gauges within the monocrystalline top silicon layer and protection with SiO_2; c) epitaxy of a thick monocrystalline silicon layer and deposition of magnetic material, which will be presented in chapter 3; d) DRIE etching of the MEMS structures and subsequent release by vapor hydrofluoric acid etching.

2.2 Functional principle

2.2.1 Description of the sensor's transduction chain

A major target of this work is to apply the M&NEMS functional principle to a magnetic field sensor with integrated 3-axis measurement. Therefore, a mobile MEMS structure is needed to deform piezoresistive nano-gauges. In M&NEMS technology, this mobile structure is made of silicon and built within a surface micromachining process on a SOI (Silicon On Insulator) wafer. Magnetic material has either to be embedded into this structure or to be deposited onto it. So, in presence of a magnetic field $\vec{B}$, the magnet with its volume V_{mag} and its magnetization $\vec{M}$ will be submitted to a torsional moment

$$\vec{\Gamma} = (\vec{M} \wedge \vec{B}) V_{mag}, \tag{2.1}$$

which will cause the MEMS device to turn around a defined rotation axis (Fig. 2.3). Two piezoresistive nano-gauges are used to compensate this resulting motion by exerting reset forces on the MEMS structure. These forces cause stress inside the gauges, changing their resistance because of the piezoresistive effect. As the dimensions of the nano-gauges are small compared to the silicon brick, the stress is distributed over a very small section, which enables reduction of the sensor's size without sensitivity loss. For realization of a 3D compass, three individual MEMS structures are required for independent measurement of x-, y- and z-components of the magnetic field. This requires two mobile structures optimized for transduction of an in-plane torque and one structure optimized for transduction of an out-of-plane torque. Further needed are two independent in-plane magnetization directions as

presented by figure 2.4. Finally, resistance changes can then be detected by electric circuits such as a Wheatstone bridge. Fig. 2.5 schematically presents the sensor's transduction chain, including the option of a control loop. This control loop can be designed for actuation of the MEMS structure by electrostatic forces in order to increase the sensor's linear full scale range.

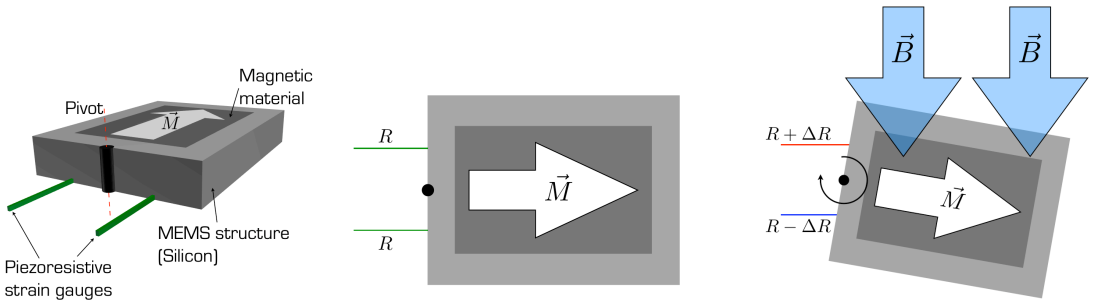

(a) (b) (c)

Fig. 2.3: Principle of a M&NEMS magnetic field sensor: (a) A silicon brick contains the magnetic material and is connected to two piezoresistive nano-gauges; (b) both strain gauges show same resistance when there is no surrounding magnetic field; (c) in presence of a magnetic field, the MEMS structure rotates around a pivot and deforms piezoresistive nano-gauges.

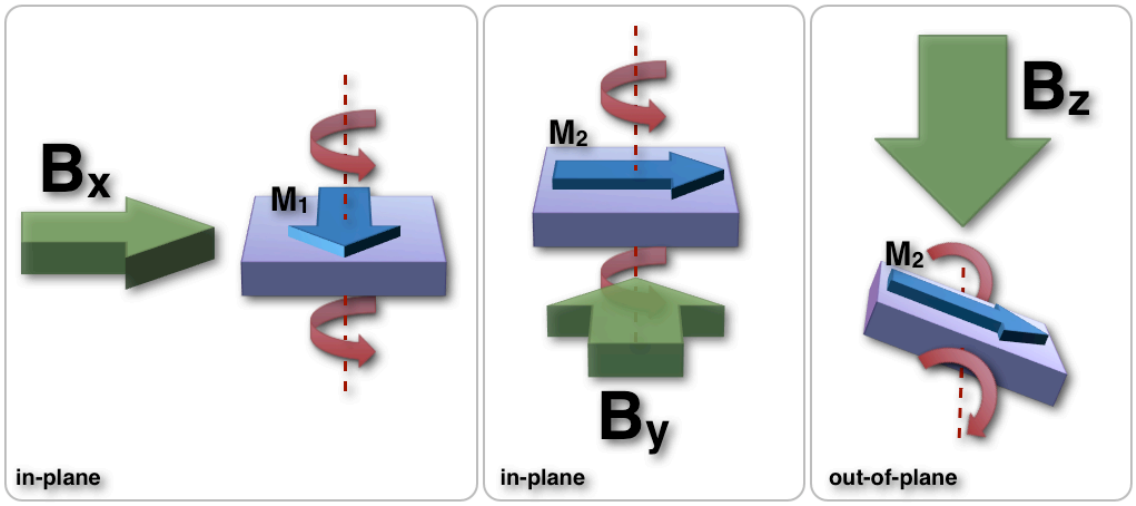

Fig. 2.4: Three independent structures with two in-plane magnetizations M_1 and M_2 are needed for measurement of the three magnetic field components B_x, B_y and B_z.

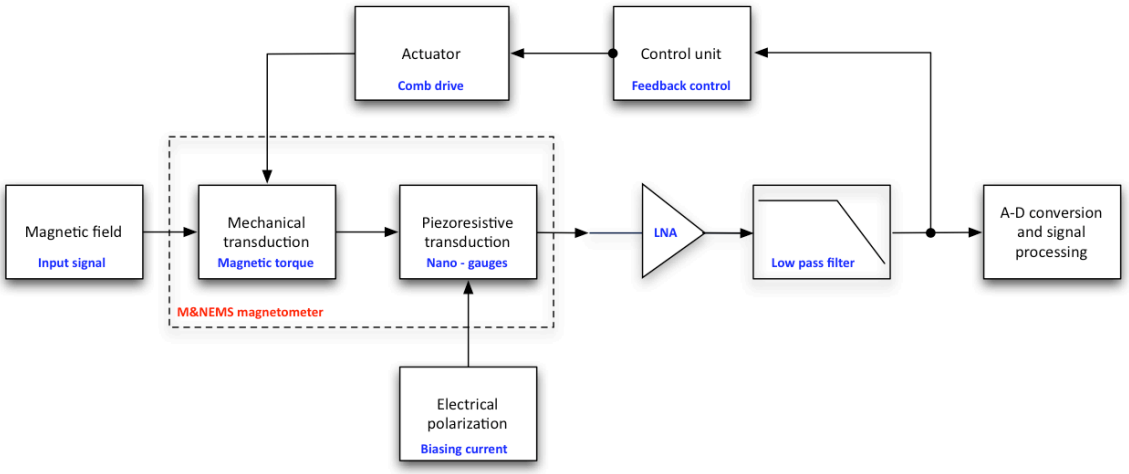

Fig. 2.5: Model of the transduction chain for the considered sensor. An optional control circuit may be conceived for closed loop detection and is schematically presented as a simple feedback loop with a control unit, a low noise amplifier (LNA) and capacitive comb drives or electrodes as actuation units.

2.2.2 Integration of magnetic material

Integration of magnetic material into the sensor is required by the functional principle and represents a great technological challenge in this work. Different technologies like electrodeposition, pulsed-laser deposition (PLD) and sputtering have been used in microtechnology to integrate permanent magnets into MEMS devices [24]. However, reliable technological solutions for integration of magnets in micromechanical fabrication processes remain still an important issue. Using permanent magnets for sensing applications requires good magnetic properties of the used materials. High remanence is needed for high sensitivity and it must exhibit good stability in the application's temperature range. Coercitivity must be high enough so that the device can withstand a specific maximum external magnetic field. In this work, two basic technological approaches will be explored for integration of magnetic material in the sensor. In the first concept, rare earth magnets like NdFeB or SmCo will be buried in a thick silicon brick, while alternating thin layers of ferromagnetic and antiferromagnetic material (AF/F layers) are stacked onto the thick silicon structure in the second approach (Fig. 2.6). The concept of exchange-bias coupled thin layers of ferromagnetic and antiferromagnetic materials is already known from GMR and MRAM devices and was even used for magnetic actuation at the nanoscale in the Ph.D. thesis of L. Bilhaut [25].

For the design of our sensor, good magnetic properties are crucial in order to increase sensitivity and to reach a high robustness of the device. It should be noted that the most important parameter to be considered here is remanence, as the required minimum volume of magnetic material is determined by this value in order to agree with given sensor specifications. In the case of integrated rare earth magnets, we will base our design upon the magnetic properties which have been found during earlier research in our laboratory [26] and in cooperation with the Néel laboratory [27, 28]. These properties are listed in table 2.1. As far as magnetic properties of exchange-bias coupled AF/F multilayers are concerned, magnetometer design will be based on experience values which were obtained prior to this work

at Leti. A remanence of $\mu_0 M = 1.8\text{T}$ is assumed for CoFe which is used as ferromagnet, even though CoFe was shown to be able to exhibit higher remanence magnetization up to $\mu_0 M = 2.4\text{T}$ [29].

A detailed discussion presenting the development of MEMS-compatible magnetic materials which are suitable to be used in MEMS magnetometer applications will be given in the seperate chapter 3.

Material	Intrinsic coercivity [kA/m]	$\mu_0 M_r$ (in-plane) [T]	Energy product [kJ/m^3]
SmCo	1035	0.8	140
NdFeB	1280	0.7	100

Table 2.1: Achievable magnetic properties for rare earth magnets

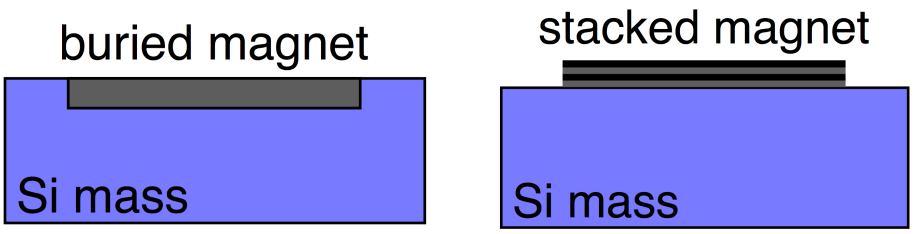

Fig. 2.6: Scheme of the two methods used to integrate magnetic material: (a) burying of hard magnetic material into a silicon mass; (b) stacked thin layers of ferromagnetic and antiferromagnetic material onto a silicon mass.

2.2.3 Piezoresistivity

Theory

In the context of this work, piezoresistive transduction is used for signal acquisition. The piezoresistive effect explains the change in electrical resistivity of a material when it is subjected to mechanical stress. The effect was first discovered in 1856 by William Thompson (commonly known as Lord Kelvin) [30] and later by J. S. Smith for Germanium and Silicon [31]. When a piezoresistive material is deformed, a relative change $\frac{dR}{R}$ in electrical resistance is induced by a geometric and an electronic component and can be described by:

$$\frac{\mathrm{d}R}{R} = \underbrace{\frac{\mathrm{d}l}{l} - \frac{\mathrm{d}A}{A}}_{\text{geometric}} + \underbrace{\frac{\mathrm{d}\rho}{\rho}}_{\text{electronic}}, \tag{2.2}$$

where l is the resistor length, A its section and ρ its resistivity. Changes in dimensions induced by compression or extension of the material are the cause for the geometric component, while the electronic component is caused by properties of the material's band structure. In semiconductors like Silicon, this latter contribution prevails over the geometric component and depends amongst others on the character of doping (p-type or n-type), on the carrier

concentration, on carrier mobility and on temperature [32, 33]. The piezoresistive coefficient π_{pr} is defined by the relative change of resistivity per mechanical stress:

$$\pi_{pr} = \frac{\frac{d\rho}{\rho}}{\sigma} \tag{2.3}$$

where σ is the mechanical stress. In case of crystalline Silicon, the piezoresistive effect shows strong anisotropic behaviour, so relation 2.3 has to be reformulated in tensor notation. Resistivity ρ and stress σ are represented by tensors of second order. Relative change in resistivity is then related to mechanical stress by a tensor of fourth order:

$$\frac{d\rho_{ij}}{\rho} = \pi_{ijkl}\sigma_{kl} \qquad \text{with} \qquad i,j,k,l = 1,2,3 \tag{2.4}$$

Thanks to the symmetric diamond structure of crystalline Silicon, the 81 components of the tensor π_{ijkl} can be reduced to a 6x6 matrix with just three components π_{11}, π_{12} and π_{44} [34]. Also the resistivity tensor and stress tensor can be simplified due to symmetry considerations (Fig. 2.7 and Tab. 2.2).

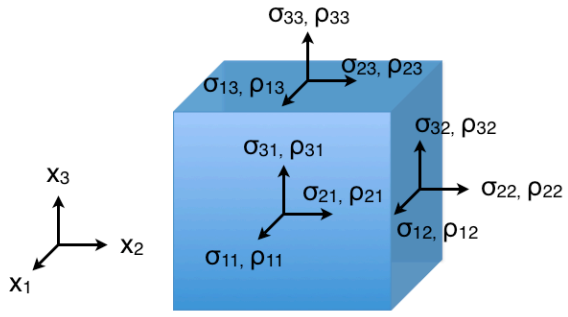

Fig. 2.7: Symmetry considerations for second order stress tensor and second order resistivity tensor.

Tensor notation	11	22	33	23;32	13;31	12;21
Matrix notation	1	2	3	4	5	6

Table 2.2: Index conversion for resistivity and stress tensors

Thus, equation 2.4 can be represented in matrix form:

$$\begin{pmatrix} r_1 \\ r_2 \\ r_3 \\ r_4 \\ r_5 \\ r_6 \end{pmatrix} = \begin{pmatrix} \pi_{11} & \pi_{12} & \pi_{12} & 0 & 0 & 0 \\ \pi_{12} & \pi_{11} & \pi_{12} & 0 & 0 & 0 \\ \pi_{12} & \pi_{12} & \pi_{11} & 0 & 0 & 0 \\ 0 & 0 & 0 & \pi_{44} & 0 & 0 \\ 0 & 0 & 0 & 0 & \pi_{44} & 0 \\ 0 & 0 & 0 & 0 & 0 & \pi_{44} \end{pmatrix} \begin{pmatrix} \sigma_1 \\ \sigma_2 \\ \sigma_3 \\ \sigma_4 \\ \sigma_5 \\ \sigma_6 \end{pmatrix} \qquad \text{with} \qquad r_i = \frac{d\rho_i}{\rho} \tag{2.5}$$

It is distinguished between three main directions for the piezoresistive effect in crystalline Silicon (cf. figure 2.8):

- [100] along a cube edge. Both other cube edges ([010] direction and [001] direction) are equivalent due to symmetry considerations
- [110] along the diagonal of an area
- [111] along a space diagonal

Piezoresistive coefficients can be calculated for any other discrete direction using tensor transformation. Table 2.3 shows an example of piezoresistive coefficients for Silicon at room temperature (300K) which have been measured by Smith [31]. This example is valid for a current direction along the [110] axis. Generally, one considers a longitudinal piezoresistive

	ρ [Ω cm]	π_{11} [10^{-11}/Pa]	π_{12} [10^{-11}/Pa]	π_{44} [10^{-11}/Pa]
n-Si	11.7	-102.2	53.4	-13.6
p-Si	7.8	6.6	-1.1	138.1

Table 2.3: Resistivity and piezoresistive constants for the [110] direction of crystalline Silicon (doped with $N = 10^{16}/\text{cm}^3$) at room temperature (300K) [35].

coefficient π_L, where the current and field are aligned with the direction of mechanical stress, and a transverse piezoresistive coefficient π_T, where current and field are perpendicular to the direction of mechanical stress [36]:

$$\pi_L = \pi_{11} - 2(\pi_{11} - \pi_{12} - \pi_{44})k_1 \tag{2.6}$$

and

$$\pi_T = \pi_{12} + (\pi_{11} - \pi_{12} - \pi_{44})k_2, \tag{2.7}$$

where k_1 and k_2 are obtained from coordinate transformation between the respective crystallographic reference coordinate systems[2]. Based on the measurements of Smith (table 2.3), numerical evaluation yields $\pi_L = 71.8 \times 10^{-11}$/Pa and $\pi_T = -1.1 \times 10^{-11}$/Pa for the [110]-direction, which is the direction of interest in this work because of a maximum π_L.

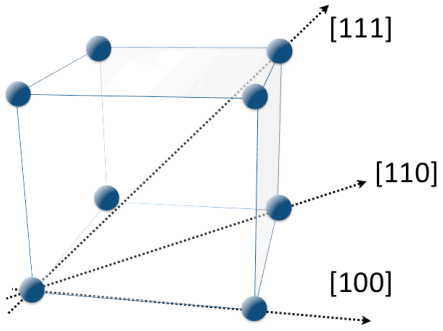

Fig. 2.8: Nomenclature for directions in crystalline Silicon

The total relative change in resistivity in dependence of the material's deformation is known

[2]for detailed explantion cf. [36]

by combining the geometric and electronic component. It is commonly expressed as a dimensionless parameter, the *gauge factor*:

$$GF = \frac{\frac{dR}{R}}{\varepsilon} = \frac{\frac{dR}{R}}{\frac{dl}{l}} = 1 + 2\nu + E\pi_{pr}. \tag{2.8}$$

ν is the poisson ratio, ε the strain and E the Young's modulus. ν is situated between 0 and 0.5 for most materials. For metals, the small piezoresistive constant π_{pr} makes the elastoresistive coefficient $E\pi_{pr}$ become small compared to the geometric component, therefore most metals exhibit a gauge factor between 1 and 2. In semiconductors like Silicon, the relative change in resistance is dominated by the electronic contribution and makes the gauge factor increase significantly. The gauge factor may, in dependence of doping, appear with both, a positive or a negative sign. Table 2.4 shows several typical gauge factors for different materials:

Material	Gauge factor
Cu	1.6
Ni	-12.62
Al	1.4
Pt	2.6
Fe	0.44
Co	0.84
Mo	0.8
Ta	1.3
W	1.16
Sn	3.34
Bi	-11.36
Si(c)	-102 to 135

Table 2.4: Gauge factors for different materials [35]

Comparison between piezoresistive and capacitive signal acquisition

Piezoresistivity is the transduction principle used in this work. In current MEMS applications, it is often in competition with the capacitive working principle. Depending on specifications, a decision is made either for piezoresistive or capacitive sensing. Table 2.5 shows a comparison of several important advantages and disadvantages which have to be taken into account for the choice of transduction principle.

Using piezoresistive detection, one can also avoid the disturbing influence of parasitic capacitance. Basically, capacitive sensing leads to a sensitivity of

$$S \propto \frac{\Delta C}{C_0 + C_p}, \tag{2.9}$$

where C_0 is the offset capacitance, C_p the parasitic capacitance, and ΔC the change in capacitance to be detected. With decreasing capacitor size, C_p prevails over ΔC and leads to decreased sensitivity.

As the ambition of this work is to develop a low-cost integrated 3D MEMS compass, some

	piezoresistive	capacitive
Stability in time	☹ (aging in piezoresistors)	☺ (not subjected to aging)
Linearity	☺	☹
Signal acquisition	☺ (resistance)	☹ (signal conversion required)
Power consumption	☹ (current biasing)	☺
Downscaling	☺	☹
Technological complexity	☺	☺

Table 2.5: Comparison of advantages and disadvantages between piezoresistive and capacitive sensing.

important criteria orientate the choice for the piezoresistive effect. Reduced device complexity and small device size are requested to reach high quantites of devices per wafer, so that fabrication costs are limited. Downscaling is even advantageous for the piezoresistive effect, while it is unfortunate for capacitive transduction. A further advantage is the linear behaviour of the piezoresistive effect in a large range of strain. Figure 2.9 shows an example for the linear behaviour of a piezoresistive silicon nanowire, measured by Chen [37]. Even if piezoresistive detection generally requires more power than capacitive detection due to the need of a biasing current, it is still an adequate choice for a low-power MEMS device, as the readout electronics are of less complexity than for capacitive readout.

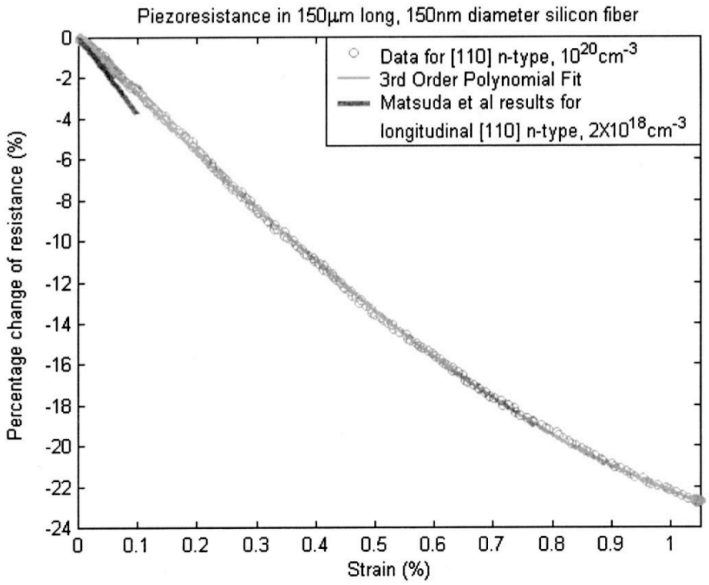

Fig. 2.9: Relative change in resistance of a silicon nanowire depending on strain, as measured by Chen [37]. Measurement data is compared to formerly obtained results by Matsuda [38]. Nanowires in the [110] orientation with a doping rate of 10^{20}cm^{-3} were used. The piezoresistive effect is linear in a large range.

Thus, the use of piezoresistive transduction is an adequate choice for our application, because it allows to match requirements for low-cost production, high sensitivity and linearity.

2.3 Sensor performances

2.3.1 Sensor specifications

The sensor to be fabricated aims principally for compass application and has to be designed for measurement of earth's magnetic field. It can be used for navigation purposes, motion and trajectory measurement, monitoring of patients in healthcare applications and many more. In cooperation with this work, sensor specifications were provided by MOVEA[3], which uses the magnetic field sensor in sports application in order to monitor human motion. At the equator, the strength of earth's magnetic field is about 30µT and about 60µT at the poles[4]. We aim for an angular resolution of 1° in measurement of earth magnetic field, so the minimum detectable field has to be

$$B_{min} = 30\mu\mathrm{T} \cdot \tan 1^\circ \approx 524\mathrm{nT}. \tag{2.10}$$

The full scale range of the sensor is theoretically given by the maximum value of the earth magnetic field, but magnetic perturbations different from this field may cause offsets and high peak values and have to be considered as well. Table (2.6) gives an overview of the required specifications of the magnetic field sensor. These specifications are used as design guideline for the magnetometers conceived in this work.

Dimensions	2 x 2 x 1mm
Alignment of sensitivity axes	0.1°
Full scale range	$>150\mu$T
Resolution	$\leq$500nT at 15Hz bandwidth
Temperature range	-10°C to 50°C
Max. polarization voltage	3.6V
Resistance against mechanical shocks	10000g
Resistance against magnetic shocks	1T

Table 2.6: Sensor performances, specified by MOVEA.

2.3.2 Sensitivity

Following to the description of the functional and transductional principle, we will now establish a model for the magnetometer's sensitivity and discuss important parameters which can be modified in a way that the sensor's sensitivity increases. Referring to fig. 2.10, the magnetic moment from eqn. 2.1 is transduced into a force acting on two piezoresistive strain gauges, where any of the gauges experiences the force

$$F_g = \gamma_g \frac{MBV_{mag}}{n_g d_g}, \tag{2.11}$$

[3] http://www.movea.com

[4] According to established theory, earth's magnetic field is induced by the liquid outer core of the earth which contains much of Iron. Due to high temperatures in the inner earth, matter exceeds its Curie temperature and does not show properties of permanent magnets. However, matter becomes ionized at the present temperatures. Liquid flows of this matter mainly induces the earth's magnetic field.

where d_g is the distance between a gauge and the fulcrum, and γ_g a correction factor considering that the moment is not entirely absorbed by the strain gauges only, but also by the suspension of the MEMS structure which cannot be considered as an ideal pivot (cf. chapter 2.6). The number of gauges is $n_g = 2$ in our case.

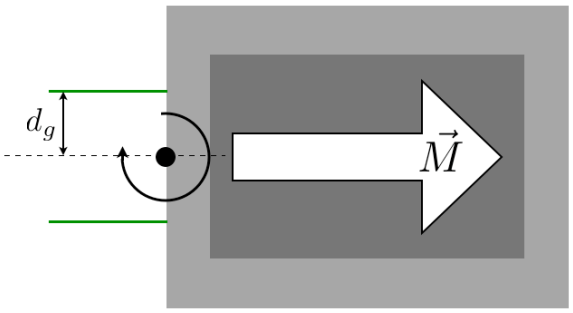

Fig. 2.10: Transduction of the moment into strain in the gauges

The stress acting on a single gauge with the section A_g is

$$\sigma_g = \frac{F_g}{A_g}, \tag{2.12}$$

thus the relative resistance variation due to the piezoresistive effect is given by

$$\frac{\Delta R}{R_0} = \pi_{pr}\sigma_g. \tag{2.13}$$

Actually, the piezoresistive coefficient π_{pr} of the gauge is amongst others a function of doping and temperature (cf. 2.2.3):

$$\pi \rightarrow \pi(N, T),$$

as well as the gauge resistance R_0:

$$R_0 = \rho_{Si}\frac{l_g}{A_g} \rightarrow R_0(N, T) = \rho_{Si}(N, T)\frac{l_g(T)}{A_g(T)}, \tag{2.14}$$

where ρ_{Si} is the resistivity of crystalline Silicon and l_g the length of the gauge. However, in a first approach they will be considered as constant values to simplify the model. As the sensor is designed with two gauges, there are mainly two options for signal readout. The first one is to apply a constant current, the second one to apply a constant voltage as presented in figure 2.11. With equations 2.11 - 2.13 and by choosing the first mode of signal readout, we get for the sensitivity:

$$S_i = \frac{V_{out}}{B} = i_a R_0 \pi_{pr}\gamma_g \frac{MV_{mag}}{n_g d_g A_g}, \tag{2.15}$$

and for the constant voltage case respectively:

$$S_V = V_0 \pi_{pr}\gamma_g \frac{MV_{mag}}{2n_g d_g A_g} \tag{2.16}$$

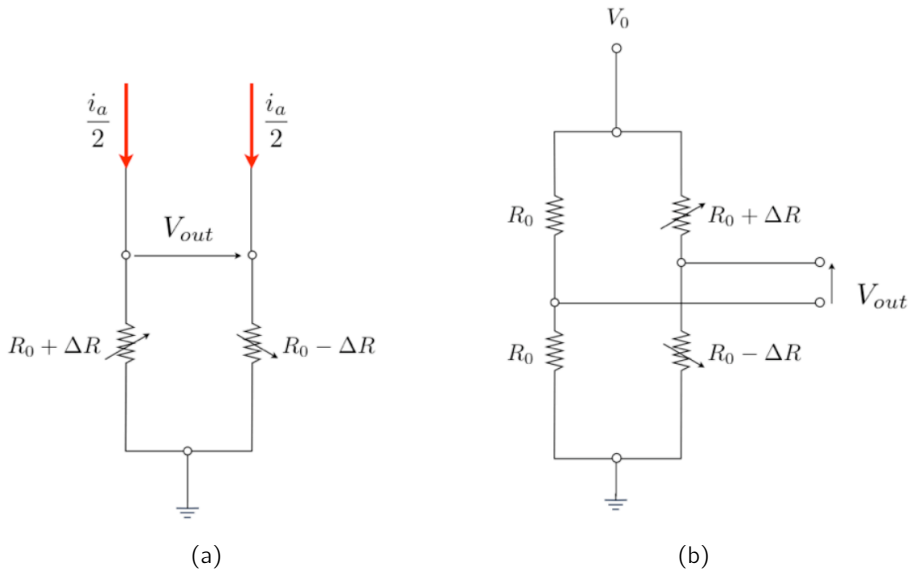

(a) (b)

Fig. 2.11: Two different configurations for signal readout: (a) constant current supply; (b) constant voltage supply.

In both cases, we find that sensitivity increases proportional to the magnetization M and the effective magnetic volume V_{mag}, where M is primarily given by material properties and V_{mag} can be modified by design of the MEMS structure. Sensitivity can also be raised by application of higher readout currents or voltages. Equally, gauge section A_g has to be minimized, as well as the lever arm d_g between gauge and fulcrum. The optimization of γ_g will be discussed in chapter 2.6. For the M&NEMS concept, applied current mode was chosen because only two resistances instead of four need to be included into design. This is advantageous because it enables to save space which would be required to establish electrical connections with the gauges for biasing and signal readout.

2.3.3 Full scale range

The full scale range of the sensor is determined by the maximum stress in the strain gauges. As a great advantage, piezoresistive strain gauges of crystalline Silicon exhibit high linearity over a large range [37]. However, a maximum stress in the gauges should not be exceeded in order to assure linear behaviour. For this reason, the full scale gauge stress σ_{FS} is set to 100MPa. σ_{FS} is far below the mean fracture stress of Silicon, which was measured to be 2.8GPa by Hu [39]. To ensure that the fracture stress of Silicon will not be reached in case of inertial shocks, edge stops are designed for the displaced Silicon structure which is directly connected to the gauges. By use of eqns. 2.11 and 2.12, the linear full scale range B_{FS} of the sensor is then given by

$$B_{FS} = \sigma_{FS} \frac{n_g d_g A_g}{\gamma_g M V_{mag}}. \tag{2.17}$$

According to equation 2.13 and with a piezoresistive constant $\pi_{pr} = 70 \times 10^{-11}$ Pa^{-1}, the theoretical linearity limit is reached for a variation in gauge resistance of 7%.

2.3.4 Resolution

Apart from the proper signal delivered by the sensor, different noise sources cause parasitic signals, which are superposed to the sensor's output signal and limit its resolution. There are interfering perturbations due to inductive or capacitive coupling with the sensor's environment and randomly generated signals caused by the sensor's proper components [40]. Latter influences are the most disturbing ones because they are statistical in nature. To develop a noise model of the sensor, we will hence principally focus on random noise. An approach to sensor design is to maximize its signal-to-noise ratio (SNR), which is defined as the mean-square signal over the mean-square noise, where the voltage noise power density is measured in $[V^2/Hz]$:

$$SNR = \frac{\overline{V_s^2}}{\overline{V_n^2}}. \tag{2.18}$$

So the first target is to design all sensor components in such way, that the resulting noise is minimized [41], [42]. The sensor's noise threshold limits the minimum detectable signal and is thus an important parameter to be optimized. We distinguish between intrinsic and extrinsic noise components which finally compose the total noise at the sensor's output [43]. Intrinsic noise comes from the sensitive element itself, which, in our case, is the piezoresistive strain gauge. Extrinsic noise sources are independent from the sensitive element and can be caused by random interactions of the sensor with its environment, or electronic noise, which is the input-referred equivalent noise of the first amplification stage. Four different noise sources are discussed in the following paragraphs and included to model the sensor's total noise.

Thermo-mechanical noise

Thermo-mechanical noise is generated by the Brownian motion, which is a thermally induced interaction between air molecules with the sensor's surface. It becomes an influent noise source in the case of miniaturized sensors [44]. This extrinsic noise is mechanically amplified through the sensor's sensitivity as it is transduced into a force acting on the strain gauges. If we consider thermo-mechanical noise as being uniformly distributed over the MEMS structure, it can be represented as a white noise of moment M_B which is transduced into a force acting onto the two nano-gauges. The sensor is designed for a frequency range of 0-20Hz, which is far below its resonance frequency $f_0 = \frac{\omega_0}{2\pi}$ (typical resonance frequencies of our sensor amount to several kHz). In this bandwidth, the spectral density of thermo-mechanical noise is constant over the entire frequency range. M_B^2 is measured in units of $[(Nm)^2/Hz]$ and calculated analog to Johnson noise in resistors (2.3.4):

$$M_B^2 = 4k_B T \frac{I\omega_0}{Q}. \tag{2.19}$$

Here, k_B is the Boltzmann constant, T the temperature, I the structure's mass moment of inertia with respect to its fulcrum, and Q the quality factor[5]. Referring to Fig. 2.10, any of

[5]The quality factor is a dimensionless paramater representing the influence of damping on the sensor. Squeeze film air damping has an important impact on MEMS devices because of prevailing surface forces over volume forces [45]. In our case, quality factors in the range about 10 are assumed, based on experimentally obtained estimations on M&NEMS accelerometers in our laboratory. In order to reduce the influence of Thermo-mechanical noise, increased quality factors are required which may be reached by operating the sensors in vacuum environment.

the two strain gauges then experiences the force

$$F_g = \gamma_g \frac{M_B}{2d_g}. \tag{2.20}$$

Given that the sensor's gauge configuration was conceived for readout by an applied current, the resulting signal induced by mechanical-thermal noise is then calculated by

$$V_{B_i} = i_a \Delta R = i_a R_0 \pi_{pr} \gamma_g \frac{\sqrt{k_B T \frac{I\omega_0}{Q}}}{d_g A_g}, \tag{2.21}$$

where i_a is the current which is applied to the readout bridge, and A_g the section of the nano-gauge. If we consider the constant voltage case, the noise threshold is given by

$$V_{B_V} = V_0 \pi_{pr} \gamma_g \frac{\sqrt{k_B T \frac{I\omega_0}{Q}}}{2d_g A_g}. \tag{2.22}$$

Thermal noise (Johnson noise)

Johnson noise is an intrinsic property of any electrical resistor and caused by thermal agitation of mobile charges inside the resistance, which causes a voltage fluctuation. The amount of its power density is proportional to resistance and temperature and does not depend on frequency. Because of its constant spectral density, it is also often called white noise. To model Johnson noise, we represent the gauge as a perfect resistance R_0 in series with a voltage source V_J, which is exposed to the temperature T, as shown in fig. 2.12. Its spectral power density is given by

$$V_J^2 = 4 k_B T R_0 \tag{2.23}$$

and measured in [V^2/Hz].

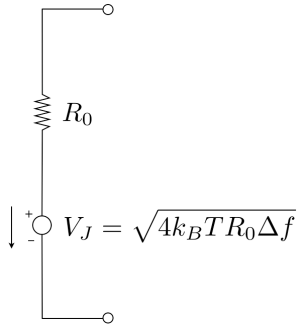

Fig. 2.12: Modeling Johnson noise in a piezoresistive gauge

1/f - noise

1/f - noise is an intrinsic property of the piezoresistive strain gauge. Its spectral density decreases with frequency, therefore the name. A theoretical base to explain this phenomenon has not been clearly established yet, but its origin has been explained by fluctuation in electrical conductivity [41]. This is caused by crystal defects (traps), which favor fluctuation in

mobility and in the number of charge carriers [46]. If we consider the applied current mode for our sensor, the spectral density of 1/f noise (measured in [V^2/Hz]) is described by the empirical Hooge's relation

$$V_{F_i}(f)^2 = \frac{V^2\alpha}{Nf} = \frac{i_a^2 R_0^2 \alpha}{4Nf}, \tag{2.24}$$

where f is the frequency and N the number of free charge carriers inside the piezoresistive gauge, given by

$$N = n_D A_g l_g, \tag{2.25}$$

and n_D is the carrier density. The Hooge's constant α is a material-specific constant indicating the lattice quality. The better the lattice quality, the lower the value of α. Values for α have been measured to be in the range of $10^{-7} \leq \alpha \leq 2 \times 10^{-3}$ [47]. As shown by Vandamme and Oosterhoff [47], annealing of ion-implanted resistors reduces the amount of crystal defects as well as the amount of 1/f noise. They found the empirical relation between the dimensionless Hooge's parameter α and the annealing temperature T_{an}

$$\alpha \propto e^{\frac{\Delta E}{kT_{an}}},$$

with $\Delta E = 1.1eV$. The amount of 1/f noise for a special bandwidth $\Delta f = f_{max} - f_{min}$ referred to Δf is then given by integration of eqn. 2.24 over the bandwidth:

$$\frac{V_{F_i}^2}{\Delta f} = \frac{1}{\Delta f}\int_{f_{min}}^{f_{max}} \frac{i_a^2 R_0^2 \alpha}{4Nf} \mathrm{d}f = \frac{i_a^2 R_0^2 \alpha}{4N\Delta f} \ln\left(\frac{f_{max}}{f_{min}}\right). \tag{2.26}$$

If we consider the constant voltage case, we get respectively:

$$\frac{V_{F_V}^2}{\Delta f} = \frac{V_0^2 \alpha}{N\Delta f} \ln\left(\frac{f_{max}}{f_{min}}\right). \tag{2.27}$$

1/f noise diverges, if the lower bandwidth limit f_{min} tends towards zero. In practice, as the time needed for observation of 1/f noise grows with decreasing frequencies, the lower bandwidth limit is often set to values of 10^{-2} or 10^{-3} Hz.

Amplifier noise

The amount of noise coming from the signal amplification unit is independent from the sensor itself and cannot be influenced by design. Noise added at the pre-amplification stage is especially critical because of the amplifier's gain. All noise added by the amplification stage until the sensor output can be expressed as a noise which is referred to the amplifier's input. Today's low-noise-amplifiers (LNA) have an input-referred noise floor V_A in the order of some nano-volts[6]:

$$10^{-9}\frac{V}{\sqrt{Hz}} \leq V_A \leq 5 \times 10^{-8}\frac{V}{\sqrt{Hz}}.$$

[6] mentioned in [48]

Total noise

If we consider now the resulting signal of all noise sources, we get the sensor's total noise threshold, which will be the crucial limit for the sensor's resolution. As the noise sources are uncorrelated, we have to consider the root-mean-square (RMS) of the sum of n noise contributions:

$$V_N = \sqrt{\sum_{i=1}^{n} V_i^2} \tag{2.28}$$

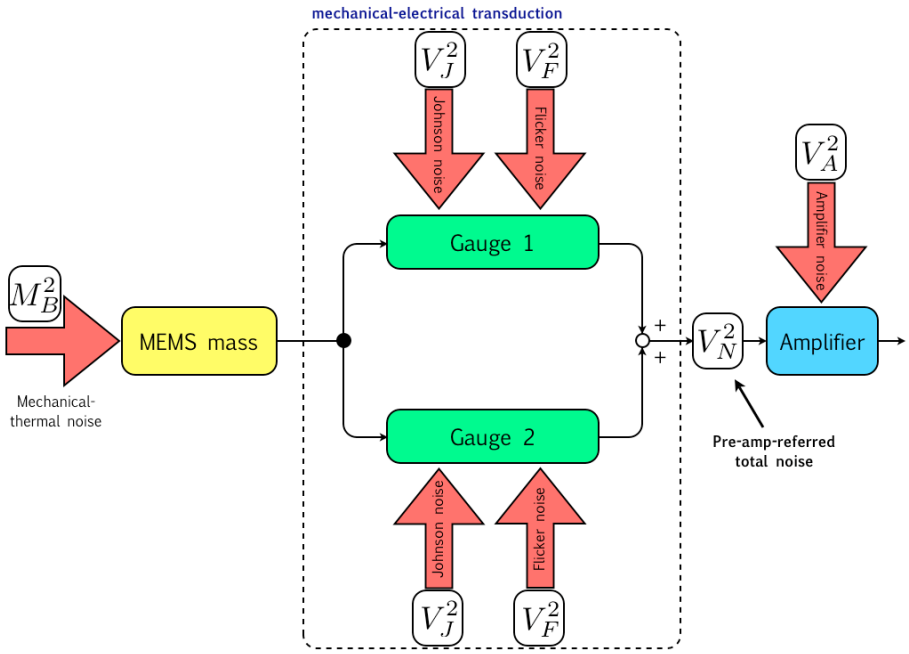

Fig. 2.13: Noise model for the applied current case with two piezoresistive strain gauges

Based on the total noise model presented in fig. 2.13, the total noise spectral density V_N^2 is then calculated by

$$V_N^2 = 2\left(V_J^2 + V_F^2\right) + V_B^2 + V_A^2, \tag{2.29}$$

leading to a total noise floor of

$$V_N = \sqrt{2\left(V_J^2 + V_F^2\right) + V_B^2 + V_A^2} \tag{2.30}$$

Intrinsic noise sources can basically be influenced by geometrical parameters and the properties of the gauge (A_g, l_g and d_g), by mechanical properties of the hinge (γ_g), and by doping (n_D). Apart from 1/f noise, the mean square amount of other noise sources is constant over the entire frequency range. As the magnetometer is conceived to be operated at low frequencies up to 20Hz, 1/f noise is the dominant noise source at this scale, as shown in fig. 2.14. The quantitative evaluation of the different spectral noise power densities is based on the assumptions listed in table 2.7.

Parameter	Symbol	Value	Unit
Bias current	i_a	100	μA
Gauge resistance	R_0	1840	Ω
Piezoresistivity coefficient	π_{pr}	70×10^{-11}	Pa^{-1}
Boltzmann constant	k_B	1.3807×10^{-23}	J/K
Density of Silicon	ρ	2329	kgm^{-3}
Elasticity modulus of Si	E_{110}	169	GPa
Hooge's constant	α	10^{-5}	-
Carrier density	n_D	5×10^{25}	m^{-3}
Gauge section	A_g	250×250	$(nm)^2$
Gauge length	l_g	5	μm
Distance gauge-fulcrum	d_g	2.5	μm
Dimensions of Silicon mass	-	300×300×10	$μm^3$
Hinge correction coefficient	γ_g	1	-
Temperature	T	293	K
Quality factor	Q	10	-

Table 2.7: List of assumptions made for quantitative evaluation of different spectral noise power densities

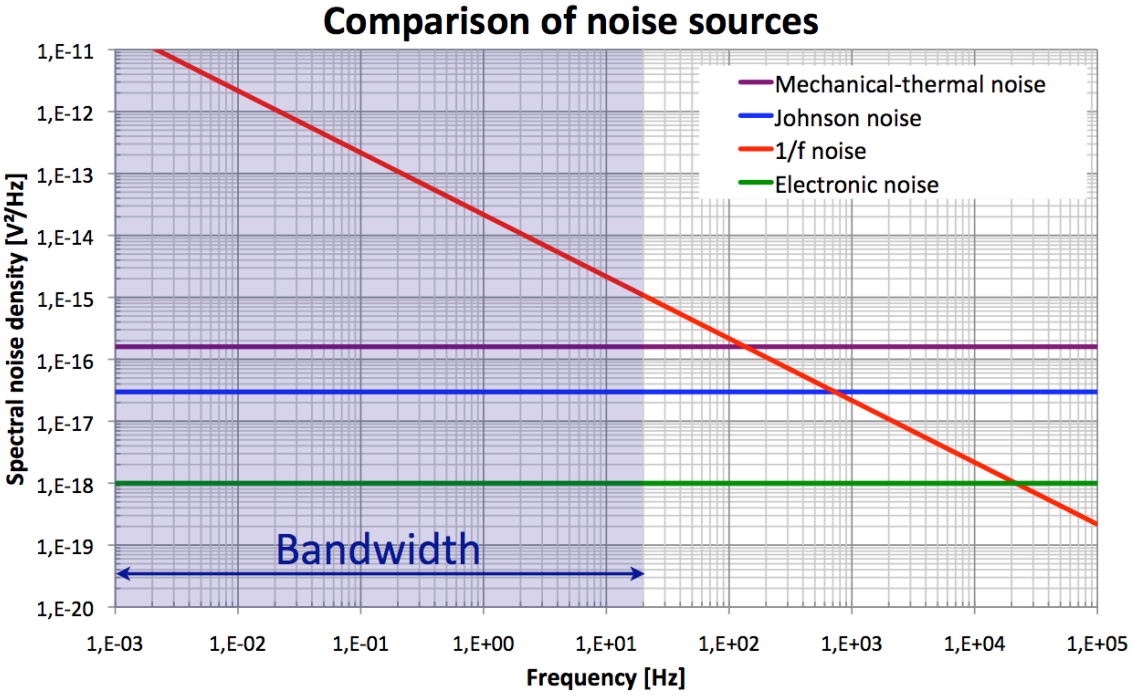

Fig. 2.14: 1/f noise is predominant in the low-frequency range

Resolution

Based on the developed noise model, the sensor's resolution is calculated by the amount of noise over sensitivity:

$$R = \frac{V_N}{S}. \tag{2.31}$$

A comparison of sensor resolutions between two options of integrated magnets is shown in fig. 2.15. As briefly mentioned in section 2.2.2, one option to integrate magnets in the sensor is the embedding of hard magnetic material (NdFeB); a second option consists in deposition of exchange-bias coupled antiferromagnetic (PtMn) and ferromagnetic (CoFe) thin layers. Presumptions made for calculation are the same as presented in table 2.7. In addition to these presumptions, geometric and magnetic properties were assumed as presented in table 2.8. It should be noted that the maximum integratable thickness of magnetic material was limited by technological constraints. This aspect will be further discussed in chapter 3.

Parameter	NdFeB	CoFe/PtMn
Volume V_{mag} [m^3]	63000µm^2×1µm	135000µm^2×100nm
Magnetization μ_0M [T]	0.7	1.8

Table 2.8: Assumed geometric and magnetic properties for calculation of the sensor's resolution. The magnetization of NdFeB is given for the isotropic case. The value for CoFe/PtMn is the magnetization of CoFe. Referred to the complete multilayer stack, magnetization is reduced depending on the thickness of the antiferromagnet.

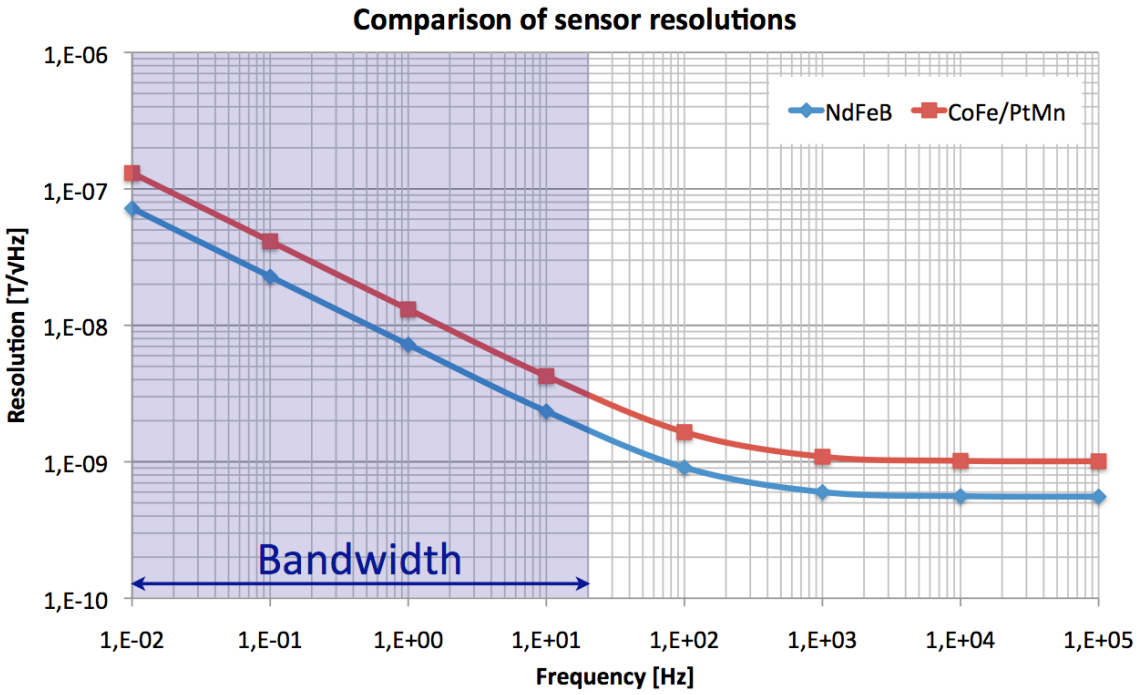

Fig. 2.15: Evaluation of sensor resolutions for two different integrated magnets.

As the graph shows, the sensor's resolution is dominated by 1/f noise in both cases, if a

bandwith of 20Hz is defined. Predominance of particular noise sources allows to reduce the complexity of the presented noise model by neglecting weak noise sources. A case study for both polarization methods (constant voltage and constant current) and for predominance of the two intrinsic noises arising from the nano-gauges is presented in section 2.4.1.

2.3.5 Summary

Most important aspects concerning sensor performances can briefly be summarized as follows:

- sensitivity is proportional to the volume of magnetic material and to remanent magnetization. The small section of nano-gauges leads to sensitivity amplification as $S \propto 1/A_g$. A further important influence on sensitivity is the mechnical stiffness of the MEMS structure's suspension, which has to be minimized.
- linear full scale range is limited by the maximum acceptable mechanical stress in the nano-gauges for which the linearity of the relation $\Delta R/R \propto \pi_{pr}\sigma$ is given. This maximum stress was fixed to 100MPa.
- 1/f noise is predominant in the specified bandwidth of 15Hz.

2.4 Design of piezoresistive strain gauges

2.4.1 Geometry optimization for noise reduction

Now, the noise model developed in section 2.3.4 will be applied to optimize the geometrical design of the piezoresistive strain gauges. In calculation, the number of gauges is $n_g = 2$. For the design of nano-gauges, it is reasonable to consider exclusively the *intrinsic* noises generated on the gauge level, thus Johnson noise and 1/f noise.

Case study for 1/f noise

Especially 1/f noise is critical in the low-frequency range, as shown in fig. 2.14. Another important point is the predominance of 1/f noise due to small gauge sizes. By interpretation of eqn. 2.24 it could be found that reduction of gauge size raises the amount of 1/f noise, because V_F^2 is inversely proportional to the amount of carriers which decreases proportionally to volume. So we consider 1/f noise to be predominant, which enables to neglect other noise sources and find the following expression of the sensor's resolution R_i in the case where current is applied to the gauges, using eqns. 2.15 and 2.26:

$$R_{i,1/\mathrm{f}} = \frac{d_g}{\pi_{pr}\gamma_g M V_{mag}} \sqrt{\frac{\alpha A_g}{n_D l_g}} \sqrt{\frac{\ln\left(\frac{f_{max}}{f_{min}}\right)}{\Delta f}} \tag{2.32}$$

If the case of a constant voltage is studied, we get the same relation multiplied by 4:

$$R_{V,1/\mathrm{f}} = 4R_{i,1/\mathrm{f}} \tag{2.33}$$

Important parameters which appear in equation 2.32 are reminded in fig. 2.16.

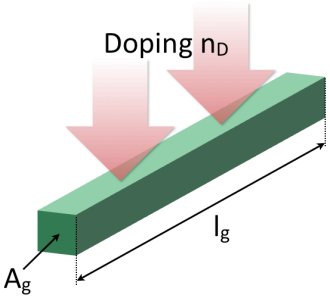

Fig. 2.16: Illustration of the important parameters to be considered for design of the nano-strain-gauge

Interpretation of the formula shows that several parameters can be designed for reduction of the sensor's resolution. Gauge section A_g and the distance d_g between gauge and pivot of the MEMS structure should be minimized, the gauge length l_g maximized. The Hooge's constant α is inherent to the gauge, but its value can be manipulated by annealing [47]. The resolution can also be reduced by higher doping n_D. Other parameters are primarily determined by design of the MEMS structure (hinge absorbtion factor γ_g and magnetic volume V_{mag}) and by the magnetization M of the magnetic material. If 1/f noise is considered to be the only noise source, polarization does not affect the resolution.

Case study for Johnson noise

To get an idea of the influence of Johnson noise on the sensor's resolution, we neglect any other noise source. If we consider the constant current case, we find for the resolution by using eqns. 2.23 and 2.15:

$$R_{i,\text{Johnson}} = \frac{4d_g}{i_a \pi_{pr} \gamma_g M V_{mag}} \sqrt{\frac{A_g^3 k_B T}{\rho_{Si} l_g}} \tag{2.34}$$

For the constant voltage case, we get respectively

$$R_{V,\text{Johnson}} = \frac{8d_g}{V_0 \pi_{pr} \gamma_g M V_{mag}} \sqrt{A_g l_g \rho_{Si} k_B T} \tag{2.35}$$

As it is intended to use the constant current mode for signal readout, we find for both, 1/f and Johnson noise, that the gauge section A_g and the distance d_g between gauge and pivot have to be minimized, while l_g should be maximized in order to minimize the noise amount. Different from 1/f noise, the amount of Johnson noise can be reduced by increasing the bridge current or voltage. A minimum gauge polarization is required in order to achieve the specified resolution. As an example, the minimum polarization current can be estimated from eqn. 2.34, based on the assumptions listed in tables 2.7 and 2.8. It is $\sim$ 400nA for magnetometers using NdFeB and $\sim$ 700nA for magnetometers using coupled CoFe/PtMn multilayers.

2.4.2 Euler buckling

For a reliable working principle, we assume an ideal case in which both gauges are submitted to the same amount of mechanical stress and that its sign does not affect the linearity of the

piezoresistive effect. In particular, the case of Euler buckling of the gauges due to compressive stress is excluded. For elastic beam buckling (assuming that both ends are fixed), the critical compressive stress σ_c is calculated by

$$\sigma_c = 4\frac{\pi^2 E I}{A_g l_g^2}, \tag{2.36}$$

where E is the gauge's elasticity modulus in the (110) direction, I its second moment of area, A_g its section and l_g its length. In case of a quadratic section of $A_g = t_g^2$, critical stress becomes

$$\sigma_c = \frac{\pi^2 E t_g^2}{3 l_g^2}. \tag{2.37}$$

For a Silicon strain gauge with variable length and constant $t_g = 250\text{nm}$, critical stress is shown in figure 2.17 and has to be taken into account for design. If a typical gauge length of 5µm is used, there is no buckling risk in the fixed linear full-scale range of 100MPa, because the critical stress is calculated to be 1.4GPa.

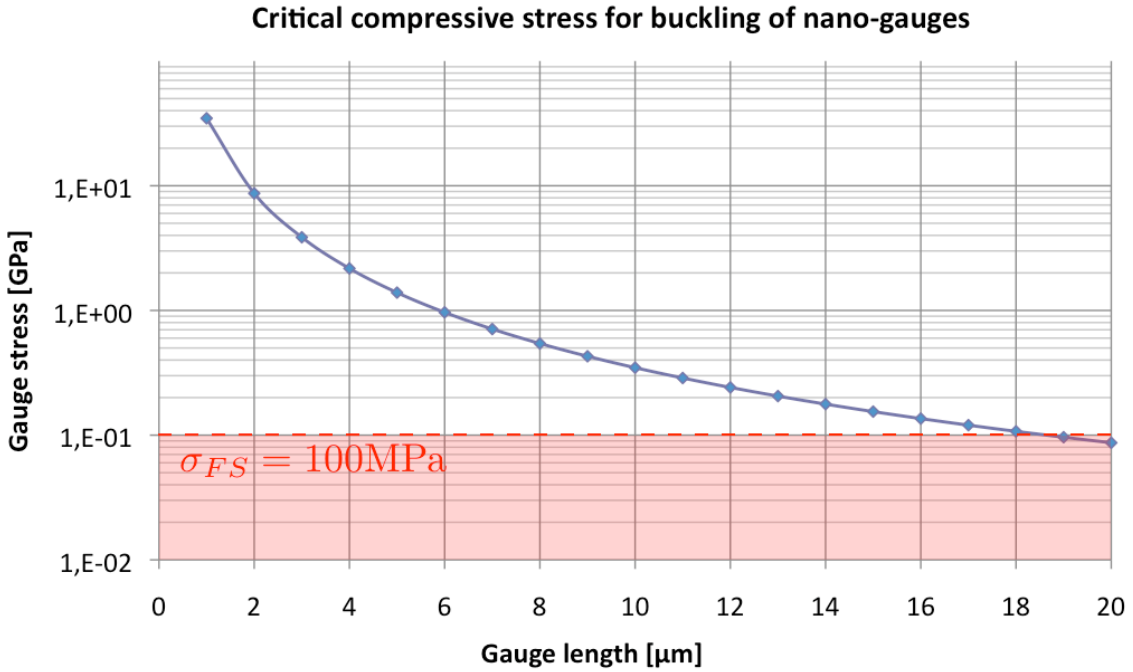

Fig. 2.17: Critical stress where Euler buckling of nano-gauges appears for different gauge lengths.

2.4.3 Gauge heating

After the study of design rules for noise reduction and consideration of Euler buckling, we will now take into account the effect of gauge heating for the case where a readout signal is applied. This effect has been used for several applications (e.g. for fuses in electrical circuits, for light sources etc.), using polysilicon microbridges [49]. In our case, it is a disturbing effect. Given that the gauges exhibit only a small cross-sectional area, high current densities are generated by a readout current. So the problem of heating deserves special consideration

for the given gauge dimensions. In the worst case, heat may destroy the gauges. An example for a damaged gauge due to heating is presented in figure 2.18(b). Other perturbing effects

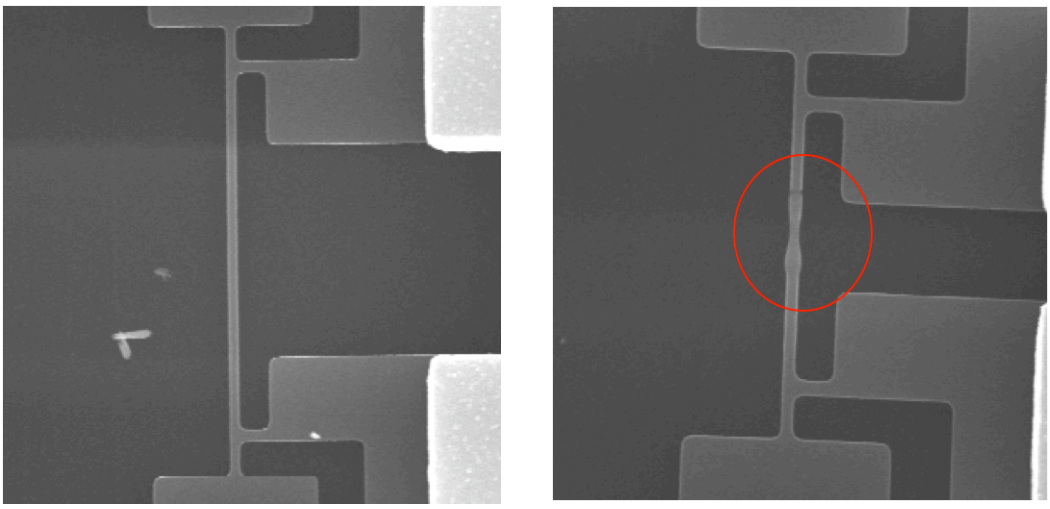

(a) (b)

Fig. 2.18: Influence of heating due to high current densities on silicon gauges: (a) A silicon gauge in its initial state; (b) Irreversible damage to the gauge due to heating.

consist in the modification of the sensor's performances as sensitivity and linear behaviour, because Silicon's resistivity and piezoresistive coefficient π_{pr} depends on temperature. To investigate this problem theoretically, we model a gauge with resistivity ρ_{Si} and of length l_g as presented in fig. 2.20 and assume it to be flown through by a current density j, so the density of power dissipated in the gauge is given by the relation

$$q = j^2 \rho_{Si}. \tag{2.38}$$

Heat transfer occurs by three different manners, namely by conduction, convection and radiation. In the case of conduction, thermal energy is transferred by matter through the kinetic energy of neighbor particles. For convection, energy is dissipated by heat exchange between the solid and an ambient fluid flow. Herein a distinction is made between forced convection, where the fluid flow is generated externally, and free convection, where the fluid flow is not induced by external influences. Radiation is dissipation of energy through electromagnetic waves according to Boltzmann law. In the considered application, the power dissipated by conduction can be estimated by

$$Q_{cond} = A_g \kappa \frac{\Delta T}{l_g}, \tag{2.39}$$

where l_g and A_g are length and section of the gauge, and κ the thermal conductivity of silicon. The power emitted by convection is given by

$$Q_C = h_T A_S \Delta T, \tag{2.40}$$

where A_S is the gauge surface adjacent to the surrounding medium and h_T is the heat transfer coefficient (measured in $\frac{\mathrm{W}}{\mathrm{m^2K}}$), which depends amongst others on the fluid density and on

the velocity of the fluid flow. At the chosen gauge scale, we are near vacuum conditions and it is appropriate to assume the case of free convection in an environment of steady air. The power dissipated by radiation is given by the relation

$$Q_R = A_S e \sigma \Delta T^4, \tag{2.41}$$

where e is the dimensionless emission ratio, varying between 0 and 1 for different surface conditions, and $\sigma = 5.67 \times 10^{-8} \frac{\mathrm{W}}{\mathrm{m^2 K^4}}$ the Stefan-Boltzmann constant. A comparison of the powers emitted by conduction, convection and radiation for different temperatures is given in figure 2.19, based on the assumptions listed in table 2.9. It shows that losses through convection and radiation are insignificant compared to the power dissipated through conduction within the considered temperature range.

Parameter	Symbol	Value
Gauge length	l_g	5µm
Gauge section	A_g	250×250 μm^2
Gauge surface	A_S	5μm^2
Thermal conductivity	κ	148 $\frac{\mathrm{W}}{\mathrm{mK}}$
Heat transfer coefficient	h_T	1 $\frac{\mathrm{W}}{\mathrm{m^2 K}}$
Emission ratio	e	1
Stefan-Boltzmann constant	σ	$5.67\times10^{-8} \frac{\mathrm{W}}{\mathrm{m^2 K^4}}$

Table 2.9: Assumptions for calculation of the power for different heat transfer modes. Geometrical dimensions of the gauge are representative for the gauges used in the application presented in this manuscript.

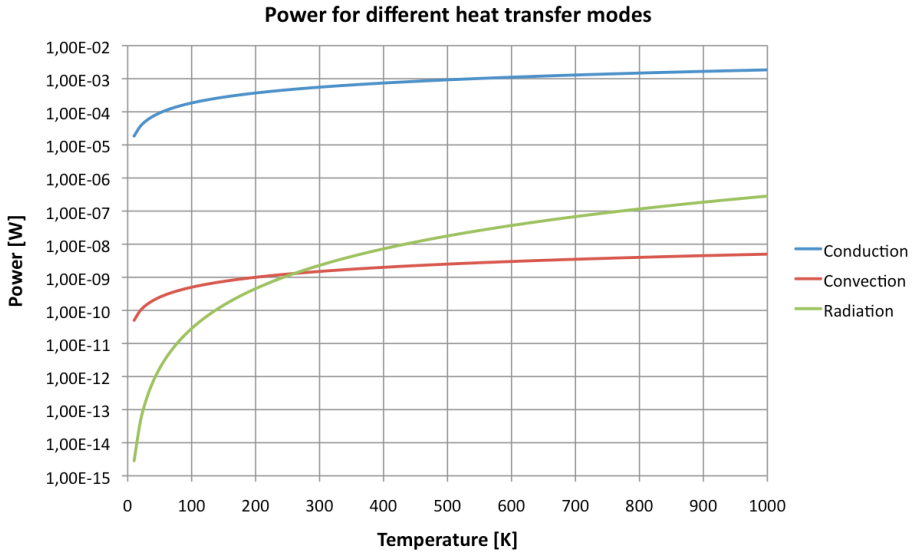

Fig. 2.19: Power dissipated by conduction, convection and radiation for different temperatures

Temperature profile along a nano-gauge

For modeling, we consider a silicon gauge to be fixed at both ends to infinitely large heat reservoirs as illustrated in fig. 2.20, with T_0 as the temperature at the gauge's boundaries. By neglecting surface-related effects of thermal exchange, heat transfer is assumed to occur along the x-direction only, so that the problem is reduced to a 1D-model. Based on the comparison given in figure 2.19, heat transfer through convection and radiation are neglected.

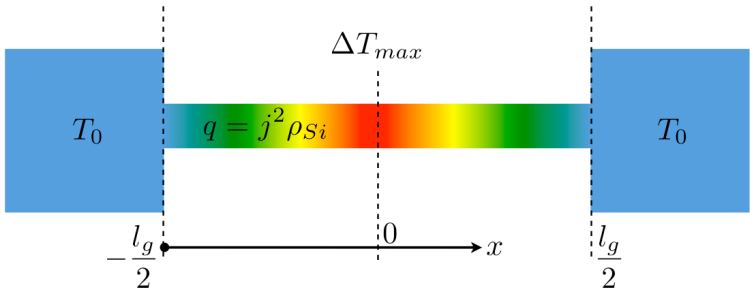

Fig. 2.20: 1D model of current-induced joule heating in a nano-gauge. The gauge is fixed to two infinitely large heat reservoirs, so that there is no temperature difference between the gauge's end and its clamping.

Heat transfer by conduction inside the a nano-gauge is described by the second-order differential equation

$$c\frac{\partial T}{\partial t} = \kappa\frac{\partial^2 T}{\partial x^2} + q, \tag{2.42}$$

where c is the specific heat capacity of the material and $q = j^2\rho_{Si}$ the dissipated power. Temperature dependency of resistivity will be taken into account by the first-order approximation

$$\rho(T) = \rho_{Si}(1 + \alpha_T(T - T_0)), \tag{2.43}$$

where α_T is the temperature coefficient of resistivity. In our problem, a steady-state case is assumed in which the time-dependent term vanishes, so that eqn. 2.42 becomes

$$\frac{\partial^2 T}{\partial x^2} + \frac{j^2\rho_{Si}\alpha_T}{\kappa}T = -\frac{j^2\rho_{Si}}{\kappa}(1 - \alpha_T T_0). \tag{2.44}$$

The temperature profile along $-\frac{l_g}{2} \leq x \leq \frac{l_g}{2}$ (l_g is the length of the nano-gauge) is obtained by solving of eqn. 2.44:

$$T(x) = \frac{1 - \alpha_T T_0}{\alpha_T}\left[\frac{\cos\left(j\sqrt{\frac{\rho_{Si}\alpha_T}{\kappa}}x\right)}{\cos\left(\frac{jl_g}{2}\sqrt{\frac{\rho_{Si}\alpha_T}{\kappa}}\right)} - 1\right] \tag{2.45}$$

Maximum heating is found at the center of the nano-gauge:

$$T_{max} = \frac{1 - \alpha_T}{\alpha_T}\left[\frac{1}{\cos\left(\frac{jl_g}{2}\sqrt{\frac{\rho_{Si}\alpha_T}{\kappa}}\right)} - 1\right] \tag{2.46}$$

An estimation of maximum heating of nano-gauges with $\rho_{Si} = 2.3 \times 10^{-5}\Omega$m, l_g=5µm and a section of $A_g = 250{\times}250\mu m^2$ is given in table 2.10. For numerical evaluation, the temperature coefficient of resistivity was assumed to be $\alpha = 1000$ppm/°C.

l_g	i=100µA	i=200µA	i=300µA	i=400µA	i=500µA
2µm	0.1	0.6	1.3	2.3	3.5
4µm	0.6	2.3	5.1	9.1	14.3
5µm	*0.9*	*3.5*	*8.0*	*14.3*	*22.6*
6µm	1.3	5.1	11.6	20.8	32.9
8µm	2.3	9.1	20.8	37.6	60.2
20µm	14.3	60.2	148.7	305.5	596.0

Table 2.10: Maximum heating in nano-gauges (in °C) with different lengths for different polarization currents. A resistivity of $\rho_{Si} = 2.3 \times 10^{-5}\Omega$m and a temperature coefficient of resistivity $\alpha_T = 1000$ppm/°C was assumed. The emphasized row for $l_g = 5$µm represents the case of the nano-gauges which were finally used in this work.

Effect of heating on gauge resistance

Due to the temperature dependency of resistivity, the gauge resistance is a function of temperature:

$$\mathrm{d}R = \frac{\rho_{Si}(1 + \alpha_T(T(x) - T_0))}{A_g}\mathrm{d}x, \tag{2.47}$$

where A_g is the gauge section. The total gauge resistance can then be expressed as

$$R_T = \int_{-l_g/2}^{l_g/2} \mathrm{d}R\mathrm{d}x = R_0 \left[1 - \alpha_T T_0 + \frac{\alpha_T}{l_g}\int_{-l_g/2}^{l_g/2} T(x)\mathrm{d}x\right] + C, \tag{2.48}$$

which is solved as

$$R_T = R_0 \left[\frac{2(1 - \alpha_T T_0)}{j l_g \sqrt{\frac{\rho_{Si}\alpha_T}{\kappa}}} \tan\left(\frac{j l_g}{2}\sqrt{\frac{\rho_{Si}\alpha_T}{\kappa}}\right) + 1\right]. \tag{2.49}$$

For verification of the model, nano-gauges with different lengths (6µm, 8µm and 20µm) were polarized by a current varying in the range of ±500µA, using an up-and-down ramp. The voltage over the resistance was measured by four-wire measurement. No hysteresis was observed in the applied range of polarization current, meaning that thermal effects had no irreversible impact on the gauges. As the current increases, the nonlinear evolution of voltage drop is well observed for growing gauge lengths, shown in figure 2.21. For fitting of the model to measurements, a Silicon resistivity of $\rho_{Si} = 1.44 \times 10^{-5}\Omega$m and an α_T of 1400ppm/°C were assumed[7]. The $V(i)$-curve was first fitted in the linear region (i.e. in the range of weak polarization currents) by application of a corrective factor for R_0 in order to take into account geometric dispersion of the gauge section. The variable fit parameter was the thermal conductivity. According to Li *et al.*, thermal conductivity in silicon nanowires can be reduced to two orders of magnitude below the value of bulk thermal conductivity and strongly depends on the diameter of the nanowire. This phenomenon was ascribed to increased phonon boundary scattering [50].

[7] The resistivity value is based on measurements which have been carried out by G. Jourdan on samples of the same batch (S274P).

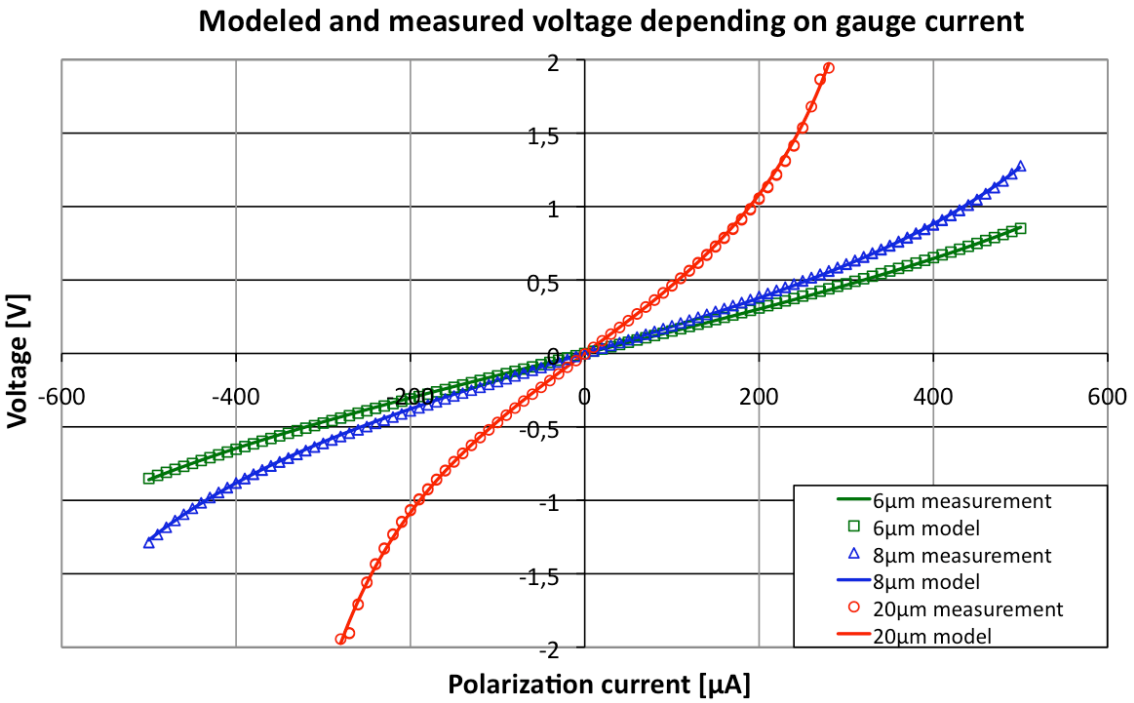

Fig. 2.21: Modeled and measured voltage as a function of the gauge polarization current

Parameters for the fitted model are listed in table 2.11. The values for κ are found to be one order of magnitude below thermal conductivity of bulk silicon ($\kappa_{Si,bulk} \sim 148 W/m/K$). Resistances were ~30% below theoretical values, indicating a reproducible technological error, as the fitted coefficients are close one to another.

Gauge length	Corrective factor for R_0	fitted value for κ
6µm	0.68	15
8µm	0.67	17
20µm	0.64	25

Table 2.11: Parameters for fitted model

Time-dependency of temperature

A further issue to be taken into account is the variation of gauge temperature in time. Once the polarization is applied to the gauge, the temperature increases in time until it reaches its stationary limit. In this transition region, resistance varies and disturbs a proper signal readout. This is of special importance when polarizations other than DC signals are applied, as a thermally induced $\frac{\Delta R}{R}(t)$ limits the readout current frequency. Simulations were done in order to evaluate the transient of temperature for different gauge lengths (2, 6, 8 and 20µm). As shown by fig. 2.22, the duration of the transition region depends on the gauge length.

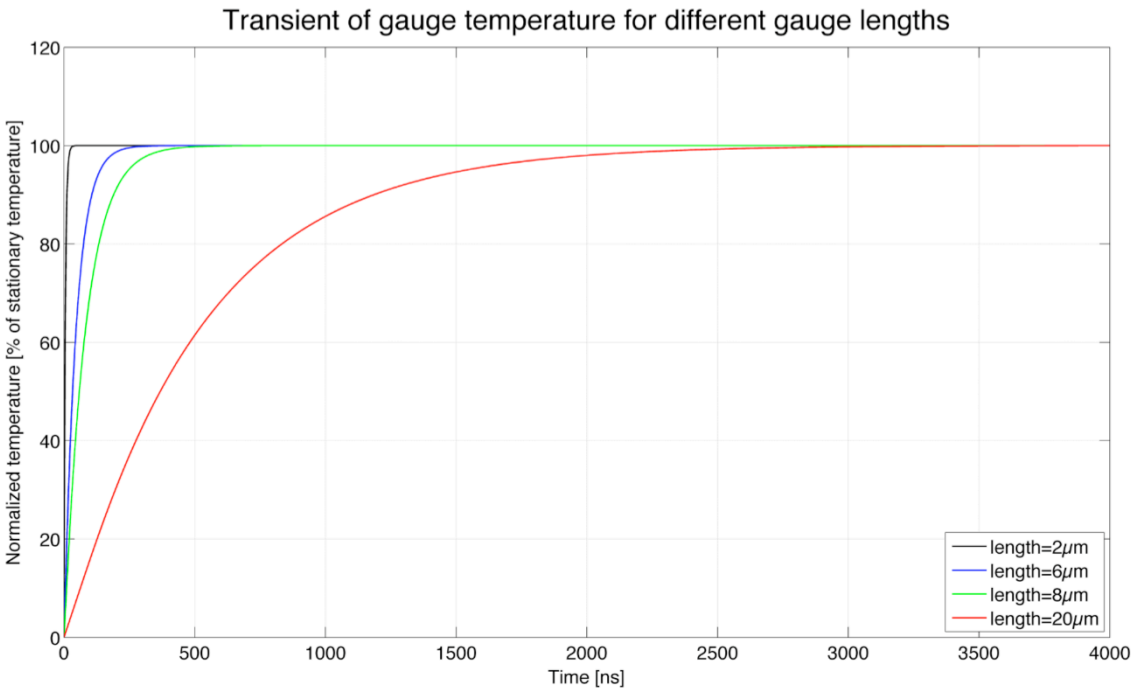

Fig. 2.22: Simulation (COMSOL) of the temperature transient for different gauge lengths and a polarization of 100µA.

For typical gauge lengths of 5µm, saturation times for temperature are inferior to 0.5µs. This is disturbing for AC gauge polarization in the range below 1MHz, as the temperature follows the polarization. For higher polarization frequencies, temperature reaches a steady state after a short raise time.

Summary

It has been shown that sensor resolution benefits from a reduction of gauge section and from an increased gauge length. However, gauge heating is amplified by smaller gauge sections, and evacuation of generated heat inside a gauge is impeded for greater gauge lengths. Therefore, the retained heat causes resistance and transient time of the temperature to increase, leading to a nonlinear behaviour of the relation between voltage drop and polarization current. We conclude that effects coupled to signal-induced heating constrain the design of a piezoresistive nano-gauge, so that its geometry has to be adapted according to the used readout signal. A gauge with a section of $250 \times 250\text{nm}^2$ and a length of 5µm is a good compromise.

2.5 Design of MEMS structures

As already pointed out in section 2.2.1, three independent MEMS structures with different rotation axes are required. For design of these structures, different aspects have to be taken into account like technological feasibility, correct integration of magnetic material and optimized structure geometries for minimization of the sensor's sensitivity to acceleration.

2.5.1 Optimization for integration of magnetic material

As the sensor's working principle requires integrated magnets, the optimization of their integration into the MEMS device is of great importance. This particularly implies maximization of the volume of magnetic material, but also consideration of technological boundary conditions as well as the disposition of magnets in favour of the aimed magnetization direction. According to equation 2.15, the amount of integrated magnetic material has to be maximized in order to enhance the sensing performances of the compass to be designed. However, the achievable volume of magnetic material is limited by the surface of the silicon support element.

To estimate the required magnetic volume V_{mag} for both cases of integrated magnetic material, i.e., NdFeB as hard magnetic material and alternating thin CoFe/PtMn layers as coupled ferromagnetic and antiferromagnetic (F/AF) materials, we assume 1/f noise in our sensor to be predominant, so its resolution is determined by eqn. 2.32. Our estimation is based on the typical sensor parameters presented in table 2.12. Furthermore, we presume in-plane remanence of 0.7T for NdFeB and 1.8T for the coupled thin F/AF layers. For

Parameter	Symbol	Value	Unit
Gauge section	A_g	250×250	nm^2
Gauge length	l_g	5	µm
Distance gauge-fulcrum	d_g	5	µm
Hinge factor	γ_g	1	-
Piezoresistive constant	π_{pr}	70	$10^{-11}Pa^{-1}$
Charge carrier density	n_D	5×10^{25}	m^{-3}
Hooge parameter	α	10^{-5}	-

Table 2.12: Assumed parameters for estimation of the magnetic volume V_{mag}

the specified resolution of 500nT in a bandwidth of 20Hz, the minimum needed magnetic volume is listed in table 2.13. The minimum required magnetic volume can be represented by a square of magnetic material with a specific thickness. These thicknesses are mainly imposed by technological constraints, as further detailed in chapter 3. It can be seen that magnetic material of these dimensions fits well for integration devices of typical MEMS dimensions.

	Required magnetic volume	Magnet thickness	Square side length
NdFeB	$3.5 \times 10^{-15}m^3$	1µm	$\sim$ 60µm
CoFe/PtMn	$1.4 \times 10^{-15}m^3$	100nm	$\sim$ 120µm

Table 2.13: Minimum required magnetic volume for NdFeB and AF/F multilayers

As it is intended to release the MEMS structure by an isotropic HF etching process by complete removal of the sacrificial oxide layer underneath the structure, etching holes have to be included which will traverse the silicon brick. These holes reduce the etching time and make the release process becoming more reliable. The required etching time to entirely release the structures is determined by the distance between etching holes and etching speed. In both technological approaches, the disposition of etching holes requires a fragmentation

of the magnets in order to avoid their perforation.

Ideally, the magnetic material should be uniformly distributed over the support structure for insensitivity to magnetic field gradients. If a magnetic field exhibits a gradient, a magnet surrounded by this field experiences a force which is proportional to the gradient of the magnetic field:

$$F_x = V_{mag} M \frac{\partial B}{\partial x}, \tag{2.50}$$

where the magnet has volume V_{mag} and magnetization M and B is the magnetic field. If F_x acts at a lever arm distance l from the fulcrum, a moment Γ_{grad} is induced which relates to the magnetic moment $\Gamma_{mag} = M V_{mag} B$ induced by earth magnetic field as

$$\frac{\Gamma_{grad}}{\Gamma_{mag}} = \frac{l}{B} \frac{\partial B}{\partial x}. \tag{2.51}$$

To assess the magnitude of the magnetic field gradient which would lead to $\Gamma_{grad}/\Gamma_{mag} = 1$, we assume the parameters listed in table 2.14. A magnetic field gradient of $\sim$ 333mT/m

Parameter	Magnitude	Characteristics
B	50µT	Typical for earth's magnetic field
$\mu_0 M$	0.7T	In-plane remanence magnetization of NdFeB
l	150µm	lever arm between magnetic force and pivot

Table 2.14: Parameters for estimation of the magnetic field gradient

would be necessary for generation of a moment which is of the same order of magnitude as the moment induced by the magnetic field of the earth. This is a very large and untypical perturbation, so that the influence of typical external magnetic field gradients is negligible for the given example. However, a 3-axis magnetometer consists of three individual structures (fig. 2.4). There is thus a perturbation magnetic field generated by neighbour structures. To evaluate the impact of these perturbations, we assume a magnet with dimensions of $500 \times 500\mu m^2$ and a magnetization of $\mu_0 M = 0.7$T, which is representative for a 1D-magnetometer. Its surrounding magnetic field was calculated with MATLAB and is shown in fig. 2.23[8]. Greatest field magnitudes are found along the magnet's center line in the direction of magnetization, therefore it is interesting to consider the magnetic field along this axis. Assuming a distance of 1000µm between two neighbour magnets, we find a mean magnetic field gradient of about 130mT/m (fig. 2.24).

[8]For calculation cf. appendix A.

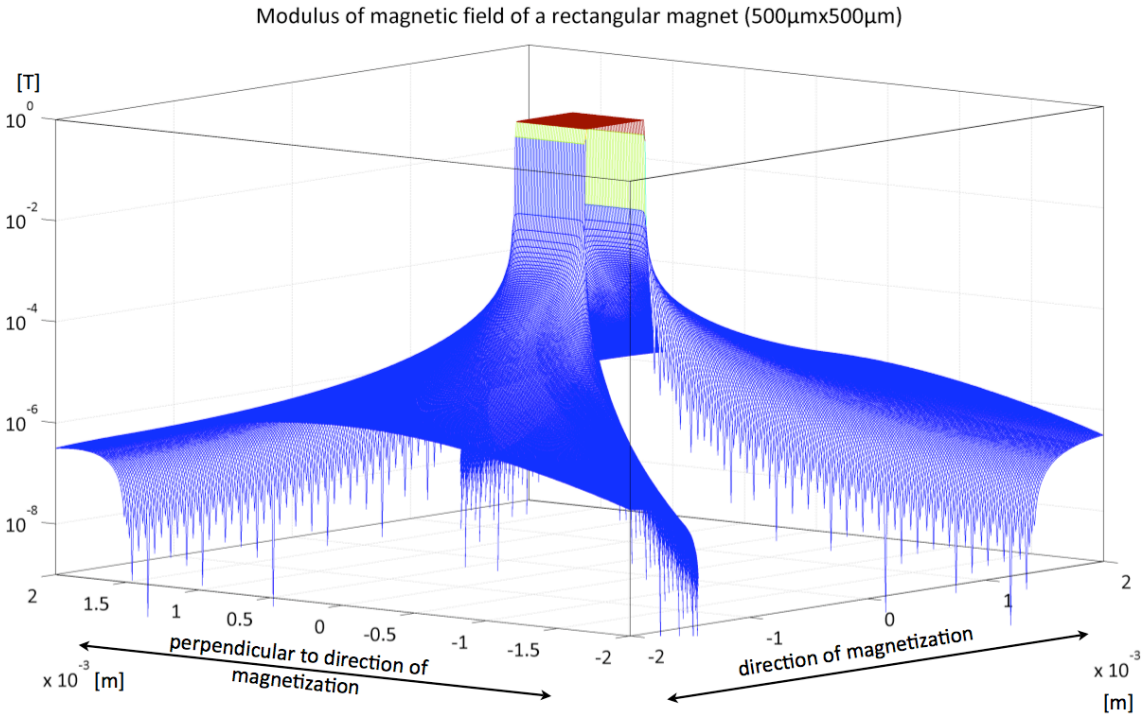

Fig. 2.23: Calculated magnetic field of a permanent magnet with a magnetization of 0.7T and a size of $500 \times 500 \times 1\mu m^3$. Greatest field magnitudes are situated along the direction of magnetization.

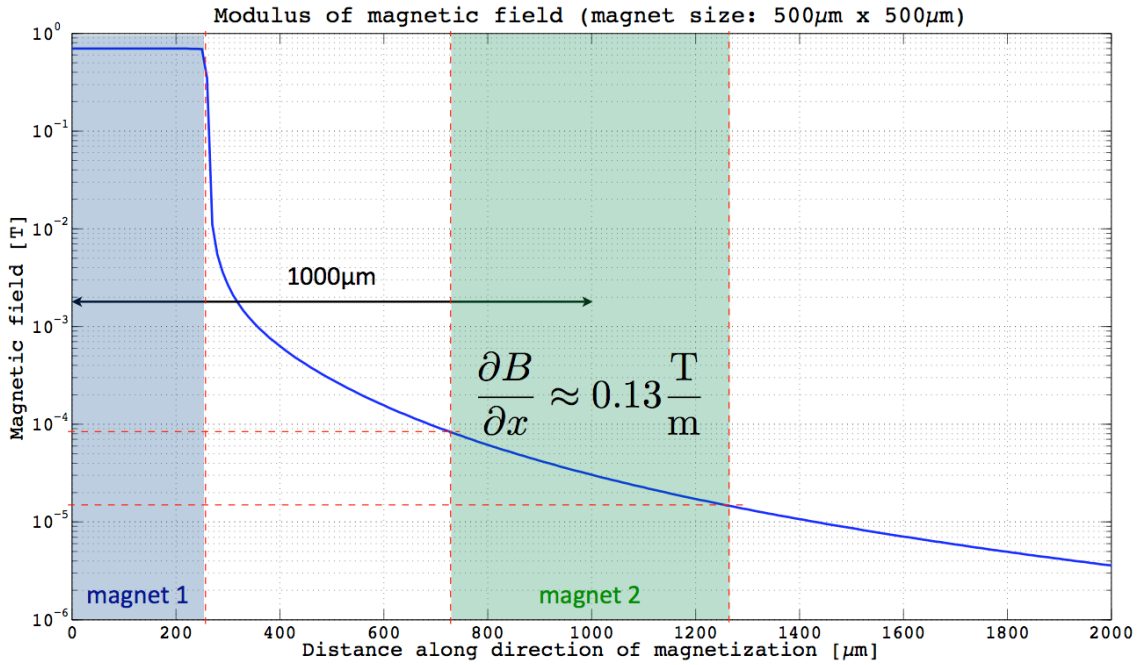

Fig. 2.24: Magnitude of the magnetic field along the direction of magnetization of the same magnet as is in fig. 2.23.

This field gradient is high enough to induce a signal which is situated in the same order of

magnitude as the intrinsic signal to be measured. Thus, it is important to distribute the magnetic material uniformly over the entire MEMS structure, so that the same forces are generated on each side of the structure, leading the resulting torque around the rotation axis to vanish (fig. 2.25). Otherwise, a torque would be generated on the structure due to unequilibrated forces which leads to an offset in the sensor signal. This is actually the case if the field gradient is not constant, i.e. $d^2B/dx^2 \neq 0$. Such field gradients are difficult to be taken into account for design. The influence of the magnetic field generated by adjacent magnetometer structures on an individual magnetometer structure leads to a perturbing sensor offset. This offset depends on the distance between individual structures and has to be compensated by the electronics part. Another more challenging option would consist in a more enhanced sensor design.

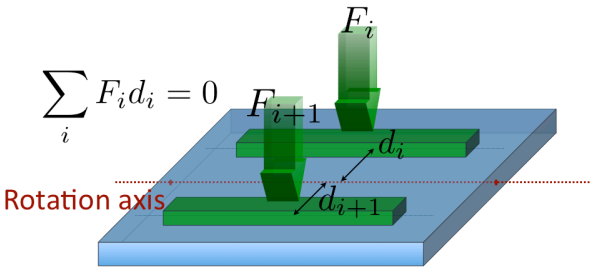

Fig. 2.25: Distribution of the magnetic volume over the structure in a way that the torque resulting from forces generated by a magnetic field gradient is eliminated.

A further aspect to be considered for integration of magnetic materials is the direction in which the integrated magnets have to be magnetized. This depends on the sensitivity direction which has been designed for the sensor (fig. 2.4). For realization of a 3D compass, two different magnetization directions are required. Magnetic anisotropy is used in the case of stacked ferromagnetic and antiferromagnetic layers in order to orientate the direction of magnetization by design of an appropriate geometry of the magnetic layers. For hard magnetic material, no geometrical design constraints are given because no anisotropic effect is used.

2.5.2 Minimization of inertial effects

A further point to be taken into account for design of the MEMS structures is the appearance of effects due to their inertia. The integration of magnets in thick Silicon bricks as explained above leads the sensor to become a typical mass-spring system, as it is suspended by a hinge and connected to two nano-gauges. If the hinge is situated in the middle of the two nano-gauges, the stiffness k of the system will be dominated by the stiffness of the two nano-gauges:

$$k = \frac{2EA_g}{l_g} d_g^2, \tag{2.52}$$

where E represents the gauges' Young's modulus, A_g their section, l_g their length and d_g their distance with respect to the rotation axis. The sensor's resonance frequency ω_0 can then be estimated by:

$$\omega_0 = \frac{1}{2\pi}\sqrt{\frac{k}{I}}. \tag{2.53}$$

I is the moment of inertia of the Silicon structure with respect to its rotation axis which is given by

$$I_{ip} = \frac{m}{12}\left(W^2 + L^2\right) \tag{2.54}$$

for in-plane structures and

$$I_{oop} = \frac{m}{12}\left(T^2 + L^2\right) \tag{2.55}$$

for out-of-plane structures. Here, m is the mass of the structure, W its width, L its length and T its thickness. Hence, the sensor is generally susceptible to vibration. An approximation for the sensor's resonance frequency is obtained by assuming the typical parameters listed in table 2.15 and a thickness T of the Silicon support element: The resonance frequency is

E	A_g	l_g	d_g	$W = L$	T	f_0
169MPa	$6.25 \times 10^{-14}\text{m}^2$	10µm	2.5µm	300µm	10µm	20kHz

Table 2.15: Parameters for evaluation of the sensor's resonance frequency.

found to be situated in the 20kHz range. Thus, there is no critical limitation for the target application, because typical frequencies of only 20Hz are expected here. Nevertheless, a quasi-static displacement of the mobile structure can be induced at any time by acceleration. Basically, the structure's moment of inertia intervenes for angular accelerations and its mass for translational accelerations. It has already been shown in chapter 1 that the impact of angular accelerations is negligible compared to the sensor's main sensitivity for a magnetic field, if typical sensor dimensions remain unchanged. However, an unwanted output signal of the sensor may be induced at any time due to translatonial accelerations, in dependence of their direction. Another problem consists in the mechanical fragility of the nano-gauges, which may be overstressed during incidents like inertial shocks and so lead to the sensor's destruction. To prevent the latter problem, bulk stops can be conceived in order to limit the maximum possible displacement of the structures. Those have to be designed according to the critical strain of the nano-gauges, but the distance between Silicon structure and bulk stops cannot be chosen arbitrarily small due to technological limitations. Another possibility is to reduce size and mass of the Silicon support structure in order to reduce the resulting force upon the nano-gauges which is caused by acceleration. Once the mechanical resistivity of the device is assured, further measures have to be taken for minimization of a possibly generated disturbing signal. Any discrete volume of a body with constant density ρ being subjected to an acceleration as presented in figure 2.26 experiences the force

$$\mathrm{d}F = \rho a. \tag{2.56}$$

The resulting torque experienced by the body with respect to its rotation axis R is given by

$$M = \int_V x \mathrm{d}F \mathrm{d}V, \tag{2.57}$$

where x_i is the distance of a discrete volume element in perpendicular direction to the rotation axis and F_i the force experienced by this volume element. In figure 2.26(a), the center of gravity is distant from the rotation axis which results in a torque, if the structure is subjected to acceleration. In figure 2.26(b), the center of gravity is situated inside the rotation axis,

so that the torque disappears. A torque around the rotation axis caused by acceleration superposes an undesired part to the actual signal delivered by the sensor. For this reason, all inertial structures in this work are designed in a way that their center of gravity is situated in the rotation axis. The resulting force induced by acceleration then acts in the rotation axis which causes the torque to vanish.

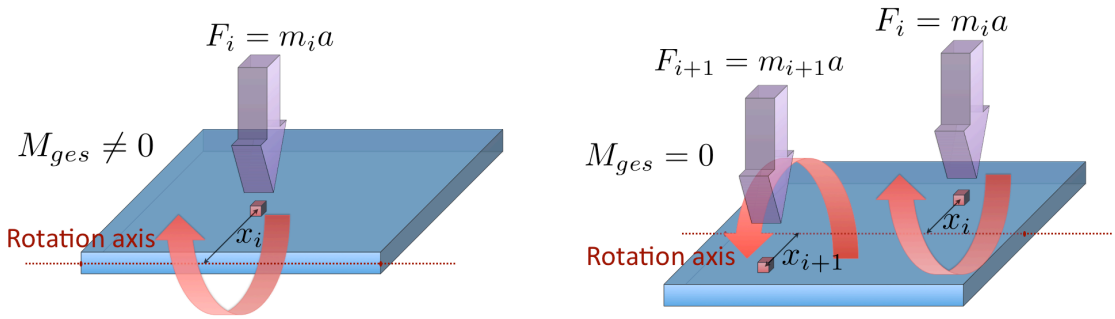

Fig. 2.26: Impact of acceleration on the sensor's Silicon mass: (a) resulting moment for unbalanced structures; (b) the moment vanishes for balanced structures.

However, the force acting in the rotation axis produces a deformation of the structure which leads to a change in resistance of both nano-gauges. There is no impact on the sensor signal if both gauges are deformed in the same way, because changes are compensated by differential configuration. Otherwise, the sensor exhibits a sensitivity to acceleration which has to be quantified. In the ideal case, this sensitivity should be lower than the sensor's minimum resolution of the magnetic field in the range of typically arising accelerations.

2.5.3 Actuation electrodes

Electrostatic actuation is an effective way to generate forces on microscale structures [51]. In our case it will be used to generate forces on the MEMS structure in order to characterize them indirectly, even without an external magnetic field. A further option consists in the design of a feedback loop for the sensor (cf. section 2.2.1). Hence, integration of actuation electrodes has to be involved for MEMS design. Comb drives were chosen for in-plane magnetometers and plane electrodes underneath the suspended MEMS structure for out-of-plane magnetometers. In the latter case, it has to be taken into account that great electrode surfaces favour the pull-in effect of the electrodes. However, typical deflections of out-of-plane magnetometers are about some nm in the actuation range we are interested in, hence widely below the critical gap of about 330nm which is needed for the pull-in effect, so the electrostatic force can be considered as linear. The purpose of using electrostatic actuation is to generate stresses of some tens of MPa inside the nano-gauges without exceeding the linearity limit of $\sigma_{FS} = 100$MPa which has been determined before. These stresses should be attained with low DC voltages below 10V. Integration of actuation electrodes has to be optimized for any designed structure.

Comb drives for in-plane magnetometers

Comb drives are an adequate choice to move micromachined structures in the wafer plane. This technique has been widely used in microtechnology for actuation and it will also be used in this work for rotation of in-plane magnetometers around their pivot. The principle of electrostatic actuation by comb drives is illustrated in figure 2.27. We assume n electrode pairs, a comb height h_c, a gap g_c between the electrodes, an initial comb overlap l_0 and a voltage V_c between the static and the movable part of the comb drive. A displacement x of the movable part is then caused by the applied voltage.

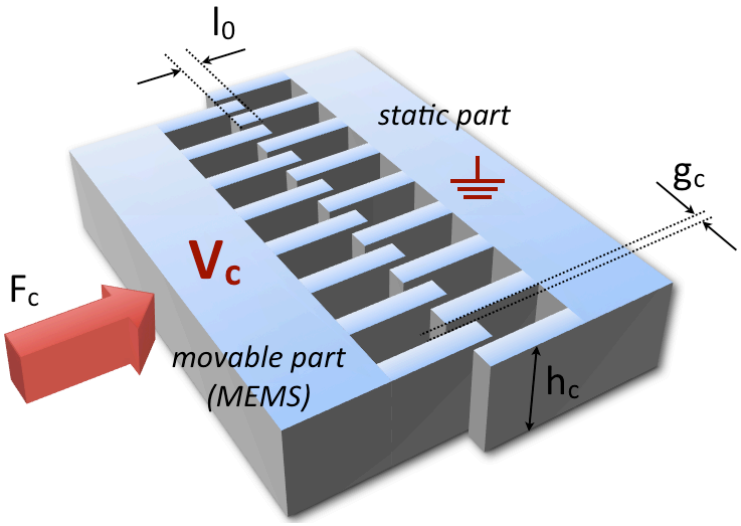

Fig. 2.27: Electrostatic actuation by comb drives

The capacitance between the movable and the static part is given by

$$C = 2n\varepsilon_0 \frac{(l_0 + x)h_c}{g_c}, \tag{2.58}$$

where ε_0 is the vacuum permittivity, so that the resulting electrostatic force F_c is calculated by

$$F_c = \frac{1}{2}\frac{dC}{dx}V_c^2 = n\varepsilon_0 \frac{h_c}{g_c}V_c^2. \tag{2.59}$$

As the effective surface provided by the comb drive is rather small, the electrodes have to be designed at maximum distance from the pivot in order to act with a great lever arm.

Plane electrodes for out-of-plane magnetometers

For actuation of out-of-plane magnetometers, plane electrodes underneath the MEMS structure are used. If a voltage V_e is applied between the MEMS structure and the electrode, the overlapping surface A and the gap g_e between electrode and MEMS structure determine the electrostatic force F_e:

$$F_e = \frac{1}{2}\varepsilon_0 \frac{A}{g_e^2}V_e^2. \tag{2.60}$$

As for in-plane magnetometers, the electrodes have to be placed at maximum distance away from the pivot in order to reach a greater leaver arm.

2.5.4 Integration of electrical contacts

For any structure, electrical contacts have to be integrated. The number of contacts per device depends on the chosen signal readout. In our application, the rotating MEMS structure is suspended by a hinge, connected to two gauges and contains two actuation electrodes. In consequence, the choice of current biasing of the gauges (cf. fig. 2.11(a)) requires an electrical circuit as shown in figure 2.28.

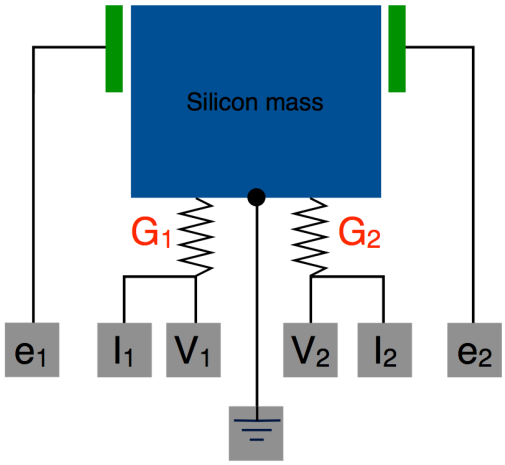

Fig. 2.28: Electrical connections needed for electrostatic actuation of the Silicon mass (e_1 and e_2), current biasing (I_1 and I_2) of the nano-gauges (G_1 and G_2), voltage measurement (V_1 and V_2) and connection of the mass.

Bondpads usually occupy surfaces of approximatively $100 \times 100\mu m^2$, which should be considered for surface optimization of an integrated 3D sensor. Electrical contacts between bondpads and sensor parts are established by thin conducting layers deposited upon bulk Silicon. If conductor lines are too narrow, the top Silicon layer on the SOI substrate which carries the conducting layer may be released during HF etching by removal of sacrificial SiO_2 (cf. section 2.1). For this reason, conductor lines have to be sufficiently large in order to assure their reliable hold on the substrate (fig. 2.29).
Typical values for underetching distances are situated in the order of 10µm. The need for relatively large conductor paths imposes significant limitations for the design of MEMS structures. This is particularly problematic for balanced Silicon bricks, because the optimum position of the nanogauges requires to cut the geometry of the MEMS structure in order to free the space for sufficiently large conductor paths. As a result, the amount of magnetic material is reduced and sensor performances deteriorated. So it is important for the design of MEMS geometry to integrate electrical contacts in a way that degradation of sensor performances are minimized.

2.5.5 Summary

Design of MEMS structures can be summarized by the following short list:

- inertially balanced MEMS structures for minimization of sensitivity to acceleration

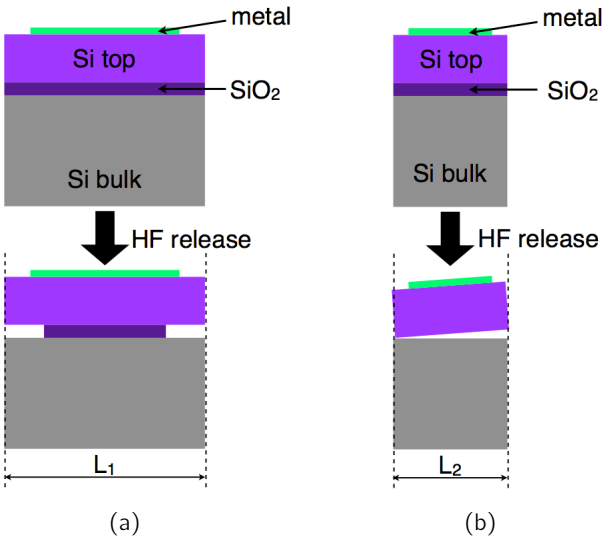

Fig. 2.29: Influence of the conducting path's line width on its mechanical stability: (a) sufficient line width L_1 to assure stability of the conductor path after HF release; (b) loss of electrical contacts for narrow line width L_2 due to complete removal of the sacrificial SiO_2 layer.

- equal distribution of magnetic material for minimization of sensitivity to magnetic field gradients
- design of actuation electrodes for self-test and potential closed-loop detection
- adaptation of MEMS geometry for integration of electrical contacts for biasing and signal readout

2.6 Hinge design for the structures

2.6.1 General requirements for MEMS pivots

After discussion of important design criteria for the MEMS structures, attention will be turned towards the design of hinges for these structures. Generally, three main aspects have to be considered for an adequate magnetometer pivot:

- it should exhibit weak mechanical stiffness for rotation of the MEMS structure
- it should exhibit high mechanical stiffness for directions different from the desired rotation and so limit the structure's degrees of freedom
- it must assure a stable suspension of the MEMS structure.

Magnetometers which measure B_x and B_y components of the magnetic field need to rotate in the wafer plane. For measurement of the B_z component, the corresponding structures need to rotate out of the wafer plane (cf. fig. 2.4). Thus, an appropriate hinge design is required for any type of magnetometer. Apart from that, hinge design is inevitably connected to the positioning of the nano-gauges relative to the pivot. This is because the case of an

ideal pivot with zero stiffness cannot be assumed. In fact, pivot and gauges have individual mechanical stiffnesses which interact one with each other. For this reason, the induced gauge force (cf. eqn. 2.11) depends not only on the lever arm d_g between the gauges and the pivot, but also on the parameter γ_g which is used to describe the influence of the pivot's stiffness on sensitivity:

$$\gamma_g = \frac{\sigma_{\text{real}}}{\sigma_{\text{ideal}}}, \tag{2.61}$$

where σ_{real} is the actual stress inside the gauge and σ_{ideal} the stress the nano-gauge would be subjected to for zero hinge stiffness. It is evident that γ_g varies for any gauge-hinge combination and has to be optimized by design. For instance, if the distance d_g is chosen too small, the structure's stiffness is dominated by the hinge and a great part of the magnetic moment is absorbed by the hinge instead by the nano-gauges. In contrast, if d_g is too large, the sensor's sensitivity declines with $1/d_g$. Hence, there is an optimum position for the gauges relative to the pivot, where the induced stress in the nano-gauges attains its maximum. For any magnetometer designed in this work, d_g was optimized by FEM analysis.

2.6.2 Pivot for X/Y magnetometer

Bending beams have often been used in microtechnology to fabricate hinges for rotation around an axis which is perpendicular to the wafer plane. Figure 2.30 demonstrates possible solutions for an in-plane hinge where the MEMS structure is balanced. In the first case (fig. 2.30(a)), four long flexible beams enable the structure's rotation. However, the nanogauges have to be connected at the outer side of the structure, so that the lever arm d_g becomes large which would lead to a reduction of sensitivity. In the second case (fig. 2.30(b)), the structure's rotation is enabled by two flexible beams which join each other in a virtual fulcrum. This solution favours the disposition of the nano-gauges next to the pivot in order to obtain higher sensitivities.

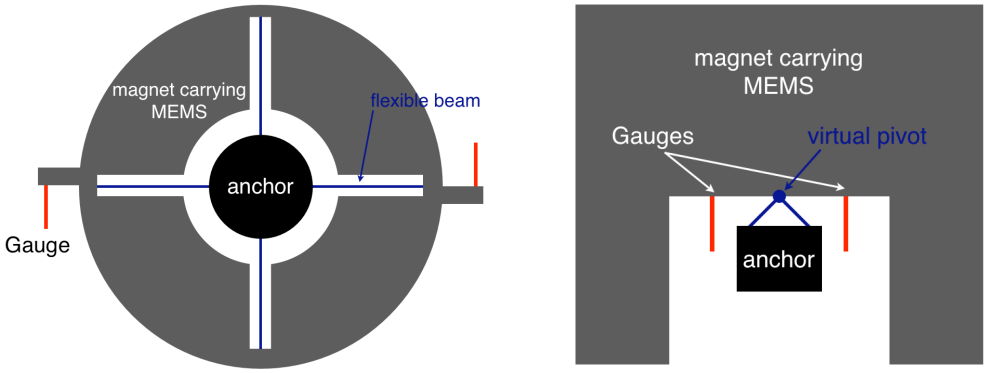

Fig. 2.30: Different manners for design of a pivot for in-plane rotating balanced structures: (a) circular structure using long flexible beams for the pivot; (b) combination of two flexible beams.

Ideally, the gauges should be connected to the MEMS structure in a plane which includes the rotation axis, as presented in fig. 2.31(a), so that they are not subjected to shear stress when they are deformed by a magnetic torque. However, placing the gauges on the same side

as the hinge limits the gauge's geometry design and obstructs the positioning of electrical contacts (cf. chapter 2.5.4). To avoid this problem, nano-gauges may also be positioned opposed to the pivot as shown in fig. 2.31(b). This leads to much more liberty in design of the gauge's geometry and allows to reduce d_g as it is needed for sensitivity optimization. A shear stress component may be induced in this case though, due to the fact that the gauges are not connected to the MEMS structure at the fulcrum level. Even though, FEM analysis shows that the shear deformation of the gauges is negligibly small compared to the gauge length (less than 6nm of shear deformation for a gauge length of 5µm with an imposed torque of 10^{-11}Nm), so this does not affect the sensor's sensitivity.

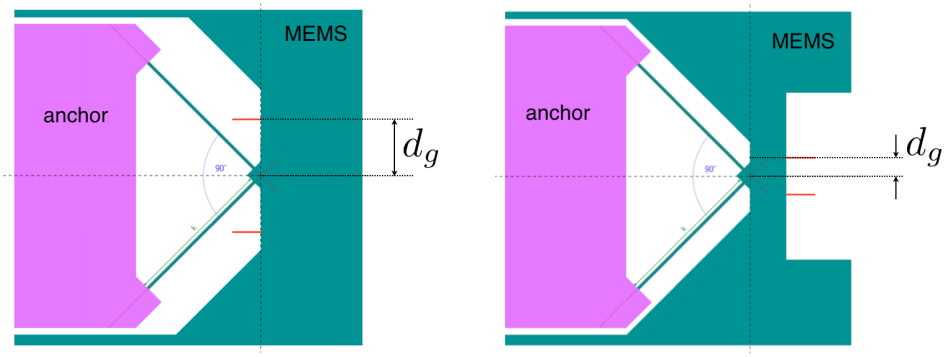

Fig. 2.31: Two options to dispose the nano-gauges: (a) positioning at the fulcrum level on the pivot side; (b) positioning on the side opposite to the pivot.

In this work, 53µm and 58µm long beams of 1µm width are used to build the hinge[9]. Longer beams soften the pivot stiffness for increased sensitivity, shorter beams harden the pivot stiffness which reduces the influence of disturbing accelerations. However, beams lengths were limited in order to restrain the area occupied by the anchor (fig. 2.31). For constant geometry of the nanogauges ($l_g = 5$µm and $A_g = 250 \times 250$nm^2), the optimum length of lever arm d_g varies depending on hinge geometry. The optimum length for d_g is found by FEM analysis in the range of about 2.5µm (fig. 2.32).

[9]The two different beam lengths were dictated by the geometry of the MEMS hinge. They represent two variations which were implemented in the design in order the compare the resulting sensitivites.

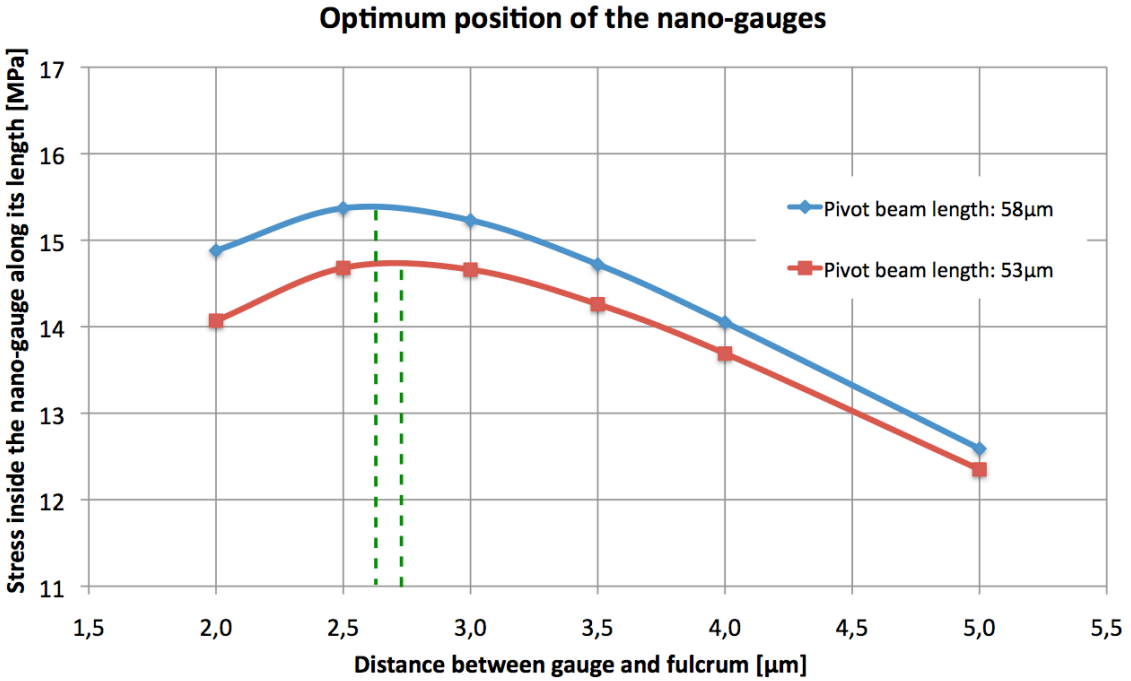

Fig. 2.32: Optimum positioning of the nanogauge relative to the fulcrum is found by FEM analysis with COMSOL. The moment applied was 10^{-10}Nm.

2.6.3 Pivot for Z magnetometer

For rotation of MEMS structures around a horizontal axis, torsion beams have often been used, for example in case of the digital micromirror device (DMD). Another possibility consists in the use of elastic beams for out-of-plane bending. Both options are used in this work.

Torsion beam hinge

An example for an out-of-plane rotating magnetometer with torsion beams is given in figure 2.33. If a torsion beam has length L_b and is distorted by a moment M, the resulting deformation angle φ_T is given by

$$\varphi_T = \frac{ML_b}{GI_p}, \tag{2.62}$$

while G is the beam's shear modulus and I_p its polar moment of area. However, if we consider an ideal hinge, the beam's torsional stiffness is considered to be negligible compared to the gauge's stiffness. The pivot axis is considered to be fixed in place and situated at half beam thickness, so the lever arm length d_g is directly determined by the beam thickness divided by two, if the gauge height is small compared to the beam height. Other than for in-plane rotating magnetometers, d_g has now to be considered as a constant due to a given beam thickness and cannot be optimized. Also the positioning of the nano-gauges is imposed by the geometry of the MEMS structure. So the remaining objective for torsional hinge design is an optimized geometry of the torsion beam. Ideally, the beam should exhibit low mechanical resistance against rotation around the pivot axis and high stiffness against other

deformations. It is seen from eqn. 2.62, that the beam's length has to be increased and its polar moment of area reduced for reduction of the torsional stiffness. Its polar moment of area is given by

$$I_p = c_{H,B} H B^3, \tag{2.63}$$

where H is the beam's thickness, B its width and $c_{H,B}$ a factor depending on the beam's height-to-width ratio which converges to $1/3$ for growing H/B ratio. So the thickness and in particular the width have to be reduced for low torsional beam stiffness. As the beam's rotational stiffness becomes larger with decreasing length and smaller with increasing length, an optimum beam length has to be found. If torsion beams are too short, they exhibit high stiffness. If they are too long, their torsional stiffness diminishes, but also flexural rigidity becomes smaller, so a great part of the stress is no longer absorbed by the nano-gauges, but by the bending deformation of the torsion hinge. In both cases, sensor sensitivity would be decreased. To find the optimal beam length adapted to the different MEMS structures, FEM analysis was used (fig. 2.35).

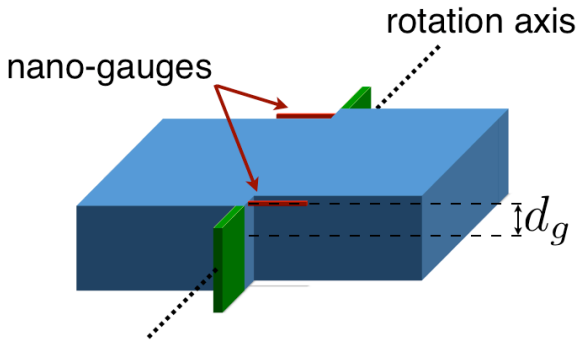

Fig. 2.33: Example for a torsion beam hinge

A disadvantage of this hinge is its low mechanical resistance against accelerations perpendicular to the beam for growing beam lengths. Figure 2.34 shows potential influences of an acceleration on the signal. The risk of destroying the nano-gauges at acceleration shocks can be eliminated by bulk stops, nevertheless a parasitic signal may be generated in the case presented in figure 2.34(b).

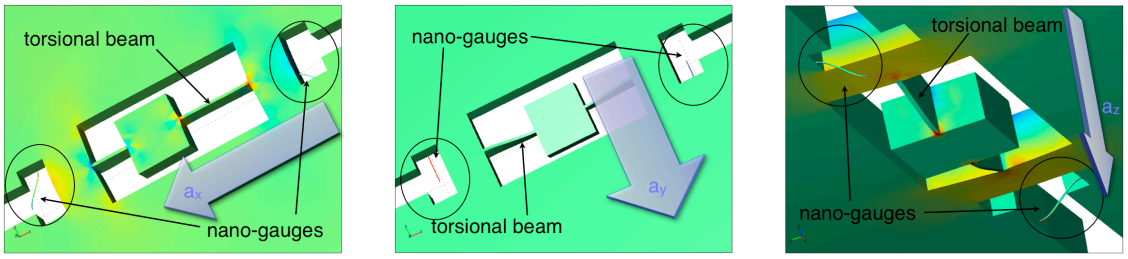

(a) (b) (c)

Fig. 2.34: Influence of acceleration on structures using torsion hinges for out-of-plane rotation: (a) if accelerations in the direction of the beam's long axis occur, the shock is well intercepted by the hinge and the nanogauges are deformed in a way that no parasitic signal is generated; (b) for accelerations perpendicular to the beam's long axis, the hinge shows relatively low stiffness and a signal is generated by the nano-gauges; (c) an acceleration in vertical direction is also well intercepted by the beams and no signal is generated by the gauges.

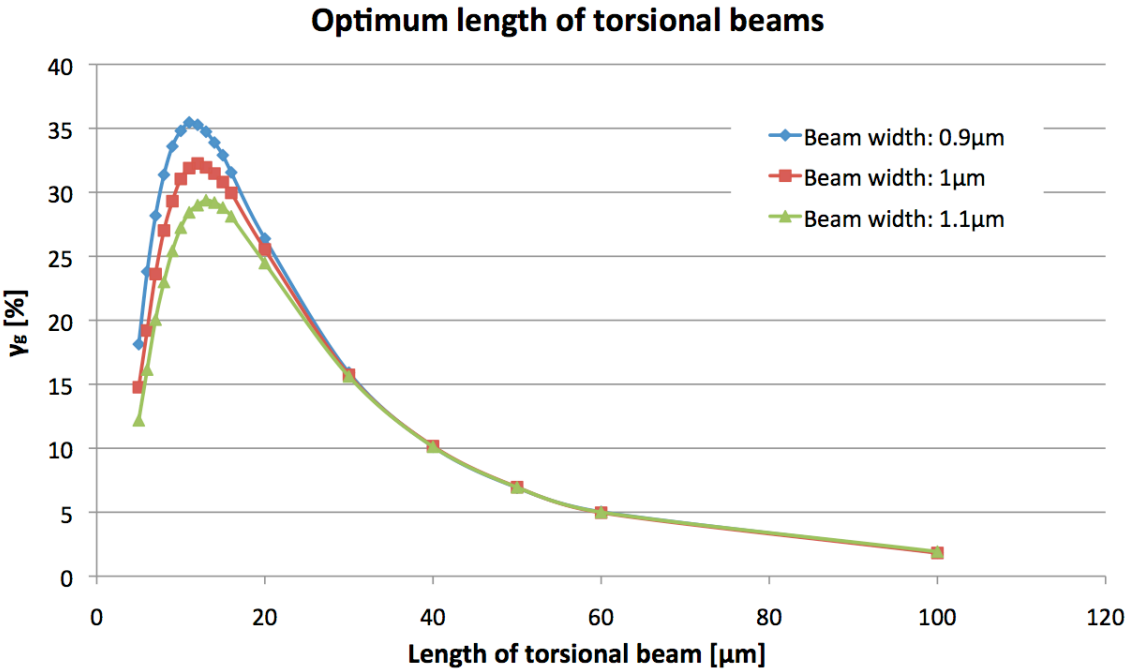

Fig. 2.35: Optimum lengths for 10 µm thick torsional beams with variable width, as obtained from FEM analysis using COMSOL. Relative stress in the gauges is expressed in terms of γ_g, which is defined in eqn. 2.61.

Bending beam hinge

A second option to build out-of-plane pivots is to use bending beams (fig. 2.36). Here, the virtual pivot is situated at half beam length and half beam height. In contrast to a torsion beam, the rotation axis does not remain in a fixed position, because it is displaced vertically besides the pure rotation. For a pure moment, the bending line w of a bent beam is derived

from the Euler-Bernoulli beam equation:

$$\frac{d^2w}{dx^2} = -\frac{M(x)}{EI} \qquad \text{with} \qquad I = \frac{BH^3}{12}, \tag{2.64}$$

where x is the coordinate lengthwise the beam, $M(x)$ the bending moment at a position x, E the elasticity modulus and I the area moment of inertia of the beam's cross section. B and H are the beam's width and thickness. For a beam with length L_b, the deflection angle φ induced by a moment is then given by

$$\varphi = \arctan\left(-\frac{ML_b}{EI}\right). \tag{2.65}$$

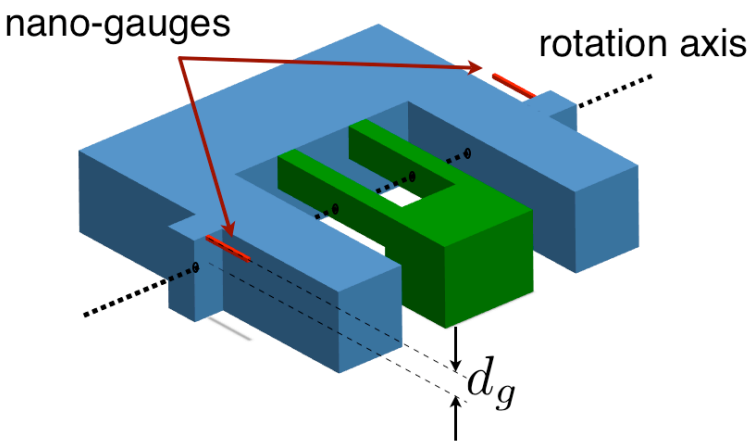

Fig. 2.36: Principle of flexural beams for a hinge adapted to out-of-plane rotation

As bending beams do not represent an ideal hinge, we identify the beam parameters to be designed in order to reduce the beam's stiffness. For that purpose, the beam's stiffness is considered to be isolated from the gauges. According to figure 2.37 where a side view of the virtual pivot is presented and with eqn. 2.65, the resulting length variation Δl of both gauges is then given by

$$\Delta l = \pm d_g \frac{6ML_b}{EBH^3}. \tag{2.66}$$

As d_g is not a variable parameter in this case, it can be seen that L_b should be increased and the beam's width B and in particular its thickness H should be reduced in order to enhance the sensors sensitivity. However, it has to be taken into account that long bending beams are inappropriate for avoiding the sensor's sensitivity to acceleration. As schematically presented in figure 2.36, we use two bending beams in this work to increase the pivot's mechanical stability and to reduce effects like sensitivity to acceleration and cross-sensitivity to other directions of the magnetic field.

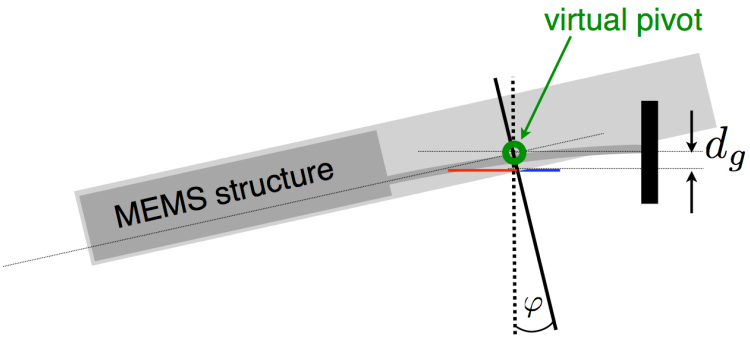

Fig. 2.37: Scheme of the virtual pivot in case of a bending beam.

Combination of bending and torsion beams

The use of either torsion or bending beams limits the structure's mechanical resistance to acceleration. For this reason, pivots for out-of-plane rotation can be designed by combining the advantages of torsion- and bending beams. It is intended to design a combination of bending and torsion beams in a way that their rotation axes coincide as presented in figure 2.38.

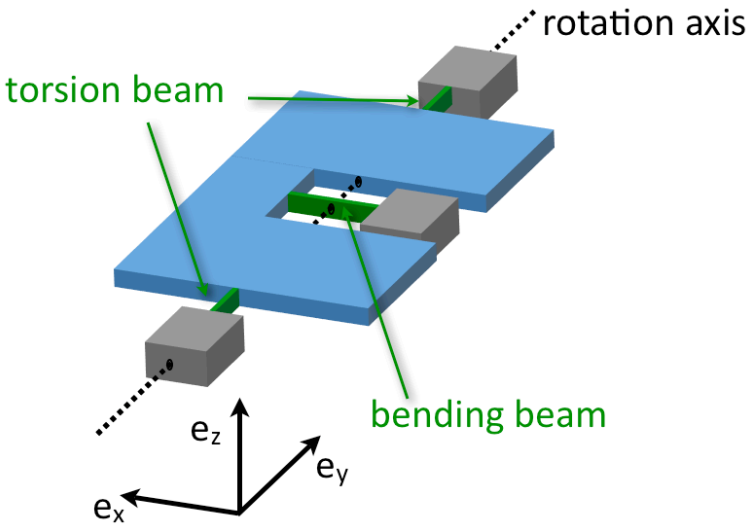

Fig. 2.38: Combination of bending and torsion beams. Both beams have to be placed in a way that their rotation axes coincide.

Table 2.16 shows a comparison of the structure's degrees of freedom which can or cannot be locked by a dedicated configuration of bending and/or torsion beams. It is possible to achieve low torsional stiffness for the desired rotation axis and high stiffness against any other deformation of the structure by combination of both beam options.
Combining both options for out-of-plane hinges provides enhanced mechanical stability for the structure and enables to design it with only one flexural beam instead of two. So the sensitivity loss due to the added torsion beams is compensated or even increased. As an example, we consider a structure which has been conceived for out-of-plane rotation with

Beam configuration	Rotation around			Translation along		
	e_x	e_y	e_z	e_x	e_y	e_z
1 bending beam	✔	✔	✔	✘	✔	✔
2 bending beams (fig. 2.36)	✔	✔	✘	✘	✔	✔
torsion beams (fig. 2.33)	✘	✔	✘	✔	✘	✘
combination of bending & torsion beam (fig. 2.38)	✘	✔	✘	✘	✘	✘

Table 2.16: Locking of different degrees of freedom for deformation of the structure using different beam configurations for torsion or bending beams. A "✔" indicates that the respective deformation along or around the indicated axis is free; a "✘" indicates that it is possible to mechanically lock the degree of freedom with the respective beam configuration.

two bending beams, where torsion beams will be added. Dimensions are shown in table 2.17. By imposing a torque of $M = 10^{-10}$Nm, we simulate the stress σ_g in a nano-gauge fixed to

Object	Length [µm]	Width [µm]	Thickness [µm]
MEMS structure	320	400	10
Bending beam	100	1	5
Torsion beam	variable	1	5

Table 2.17: Dimensions set for the simulated structure. All parts are made of crystalline Silicon.

this structure before and after inclusion of torsion beams. Note that the structure comprizes two bending beams in both cases. It is found that the sensitivity reduction ΔS is relatively small, depending on the length of torsion beams:

	σ_g [MPa]	ΔS
Without T-beam	35.47	-
T-beam 100µm length	34.81	-2%
T-beam 30µm length	32.86	-8%

Table 2.18: Sensitivity loss due to adding of torsion beams

Another advantage of combining both hinge options is that the nano-gauges are protected against inertial shocks and withstand accelerations of 10000g. The critical part in the sensor is the nano-gauge, because stress is amplified due to the small section and can easily reach critical magnitudes. For our design, we fix the critical stress limit to 500MPa inside the gauges. To evaluate the von-Mises stress σ_{vM} inside the gauges for inertial shocks of 10000g along the e_x, e_y and e_z direction (fig. 2.38), three different cases were simulated as shown in table 2.19:

Direction of acceleration	Without T-beam	T-beam 100µm	T-beam 30µm
e_x	527MPa	4MPa	3MPa
e_y	13MPa	13MPa	13MPa
e_z	544MPa	219MPa	41MPa

Table 2.19: Von-Mises stress σ_{vM} inside a nano-gauge for different configurations of torsion beams. Without adding torsion beams, stress exceeds the limit of 500MPa.

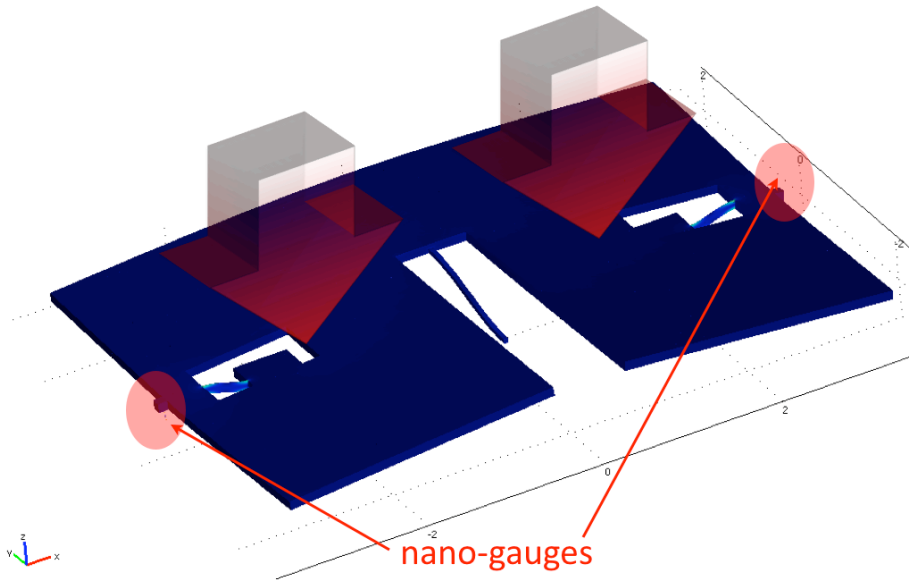

Fig. 2.39: Increased device stability by combination of bending- and torsion beams: Protection of the nano-gauges in case of an acceleration shock.

2.6.4 Summary

Following list summarizes most important aspects of hinge design:

- bending beams are used for x- and y-magnetometers to define the axis for in-plane rotation of the MEMS structure. The position of nano-gauges relative to the fulcrum is optimized for transmission of maximum stress onto the nano-gauges
- two solutions were studied for suspensions of z-magnetometer with out-of-plane rotation. Torsion beams are used in a first solution; a second solution consists in the combination of torsion- and bending beams for increased resistance against inertial shocks. Beam geometry has to be optimized for a maximum transmission of mechanical stress onto the nano-gauges.

2.7 Effects of technological imprecision

2.7.1 Deficient control of gauge dimensions

When dealing with technological imprecision, we consider here all kinds of geometrical errors which may occur during the fabrication process, including the deposited layer thicknesses and the alignment of photolithography masks in particular. As these effects limit the technological implementation of the sensor, it is interesting to assess their possible consequences. A critical step is the control of the section of the nano-gauges, because variations in thickness and width lead to a change in electrical resistance. As nominal dimensions of a nano-gauge are very small (with a section of about 250×250 nm^2), gauge width is near to the maximum resolution of the deep ultraviolet (DUV) stepper which was used. An irregularity of the section may show a significant influence on the gauge resistance. Generally, the gauge thickness is well controlled by in-line characterization methods, i.e., the thickness is monitored during the process and variations are only about a few nm. There is more difficulty to control the gauge width, because even with a perfect mask, variations in thickness are related to the etching process and often depend on the position on the processed wafer. In our process, we encountered width standard deviations in the order of 20nm along the nano-gauge.

Sensor offset

We can estimate the effects of deficient gauge geometry on offset and sensitivity by the principle of error propagation. The expected error Δy of a function y which depends on variables x_i that are prone to small statistical errors Δx_i is calculated by the total derivative of y. As a consequence of disparate resistances R_1 and R_2 of two adjacent nano-gauges, the sensor's sensitivity deviates from its nominal value and an offset is created. Assuming the applied current case, we set for the offset voltage

$$V_{off} = \frac{i}{2}\Delta R = \frac{i}{2}(R_1 - R_2), \tag{2.67}$$

where i is the current applied to the readout bridge and

$$\Delta R = \frac{\partial R}{\partial w_g}\Delta w_g + \frac{\partial R}{\partial t_g}\Delta t_g. \tag{2.68}$$

Here, w_g and t_g are gauge width and length, and Δw_g and Δt_g the respective errors. With a nominal resistance

$$R = \rho_{Si}\frac{l_g}{w_g t_g}, \tag{2.69}$$

(ρ_{Si} is Silicon piezoresistivity and l_g the gauge length) we obtain for the sensor offset

$$V_{off} = -i\rho_{Si}\frac{l_g}{w_g t_g}\left(\frac{\Delta w_g}{w_g} + \frac{\Delta t_g}{t_g}\right). \tag{2.70}$$

Fig. 2.40 shows the maximum sensor offset as a function of Δw and Δt. For numerical evaluation, a polarization current of 100µA and silicon resistivity of $2.3\times10^{-5}\Omega$m were used in combination with nominal dimensions of $0.25\times0.25\times5\mu$m^3. It can be seen that the offset is greater than the full-scale output signal in worst cases. However, maximum geometrical

errors have to be considered as a distribution over the entire wafer. It is thus unlikely that maximum geometrical errors occur for two adjacent nano-gauges, which reduces the offset.

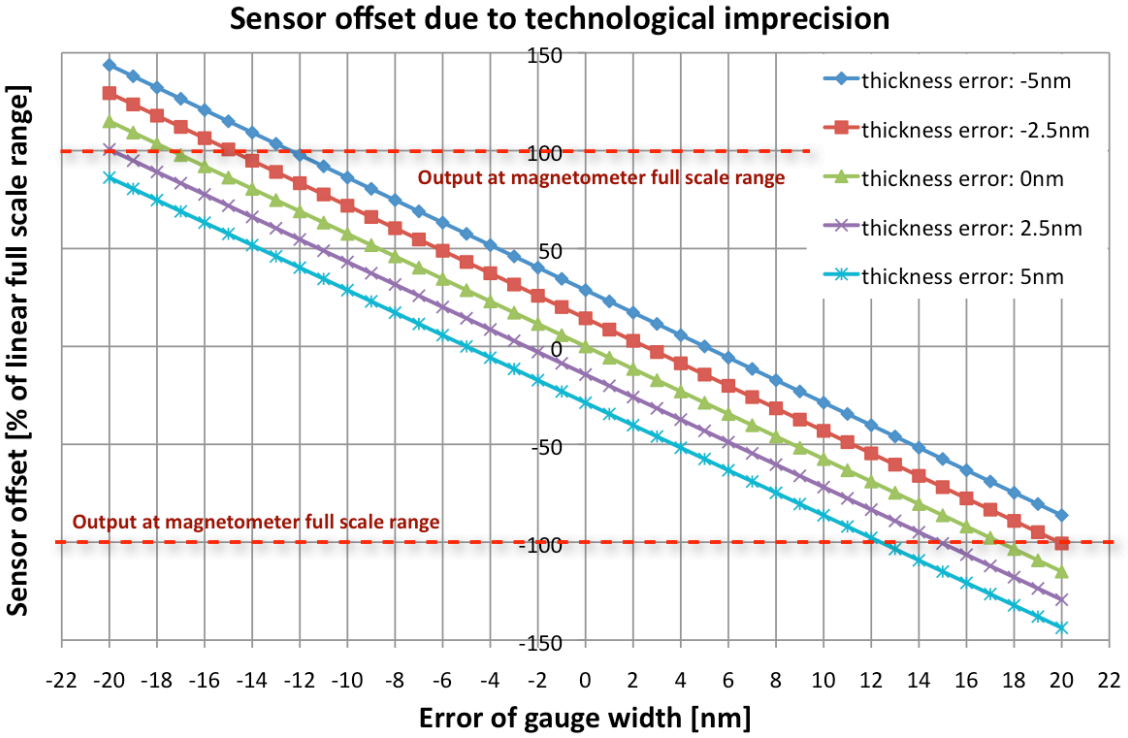

Fig. 2.40: Maximum possible sensor offsets for different deviations from nominal gauge width and nominal gauge thickness, calculated for a polarization current of 100µA, a silicon resistivity of $2.3\times10^{-5}\Omega$m and nominal gauge dimensions of $0.25 \times 0.25 \times 5\mu m^3$. Offset values can even reach the level of the output signal at full scale which is reached for a gauge stress of 100MPa.

Deviation from nominal sensitivity

A further consequence of imprecise gauge dimensions is a dispersion of sensitivity over the processed wafer. First, it can briefly be shown that mechanical stress is equal for two adjacent nano-gauges, according to figure 2.41 which represents the case where both gauges are situated at the same distance from the pivot point.

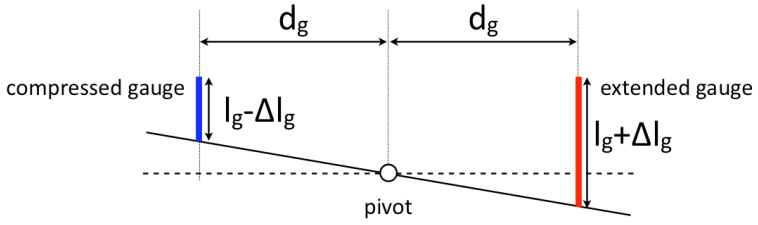

Fig. 2.41: Geometrical configuration of nano-gauges

Due to individual geometrical deviations from nominal gauge section

$$A_{g,i} = (w_g \pm \Delta w_{g,i})(t_g \pm \Delta t_{g,i}), \tag{2.71}$$

the force acting on an individual gauge is

$$F_i = \frac{E A_{g,i}}{l_g} \Delta l_g, \tag{2.72}$$

where E is the elasticity modulus of silicon. The mechanical stress inside a gauge is then

$$\sigma_i = \frac{F_i}{A_{g,i}} = E \frac{\Delta l_g}{l_g} \tag{2.73}$$

and is thus equal for both adjacent gauges, as it is independent of errors in gauge section. It is interesting to estimate the maximum change in sensitivity due to absolute geometrical errors Δw_g and Δt_g. Therefore, we define the sensor output voltage by the expression

$$V_{out} = i \rho_{Si} \frac{l_g \sigma_g \pi_{pr}}{w_g t_g}, \tag{2.74}$$

where σ_g is the stress on a gauge. The maximum absolute deviation from nominal output voltage is estimated by the total derivative

$$\Delta V_{out} = \left| \frac{\partial V_{out}}{\partial w_g} \right| \Delta w_g + \left| \frac{\partial V_{out}}{\partial t_g} \right| \Delta t_g, \tag{2.75}$$

and we obtain for the maximum possible variation of sensitivity:

$$\frac{\Delta S}{S} = \frac{\Delta V_{out}}{V_{out}} = \frac{\Delta w_g}{w_g} + \frac{\Delta t_g}{t_g}. \tag{2.76}$$

Fig. 2.42 shows the estimated relative error in sensitivity for different maximum geometric errors in gauge width and thickness.

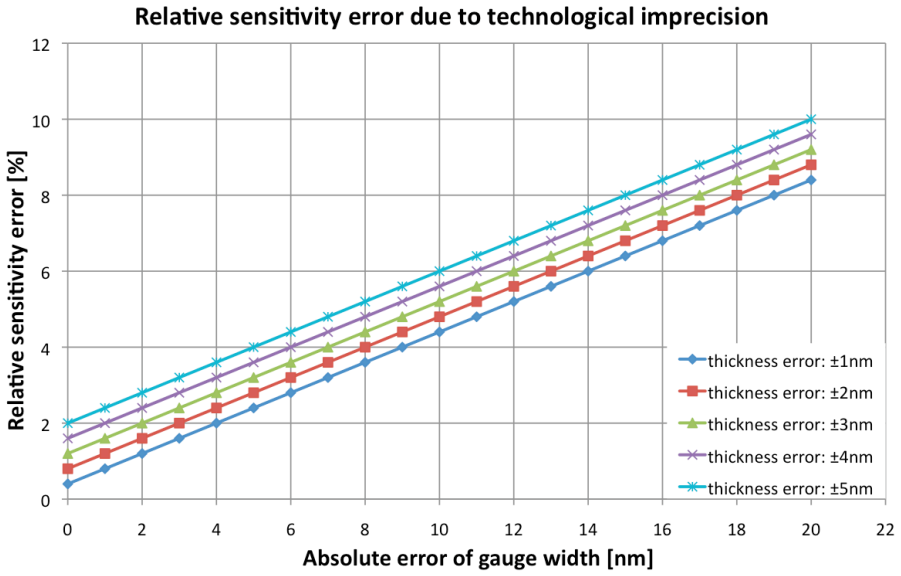

Fig. 2.42: Maximum possible variation in sensitivity depending on errors of gauge width and gauge thickness. A polarization current of 100µA, a silicon resistivity of $2.3 \times 10^{-5}\Omega$m and nominal gauge dimensions of $0.25 \times 0.25 \times 5\mu m^3$ were assumed for numerical evaluation.

2.7.2 Disalignment between masks during fabrication

Another problem is related to the alignment precision of the masks used for photolithography. This is especially important for the disposition of the gauges relative to the fulcrum. If Δd is the relative shift between masks, the gauge configuration with respect to the fulcrum is modified as represented by fig. 2.43.

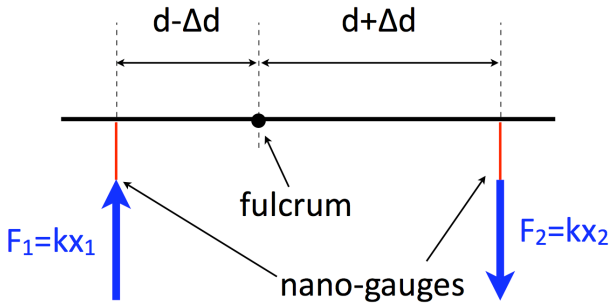

Fig. 2.43: Unequal lever arms of the two nano-gauges caused by a disalignment of the photolithography masks.

In this case, the reaction forces $F_1 = kx_1$ and $F_2 = kx_2$ of the two gauges to compensate a magnetic moment Γ_{mag} are different. By assuming an equal mechanical stiffness k of the gauges, we get the relation

$$\Gamma_{mag} = F_1(d - \Delta d) + F_2(d + \Delta d) = k\left(x_1(d - \Delta d) + x_2(d + \Delta d)\right). \tag{2.77}$$

If the MEMS structure is rotated due to a magnetic moment, the relation between the two gauge deformations x_1 and x_2 is

$$\frac{x_1}{d - \Delta d} = \frac{x_2}{d + \Delta d} \qquad \Longrightarrow \qquad x_2 = x_1 \frac{d + \Delta d}{d - \Delta d}. \tag{2.78}$$

Using eqn. 2.78 in eqn. 2.77, the reaction forces of the gauges can be expressed as

$$F = \Gamma_{mag} \frac{d \pm \Delta d}{2(d^2 + \Delta d^2)}. \tag{2.79}$$

This results in an unequal stress inside both nano-gauges and leads to a loss in sensitivity which is given by

$$\frac{\Delta S}{S} = -\frac{\Delta d^2}{d^2 + \Delta d^2}. \tag{2.80}$$

Assuming a nominal distance between gauge and fulcrum of $d = 2.5\mu m$ and a maximum mask disalignment of $\Delta d = 0.5\mu m$, we get hence a sensitivity loss $\Delta S/S$ of about -4%.

2.7.3 Disalignment of magnetic easy axes

Ideally, both magnetization directions in a 3D magnetometer have to be perpendicularly aligned in order to maximize sensitivity and to minimize cross-sensitivity to other components of the magnetic field. However, due to technological imprecisions, a perfect alignment may be difficult to be obtained, depending on the method for integration of both magnetic

easy axes, whereas the alignment of MEMS structures is well defined.

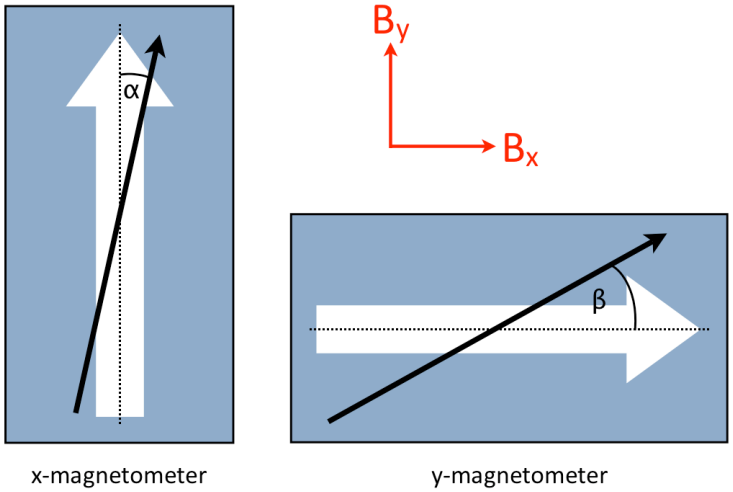

Fig. 2.44: Disalignment of magnetic easy axes in case of a x- and a y-magnetometer.

Fig. 2.44 shows the case of a x- and y-magnetometer, where magnetic easy axes are not perfectly aligned with the ideal position. We assume that both magnetometer structures exhibit an infinite mechanical stiffnes for out-of-plane rotation, so that they are insensitive to z-components of magnetic fields. This assumption is realistic for the M&NEMS magnetometer, as the designed suspension beams exhibit high flexural rigidity for out-of-plane bending. In this case, the output signals S_{MX} of the x-magnetometer and S_{MY} of the y-magnetometer are composed of two different signals S_{Bx} and S_{By}, which would be the output signals if magnetic easy axes would be perfectly aligned. With α and β as disalignment angles of magnetic easy axes, the superposed signals lead to the actually measured output signals

$$S_{MX} = -S_{Bx}\cos\alpha + S_{By}\sin\alpha \tag{2.81}$$

$$S_{MY} = -S_{Bx}\sin\beta + S_{By}\cos\beta. \tag{2.82}$$

These two equations allow us to extract the corrected signals which correspond to the actual magnetic field components:

$$S_{Bx} = \frac{S_{MX}\cos\beta - S_{MY}\sin\alpha}{\sin\alpha\sin\beta - \cos\alpha\cos\beta} \tag{2.83}$$

$$S_{By} = \frac{S_{MX}\sin\beta - S_{MY}\cos\alpha}{\sin\alpha\sin\beta - \cos\alpha\cos\beta}. \tag{2.84}$$

If $\alpha = \beta$, eqns. 2.83 and 2.84 simplify to

$$S_{Bx} = \frac{S_{MX}\cos\alpha - S_{MY}\sin\alpha}{\sin^2\alpha - \cos^2\alpha} \tag{2.85}$$

$$S_{By} = \frac{S_{MX}\sin\alpha - S_{MY}\cos\alpha}{\sin^2\alpha - \cos^2\alpha}. \tag{2.86}$$

Therefore, if the disalignment angles of magnetic easy axes are known, cross-sensitivites of x-magnetometers to y-components of magnetic fields and vice versa are not a serious problem,

because both signals S_{Bx} and S_{By} can be decorrelated. The only disadvantage consists in a loss of sensitivity. Nevertheless, cross-sensitivity to in-plane magnetic field components may become an issue for z-magnetometers, depending on the design of torsion- and bending beams. The effect can be minimized though by a combination of torsion- and bending beams, as presented earlier (fig. 2.39).

The relative loss in sensitivity $\Delta S/S$ for a single-axis magnetometer is directly related to the disalignment angle α:

$$\frac{\Delta S}{S} = 1 - \cos\alpha. \tag{2.87}$$

For example, $\Delta S/S$ would be $\sim$0.4% in case of a disalignement of $\alpha = 5°$.

2.7.4 Summary

The studied impacts of technological imprecision can be summarized by following aspects:

- for errors in gauge width and thickness, an offset is generated which can reach the value of nominal sensor output at full scale range
- for errors in gauge width and thickness, a loss in sensitivity down to 80% of nominal sensitivity is possible
- a sensitivity loss down to 96% of nominal sensitivity can be induced in case of a disalignment between gauges and the rotation axis of the magnetometer.
- an angular disalignement of magnetic easy axes leads to a cross-axis sensitivity. However, this error can be corrected by the ASIC[10]. Further, a sensitivity reduction results from this disalignment.

2.8 Thermal offset and sensitivity drift

It is also worth to investigate the influence of thermal variations on the sensor offset and on sensitivity, expressed in terms of a temperature coefficient of offset (TCO) and temperature coefficient of sensitivity (TCS). For this purpose, we consider a readout system as presented in fig. 2.45 with two gauges R_1 and R_2 and a temperature difference ΔT relative to a reference temperature. Three major thermal influences can then be considered for the magnetometer application:

- a change in resistance due to the temperature coefficient of resistance $TCR = \frac{1}{R}\frac{\partial R}{\partial T}$,
- a variation of the piezoresistive coefficient π_{pr} which is related to the temperature coefficient of piezoresistivity $TC\Pi = \frac{1}{\pi_{pr}}\frac{\partial \pi_{pr}}{\partial T}$, and
- a variation in remanence of the magnetic material, expressed in terms of the temperature coefficient of magnetic remanence $TCM = \frac{1}{M_r}\frac{\partial M_r}{\partial T}$.

[10] Application-specific integrated circuit

Considering all three contributions, a thermally modified resitance change can be modeled by

$$\Delta R_i = R_i \pi_{pr} \sigma (1 + TCR_i \cdot \Delta T)(1 + TC\Pi_i \cdot \Delta T)(1 + TCM \cdot \Delta T), \tag{2.88}$$

where R_i is the nominal gauge resistance and σ the stress applied on the gauge section. For small temperature coefficients (TCR, $TC\Pi$, $TCM << 1$), the thermally modified resistance change can be expressed by the first-order approximation

$$\Delta R_i \approx R_i \pi_{pr} \sigma [1 + (TCR_i + TC\Pi_i + TCM) \cdot \Delta T]. \tag{2.89}$$

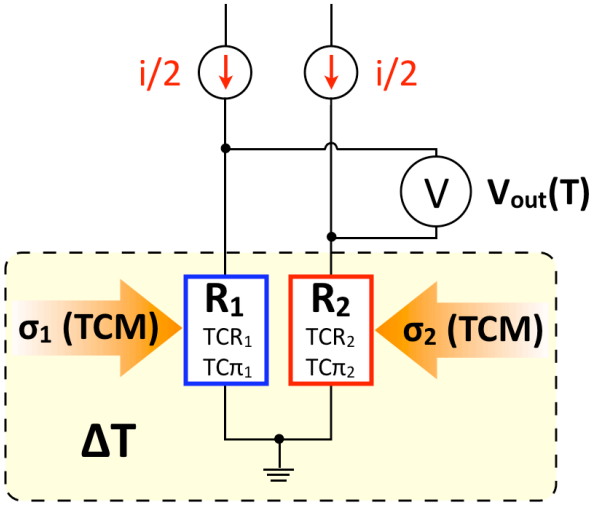

Fig. 2.45: Readout configuration considered for investigation of thermal effects

2.8.1 Thermal offset

For a standard readout configuration with two gauges R_1 and R_2 which are both polarized by a current $i/2$ (fig. 2.45), an initial sensor offset V_{off} is generated if both gauges do not have the same resistance[11]. The offset for a given temperature variation ΔT is expressed as

$$V_{off} = \frac{i}{2}(R_1 - R_2 + (R_1 TCR_1 - R_2 TCR_2) \cdot \Delta T). \tag{2.90}$$

The TCO is defined as

$$TCO = \frac{1}{V_{off,n}} \frac{\partial V_{off}}{\partial T}, \tag{2.91}$$

where $V_{off,n}$ is the nominal (thermally unmodified) offset voltage. This leads to

$$TCO = \frac{R_1 TCR_1 - R_2 TCR_2}{R_1 - R_2}. \tag{2.92}$$

Resistance and TCR values have been measured on an entire wafer[12]. Based on these measurements, we assume two gauges with $R_i = 1840\Omega \pm 5\%$ and $TCR_i = 1360 \pm 30\text{ppm}/°\text{C}$, leading to a TCO of $\sim 0.2\%/°\text{C}$.

[11] For example, differences in resistance can be generated by technological imprecision.

[12] These measurements were carried out by G. Jourdan on batch No. T134A P01

2.8.2 Thermal sensitivity drift

For the same readout configuration and a given temperature difference ΔT, the TCS can be calculated by the definition

$$TCS = \frac{1}{V_{out,n}} \frac{\partial V_{out}}{\partial T}, \tag{2.93}$$

where $V_{out,n}$ is the nominal (thermally unmodified) sensor output voltage. With the thermally modified output voltage

$$V_{out} = \frac{i}{2}[R_1(1 + \pi_{pr}\sigma(\alpha_1 + \beta_1 + \gamma) \cdot \Delta T) - R_2(1 - \pi_{pr}\sigma(\alpha_2 + \beta_2 + \gamma) \cdot \Delta T)], \tag{2.94}$$

where $\alpha_i = TCR_i$, $\beta_i = TC\Pi_i$ and $\gamma = TCM$, the TCS is expressed as

$$TCS = \frac{\pi_{pr}\sigma[R_1(\alpha_1 + \beta_1 + \gamma) + R_2(\alpha_2 + \beta_2 + \gamma)]}{R_1 - R_2 + \pi_{pr}\sigma(R_1 + R_2)}. \tag{2.95}$$

A numerical example for the TCS in the full scale range of $\sigma_{FS} = 100$MPa is given in table 2.20.

Parameter	**Value**
$R_{\pm}$	1840Ω ±5%
$TCR_{\pm}$	1360ppm/°C ±2.2%
$TC\Pi_{\pm}$	2000ppm/°C ±2%
TCM of NdFeB	-1000ppm/°C [52]
TCM of PtMn/CoFe	-53ppm/°C (cf. chapter 3)
TCS for NdFeB at σ_{FS} =100MPa	∼0.14%/°C
TCS for PtMn/CoFeat σ_{FS} =100MPa	∼0.19%/°C

Table 2.20: Numerical example for the TCS in the sensor full scale range ($\sigma_{FS} = 100$MPa).

Apart from the thermal effects discussed above, there is also the influence of magnetic cross-talk, i.e. the influence of magnetic fields created by neighbour independent magnetometers on an individual magnetometer. Due to the thermal coefficient of remanence, this field also depends on temperature and thus creates an additional superposed sensor offset. It is possible to compensate thermal offset- and sensitivity drifts by a dedicated ASIC.

2.9 Conclusion for this chapter

2.9.1 Summary of design rules

Most important design rules for the M&NEMS magnetometer can be summarized by the following list:

- Design of nano-gauges
  - For increased sensitivity and reduced noise, it is necessary to decrease the gauge section and to increase the gauge length.

  - Gauge geometry is limited by technological constraints such as the resolution of the DUV stepper.
  - Another limiting issue is possible buckling of the nano-gauge due to high compressive stress.
  - Heating of the nano-gauges due to the polarization current is also limiting factor. For the last two reasons, gauge length was limited to 5µm.

- Design of MEMS structures
  - MEMS structures were optimized for equal distribution of magnetic material in order to minimize sensitivity to magnetic field gradients.
  - MEMS structures are inertially balanced, so that no parasitic moment is generated in case of accelerations.
  - For protection against inertial shocks, bulk stops are designed at the outer edge of the MEMS structure in case of x/y-magnetometers. For z-magnetometers, the problem of inertial shocks has to be solved by assuring a sufficient mechanical rigidity of the structure's suspension, so that overall stress in the nano-gauges does not exceed the value of 500MPa for the specified acceleration limit of 10000g.
  - Actuation electrodes were designed for self-test and potential closed-loop sensing mode. Comb drives are used for x/y-magnetometers, and planar electrodes underneath the MEMS structures for z-magnetometers.

- Hinge design
  - Bending- and torsion beams were used to build the pivot point for rotation of the MEMS structures.
  - For larger structures of z-magnetometers, the resistance against inertial shocks has to be assured by combined use of torsion- and bending beams.
  - For maximum transmission of stress on the surface of nano-gauges, the distance between gauge and pivot point has to be optimized in case of x/y-magnetometers, and torsion/bending beam geometry has to be optimized in case of z-magnetometers.

- Geometrical errors and thermal drifts are due to the fabrication process and environmental conditions:
  - The fabrication process allows to achieve high precision for gauge length, so that an error in gauge length does not need to be considered.
  - Errors in gauge width and height lead to an offset and to a modification of nominal sensitivity.
  - An error in the alignment between lithography masks leads to a reduction in sensitivity.
  - Sensor offset and sensitivity are a function of temperature due to the temperature dependency of resistivity, piezoresistivity and magnetic remanence. For a sensor with typical physical properties, the temperature coefficient of offset (TCO) was estimated to be $\sim 0.2\%/°C$, and the temperature coefficient of sensitivity

(TCS) was estimated to be ∼0.14%/°C for magnetometers using NdFeB and ∼0.19%/°C for magnetometers using CoFe/PtM multilayers.

2.9.2 Presentation of designed structures

This section gives a succinct overview of the designed sensors and their theoretical performances. Assumptions for numerical estimation of sensor performances are listed in table 2.21. For the assumed polarization current, heating of a gauge is estimated to be only ∼ 0.3°C.

Parameter	Value
Gauge dimensions	$250 \times 250\text{nm}^2 \times 5\mu\text{m}$
Bridge polarization current	100µA
MEMS layer thickness	10µm

Table 2.21: Assumptions for numerical estimation of sensor performances

X-Y magnetometers

Magnetometers to detect the in-plane components were designed with two bending beams to build the pivot with two nano-gauges at the opposite side, as presented in fig. 2.46. Typical performances are listed in table 2.22.

Parameter	Integrated NdFeB	CoFe/PtMn coupled multilayers
Structure size	$100 \times 500\mu\text{m}^2$	$200 \times 800\mu\text{m}^2$
Sensitivity (@ 100µA)	3.4V/T	930mV/T
Resolution (15Hz bandwidth)	$26\text{nT}/\sqrt{\text{Hz}}$	$100\text{nT}/\sqrt{\text{Hz}}$
Linear full scale range	3.7mT	14mT

Table 2.22: Typical performances the in-plane rotating (X-Y) magnetometers have been designed for. The linear full scale range is determined by a gauge stress of $\sigma_{FS} = 100\text{MPa}$. The MEMS layer thickness is 10µm.

Z magnetometers

For of Z-magnetometers, two types of structures were designed. A first option uses a combination of bending- and torsion beams, a second option uses torsion beams. MEMS

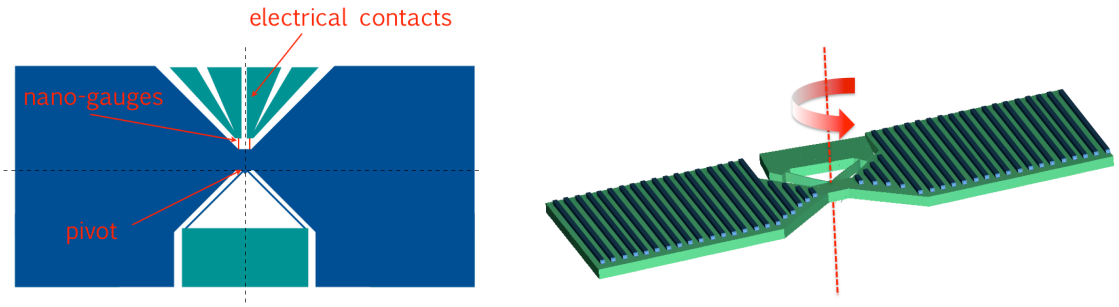

Fig. 2.46: Magnetometer design for detection of in-plane-field components: (a) schematic top view; (b) schematic 3D view, representing the case of deposited CoFe/PtMn multilayers on top of the structure (cf. section 2.2.2).

structures are smaller in case of integrated rare earth magnets, which results in a reduced MEMS mass. This is advantageous for resistance against inertial shocks, so that there is no need to add torsion beams. Therefore, only bending beams are used for smaller MEMS structures (fig. 2.47(a)). For integration of coupled ferromagnetic and antiferromagnetic multilayers, a larger sensor surface was required, so that the structure had to be stabilized by a combination of bending- and torsion beams because of the increased mass of the MEMS structure (fig. 2.47(b)). The option using torsion beams is illustrated in figures 2.47(c) and 2.47(d). Expected sensor performances are listed in tables 2.23 and 2.24. A bridge polarization current of 100µA was assumed.

Parameter	**Integrated NdFeB**	**CoFe/PtMn coupled multilayers**
Structure size	$340 \times 200\mu m^2$	$700 \times 500\mu m^2$
Sensitivity (@ 100µA)	230mV/T	370mV/T
Resolution (15Hz bandwidth)	$380nT/\sqrt{Hz}$	$240nT/\sqrt{Hz}$
Linear full scale range	56mT	35mT

Table 2.23: Expected performances at 100µA bridge polarization current for Z magnetometers using bending beams (cf. figs. 2.47(a) and 2.47(b)). Performances were calculated for a bending beam thickness of 10µm. The linear full scale range is determined by a gauge stress of $\sigma_{FS} = 100MPa$.

Parameter	**Integrated NdFeB**	**CoFe/PtMn coupled multilayers**
Structure size	$400 \times 200\mu m^2$	$600 \times 560\mu m^2$
Sensitivity (@ 100µA)	2V/T	630mV/T
Resolution (15Hz bandwidth)	$30nT/\sqrt{Hz}$	$80nT/\sqrt{Hz}$
Linear full scale range	6mT	20mT

Table 2.24: Expected performances for Z magnetometers using torsion beams (cf. figs. 2.47(c) and 2.47(d)). Beam thickness was fixed to 10µm. The linear full scale range is determined by a gauge stress of $\sigma_{FS} = 100MPa$.

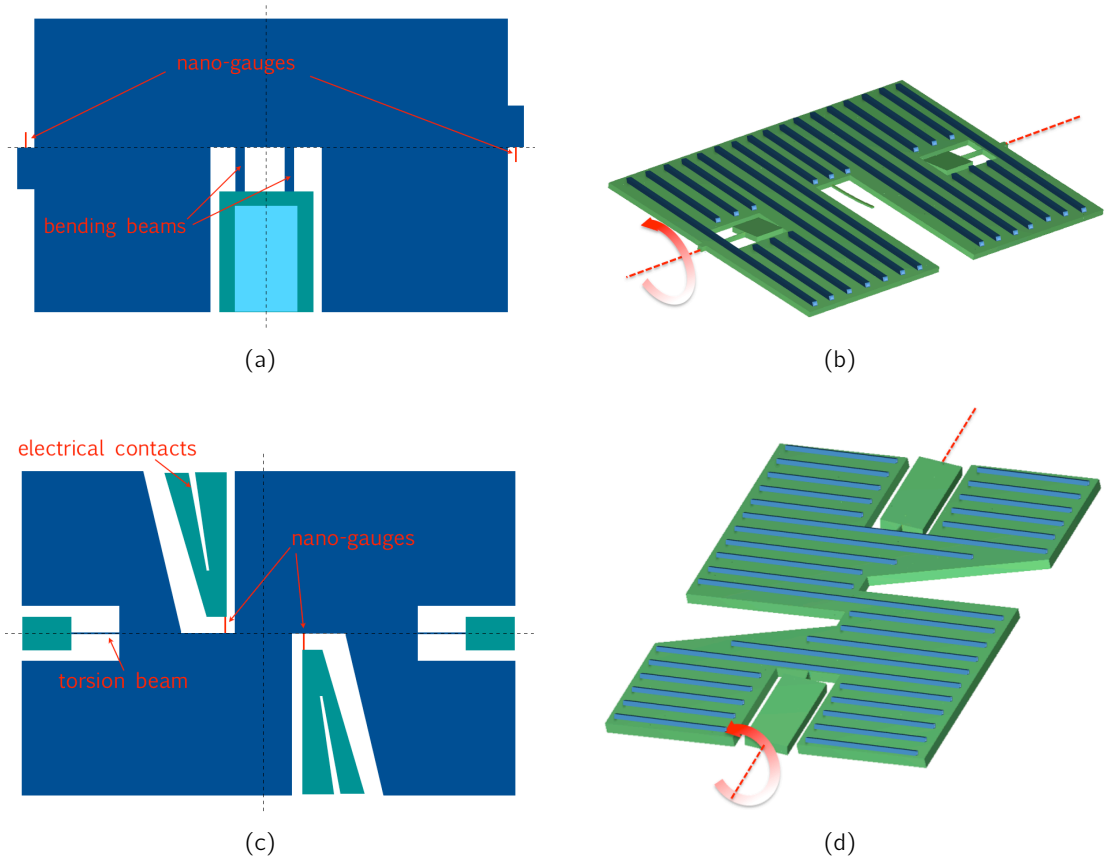

Fig. 2.47: Schematic view of the two types of Z magnetometers, where exclusively the case of a deposited stack of coupled antiferromagnetic and ferromagnetic layers is presented. (a) schematic top view of magnetometers using bending beams; (b) schematic 3D view of a magnetometer combining bending and torsion beams; (c) top view of a magnetometer using torsion beams; (d) schematic 3D view of the same structure.

2.9.3 Discussion

Suspensions for x/y- magnetometers show weak mechanical stiffness for in-plane rotation, leading to higher sensitivity. Expected resolutions are in agreement with specifications. However, mechanical stiffness for out-of-plane rotation in case of z-magnetometers using bending beams is much higher because of the 10µm thick MEMS layer which also defines the bending beam thickness. Specified sensor resolutions are not obtained in this case. An option to solve this issue consists in an additional technological step for reduction of the bending beam thickness.

Magnetometers using torsion beams theoretically satisfy design specifications, as torsional stiffness is weak compared to the stiffness of bending beams, which leads to higher sensitivity.

Chapter 3

Development of MEMS-compatible magnetic materials

3.1 Introduction

3.1.1 Scope of this chapter

This chapter presents the development of magnetic materials which are compatible with the M&NEMS fabrication process and which can thus be integrated into the magnetometer. For this purpose, magnetic materials must fulfill several requirements concerning their magnetic properties and their compatibility with the fabrication process. Most important physical properties are predetermined by the required magnetometer performances as already specified in chapter 2. For example, sensor sensitivity is directly related to remanence magnetization and the volume of magnetic material. The chosen material must also be able to withstand strong magnetic perturbation fields in a specified range of magnetic field strength. A further important aspect for the choice of magnetic material is its price, as the fabrication process should also be applicable in industry. Several properties are also determined by the needed compatibility with the fabrication process, during which high temperatures may arise. In its magnetized state, the material must be able to withstand these temperatures. Questions regarding deposition- and processing techniques for the material have also to be solved. After a brief introduction to the very basics of magnetism, two different methods are explored in order to meet above-mentioned requirements by use of two different kinds of magnetic material. In a first part, the development of rare-earth-type hard magnetic materials will be considered. A second part will be devoted to the development of exchange-bias-coupled antiferromagnetic and ferromagnetic (AF/F) layers, where soft ferromagnets are pinned by an antiferromagnet and, in consequence, exhibit magnetic properties which are similar to those of hard magnets. The development of these materials was part of the former mentioned "Capucine" project and was carried out by Leti for coupled antiferromagnetic/ferromagnetic multilayers and by the Néel laboratory for rare earth magnets. A major contribution of this work consisted in the characterization of magnetic and mechanical properties of the respective materials and mainly involves VSM measurements and measurement of residual stresses.

For both types of magnetic material, the technological development and their magnetic properties are presented, whereas mechanical aspects will be presented in chapter 4.

3.1.2 What is magnetism?

Since its discovery, men has always been fascinated by magnetism. Today we have integrated many useful applications of magnetism in our all-day life. Eldest known records about magnetism are attributed to Thales of Milet (624-564 b.c.), where he described the attraction of iron towards a certain type of stone. The first description of a magnetic compass needle was made by the Chinese in 1086. About the 12th century, magnetic compasses were reported to be used on ships for navigation [53]. In 1820, H.C. Oersted discovered that an electric current dislocates a compass needle and J.-B. Biot and F. Savart reported on the forces excerted on a magnet by a conductor flown through by a current, which was later known as the "Biot-Savart law". With the discovery of induction by M. Faraday in 1831, many discoveries followed in the domain of electromagnetism. In 1864, J.C. Maxwell formulated his well-known Maxwell-equations to commonly describe electricity and magnetism.

As an overview, basic magnetic properties of matter will be briefly discussed in this paragraph. The analogy between electricity and magnetism has led to model the elementary source of magnetic fields by magnetic dipoles, as magnetic monopoles have not been observed in nature before 2009 [54], contrary to electric charges in electrostatics. Corresponding to figure 3.1, a magnetic dipole moment $d\vec{m}$ can be described by a closed current (i) loop with area $d\vec{A}$:

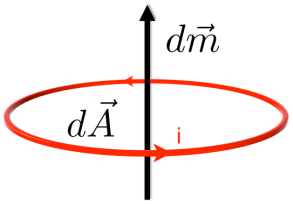

Fig. 3.1: Closed current loop for modeling of a magnetic dipole moment

$$d\vec{m} = i d\vec{A}. \tag{3.1}$$

In analogy, magnetic dipole moments at the atomic level can be expressed by means of the classical orbital angular momentum $\vec{L}$ of the electron:

$$\vec{m}_a = -\frac{e}{2m}\vec{L}, \tag{3.2}$$

where e is the electron unit charge and m its mass. From the perspective of quantum mechanics, the orbital angular momentum appears only at multiples of $\hbar$, the Planck constant, so the magnetic dipole moment can be expressed as

$$m_a = -k\mu_B \qquad \text{with} \qquad \mu_B = \frac{e\hbar}{2m} \qquad \text{and} \qquad k = 0, 1, 2, \ldots \tag{3.3}$$

where μ_B is the Bohr magneton. So the elementary magnetic dipole moment of an electron with spin $\vec{S}$ is

$$\vec{m}_e = -\mu_B g_L \frac{\vec{S}}{\hbar}, \tag{3.4}$$

where g_L is the Landé factor. The overall magnetization $\vec{M}$ in matter is the sum of all elementary magnetic dipole moments per volume V:

$$\vec{M} = \frac{1}{V} \sum_{V} \vec{m}. \tag{3.5}$$

In the non-saturated state, magnetization of matter is associated to the external field $\vec{H}$ by the magnetic susceptibility χ of the material:

$$\vec{M} = \chi \vec{H}. \tag{3.6}$$

A magnetic field $\vec{B}$ is modified by magnetization:

$$\vec{B} = \mu_0(\vec{H} + \vec{M}) = \mu_0 \mu_r \vec{H} \qquad \text{with} \qquad \mu_r = 1 + \chi, \tag{3.7}$$

where $\mu_0 = 4\pi \times 10^{-7} \frac{\mathrm{Tm}}{\mathrm{A}}$ is vacuum permeability and μ_r relative permeability which is a factor indicating magnetic field strength amplification or reduction by a material.

3.1.3 Basic magnetic properties

A main parameter to characterize matter in terms of its magnetic properties is its permeability μ_r as illustrated in figure 3.2(a). For magnetic materials, the characteristic hysteresis $M(H)$ curve is often used for characterization (fig. 3.2(b)). Specific intrinsic properties as saturation magnetization M_S, anisotropy and magnetoresistance, or extrinsic properties such as geometrically specified magnetic shape anisotropy and the magnetostriction effect can also be used for characterization. Depending on its behaviour in an external magnetic field, matter is classified in different categories of magnetic properties:

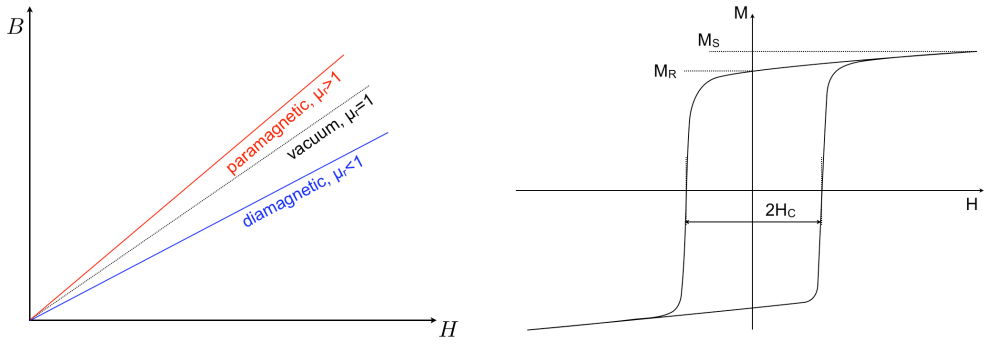

Fig. 3.2: Properties of magnetic materials: (a) Classification of materials by means of their magnetic permeability; (b) Typical $M(H)$ hysteresis loop of a ferromagnetic material. H_C is the coercive field, M_R the remanent magnetization and M_S the saturation magnetization.

Diamagnetism

Diamagnetism is a property of any material and was discovered by Faraday in 1846. It appears when molecular orbitals are fully occupied by electron pairs, where the electron

spins must be different due to the Pauli principle. This results in a net zero magnetization of the electron pair. However, a dipole moment is induced in opposite direction to the external magnetic field, leading the diamagnetic material to be repelled when it is introduced into the field. The susceptibility of diamagnetic materials is negative, leading to $\mu_r < 1$; susceptibility is temperature-independent. An example for a perfect diamagnet ($\chi = -1$) is a superconductor. Classical examples for diamagnetic materials are given in table [3.1].

Material	χ
Copper	-1×10^{-5}
Silver	-2.6×10^{-5}
Nitrogen	-5×10^{-9}

Table 3.1: Examples of diamagnetic materials [55]

Paramagnetism

In case of paramagnetic materials, molecular orbitals are not completely occupied by electron pairs, so that a net magnetic dipole moment remains which tends to align with the direction of an external magnetic field. Susceptibility can be several orders of magnitude higher than in case of diamagnetism and positive, leading to $\mu_r > 1$, so paramagnetic materials are attracted by a magnet, while the diamagnetic component becomes insignificant. Thermal agitation counteracts the orientation of magnetic dipoles, so that susceptibility decreases with temperature ($\chi \propto 1/T$). Examples of paramagnetic materials are shown in table [3.2].

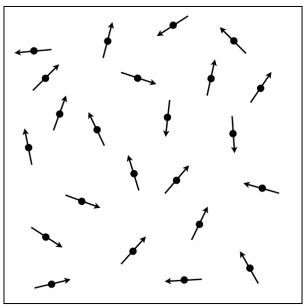

Fig. 3.3: Paramagnetism - magnetic dipole moments free to align with an external magnetic field

Material	χ
Aluminium	2.3×10^{-5}
Tungsten	6.8×10^{-5}
Liquid Oxygen	3.6×10^{-4}

Table 3.2: Examples of paramagnetic materials [55]

Ferromagnetism

Ferromagnetic materials exhibit a spontaneous magnetization which remains even without an external magnetic field (fig. 3.4(a)). This is due to the exchange interaction which stabilizes the orientation of electron spins and overcomes thermal energy. The reason why a ferromagnet is not magnetized up to saturation without a sufficiently high external field is the formation of magnetic domains, so-called "Weiss domains" (fig. 3.4(b)), in which the spins are aligned in parallel. As spins in different magnetic domains are not necessarily orientated along the same direction, the resulting magnetization is not at saturation. Spontaneous magnetization of a ferromagnet can be suppressed by temperatures above the Curie temperature ($T > T_C$) where ferromagnets become paramagnetic, by a demagnetizing field or by mechanical impacts. A few examples of ferromagnetic materials are listed in table [3.3].

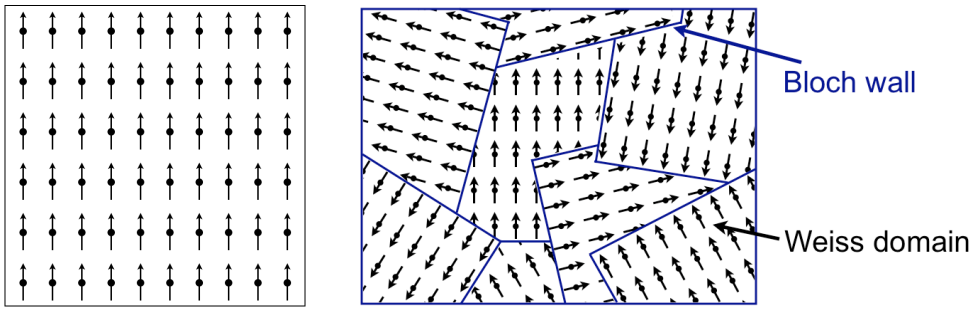

Fig. 3.4: Ferromagnetism: (a) In ferromagnetic materials, dipole moments are aligned and stabilized by the exchange interaction; (b) Separation of magnetic domains ("Weiss domains") in a ferromagnet by transition regions ("Bloch walls").

Material	χ **(**$\mu \approx \chi$**)**
Iron	500 - 10000
Cobalt	80-200
µ-Metal (75 - 80% Ni, 15% Iron)	50000 - 140000

Table 3.3: Examples of ferromagnetic materials [55]

Antiferromagnetism and Ferrimagnetism

In case of antiferromagnetism and ferrimagnetism, the crystal lattice of the solid body consists in two sub-lattices of which the electron spins are orientated in opposite direction and stabilized by a negative exchange interaction. For antiferromagnetism, the opposite magnetizations neutralize, so that the resulting macroscopic magnetization is zero. For ferrimagnetism, the opposite magnetizations differ in strength so that net magnetization remains. For $T > T_N$ (where T_N is the so-called Néel temperature), the materials become paramagnetic. Examples for antiferromagnetic and ferrimagnetic materials are listed in table [3.4]

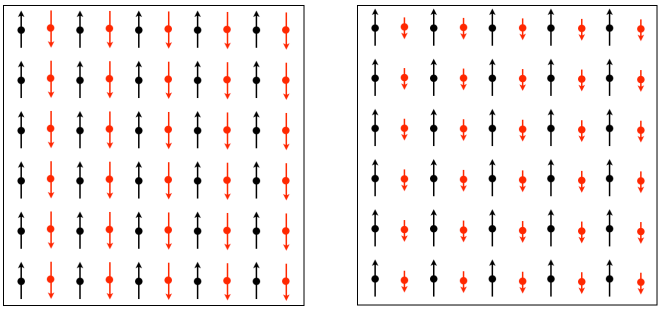

(a) (b)

Fig. 3.5: Antiferromagnetic and ferrimagnetic materials: (a) Lattice configuration of an antiferromagnetic material; (b) Lattice configuration of a ferrimagnetic material.

Material	**type**
MnO	antiferromagnetic
CoO	antiferromagnetic
NiO	antiferromagnetic
Fe_3O_4	ferrimagnetic

Table 3.4: Examples of antiferromagnetic and ferrimagnetic materials

3.2 Development of hard magnetic materials

This section presents the development of hard magnetic materials which are proper for use in the MEMS magnetometer application. The choice of a suitable material involves its basic physical properties, its technological integration into the M&NEMS magnetometer fabrication process, and its magnetic properties after technological integration. Hard magnetic materials presented in this section were developed and deposited by the Néel Institute in Grenoble and processed by Leti in the framework of the Capucine project.

3.2.1 Requirements for hard magnetic materials in the M&NEMS magnetometer application

Integration of hard magnetic material in MEMS devices has given access to new applications and technology concepts like micro-motors, loudspeakers, energy harvesters and microswitches. For the MEMS magnetometer application, high remanent magnetization is needed in order to obtain high sensitivity, and a high coercive field for insensitivity to magnetic "shocks" [1].

Different types of magnetic materials which are commonly used in industry are ferrites, the family of AlNiCo[2], and rare earth magnets [56]. Ferrites are of the composition XO-

[1] We can define a magnetic shock as a high magnetic perturbation field to which the magnetometer may be exposed (e.g. in proximity to a loudspeaker). This field is several times higher than the usual range of earth's magnetic field and is able to reverse the magnetization direction, if it is higher than the magnet's coercive field.

[2] AlNiCo is an acronym for an alloy of Aluminium, Nickel and Cobalt.

$6Fe_2O_3$, where X is a heavy metal like Ba, Sr or Pb. Usually, they exhibit weak remanent magnetization of $\sim$ 0.4T which is not suitable for our magnetometer application, as this would lead to low sensitivity. Furthermore, these materials are not adequate for deposition and processing techniques used for the fabrication of microsystems. AlNiCo are transition metal alloys with a low coercive field of $\mu_0 H_C \leq 0.2$T, leading to low resistance against magnetic shocks. In contrast, the family of rare earth magnets (NdFeB, SmCo) shows higher coercive fields and higher remanence and becomes thus interesting for use in the magnetometer application. Table 3.5 shows typical magnetic properties of different families of magnetic material. SmCo and NdFeB exhibit both high remanent magnetization. With a Curie temperature in the range of 1000K, SmCo resists even to high temperatures, while Curie temperature is lower for NdFeB ($T_C = 586$K).

	$\mu_0 M_r$ [T]	$\mu_0 H_C$ [T]	$T_C[K]$
AlNiCo	1.3	0.06	1130
Ferrites	0.4	0.4	720
$SmCo_5$	0.9	2.5	1000
Sm_2Co_{17}	1.1	1.3	1100
NdFeB	1.3	1.5	586

Table 3.5: Comparison of magnetic properties, cited after [56].

Integration of hard magnetic materials in microsystems is often achieved with casts or powders [24], as relatively thick layers of magnetic materials are required in order to obtain high magnetic interaction forces. However, it has also been achieved by classical thin film deposition techniques such as triode sputtering by researchers of the Néel Institute in Grenoble, also shown in the PhD thesis of A. Walther [57]. This process becomes particularly interesting for MEMS applications, as it facilitates integration with industrial standards.

Compatibility with the microfabrication process and physical properties determine the choice of hard magnetic material for the magnetometer application in this work. As far as compatibility with the microfabrication process is concerned, it is needed that the material can be deposited and processed using classical process conditions for MEMS fabrication. This implies primarily thermal process conditions during post-annealing steps, which are limited by the Curie temperature of the respective magnetic material.

Required phyical properties include a high remanent magnetization and a coercive field greater than 1T which is needed to obtain good sensitivity and resistance to magnetic shocks of 1T. These magnetic properties can be influenced by changing deposition- and annealing conditions.

3.2.2 Influence of magnetocrystalline anisotropy on remanence

Maximization of remanence M_R is a primary object in development of high-performance permanent magnets. In case of a perfect crystal of magnetic material, remanence reaches values which are very close to saturation magnetization M_S because of magnetocrystalline anisotropy, where the magnetic easy axis is defined by a certain crystallographic direction. In case of amorphous magnetic material, the individual magnetic moments are no longer aligned with a specific crystal axis, so that M_R is actually smaller than M_S. This can be illustrated

for the cases of volume and area magnetic isotropy and is relevant for the understanding of magnetic properties in the following section. First, we consider a magnetic film where magnetocrystalline anisotropy forces the magnetic easy axis along a direction in the wafer plane, leading to $M_R = M_S$. If this material is deposited in its amorphous state, individual magnetic moments are statistically distributed within a semicircle as shown in fig. 3.6(a). This is because it is energetically more favorable for individual magnetic moments to align with the wafer plane due to shape anisotropy. Thus, in the case of an isotropic texture of the magnetic material, M_R can be obtained by integration of the individual magnetic moments $M_S(\varphi)$ over the area of the semicircle with radius 1:

$$M_R = \frac{1}{A}\int_0^{\pi} M_S(\varphi)\,dA. \tag{3.8}$$

With $M_S(\varphi) = M_S \sin\varphi$, $dA = d\varphi/2$ and $A = \pi/2$, this leads to

$$M_R = \frac{M_S}{\pi}\int_0^{\pi} \sin\varphi\, d\varphi = \frac{2}{\pi} M_S \approx 0.64 M_S. \tag{3.9}$$

In a second case, we assume a material with magnetocrystalline anisotropy in a 3D space, where $M_R = M_S$. If the same material is deposited in its amorphous state, remanent magnetization is composed of all individual magnetic moments, integrated over the volume of a hemisphere (cf. fig. 3.6(b)). This leads to a remanence of $M_R = 0.5 M_S$ in case of magnetic material with isotropic texture.

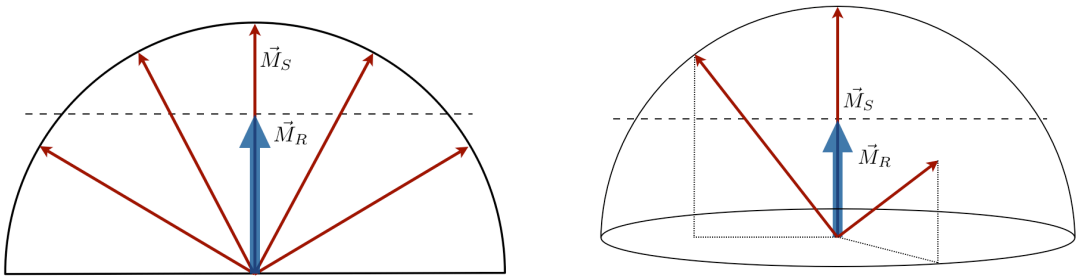

(a) (b)

Fig. 3.6: Influence of magnetocrystalline anisotropy on remanence: (a) Remanence is reduced by a factor $2/\pi$ in case of in-plane magnetization of amorphous magnetic material; (b) Remanence is reduced by a factor 0.5 for amorphous magnetic material without effects of shape anisotropy.

3.2.3 Previous work

Some of the above-mentioned aspects have previously been studied for SmCo and NdFeB films by researchers of the Néel Institute in Grenoble [27, 28]. For 5µm thick SmCo continuous films deposited at 350°C by triode sputtering, optimum physical properties were found with a maximum in-plane remanent magnetization of $\mu_0 M_R = 0.8$T and a coercive field of $\mu_0 H_C = 1.3$T [27]. A great advantage of SmCo is that no post-deposition annealing step for crystallization is required. Low deposition temperature and excellent magnetic properties make SmCo a promising candidate for integration into the MEMS magnetometer application. Yet, difficulties have been reported concerning the patterning of SmCo layers and their

adherence on silicon substrates [26]. Trenches of 6µm depth and widths in a range between 5µm - 100µm were etched into a silicon substrate and then covered by the SmCo layer. Sidewall coverage was non-uniform and discontinued. Annealing of amorphous films led to peel-off of the magnetic film due to residual stress.

Cold deposition at temperatures below 450°C can be used for 5µm thick NdFeB films, leading to an isotropic texture. In this case, a post-deposition annealing step at a temperature of 750°C was used for crystallization. Maximum remanence was $\mu_0 M_R = 0.8\text{T}$ due to the isotropic texture [28]. The high annealing temperature dictates maximum acceptable thermal conditions for the remaining fabrication process, so that demagnetization due to high process temperatures can be avoided. Another deposition process using temperatures of 500°C led to crystalline films with out-of-plane magnetization. Best obtained magnetic properties were a coercive field of $\mu_0 H_C = 1.6\text{T}$ and an out-of-plane remanent magnetization of $\mu_0 M_R = 1.4\text{T}$, which is very close to $\mu_0 M_S$ due to the effect of magnetocrystalline anisotropy. Using the same patterned silicon substrates as in case of SmCo, a uniform sidewall coverage was achieved. There was also no peel-off after annealing of amorphous films.

These former studies are a promising basis for the development of hard magnetic materials in the context of a MEMS magnetometer.

3.2.4 Technological concept for integration of SmCo and NdFeB layers

Process of integration

The integration of rare earth magnets in a microfabrication process is very challenging. Initial studies on NdFeB and SmCo layers indicated that they exhibit both high chemical reactivity during wet etching. A a dry etch step is not known for these layers. Mean overetching of $\sim 20\mu\text{m}$ was obtained for a wet etch of 2µm thick magnetic layers. Therefore, it is a reasonable approach to integrate the magnetic material as individual features into trenches which are etched into the substrate. Subsequent planarization of the magnetic layer allows to achieve low surface topology, and individual features of magnetic material can finally be covered by a protection layer for further processing. This technique also allows to achieve good control of feature size, contrary to wet etching, where high overetching occurs. Eventually, patterning of the magnetic layers creates stress relaxation zones, where residual stress can be distributed between the individual magnetic features.

The first technological approach used for integration of SmCo and NdFeB into a silicon substrate consists in DRIE (deep reactive ion etching) of trenches with vertical sidewalls, followed by triode-sputtering of magnetic material. Substrate preparation and layer processing was done by Leti, while magnetic materials were deposited by the Néel Institute using triode sputtering. However, this approach was not successful for both magnetic layers. Uniform filling of trenches could not be achieved and the layers were discontinued at the sidewalls (fig. 3.7). This is due to the scalloping roughness in combination with the deposition process, as the sidewall's scalloping pattern promotes the formation of multiple pillars of magnetic material instead of a continuous layer. Resulting problems lead principally to incompatibility with further steps of the fabrication process, but also to a degradation of magnetic propertiers.

In a modified technological approach (table 3.6), trenches with inclined sidewalls were fabricated in order to obtain a smooth sidewall coverage. Fabrication of inclined sidewalls is possible by the flowing of resin during 15min at a temperature of 170°C and subsequent silicon wet etch, as shown in fig. 3.8. Optimum depth of trenches was found to be 0.6µm,

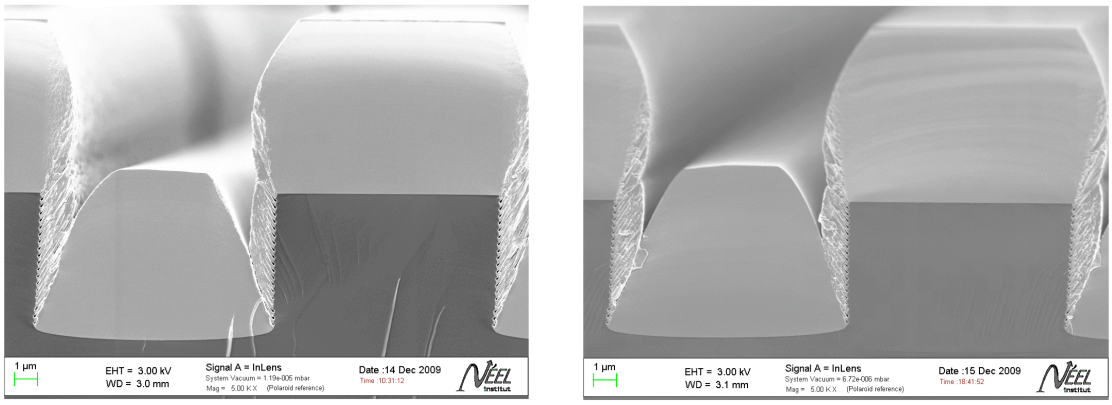

(a) (b)

Fig. 3.7: First attempt to integrate hard magnetic material into DRIE-etched trenches with vertical sidewalls, leading to poor and brittle sidewall coverage: (a) SmCo ; (b) NdFeB.

while deeper trenches led to unequal sidewall heights. A 200nm thick SiN layer is then deposited, followed by deposition of a 50nm thick Tungsten Nitride layer. SiN is often used in MEMS as diffusion barrier. In our case, it preserves magnetic material from diffusion into the Silicon brick at high process temperatures. The WN layer is deposited for better adherence of magnetic material and also establishes a good diffusion barrier up to process temperatures of 600°C [58]. Magnetic material is then deposited by triode sputtering. After a chemical-mechanical planarization step (CMP), a 200nm thick W_2N layer is deposited on top of the surface to protect magnetic material during further processing against chemical corrosion and oxydation.

Step	Description	Scheme
a)	A silicon substrate is patterned by wet-etched trenches after flowing of resin.	
b)	Deposition of a 200nm thick Si_3N_4 layer to avoid diffusion between magnetic material and the substrate.	
c)	Deposition of a 50nm thick Tungsten Nitride adhesion layer.	

d)	Deposition of hard magnetic material by triode sputtering.	
e)	Planarization step by CMP.	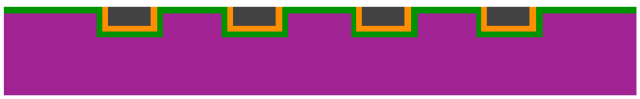
f)	Deposition of a 200nm thick W_2N capping layer for protection of magnetic material.	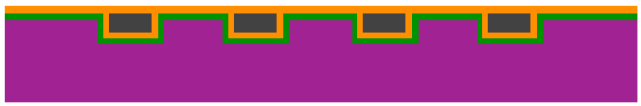

Table 3.6: Basic process for integration of SmCo and NdFeB in a silicon substrate.

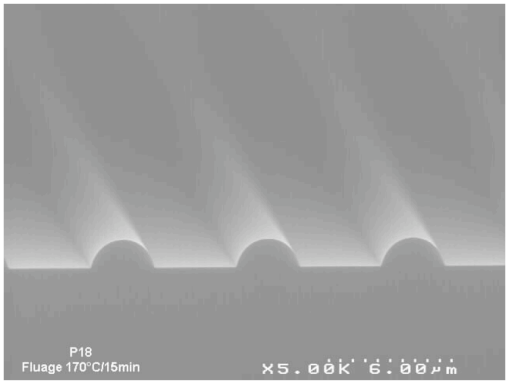

(a)

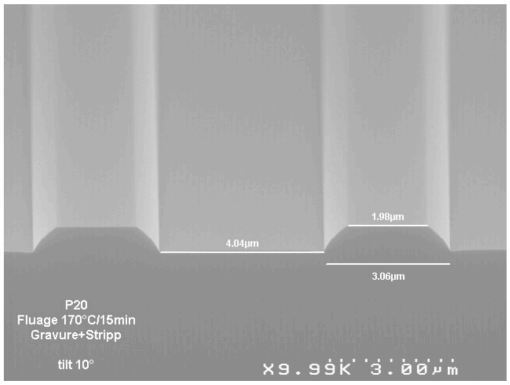

(b)

Fig. 3.8: Realization of trenches with inclined sidewalls: (a) Flown resin on top of the silicon substrate; (b) After silicon wet etch step and stripping.

The integration process was successfully validated for NdFeB, as shown by fig. 3.9. Trenches were completely filled and a good coverage of the W_2N capping layer was achieved. In contrast, no magnetic material was left in the trenches after CMP in case of SmCo layers. The origin of this problem is related to low adhesion of SmCo of the substrate during polishing and to higher corrosion when it gets into contact with the polishing colloid. As far as compatibility with fabrication process is concerned, the development of technological integration of SmCo was ceased due to limited time and ressources at this stage of development, and development of NdFeB was continued.

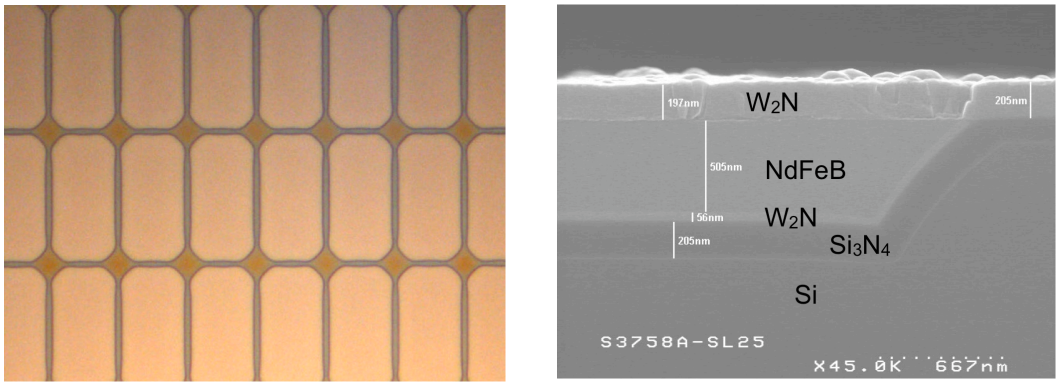

(a) (b)

Fig. 3.9: Integration of NdFeB: (a) Surface condition of trenches with integrated magnetic material after CMP ; (b) SEM view of deposited layers.

Concept for integration of two magnetization directions using thermo-magnetic patterning (TMP)

The concept of thermo-magnetic patterning (TMP) was recently developed by Dumas-Bouchiat *et al.* from the Néel laboratory [59] and is a suitable concept for integration of two magnetization directions within a single chip, if permanent magnets are used in the magnetometer. A scheme of the technological process is presented in fig. 3.10(a). Basically, the layer of hard magnetic material is uniformly magnetized in a first step. Then, the layer is locally irradiated by a pulsed excimer laser through a mask, which causes local heating of the magnetic layer. Under these circumstances, it is possible to take benefit of the property that coercivity decreases with temperature, and a relatively weak magnetic field is then sufficient to reverse or reorientate magnetization locally. Dumas-Bouchiat *et al.* validated this concept on 4µm thick NdFeB layers, where the size of individual features was $100 \times 100\mu m^2$. Reorientation of magnetization was achieved until a depth of 1.2µm. An example for integration of multiple magnetization directions is given in fig. 3.10(b).

With an adapted mask for local irradiation, TMP can principally be applied for integration of two perpendicular magnetization directions in the magnetometer application, as the NdFeB layer is only 0.6µm thick. However, heat transfer properties for the given size of the MEMS structures have not been studied before and might become a critical issue during the process. It should be noted that TMP would become more challenging for SmCo due to higher Curie temperatures. Another critical aspect is related to production costs. In particular, the step of pulsed laser irradiation is very time-demanding, because the laser beam does not cover the entire wafer area and therefore has to scan it. Without improvement of technological means, TMP is still in conflict with a low-cost production process.

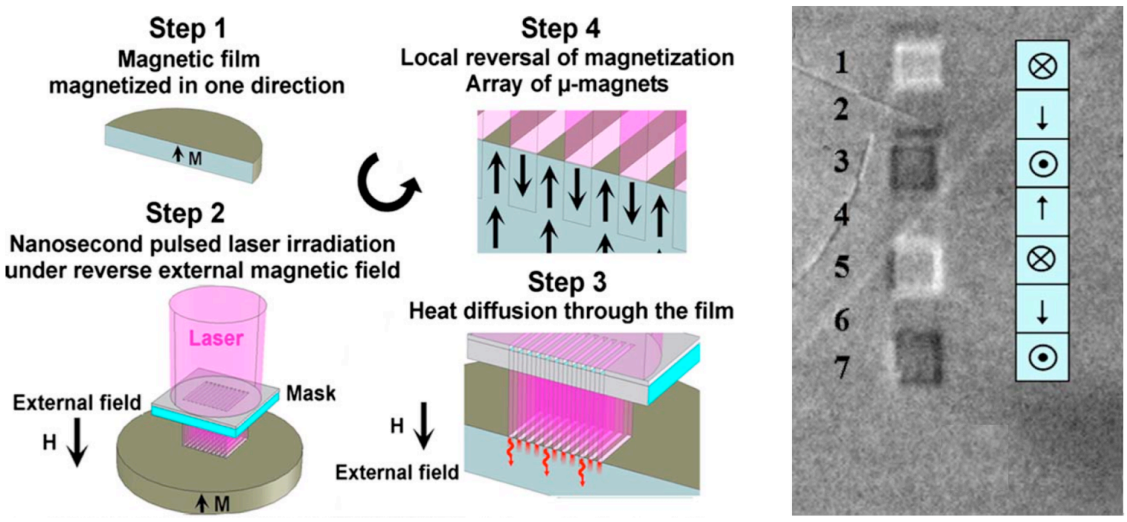

(a) (b)

Fig. 3.10: Integration of multiple magnetization directions in a thin film of hard magnetic material using TMP (the images are taken from [59]): (a) Scheme of technological process; (b) Array with multiple integrated magnetization directions.

3.2.5 Magnetic properties of integrated NdFeB

Unpatterned NdFeB layers

Unpatterned 5µm thick $Nd_2Fe_{14}B$ were first deposited at 450°C with 100nm thick Ta bottom- and capping layers and were then annealed at different temperatures between 585°C and 680°C with cooling- and heating rates of 250°C/h and a plateau time of 10 minutes. Thermal conditions applied to NdFeB during deposition and annealing lead to out-of-plane magnetization due to magnetocrystalline anisotropy. The coercive field reaches its highest value of $\mu_0 H_C = 1.2$T for an annealing temperature of 590°C, while it decreases to 0.8T for 680°C (fig. 3.11). Thus, with an optimized annealing temperature, NdFeB meets the requirement to withstand magnetic shocks.

For cold-deposited[3] NdFeB layers with in-plane magnetization, remanence is reduced by a factor ~ 0.5 due to the isotropic texture of the material. This case is shown in fig. 3.12(a).

[3]Actually, "cold deposition" indicates that deposition was carried out at room temperature, i.e. no external heating was applied to the material. Nevertheless, actual deposition temperature varies between room temperature and 200°C, as heat is generated by the sputtering process.

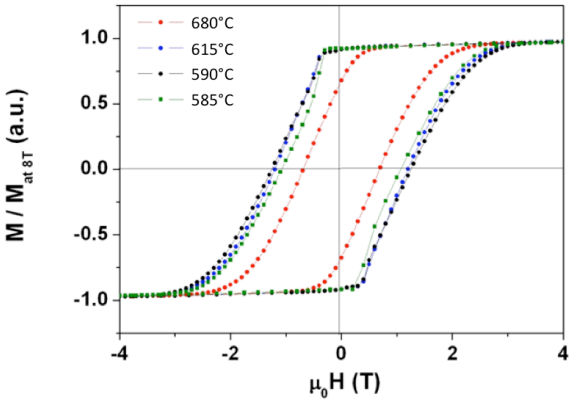

Fig. 3.11: Initial magnetic properties measured for different annealing temperatures between 585°C and 680°C on 5µm thick NdFeB layers with out-of-plane magnetization, carried out by the Néel Institute.

High temperatures during the fabrication process which follows post-deposition annealing of NdFeB may lead to a decrease in remanence. This could be the case e.g. for sensor packaging, as temperatures higher than 400°C may be required for sealing, depending on the chosen packaging method. As seen from fig. 3.12(b), a remanence loss of 10% is observed for NdFeB (only 5% for SmCo) after heating to 500K. This is very restrictive for further fabrication steps and calls for a low-temperature packaging process.

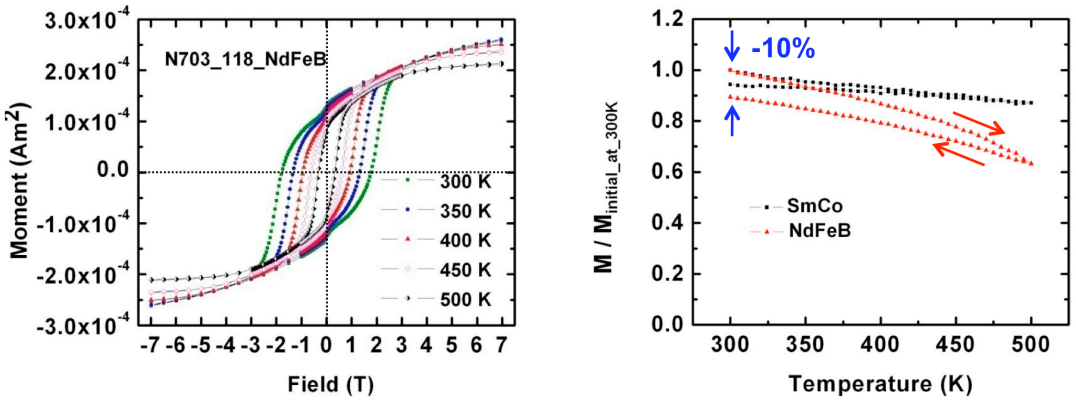

(a) (b)

Fig. 3.12: Potential loss in remanence after exposure to high processing temperatures: (a) Dependency of the hysteresis loop on temperature (cold-deposited NdFeB films with in-plane magnetization); (b) Hysteresis in remanent magnetization after a heating-cooling cycle. For NdFeB, the potential magnetization loss is about 10%.

Variation in remanence due to temperature changes within the sensor's specified operating temperature range of -10°C-50°C has a direct and significant impact on sensitivity and offset[4]. An approach to minimize temperature dependency of remanence consists in substitu-

[4]The offset of the sensor is influenced by the magnetic field which is generated by a neighbor magnet (or neighbor magnetometer). A temperature-induced change in remanence of a neighbor magnet consequently generates a temperature-dependent offset of the output signal.

tion of heavy rare-earth elements for Nd, leading to ferrimagnetic coupling [60]. Substitution of Nd for Holmium (Ho) and Dysprosium (Dy) enables to minimize remanence variation in the targeted temperature range. In comparison to $Nd_2Fe_{14}B$, two alloys were studied for the effect: $(Nd_{40}Dy_{60})_2(Fe_{40}Co_{60})_{14}B$ for substitution of Nd content by Dysprosium and $(Nd_{50}Ho_{50})_2(Fe_{50}Co_{50})_{14}B$ for Nd replacement by Holmium. In both cases, substitution of Co for Fe leads to an increase in Curie temperature. Fig. 3.13 shows that pure $Nd_2Fe_{14}B$ exhibits a remanence variation of ∼2% in the targeted temperature range. The increase in remanence for $(Nd_{40}Dy_{60})_2(Fe_{40}Co_{60})_{14}B$ is explained by poor texture in the alloy; variation in remanence is also ∼2-3%. Finally, temperature stability of in-plane remanence is obtained by substitution of Nd content for Ho.

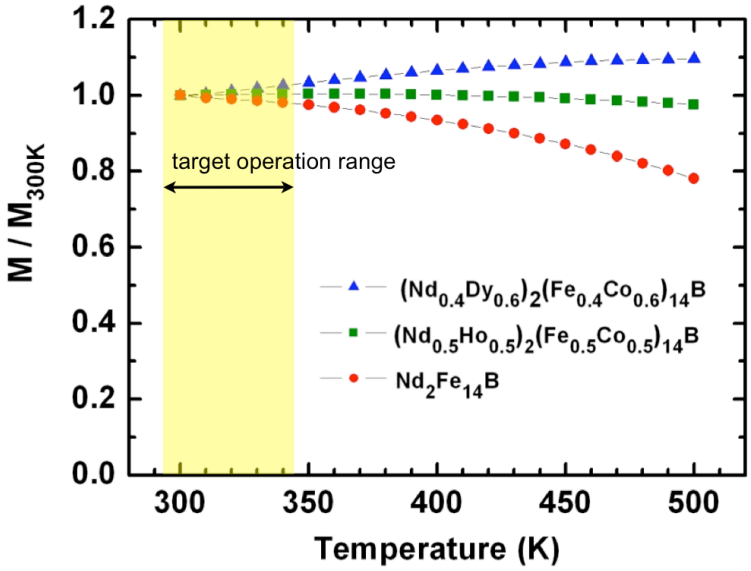

Fig. 3.13: Effect of substitution of Nd content for Dy and Ho on the temperature dependency of remanence. A stable remanence in the targeted temperature range of -10°C - 50°C is obtained by substitution of Nd content for Ho.

NdFeB integrated into trenches

Different trench geometries were applied for patterning of NdFeB layers. Trenches with a geometry of $25 \times 25\mu m^2$ are used as a representative case. As depth of trenches is imposed by the process for inclined sidewalls, the remaining effective thickness of magnetic material is 500nm. Hysteresis loops measured by a vibrating sample magnetometer (VSM) for samples which were deposited at room temperature and annealed at 600°C indicated significant deviations from magnetic properties measured on non-structured, 5µm thick cold-deposited NdFeB layers with out-of-plane magnetization and Tantalum sub- and capping layers. A two-phase behaviour indicates the presence of a magnetic soft phase on top of the layer, and remanence was reduced to 65% of saturation magnetization (fig. 3.14(a)). There is also a significant reduction in coercive field down to 0.35T; thus, the criterion for resistance against magnetic shocks is no longer satisfied.

Reduction in remanence is related to the low coercive field and low squareness of the measured hysteresis loop, which is normally characteristic for soft magnetic behaviour. One

reason for low coercivity is that film thickness is close to the order of grain size (in the range of 200-300nm), so that the impact of surface- and interface defects is of more consequence as for 5µm thick NdFeB layers, where defect-to-volume ratio is decreased. Defects at grain boundaries may lead to magnetization reversal of the entire domain due to the Barkhausen effect, and thus lead to a significant reduction in coercivity. This effect can also be partially due to the W_2N sublayer which was used instead of Ta, where the presence of W_2N during annealing may lead to formation of a magnetic soft phase.

An approach to increase coercivity consists in the addition of excess Nd to the crystalline $Nd_2Fe_{14}B$ phase, so that exchange interaction between individual domains is decoupled by the Nd-rich eutectic at the grain boundaries [61]. According to Y. Zhang *et al.*, mechanical compressive stress in the deposited layer also plays an important role for the redistribution of the boundary phase between individual domains and helps to increase coercivity [62]. However, a compromise between mechanical stress and coercivity is not worth the risk, as problems related to mechanical stress include loss in sensor reliability, malfunction and total damage[5].

An explanation for the soft phase is the influence of CMP processing on top of the NdFeB layer. The surface grains are prone to oxidation during CMP processing, which generates defects at the boundaries so that surface grains loose their coercive strength. By Ion Beam Etching (IBE), the soft phase on the top layer could be removed. Partial and complete removal of the soft phase were achieved by IBE processing times of 1'30" (fig. 3.14(b)) and 2'30" (fig. 3.14(c)) and annealing at 610°C . However, remanence was even lower than before with values situated between 56-58% of saturation magnetization ($\mu_0 M_R \approx 0.8T$).

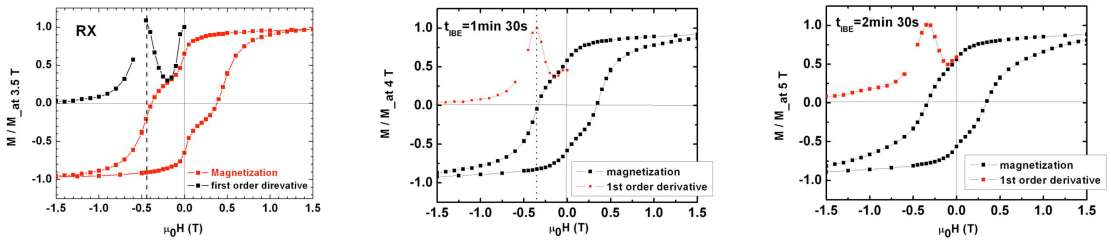

(a) (b) (c)

Fig. 3.14: Magnetic properties of patterned NdFeB layers: (a) Two-phase characteristic of the hysteresis loop after patterning of the NdFeB layer; (b) Partial removal of the soft phase on top of the magnetic layer after an ion beam etching step for 1'30" and annealing at 610°C; (c) Complete removal of the soft phase on top of the magnetic layer after an ion beam etching step for 2'30" and annealing at 610°C.

3.2.6 Discussion

Magnetic properties of NdFeB and SmCo as found prior to this work by researchers of the Néel Institute are very promising for the MEMS magnetometer application. In terms of magnetic properties, NdFeB can be preferred to SmCo because of its high remanence and high coercive field ($\mu_0 M_r = 1.4$T for films with magnetocrystalline anisotropy and $\mu_0 H_C =$

[5]This aspect will discussed in chapter 4

1.6T). However, post-deposition annealing at temperatures higher than 600°C is required for crystallization, and Curie temperature is much lower as for SmCo.

With an in-plane magnetization of $\mu_0 M_r = 0.8$T and $\mu_0 H_C = 1.3$T, magnetic properties of SmCo still satisfy requirements for use in MEMS magnetometer applications, and a post-deposition annealing step is not required, as crystallization occurs already during deposition at temperatures below 400°C. The material also resists to high temperatures because of its high Curie temperature, which allows fabrication processes with aggressive thermal processing conditions. However, the choice of SmCo is also a matter of expense, as costs for SmCo are higher than for NdFeB.

As far as compatibility with the fabrication process is concerned, a reliable integration process was only possible for NdFeB, while integration of SmCo failed because of the CMP planarization step. For NdFeB, good temperature stability of remanence can be achieved by substitution of Nd content for Ho, but a remanence loss of 10% is possible if NdFeB is exposed to temperatures of $\sim$ 200°C in the further fabrication process, which is a very limiting factor for its technological integration.

After successful integration of NdFeB, magnetic properties were deteriorated compared to those of 5µm thick continuous films. In particular, a low coercive field $\leq$ 0.5T is not acceptable for the aimed resistance against magnetic shocks (1T according to specifications). Besides the fact that integration of two different magnetization directions by TMP is complex to achieve, the reduction in coercivity after integration of NdFeB becomes a critical issue, as the magnetic field which is applied for local reorientation of the magnetization direction is also able to reverse magnetization in regions which are not supposed to be influenced by the TMP step.

Development of technological concepts to govern the integration of hard magnetic material into MEMS devices is very challenging. Unless some technological drawbacks which were encountered during the Capucine project, hard magnetic materials still remain an important option with high potential for use in MEMS devices. Nevertheless, the option of integrated rare-earth magnetic material was discontinued in the context of this work due to insufficient magnetic properties after the MEMS integration process.

3.3 Development of coupled antiferromagnetic and ferromagnetic (AF/F) multilayers

In the following section, the development of coupled antiferromagnetic and ferromagnetic multilayers for integration in MEMS magnetometers will be discussed. Specific configurations of AF/F layers shows several advantages in terms of magnetic properties for integration in MEMS devices, as they benefit from exchange bias coupling. Exchange bias is a uniaxial anisotropy induced by coupling between interfaces of ferromagnetic and antiferromagnetic materials. Actually, there are different types of magnetic anisotropies which are related to the amount of anisotropy energy E_a which has to be overcome in order to rotate spins away from their parallel alignment with the easy axis. Without magnetic anisotropy, spins in a compass needle would be rotated in presence of an external field, but the needle itself would remain in its position. A well-known anisotropy is magnetocrystalline anisotropy, which is explained by the spin-orbit interaction [63]. It appears for ferromagnets and antiferromagnets. Another form of anisotropy is shape anisotropy. It is induced by dipole-dipole interactions [64] between

individual magnetic moments within demagnetizing fields. This effect can be observed for ferromagnets, but it vanishes for antiferromagnets, as the demagnetizing field is compensated due to the antiparallel spin alignment. In case of very thin ferromagnetic layers, the anisotropy energy becomes

$$E_a = -\frac{\mu_0 M^2 \sin^2\theta}{2}, \tag{3.10}$$

where M is the magnetization and θ the angle between magnetization and the out-of-plane vector of the ferromagnetic layer. It can be seen from eqn. 3.10 that spins tend to align in the plane of the ferromagnetic layer, because the term $\sin^2\theta$ has to be minimized. Amongst others, this effect plays an important role for the magnetometer application presented in this work. As for magnetocrystalline anisotropy, spin-orbit interaction is also the cause for surface anisotropy which is observed for ultra-thin layers [65]. The effect of surface anisotropy is negligible in case of thick layers. Another effect is magnetoelastic anisotropy [66] which is also known as the inverse magnetostrictive effect. In this case, mechanical stress changes lattice distances in the material, so that spin-orbit interactions are modified, leading to an anisotropy.

In this section, the effect of exchange bias between coupled antiferromagnetic and ferromagnetic layers will be presented in a more detailed manner. Second, physical requirements and properties for integrated magnetic thin films are discussed. Finally, the approach used for the development of materials and characterization results will be presented.

3.3.1 Exchange bias in AF/F systems

Exchange bias coupled ferromagnetic-antiferromagnetic (AF/F) systems are very promising for new applications. They allow to modify magnetic properties (enhancement of coercive field, shift of hysteresis cycle) at a nanometric scale, they make it possible to overcome superparamagnetism in storage applications and exhibit hard magnetic behaviour. As an example, coupled AF/F layers are used to pin a magnetization direction in GMR[6] and MTJ[7] [67] devices. These systems have widely been used in read-heads for hard discs and are the basis for modern data storage devices (MRAM) and RF applications [68, 69]. It is also possible to use AF/F-systems for actuation at the nanometric scale, as shown by L. Bilhaut in 2009 [25].

Properties of the exchange bias effect

Unidirectional exchange anisotropy (also known as exchange bias) is a property observed for coupled ferromagnetic and antiferromagnetic layers and was first discovered by Meiklejohn and Bean in 1956 [70] by tests on oxidized Co nanoparticles. Research on exchange bias coupled systems was mainly promoted by means of thin-film technologies, as it becomes only observable for film thicknesses at the nanometric scale. A coupled system of ferromagnets and antiferromagnets is stable below the blocking temperature T_b of the antiferromagnet, where the magnetization of the ferromagnet is pinned by the antiferromagnet along a preferential direction, called magnetic easy axis (in analogy to properties of a permanent magnet).

[6] Giant magnetoresistance: In this application, AF/F coupled layers constitute a layer with a magnetic hard axis and are seperated from a ferromagnetic layer by a non-ferromagnetic layer (e.g. Cu).

[7] Magnetic tunnel junction or TMR (Tunnel magnetoresistance): Here, AF/F coupled layers constitute a magnetic hard axis which is seperated from a soft ferromagnetic layer by an insulating oxide layer (e.g. MgO).

A hard magnetic axis appears perpendicularly to the easy axis. If $T \geq T_b$ is reached, the exchange bias effect disappears. In general, T_b of an antiferromagnet is equal to its Néel temperature T_N. However, T_b can be lower than T_N in case of ultrathin antiferromagnetic layers [71]. An AF/F exchange-coupled system is build when at least a bilayer of antiferromagnetic and ferromagnetic material is annealed under a magnetic field and then cooled down below Curie temperature T_C of the ferromagnet, where the spins of the ferromagnet align, and finally below the Néel temperature T_N of the antiferromagnet, where the magnetization of the ferromagnet is pinned or "frozen" by the antiferromagnet (fig. 3.15). This principle is also valid for systems which use alternating antiferromagnetic and ferromagnetic multilayers instead of bilayers.

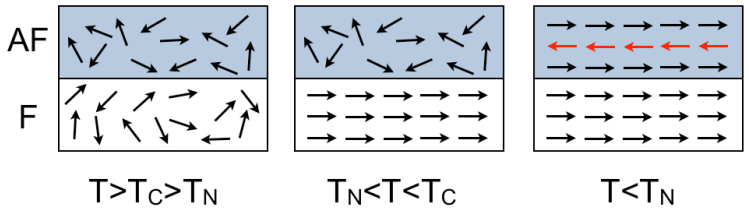

Fig. 3.15: "Freezing" process for an AF/F exchange bias-coupled system

The exchange bias effect becomes essentially manifest by a shift of the hysteresis loop, by an increased coercive field, and by unidirectional anisotropy. A shift of the hysteresis loop appears when the magnetic hardness of the pinning antiferromagnet is sufficiently high. For a simple ferromagnet, spins are directly aligned by the external field without need to overcome any exchange coupling at the boundaries, leading to a symmetric hysteresis loop. If the magnetization of the ferromagnet is pinned by the antiferromagnet (fig. 3.16(b)-1), its spins have to overcome the exchange coupling at the boundary layer (fig. 3.16(b)-2) first before they can realign with the external magnetic field (fig. 3.16(b)-3), which maintains a high remanence in the region of reversed external magnetic fields. If the field is applied back in the opposite direction, spins realign with the external magnetic field for weak or even negative field values (fig. 3.16(b)-4), leading to a shifted hysteresis loop.
The effect of an increased coercive field appears for antiferromagnets with low anisotropy. Applying a reverse magnetic field to the initial AF/F system (fig. 3.17(b)-1) reverses spins in the ferromagnet, but adjacent spins of the antiferromagnet at the boundary layers are also rotated due to the antiferromagnet's magnetic softness (fig. 3.17(b)-2). Finally, it is energetically more favorable for the spin configuration of the antiferromagnet to completely reverse (fig. 3.17(b)-3). The same spin reversal mechanism takes place in case of magnetic field applied in opposite direction, leading to a greater coercive field. Coercive field enhancement depends strongly on temperature and reaches its maximum closely below the Néel temperature of the antiferromagnet.
Unidirectional anisotropy in exchange bias coupled AF/F systems indicates a single stable magnetization direction and becomes manifest in a $M_R \propto K \sin(\Phi)$ dependence (fig. 3.18). It is explained by the fact that spin configurations in parallel and antiparallel alignment with the magnetic easy axis are not equal, from an energetic point of view.

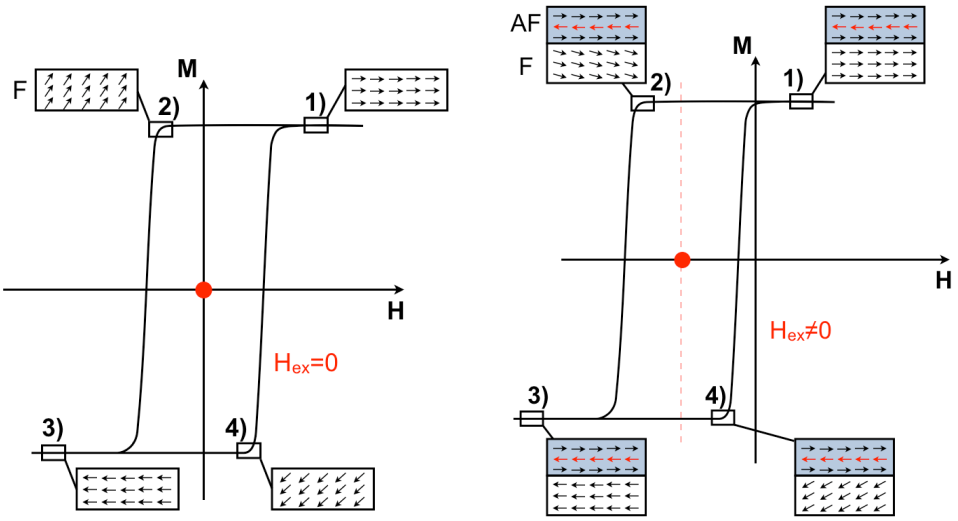

Fig. 3.16: Shift of hysteresis loop in ferromagnets and AF/F systems: (a) hysteresis loop of a simple ferromagnet; (b) shifted hysteresis loop of an exchange bias coupled AF/F system.

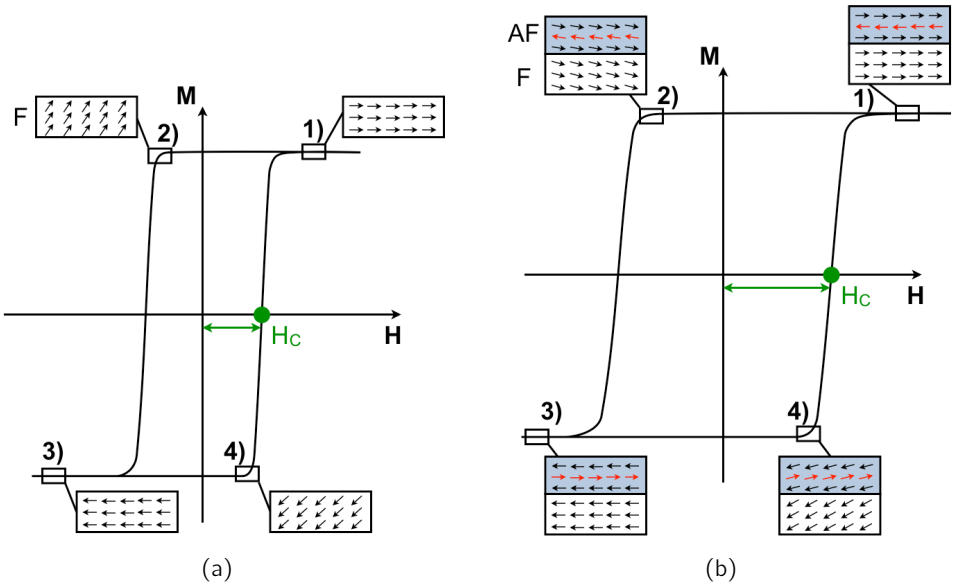

Fig. 3.17: Enhancement of coercive field: (a) coercive field of a simple ferromagnet; (b) enlarged coercive field for an exchange bias coupled AF/F system.

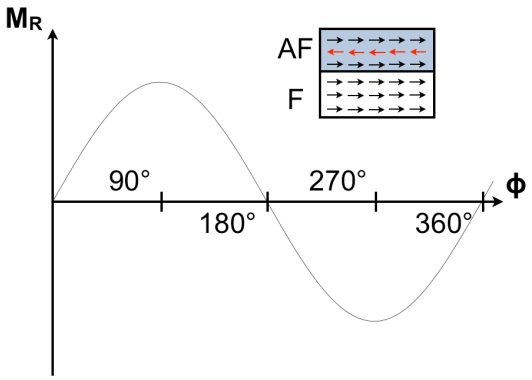

Fig. 3.18: Unidirectional anisotropy in an exchange bias coupled AF/F system.

The exchange bias field H_{ex} of coupled AF/F multilayers depends on temperature. It decreases with raising temperatures and disappears as temperature approaches the blocking temperature T_b of the antiferromagnet [72]. Besides, H_{ex} and H_C are both depending on the thickness t_F of the ferromagnet; showing that exchange bias is a boundary effect. While the exchange field behaves as $H_{ex} \propto 1/t_F$, the coercive field obeys to a power law as $H_C \propto (1/t_F)^n$ [73]. The dependency of the AF/F system on the thickness t_{AF} of the antiferromagnet is complex. In most thin film systems however, H_{ex} increases with t_{AF} until a critical thickness of the antiferromagnet is reached [74].
Exchange bias can also be influenced by the magnetic field which is applied to the AF/F system while it is cooled below T_N [75]. A further issue is the surface condition at the interface between ferromagnet and antiferromagnet. Basically, the exchange bias in thin-film systems is decreased by surface roughness of the antiferromagnet [76].

Theoretical models for exchange bias

By a basic model of the exchange bias effect shortly after its discovery, Meiklejohn and Bean showed that the energy of unidirectional anisotropy $E = -K_u \cos\phi$ (K is the anisotropy constant and ϕ the angle between the direction of external field and the easy axis) is related to a shift of the hysteresis loop by K_u/M_S [70]. They suggested coupled single-domain ferromagnets and antiferromagnets with strict uniaxial anisotropy (Ising model) and ideal interfaces. The energy E per unit surface is then expressed as

$$E = -HM_S t_F \cos(\phi-\phi_F)+K_F t_F \sin^2(\phi_F)+K_{AF} t_{AF} \sin^2(\phi_{AF})-J_{ex} \cos(\phi_F-\phi_{AF}), \quad (3.11)$$

where H is the applied magnetic field, M_S the saturation magnetization of the ferromagnet, t_F and t_{AF} the thickness of the ferromagnetic and the antiferromagnetic layer, respectively, K_F and K_{AF} the magnetic anisotropies of the ferro- and antiferromagnet, and J_{ex} the exchange coupling constant at the interface between layers. ϕ_F is the angle between the magnetic easy axis of the ferromagnet and the spin orientation, ϕ_{AF} the angle between the easy axis of the antiferromagnet and its spin orientation, and ϕ the angle between the applied field and the easy axis of the ferromagnet. The shift H_{ex} of the hysteresis loop can then be derived as [73]

$$H_{ex} = \frac{J_{ex}}{M_S t_F}. \quad (3.12)$$

However, the exchange bias calculated by this model deviates often by orders of magnitude from real values [77]. Several macroscopic models have been further proposed in order to explain the origin of exchange bias, which is not yet completely achieved. Most simple models consider surfaces with uncompensated spins and perfect anisotropy in the antiferromagnet, so lateral effects are not taken into account. However, regardless of consideration of even or rough surfaces, these models have also predicted interfacial exchange to be several orders of magnitude higher than measured values [78, 77]. In 1988, Malozemoff [79] proposed a random-field model which allows formation of magnetic domains with walls perpendicular to the interface of the antiferromagnet. Mauri *et al*. [80] proposed a model involving non-parallel alignment of spins in different layers of the antiferromagnet, which allows the formation of domain walls parallel to the interface and so cancelled the postulation of Meiklejohn and Bean that spins would be orientated exclusively in parallel or antiparallel configuration. However, the results are very close to the model of Meiklejohn and Bean, depending on the coupling strength at the interface. A micro-magnetic simulation of an atomistic Heisenberg model by Schulthess and Butler combines spin-flop mechanism and random fields which are induced by defects, but it considers only monocrystalline layers [81]. Obtained results are realistic and show the significance of consideration of defects in the boundary regions. In 1999, Stiles and McMichael introduced a model which consideres the antiferromagnet as polycrystalline and allows free spin orientation in all spatial directions, while the ferromagnet is considered to be in single-domain state [82]. A domain-state model proposed by Keller *et al*. in 2002 [83] introduces non-magnetic effects and volume defects for the antiferromagnet. This model has provided realistic results based on Monte Carlo simulations and takes also into account external influences such as temperature and the magnetic field during cooling. Also the model presented by Lederman *et al*. in 2004 is based on Monte Carlo simulation and provides realistic results [84].

3.3.2 Required properties for AF/F coupled layers in the magnetometer application

Physical properties

For use in magnetometer application, the chosen materials need to meet some physical conditions in order to guarantee a reliable functioning of the device. A first issue concerns the quantity of magnetic material and its remanent magnetization, which should both be as high as possible, as sensitivity is proportional to both of them (cf. eqn. 2.1). The used materials should exhibit stable magnetic properties when exposed to temperatures in the targeted operational range. During the fabrication process, materials will also eventually be exposed to high temperatures far beyond the blocking temperature of the AF/F stack. They also have to withstand aggressive treatment conditions like corrosion of the material during etching. The choice of appropriate materials will mainly depend on these aspects.

Another aspect concerns the integration of two differently orientated and ideally perpendicular arranged magnetic easy axes, needed for 3D sensing of the magnetic field. This can be achieved by taking advantage of the magnetic shape anisotropy. Alignment of the magnetic easy axes is needed to be achieved with high accuracy so that ideally identic sensitivity is achieved for detection axes. It is also desirable that easy axes remain stable, indepently from external influences such as temperature.

Further, the magnetic material has to resist when being exposed to high magnetic fields

(e.g. when being next to a loudspeaker). The maximum magnetic field strength the sensor has to withstand was specified to be 1T. As exchange bias coupled AF/F systems do generally not exhibit coercive fields as high as in the case of permanent magnets, a perturbation field from a loudspeaker may be sufficient to reverse the magnetization, if the exchange field is smaller than coercivity. In case of a not completely shifted hysteresis loop ($H_{ex}/H_C \leq 1$), there are two possible remanent states at zero field 3.19(a). If the loop is completely shifted ($H_{ex}/H_C > 1$), a single remanent state remains 3.19(b) and withstands high perturbation fields. The complete shift of the hysteresis loop is hence an important issue in this work and can be achieved by an appropriate design of the AF/F system, by taking advantage of the exchange bias.

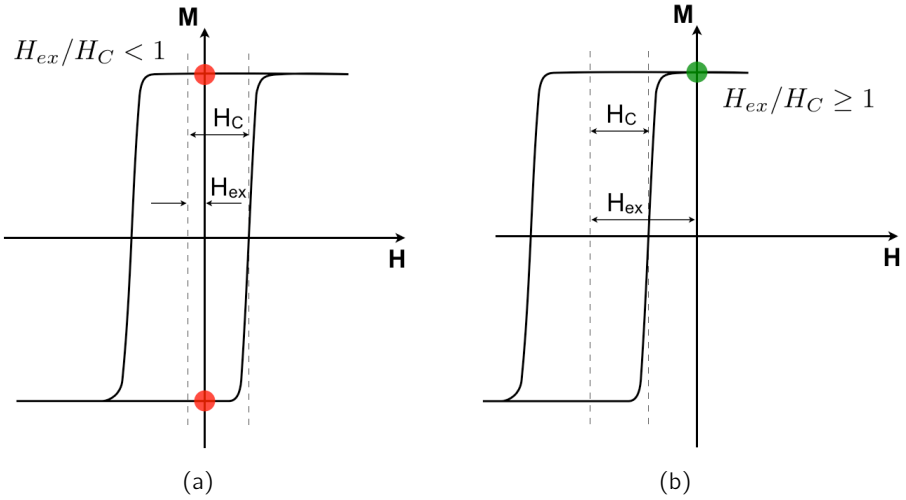

Fig. 3.19: Resistance to magnetic shocks: (a) two different possible remanent states after exposure to a high perturbation magnetic field; (b) one stable remanent state; insensitivity to magnetic shocks.

Technological constraints

For compatibility with the microfabrication process (cf. section 3.3.4), three major requirements need to be met by the AF/F layers:

1. The minimum of total $Co_{80}Fe_{20}$ thickness which is required to achieve a reasonable sensitivity for the magnetometer is $\geq$ 100nm. $Co_{80}Fe_{20}$ thickness is the only parameter to be modified in order to obtain a sufficient volume of magnetic material, once the MEMS structures are defined, as the effective area for deposition of magnetic material is limited.

2. For a good exchange interaction between ferromagnetic and antiferromagnetic layers, the thickness of a single $Co_{80}Fe_{20}$ layer needs to be $\leq$ 25nm.

3. The total thickness of the AF/F multilayer stack is also limited for compatibility with the used IBE equipment (cf. page 110). In case of the "Capucine" project, maximum stack thickness was fixed to 700nm.

3.3.3 Choice of ferromagnetic and antiferromagnetic materials

With the potential of today's thin film technology, many advances have been made during the last years in the development of exchange bias coupled AF/F multilayers. The PhD thesis of Y. Lamy [69] describes the development of such AF/F systems for use in microwave applications in a detailed way. As seen in section 3.2, remanent magnetizations of permanent magnets like SmCo and NdFeB are about 0.9T and 1.3T, respectively [56]. The advantage of soft ferromagnets like Co_xFe_{100-x} is that they exhibit high saturation magnetization of $\mu_0 M_S \geq 2.4$T in a range of $30 \leq x \leq 50$ [29]. Similar saturation magnetizations have been reported for the case where other elements are added to the CoFe alloys, e.g. for CoFeB [85]. However, they exhibit only low remanence magnetization and become hence uninteresting as individual materials. Nevertheless, by pinning the ferromagnet's magnetization to an antiferromagnet by taking advantage of the exchange bias, the remanent magnetization will be close to saturation magnetization and the exchange-bias coupled system shows hard magnetic characteristics. Yet, the most important advantage consists in the ability to design an AF/F stack in a way that $H_{ex}/H_C > 1$, so that the material becomes insensitive to magnetic shocks. Generally, this cannot be achieved with natural permanent magnets. Therefore, exchange coupled AF/F systems represent a very advantageous alternative compared to "classical" permanent magnets, particularly in the domain of MEMS applications.

The choice of an appropriate antiferromagnetic material for the pinning layer depends primarily on its coupling strength. Other important parameters to be considered are the required thickness to reach appropriate coupling, the blocking temperature and compatibility with the fabrication process in which the antiferromagnet will be used. Typical examples for antiferromagnetic materials for use in thin-film technology are insulating films such as CoO and NiO. Table 3.7 lists oxide-based antiferromagnets, which are compared in terms of their exchange coupling constant J_{ex} and their blocking temperature T_b. In case of FeO

AF material	J_{ex} [erg/cm^2]	T_b [K]
NiO	<0.2	450 - 480
FeO	<0.1	100
CoO	3.5	290

Table 3.7: Comparison of oxide-based antiferromagnetic materials (cf. PhD thesis of Y. Lamy [69]).

and CoO, the blocking temperature is far too low to these antiferromagnets as pinning layers in the magnetometer's temperature working range (-10°C - 50°C). For NiO, the blocking temperature may not be high enough to allow the AF/F coupled multilayers to withstand temperatures during the fabrication process.

Another option consists in the use of metallic antiferromagnetic films. A representative list of antiferromagnetic materials is given in table 3.8. FeMn is inappropriate for integration into the magnetometer, as it exhibits low J_{ex} and a blocking temperature which is too low for a reliable fabrication process. T_b is higher for IrMn, PtMn and NiMn, which are hence interesting candidates for integration into the fabrication process.

In 2004, Imakita *et al.* [87] reported giant exchange coupling with $J_{ex} = 1.3$erg/cm^2 for IrMn−CoFe exchange coupled systems, which is very promising. However, different results in literature are widely spread. The PhD work of Y. Lamy [69], who studied several AF/F

AF material	J_{ex} [erg/cm^2]	T_b [K]
FeMn	0.11	443
IrMn	0.18	528
PtMn	0.18	583
NiMn	0.3	673

Table 3.8: Comparison of metal-based antiferromagnetic materials according to Nozières *et al.* [86]

exchange coupled systems for integration in microwave applications, serves as an adequate reference for the frame of this work, as IrMn−CoFe exchange coupled sandwich layers have been studied within the cleanroom environment of the Leti.[8] Thus, the fabrication conditions he used are comparable to those being used in our present case. Lamy fabricated an $Ir_{20}Mn_{80}$ (8nm)/$Co_{35}Fe_{65}$ (25nm)/$Ir_{20}Mn_{80}$ (8nm) exchange coupled system and obtained a J_{ex} of 0.6 erg/cm^2 and a blocking temperature of 453K. An important advantage of IrMn is its high coupling strength for a very thin film thickness below 10nm.

In the case of NiMn, exchange coupling constants of J_{ex} of 0.3 erg/cm^2 have been reported [86, 88]. In a sandwich configuration of $Ni_{50}Mn_{50}$ (50nm)/$Co_{35}Fe_{65}$ (50nm)/$Ni_{50}Mn_{50}$ (50nm), Lamy measured an exchange coupling constant of $J_{ex} = 1$erg/cm^2 ($J_{ex} = 0.99$ erg/cm^2 if $Co_{35}Fe_{65}$ is substituted by $Co_{90}Fe_{10}$, respectively). A major disadvantage of NiMn is the minimum film thickness of about 50nm which is required in order to "pin" the ferromagnet. This becomes disturbing in such degree as it limits the quantity of ferromagnetic material being integrated into the magnetometer, because the overall thickness of the integrated AF/F stack is limited by technological constraints. However, the high blocking temperature allows to expose the AF/F system to aggressive thermal conditions during the fabrication process. Note that T_b is actually the upper limit of a distribution of blocking temperature, so partial loss of exchange bias may even occur for temperatures below T_b.

Besides NiMn, PtMn is a further promising option to be used as antiferromagnetic coupling layer, as it exhibits also a high blocking temperature. In 2000, Nozières *et al.* [86] stated that as in the case of NiMn, PtMn leads to an exchange field which is very stable in time and thus appropriate for disk-drive applications. The investigation of NiMn- and PtMn-based AF/F exchange coupled layers is hence pertinent for the magnetometer application. In the workframe of this thesis however, only a PtMn target was available for sputtering. Thus, only the properties of PtMn-based AF/F exchange coupled systems were studied.

3.3.4 Technological concept for integration of PtMn/CoFe-based exchange coupled multilayers

Technological realization of PtMn/CoFe multilayers

A simplified process flow for integration of AF/F multilayers is illustrated in table 3.9. We use $Co_{80}Fe_{20}$ (in at%) as soft magnetic material. In order to take advantage of the exchange bias effect, the CoFe layer thickness has to be less than 25 nm. However, as it is intended to maximize the volume of magnetic material, the overall CoFe thickness has to be greater than

[8] It should be noted that the materials discussed in the work of Lamy were deposited by PVD (Physical vapor deposition), whereas IBD (Ion beam deposition) was used for the materials discussed in this work.

25 nm. This leads to the deposition of an AF/F multilayer stack, principally deposited as a [PtMn/CoFe]×n/PtMn configuration on a prepared silicon substrate with a 200 nm thick Si_3N_4 layer. This Si_3N_4 layer serves to avoid diffusion of magnetic material into the silicon substrate. The first PtMn layer is grown on a 5 nm thin Ta seed layer in order to enhance PtMn crystalline quality. Deposition of all layers is achieved by IBD (Ion Beam Deposition). A 30nm thin Ta layer on top of the AF/F multilayer stack protects it against natural oxydation and chemical corrosion in the following process step of Ion beam etching (IBE). This step serves to apply a stripe pattern to the multilayer which is required for integration of two magnetic easy axes (this point will be discussed below). For this purpose, a SiO_2 mask is deposited, followed by IBE of the multilayer stack. In order to avoid corrosion during the later magnetometer fabrication process (especially during a release step by hydrofluoric acid), a Tungsten Nitride layer is deposited for its protection.

Step	Description	Scheme
a)	The process is started on a silicon substrate.	
b)	A 200nm thick Si_3N_4 layer serves to avoid diffusion between magnetic material and the substrate.	
c)	Deposition of a 5nm thin Tantalum seed layer.	
d)	Deposition of the multilayer stack by IBD. [PtMn/CoFe]×n/ PtMn/Ta	
e)	Deposition of a SiO_2 layer and lithography to build the mask for etching.	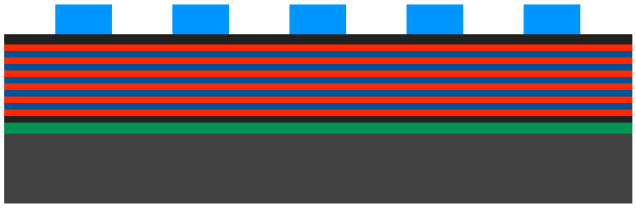
f)	IBE etching of the multilayer stack and subsequent deposition of a thin W_2N capping layer for corrosion protection.	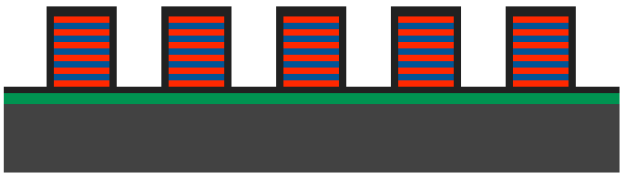

Table 3.9: Basic process for integration of an exchange coupled AF/F multilayer stack

A SEM view of an integrated [PtMn/CoFe]×10/PtMn multilayer stack is presented in fig. 3.20

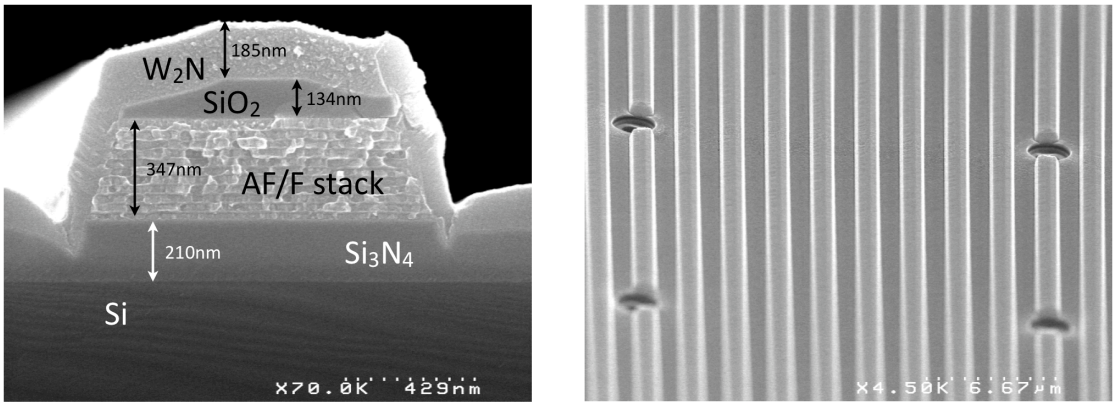

(a) (b)

Fig. 3.20: Integrated PtMn/CoFe multilayers: (a) SEM section view of an integrated [PtMn/CoFe]×10/PtMn multilayer stack; (b) SEM view of magnetic material deposited as narrow stripes.

Process for integration of two different magnetization directions

In case of thin films, spins tend to align in the wafer-parallel plane due to shape anisotropy (cf. eqn. 3.10). For 3-axis sensing of the magnetic field, two different magnetization directions need to be integrated within a chip. A concept to achieve this was patented before by O. Redon [89]. By deposition of the magnetic material as perpendicularly orientated stripes, we can take advantage of the shape anisotropy and achieve the integration of two magnetization directions which is required for 3D magnetometer (cf. fig. 2.4, p. 27). The magnetic field $H_{sat,e}$ needed to saturate the easy axes is expressed as

$$H_{sat,e} = 4\pi M_s t \frac{w}{l^2}\left[\ln\left(\frac{4l}{w}\right) - 1\right], \tag{3.13}$$

where w and l are width and length of the stripe, respectively. The total thickness of the ferromagnetic material is noted as t. M_s is the saturation magnetization of the magnetic material. In the same way, a field $H_{sat,h}$ of

$$H_{sat,h} = 4\pi M_s t \left[\frac{1}{t+w} - \frac{w}{l^2}\left[\ln\left(\frac{4l}{w}\right) - 1\right]\right] \tag{3.14}$$

has to be applied in order to saturate the stripe along the hard axis. In order to evaluate the influence of stripe geometry on the shape anisotropy by experiment, some test arrays including variable stripe geometries were designed, according to fig. 3.21(a). This was needed in order to select an appropriate geometry for integration of magnetic material in the sensor. The distance b between stripes of magnetic material was fixed to 1.5µm. This condition

was determined by technological constraints, as the stripes are defined by an IBE (ion beam) etching step, which requires an optimum angle φ between the beam orientation and the wafer top layer (cf. fig. 3.21(b)). If t_{St} is considered to be the total thickness of the multilayer stack, the minimal distance between stripes (on the mask level) is hence given by $b_{min} = 2t_{St}/\tan\varphi$. Assuming a maximal stack thickness of 2µm and $\varphi \approx 70°$ yields $b_{min} \approx 1.5$µm. However, the actual technologically integrable maximum thickness is rather below 1µm. All stripes have a length of 4.5mm. The different samples are named according to the respective stripe geometry (cf. table 3.10).

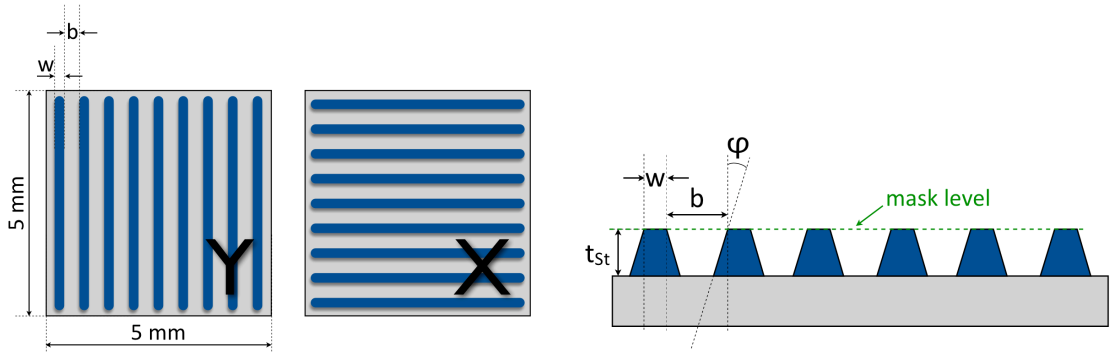

Fig. 3.21: Design of test samples for evaluation of the magnetic shape anisotropy: (a) scheme of arrays including perpendicularly orientated stripes for evaluation of magnetic shape anisotropy; (b) the limit for distance b between stripes is technologically determined, depending on the thickness of the deposited magnetic material.

Sample name	w [µm]	Filling coefficient [%]
AX, AY	5	77
BX, BY	4	73
CX, CY	3	67
DX, DY	2	57
EX, EY	1.5	50
FX, FY	1	40
GX, GY	0.5	25
HX, HY	0.25	14

Table 3.10: Different geometries used for stripes of magnetic material and resulting filling percentage of magnetic material over the sample area

Integration of two perpendicular magnetization directions is achieved by annealing the samples under a magnetic field H_a which is orientated at 45° with respect to the geometric long axes x and y of the deposited stripes (fig. 3.22(a)). The applied annealing temperature has ideally to be greater than the blocking temperature of PtMn in order to temporarily suppress exchange bias coupling. The strength of the applied magnetic field has to be sufficiently high so that the projection of H_a along the axes x and y is higher than the saturation field $H_{sat,e}$. If the sample is cooled down, both magnetization directions along x and y are pinned by

the antiferromagnet and are, in an ideal case, orientated at an angle of 90° one to another. Depending on the stripe geometry and the related shape anisotropy, a disalignement of H_x and H_y with respect to the geometric long axis of any of the stripes may occur, where actual magnetic easy axes are rotated from their ideal direction about an angle β. The consequences of this effect have already been discussed in chapter 2. The fact that magnetic material has to be deposited as stripes is disadvantageous for the sensitivity of the magnetometer, as this leads to a reduced volume of magnetic material to be deposited on the available sample area.

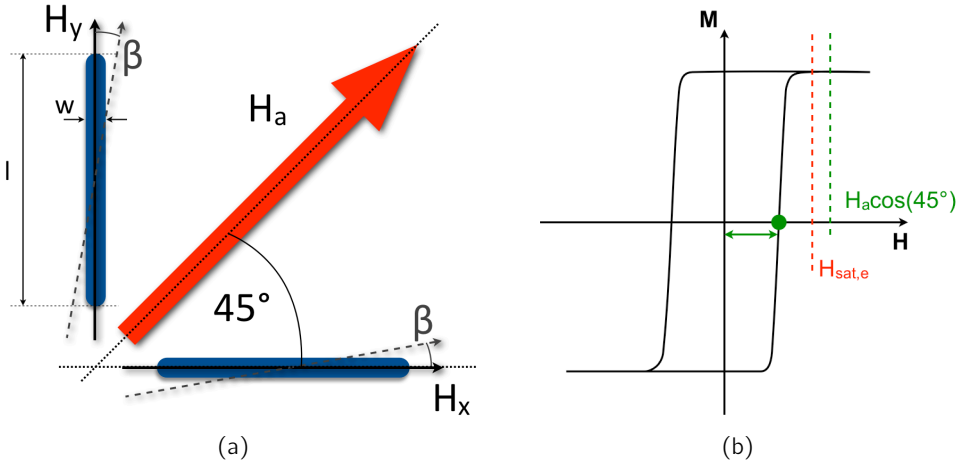

Fig. 3.22: Process for integration of two magnetic easy axes: (a) Configuration for integration of two perpendicular magnetization directions; (b) For saturation of the easy axis, the applied field during annealing must be sufficiently high, so that $H_a \cos 45° \geq H_{sat,e}$.

3.3.5 Magnetic properties of PtMn/CoFe multilayers

Choice of an appropriate AF/F stack for initial investigation

The choice of an appropriate AF/F stack depends on its magnetic properties and on limits which are imposed by technological constraints. Basically, AF/F multilayers are of the type [PtMn/CoFe]×n/PtMn. AF/F thickness is technologically limited to a maximum of ∼1µm. In order to assure exchange bias coupling, PtMn thickness was set to a constant thickness of 20nm in a first time (further investigations on PtMn thickness are discussed later), while CoFe thickness must not exceed a thickness of 25nm. A first investigation consists hence in the choice of an appropriate subdivision of CoFe in multiple layers. Therefore, three different stacks were deposited over the entire wafer without application of any surface pattern and by keeping a constant overall CoFe thickness of 100nm:

1. Ta 5nm/[PtMn 20nm/CoFe 25nm]×4/PtMn 20nm/Ta 5nm; stack thickness: 210nm
2. Ta 5nm/[PtMn 20nm/CoFe 10nm]×10/PtMn 20nm/Ta 5nm; stack thickness: 330nm
3. Ta 5nm/[PtMn 20nm/CoFe 4nm]×25/PtMn 20nm/Ta 5nm; stack thickness: 630nm

After annealing of the different stacks at 265°C under exposure to a magnetic field of 1T which saturizes the integrated magnetic material, hysteresis loops were measured by VSM (vibrating sample magnetometer). Measurement results are presented in fig. 3.23. Comparison of the H_{ex}/H_c ratios[9] for the three stacks yields 14.3%, 26.7%, and 26.4%, respectively. Thus, CoFe distribution of the second stack (Ta 5nm/[PtMn 20nm/CoFe 10nm]×10/Ta 5nm) is an interesting candidate, as the overall stack thickness also represents an uncritical thickness for integration into the fabrication process.

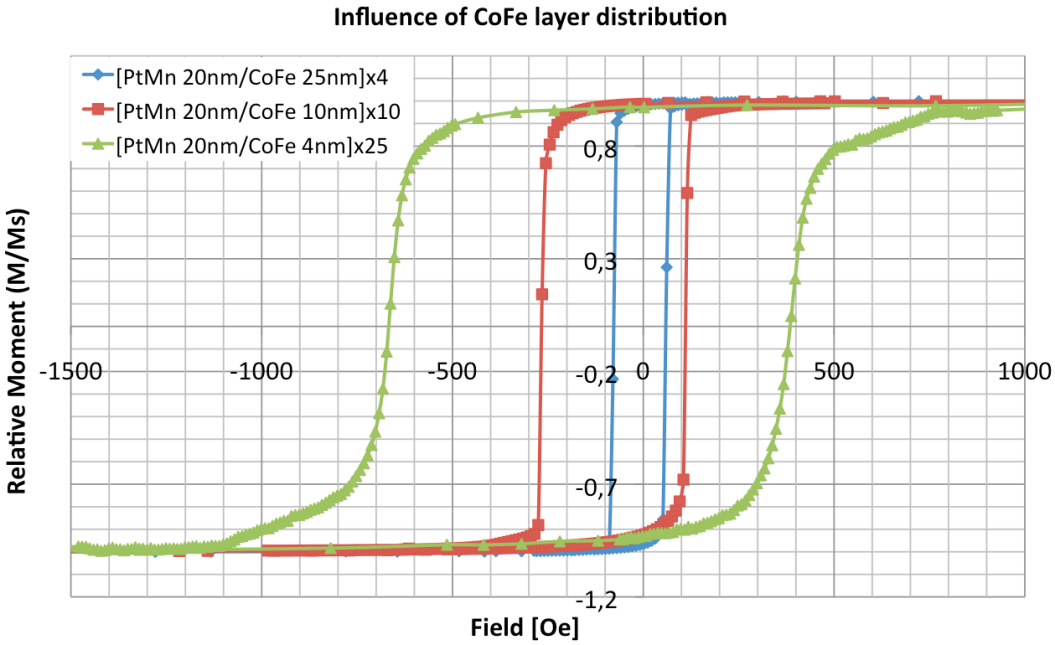

Fig. 3.23: Comparison of hysteresis loops for different CoFe layer thicknesses.

Dependency of shape anisotropy on AF/F surface geometry (before annealing)

A further step consists in the characterization of patterned AF/F multilayers. It is a particular point of interest to investigate the properties of uniaxial shape anisotropy as it depends on the stripe geometry. This point was investigated through VSM measurements on samples in their not-annealed condition with different surface geometries of the AF/F stack. The stripe pattern illustrated in fig. 3.21(a) was applied to the AF/F stacks by IBE etching. As seen from fig. 3.24, stripe width is an important parameter to control uniaxial shape anisotropy: For wider stripes, there is barely the presence of a magnetic hard axis and uniaxial shape anisotropy disappears. This is critical inasmuch as a magnetometer being designed to sense exclusively a fixed component of the magnetic field would also become sensitive to other directional components of the magnetic field, and would thus exhibit a greater cross-axis sensitivity. As the stripes become narrower, this problem vanishes and uniaxial anisotropy is better pronounced. It is thus possible to achieve an AF/F multilayer system which enables to integrate two different magnetization directions by taking advantage of shape anisotropy

[9] $H_{ex}/H_c \geq 1$ is the condition required for a completely shifted hysteresis loop with respect to zero field (cf. page 104)

which is observed in the case of narrow stripes ($w = 0.25\mu m$ and $w = 0.5\mu m$). Due to weak anisotropy, the deposition of AF/F stacks as a pattern of broader stripes is inappropriate for the magnetometer application.

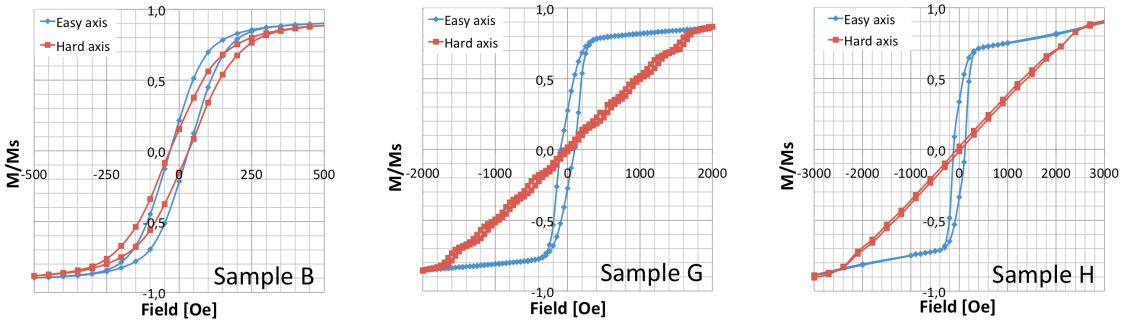

Fig. 3.24: Evolution of shape anisotropy depending on stripe width (before annealing): (a) weak shape anisotropy for sample B ($w = 4\mu m$); (b) clear presence of magnetc easy- and hard axis for sample G ($w = 0.5\mu m$); (c) the highest shape anisotropy is observed for sample H ($w = 0.25\mu m$).

Influence of AF/F surface geometry on hysteresis loop shift (after annealing)

Moreover, the influence of stripe width on the coercive field H_c, on exchange field H_{ex} and on the field required to saturate the hard axis $H_{sat,h}$ was investigated by VSM measurements. Before, the samples were annealed at a temperature of 265°C under a magnetic field in order to magnetize the CoFe layer and to pin its magnetization by the PtMn layer. Fig. 3.25 shows hysteresis loops which were measured on samples with 500nm stripe width for the magnetic hard- and easy axis after annealing for magnetization. As shown in fig. 3.26, H_c decreases with stripe width, while H_{ex} remains constant (the deviation of H_{ex} measured for the smallest stripe width of 250nm is less significant), leading thus to a decrease of H_{ex}/H_c ratio for smaller stripe widths. Reduction of hysteresis loop shift is hence mainly related to a growing coercive field for narrower stripes. We will discuss this point in a later paragraph. This is disadvantageous because insensitivity to perturbations of high magnetic fields cannot be achieved ($H_{ex}/H_c > 1$ required). However, shape anisotropy is much greater for narrow stripes as it can be seen from the growing magnetic field which is needed to saturate the magnetic hard axis ($H_{sat,h}$). Hence, it is difficult to obtain both, a completely shifted hysteresis loop such that $H_{ex}/H_c > 1$, and high shape anisotropy which is needed for minimum disalignment between the magnetic easy axis and the stripe's orientation.

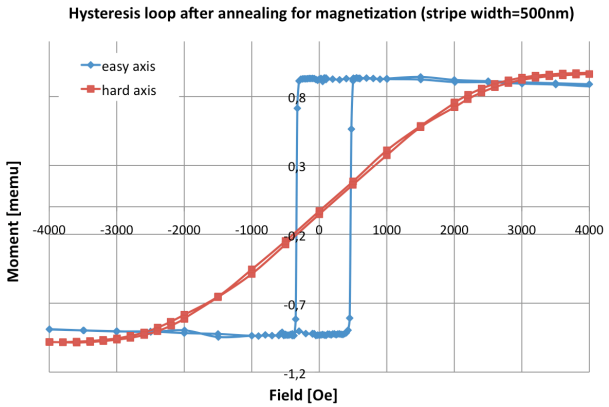

Fig. 3.25: Magnetic easy- and hard axis measured on samples with 500nm stripe width after the annealing step required for magnetization.

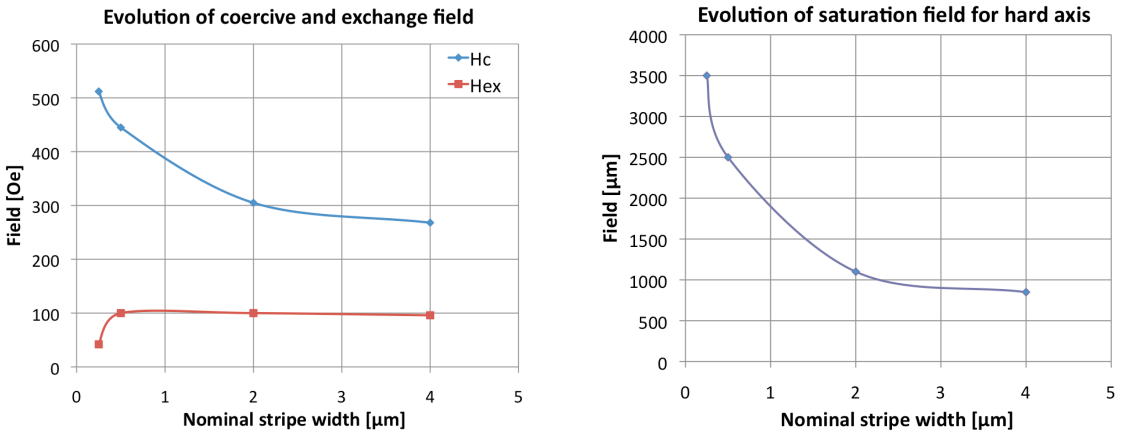

Fig. 3.26: Evolution of H_c, H_{ex} and $H_{sat,h}$ with stripe width: (a) H_{ex}/H_c ratio decreases for narrower stripes; (b) the field required to saturate the hard axis increases for narrower stripes.

Remanent magnetization of patterned AF/F stacks

From measurement of hysteresis loops, remanent magnetization M_R can now be determined for the different stripe geometries (table 3.11). The values measured for M_R are coherent for different stripe geometries and are equal to saturation magnetization M_s. Slight variations can be explained by imperfections of the deposited material (e.g. variations in stack thickness, non-uniformity of stripe width etc. It should be noted that we have been confronted with deviations in stripe width up to 200nm. The values listed in table 3.11 were corrected to take these major deviations into account.).

Nominal width [µm]	M_s **[emu/cm^3]**	$\mu_0 M_s$ **[T]**
0.25	1762	2.21
0.5	1747	2.20
2	1945	2.44
4	1629	2.05

Table 3.11: Saturation magnetization calculated from VSM measurements.

Proof of concept for integration of two different magnetization directions

With the known properties of the thin AF/F patterned stack concerning shape anisotropy, the concept of integration of two different magnetization directions can be demonstrated. In this study, we will concentrate on a stripe width of 0.5µm, as it is an acceptable compromize between shape anisotropy strength and magnetic volume. By annealing of the patterned AF/F samples under a magnetic field orientated at an angle of 45° with respect to the stripes, both magnetic easy axes are saturated (cf. fig. 3.22). The minimum field magnitude required for saturation of the magnetic easy axis was obtained by measurement of the hysteresis loop before annealing (shown in fig. 3.27(a) for samples with 0.5µm stripe width). In order to investigate the influence of the magnetic field strength on the hysteresis loop of the annealed sample, three different field magnitudes of 355 Oe, 425 Oe and 565 Oe were applied to samples at an angle of 45° with respect to the stripes. By this way, the effective magnetic field components which were applied along the orientation of the stripes were 250, 300, and 400 Oe, respectively. These magnitudes correspond to the field strength range where the hysteresis loop closes for saturation.

The results presented in fig. 3.27(b) show very good conformity between the hysteresis loops measured for x- and y stripe orientations along easy axis (hysteresis loops of hard axes are not shown in the graph). Only slight deviations of the coercive field can be observed for the easy axes. $H_{sat,h}$, the field needed to saturate the magnetic hard axis along x- and y-direction, was $\sim$ 2500 Oe, which indicates high shape anisotropy. This result is very important, as it first validates a crucial technological step which is required for realization of an integrated 3-axis magnetometer using AF/F coupled multilayers and second predicts high conformity of sensitivities along the different measurement axes. Nevertheless, a slight disalignment angle β between easy axis and geometric long axis of the stripes can be estimated by

$$\beta = \arctan\left[\frac{H_{sat,e}}{H_{sat,h}}\right]. \tag{3.15}$$

$H_{sat,e} = 250$ Oe and $H_{sat,h} = 2000$ Oe are obtained from earlier measured, not-annealed samples. The estimated disalignment angle is then $\beta \approx 7°$.

Enhancement of hysteresis loop shift by variation of PtMn and CoFe layer thicknesses

Despite successful demonstration of an AF/F multilayer stack suitable for use in 3D magnetometer application (in terms of shape anisotropy), the measured H_{ex}/H_c ratio is still $\sim$ 0.23, which is not sufficient in order to achieve insensitivity to magnetic shocks. Several ways can be explored in order to achieve a complete shift of the hysteresis loop. In a first approach, the influence of PtMn thickness variation is studied by setting CoFe thickness to a

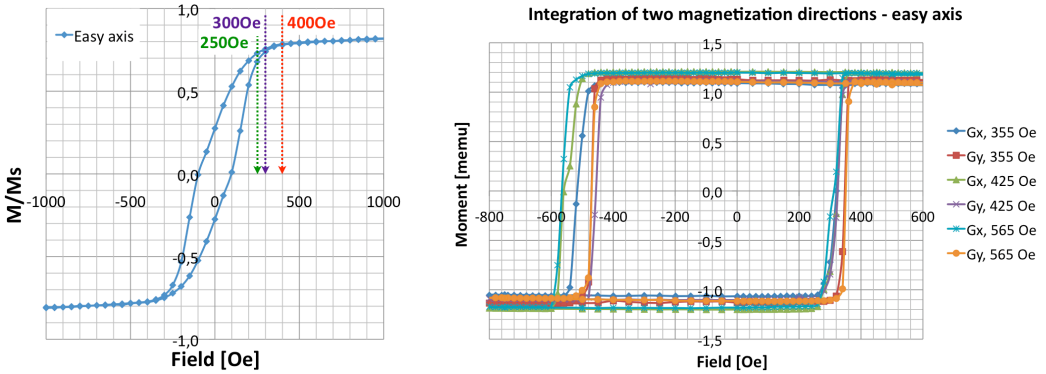

(a) (b)

Fig. 3.27: Annealing at different temperatures for magnetization of probes with 0.5µm stripe width: (a) The hysteresis loop measured for the not-annealed sample serves to determine the minimum required magnetic field to be applied during annealing; (b) Measured hysteresis loops (magnetic easy axis) for probes with 0.5µm stripe width after annealing at 265°C with applied fields of 355 Oe, 425 Oe and 565 Oe magnitude, orientated at an angle of 45°. It can be seen that all three magnetic fields applied during annealing are sufficiently high to saturate both easy axes along x- and y-direction.

fixed value of 20nm. For this purpose, AF/F stacks with varying PtMn layer thickness were deposited without patterning in a [PtMn/CoFe 20nm]$\times n$/PtMn configuration and annealed under a magnetic field of 1T in order to saturate the AF/F multilayer stack. The number of bilayers was $n = 10$ for PtMn thicknesses from 10nm to 20nm and $n = 5$ for PtMn thicknesses above 20nm. It can be seen from VSM measurements (fig. 3.28(a)) that a high H_{ex}/H_c ratio of over 2 is achieved with a PtMn layer of 50nm thickness, while H_{ex}/H_c is only in the region of 0.25-0.3 for PtMn thicknesses below 20nm. Further increase of PtMn thickness leads to less significant gain in hysteresis loop shift (H_{ex}/H_c ratio reaches only ~ 2.5 for 100nm PtMn thickness) and would contribute to technological complications, as greater thicknesses of the AF/F stack have to be dealt with. Also the costs of materials have to be considered for stack design.
A further study was carried out where CoFe thickness was varied between 10-30nm, while PtMn layer thickness was fixed to a value of 50nm. Three different stacks were studied, using following multilayer configurations:

- Ta 5nm/[PtMn 50nm/CoFe 10nm]$\times$10/PtMn 50nm/Ta 30nm; $t_{St} = 685$nm
- Ta 5nm/[PtMn 50nm/CoFe 20nm]$\times$5/PtMn 50nm/Ta 30nm; $t_{St} = 435$nm
- Ta 5nm/[PtMn 50nm/CoFe 30nm]$\times$4/PtMn 50nm/Ta 30nm; $t_{St} = 405$nm

This study confirms that H_{ex}/H_c becomes maximum for a CoFe thickness of $\sim$ 20nm (fig. 3.28(b)). A CoFe thickness of 20nm is also a good compromize for the total stack thickness t_{St}.
According to results obtained from AF/F stacks deposited on an entire wafer and using a [PtMn 50nm/CoFe 20nm]$\times$5/PtMn 50nm multilayer configuration, a completely shifted hysteresis loop with $H_{ex}/H_c \sim 2$ was observed (fig. 3.29(a)). This is a very promising result, but it needs essentially to be validated on patterned AF/F stacks. For this purpose, the

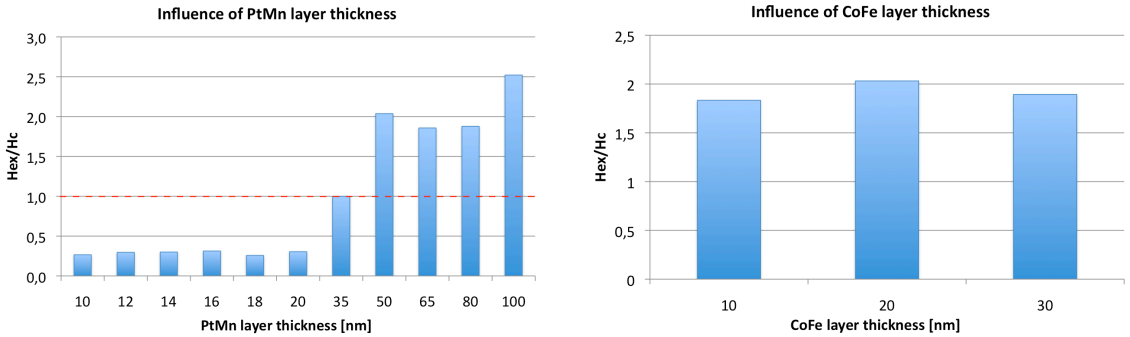

Fig. 3.28: Influence of layer thickness variation on H_{ex}/H_c ratio in case of full-sheet deposition of AF/F stacks: (a) different PtMn layer thicknesses for a fixed CoFe layer thickness of 20nm; (b) different CoFe layer thicknesses at a fixed PtMn layer thickness of 50nm.

same pattern as for former AF/F stacks was applied. The samples were annealed at 265°C under a magnetic field orientated at 45° with respect to the stripes and hysteresis loops were measured by VSM. An essential result is presented in fig. 3.30(a): a complete shift of the hysteresis loop ($H_{ex}/H_c \geq 1$) can be achieved for stripe widths greater than 0.5µm, even though H_{ex}/H_c is decreased after patterning (fig. 3.29(b)). As far as stripe width is concerned, gain in shift of hysteresis loop is on the cost of shape anisotropy, as shown by measurements presented in fig. 3.30(b): easy axis disalignment of the completely shifted hysteresis loop of sample "C" ($w = 2$µm) is almost 22°, which may lead to problems in the magnetometer application due to cross-axis sensitivity. The significant loss in H_{ex}/H_c can thus mainly be explained by an increased coercive field after structurization and annealing of the multilayer stack, as it was also the case for AF/F stacks using a PtMn thickness of 20nm. If a compromize between sensitivity to magnetic shocks and cross-axis sensitivity cannot be made, PtMn/CoFe-based multilayers do not meet all of the requirements needed for use in 3D magnetometer application. However, cross-sensitivity can be reduced to an insignificant problem by a dedicated sensor design, so that the result of weak shape anisotropy would only be a loss in sensitivity, as explained in chapter 2.

Influence of annealing conditions on hysteresis loop shift (patterned AF/F stacks)

It has already been noted that decrease in H_{ex}/H_c ratio is mainly related to an increased coercive field in case of narrow stripes of AF/F stack after annealing. When the influence of annealing is studied on patterned AF/F multilayers by comparison of hysteresis loops after annealing to those before annealing, it can be clearly seen that the coercive field is higher in case of narrow stripes, whereas H_{ex} is almost constant at a value of $\sim$ 120 Oe. In the as-deposited condition however, the coercive field H_c for 0.5µm stripe width is almost twice the value found in case of 2µm stripe width (cf. 3.31). One explanation for increase in coercivity after annealing is the size of CoFe grains [90] which are blocked by the side walls of the stripes, particularly in case of narrow stripes. It has also been reported that deposition conditions such as seed layer and deposition technique have an impact on grain quality [91]. Another way to explain this phenomenon is partial oxidation of CoFe grains at

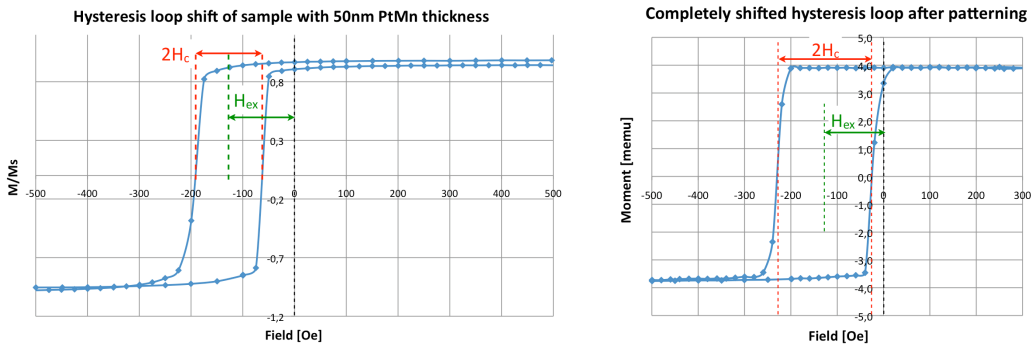

(a) (b)

Fig. 3.29: $H_{ex}/H_C > 1$ for a PtMn thickness of 50nm: (a) Completely shifted hysteresis loop ($H_{ex}/H_C \approx 2$) of a sample using a [PtMn 50nm/CoFe 20nm]×5/PtMn 50nm stack (full sheet deposition); (b) completely shifted hysteresis loop for a patterned [PtMn 50nm/CoFe 20nm]×5/PtMn 50nm multilayer stack for a stripe width of 2µm.

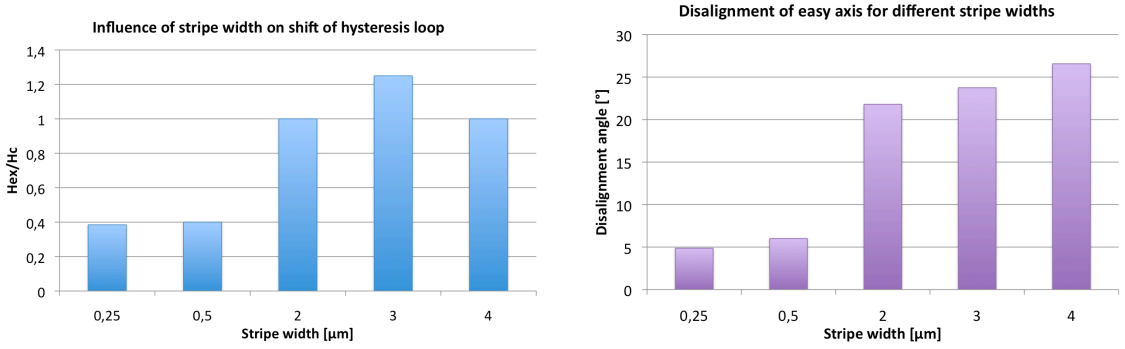

(a) (b)

Fig. 3.30: Measured characteristics of patterned [PtMn 50nm/CoFe 20nm]×5/PtMn 50nm stacks: (a) a completely shifted hysteresis loop is achieved with a stripe with of 3µm; (b) the disalignment angle β increases with growing stripe width.

their boundaries [92]. This latter effect may have an important impact in case of narrow stripes, as CoFe oxidation is favoured at the stripe boundaries. An approach to obtain a better shift of the hysteresis loop consists hence in impacting CoFe grain size and/or grain oxidation by modification of annealing conditions and thus in changing the coercive field H_c.

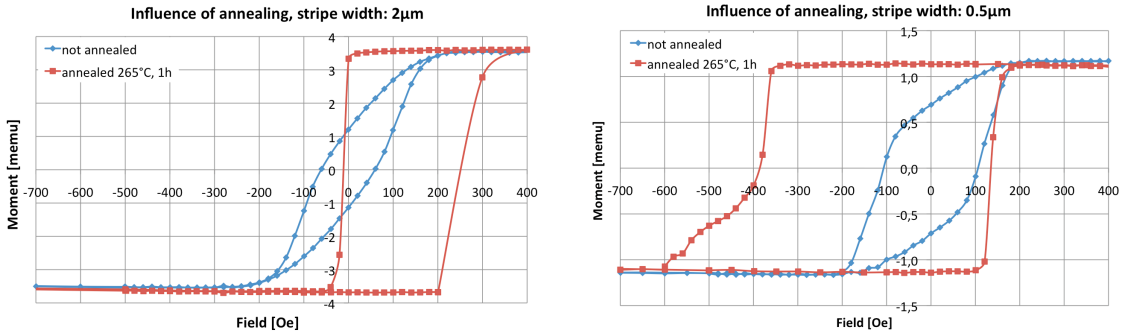

(a) (b)

Fig. 3.31: Influence of annealing (265°C for 1h) on stripe-patterned AF/F stacks ([PtMn 50nm/CoFe 20nm]×5/PtMn 50nm/Ta 50nm): (a) stripe width $w = 2$µm; (b) stripe width $w = 0.5$µm. The coercive field increases after annealing and is larger for narrow stripes.

The influence of annealing parameters on H_{ex}/H_c ratio was studied by two different approaches. In a first study, samples of 0.5µm stripe width and PtMn thicknesses of 20nm and 50nm were annealed for 1h at different temperatures. In a second approach, annealing time was varied by keeping a temperature of 265°C. Fig. 3.32 shows that neither variation of annealing temperature nor variation of annealing time leads to a completely shifted hysteresis loop. Highest values for H_{ex}/Hc are achieved for [PtMn 50nm/CoFe 20nm]×5/PtMn 50nm stacks, an annealing temperature of 265°C and an annealing time of 1h.

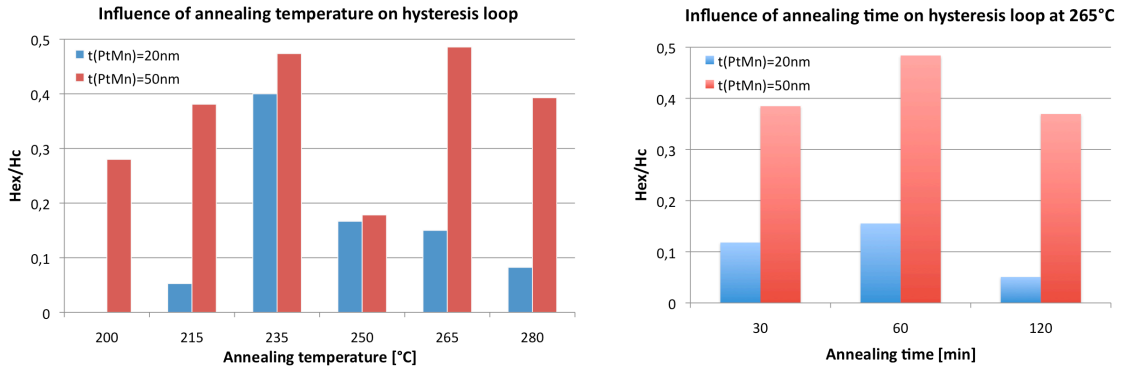

(a) (b)

Fig. 3.32: Influence of annealing conditions for two different stacks. Stack 1) Ta 5nm/[PtMn 20nm/CoFe 10nm]$_{10}$/PtMn 20nm/Ta 5nm. Stack 2) Ta 5nm/[PtMn 50nm/CoFe 20nm]$_5$/PtMn 50nm/Ta 5nm: (a) variation of annealing temperature; (b) variation of annealing time.

Dependency of magnetic properties on thermal process conditions

In the used process to integrate AF/F multilayers into the magnetometer, the magnetic stacks may be exposed to high temperatures which they have to withstand. It should be noted that, depending on the chosen packaging process, temperatures up to 490°C can be reached. Different packaging processes may be based on, e.g.: polymer sealing ($T \sim 250$°C), eutectic Au-Sn sealing ($T \sim 320$°C), anodic sealing ($T \sim 400$°C), and eutectic Al-Ge sealing ($T \sim 490$°C). Basically, there are two options to define the technological process including a packaging process:

- Annealing with an adapted magnetic field is done *before* the packaging step.
- Annealing with an adapted magnetic field is done *after* the packaging step.

In the first case, both magnetization directions are integrated into the chip by an annealing step at $T = 265$°C. This clearly limits the choice of the packaging process to polymer sealing, as the process temperature must be below the blocking temperature of PtMn, where antiferromagnetic pinning disappears. It is still interesting to estimate the influence of post-annealing heating in order to verify whether or not magnetic properties of the AF/F stack are deteriorated. For this purpose, prepared AF/F samples were first annealed at $T = 265$°C during 1h under a magnetic field, and then exposed to temperatures of 260°C and 280°C, each time during 30 minutes. Finally, respective hysteresis loops were measured by VSM and are presented in fig. 3.33. It can be seen that magnetic properties are not subjected to significant changes after exposure to temperatures ranging up to 280°C.

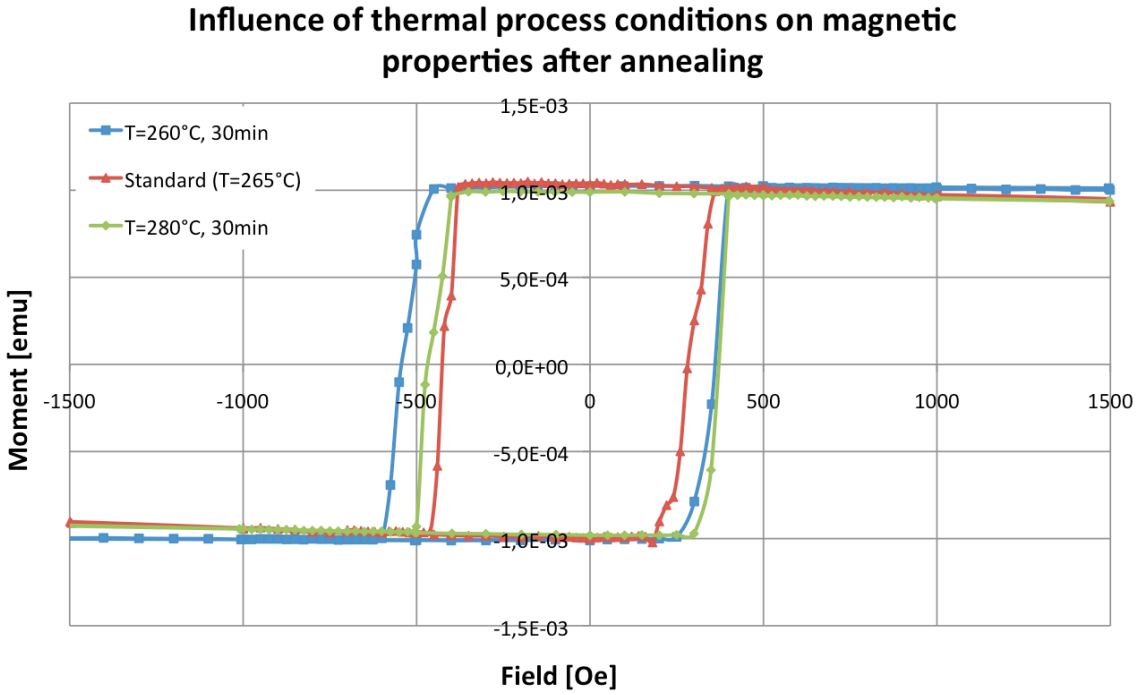

Fig. 3.33: Impact of different temperatures on magnetic properties after annealing of the PtMn/CoFe stack.

In the second case, the annealing step with an adapted magnetic field comes after the

packaging process. Generally, nothing limits the choice of the packaging process in this case. However, it has to be assured that post-packaging annealing does not affect the sealing quality. For instance, high temperatures could be responsible for a change in size of the magnetic domains and for diffusion between adjacent materials. To evaluate the impact of exposure to different process temperatures on the magnetic properties of the AF/F stack, several prepared samples were exposed to different temperatures ranging from 250°C to 490°C in order to simulate different packaging processes. After exposure, the samples were annealed at 265°C under a magnetic field for pinning of the magnetic easy axis. As seen from fig. 3.34, all of the tested samples kept their value of remanence. Slight deviations in coercive field and exchange field are negligible and can be ascribed to technological impresicion (e.g. variation of corrosion during etching and oxydation) between different samples. This allows us to conclude that there is no limit in the choice of the different packaging processes, unless the sealed chip does not withstand the post-sealing annealing temperature of 265°C.

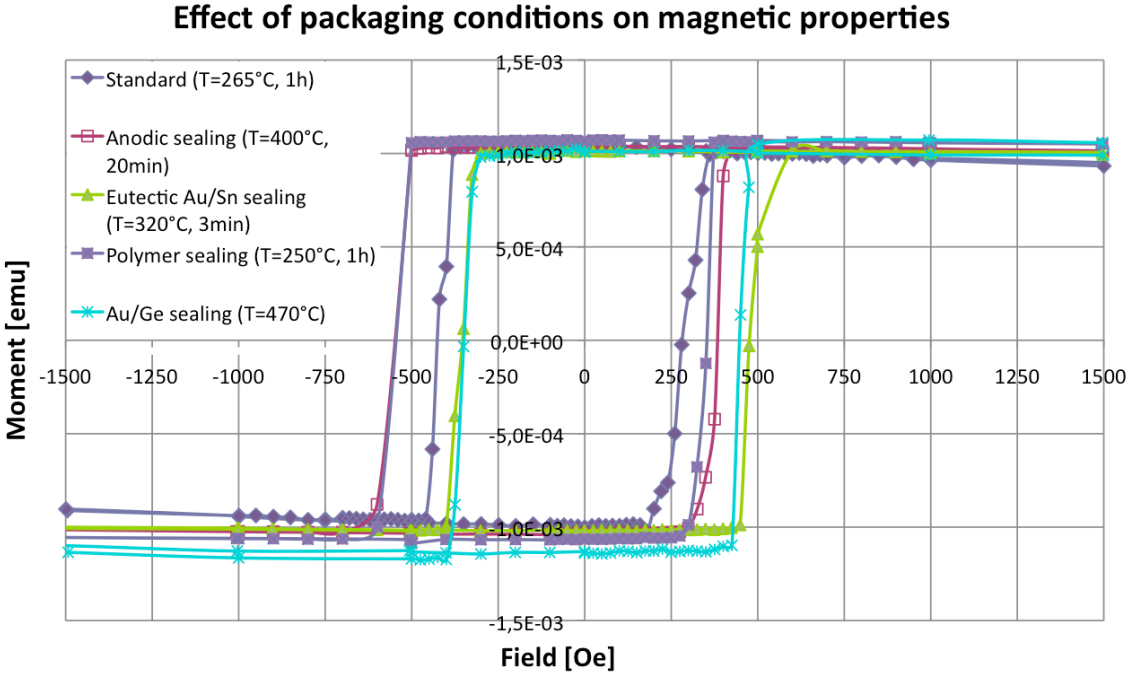

Fig. 3.34: Simulation of the effect of different packaging conditions (prior to annealing) on the PtMn/CoFe stack.

Influence of thermal environment on magnetic properties

Environmental thermal conditions have an influence on the magnetic remanence and modify thus the sensing properties of the magnetometer. An important parameter is the temperature coefficient of remanence (TCM), which modifies the sensor sensitivity. But also an influence of temperature on the hysteresis loop shift may become an important issue. For evaluation of these aspects, hysteresis loops of a [PtMn 50nm/CoFe 20nm]$_5$/PtMn 50nm stack were measured in the temperature range between 25°C and 125°C with steps of 25°C. A first important value estimated from the measurements was a weak temperature coeffi-

cient of remanence of $TCM = -53\text{ppm}/°\text{C}$. The measured evolution of H_{ex}/H_C is shown in figure 3.35. Hysteresis loop shift is decreasing with temperature, but H_{ex}/H_C is > 1 in the application temperature range, so that specifications are still satisfied.

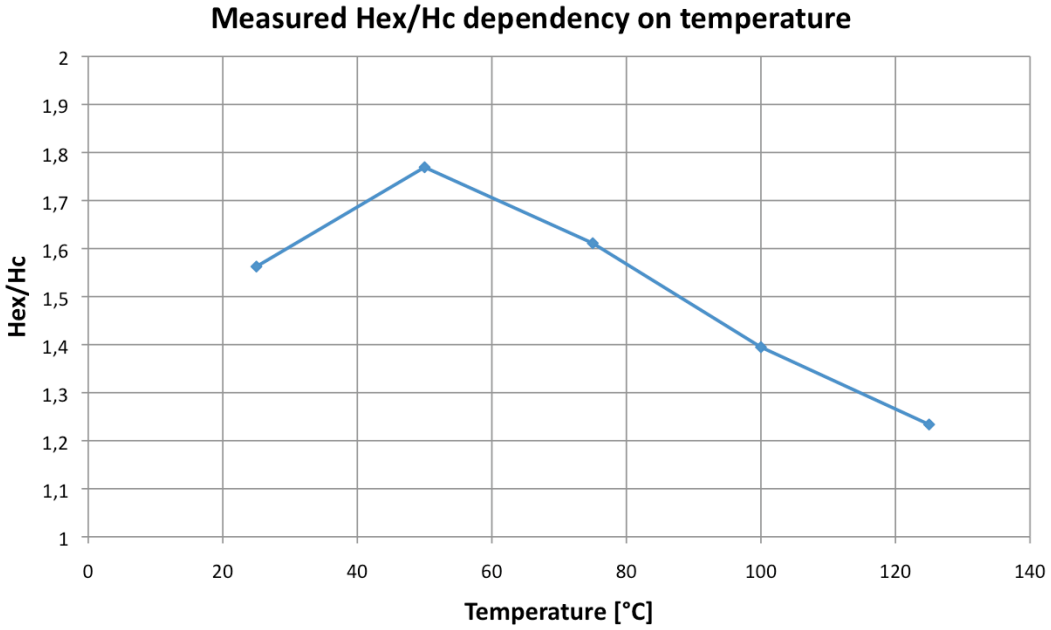

Fig. 3.35: Evolution of the hysteresis loop shift with environment temperature.

3.3.6 Discussion

The development of exchange bias coupled AF/F multilayers for magnetometer application was presented. CoFe has been chosen as ferromagnet due to its high saturation magnetization of ~ 1.8T; PtMn has been chosen as antiferromagnetic material due to a high blocking temperature, time-stable coupling properties and because of its availability in cleanroom. However, high costs of PtMn are a drawback for industrial applications. Magnetic properties of the multilayer stacks were characterized by VSM measurements.

A crucial technological step has successfully been proven to be feasible: the integration of two perpendicular magnetization directions within the same chip by taking advantage of magnetic shape anisotropy. However, AF/F multilayers have to be deposited in form of stripes as narrow as 0.5µm or even less in order to achieve a good alignment of the magnetization direction with the geometric long axis of the stripe in order to obtain maximum sensitivity for the respective detection axis in the magnetometer application. The relatively low shape anisotropy can be explained by sidewall roughness after etching of the CoFe layers. It has further been shown that a completely shifted hysteresis loop could be achieved for stripe widths of 2µm, which would lead to reduced sensitivity, as the magnetic easy axis is not well aligned with the narrow stripes of magnetic material in this case. If each sensing component of the 3D magnetometer (i.e. for x-, y-, and z-detection) is considered seperately, this property could also lead to serious cross-sensitivity problems. However, the problem of cross-sensitivity can be eliminated in case of an adapted magnetometer design (cf. chapter 2). For stripe

widths lower than 2µm, $H_{ex}/H_C \geq 1$ could not be achieved by investigation of:

- the influence of thickness variation of CoFe and PtMn layers with the major intention to enhance exchange coupling, and
- the influence of annealing conditions (temperature and time) to impact CoFe grain size and oxidation at the etched side walls, aiming to decrease the coercive field.

From a technological point of view, AF/F multilayers present the advantage to be compatible with low-temperature process steps of 200°C-300°C, which is not the case for rare-earth magnets discussed in section 3.2.

As timeframe and technological ressources to expand this study were limited, the actual magnetometer application uses AF/F stacks with 20nm PtMn thickness (layer configuration: Ta 5nm/[PtMn 20nm/CoFe 10nm]$_{10}$/PtMn 20nm/Ta 5nm), leading to thinner AF/F multilayer stacks by keeping good shape anisotropy properties in order to demonstrate the feasibility of a 3D magnetometer. Further, a stripe width of 0.5µm was chosen for the magnetometer in order to set a compromize between hysteresis loop shift and magnetization disalignment.

Chapter 4

Fabrication results

4.1 Results of the microfabrication process

This section gives an overview over sensor fabrication results which were obtained from the process flow described in table 4.1. The M&NEMS process is started on a SOI (Silicon On Insulator) substrate with a 250nm thick silicon top layer, which defines the thickness of the gauges (a). After bore doping and subsequent annealing, silicon nano-gauges are etched within the monocrystalline top silicon layer (b). Gauges are then protected by deposition of a PECVD grown SiO_2 layer (c). In the next step, a 10µm thick monocrystalline silicon layer is grown by epitaxy (d). This layer is used to define the MEMS structure of the sensor. For accelerometer and gyroscope applications, a thickness of 10µm is relevant in order to obtain enough inertia of the MEMS structure for high sensitivity. In case of the magnetometer application, this layer is used as support structure for integration of magnetic material (e). Technological integration of magnetic material has already been presented with more details in the seperate chapter 3. All relevant MEMS elements, including MEMS structures, suspension beams, actuation electrodes etc. are defined by a step of deep reactive ion etching (DRIE) (f). Release of the structures is finally achieved by a hydrofluoric acid etching step (g).

Step	Description	Scheme
a)	The process is started on a Silicon On Insulator (SOI) substrate.	
b)	Silicon strain gauges are etched within the 250nm thick silicon top layer.	
c)	The nano-gauges are then embedded into SiO_2 for protection.	

d)	A 10µm thick monocrystalline silicon layer is grown by epitaxy.	
e)	Magnetic material is integrated on top of the 10µm thick Silicon top layer.	
f)	MEMS structures are defined by a deep reactive ion etching (DRIE) step.	
g)	MEMS structures are finally released by a hydrofluoric acid etching step.	

Table 4.1: Basic process flow of the M&NEMS concept applied to the fabrication of magnetometers.

Besides the part of process for integration of magnetic material, most critical process steps were DRIE[1] etching and release of the MEMS structures by vapor hydrofluoric acid (HF) etching.

[1]Deep reactive ion etching

One difficulty of the DRIE step is related to the higher etching speed for larger trenches (fig. 4.1). However, holes with small diameter needed to be etched into MEMS structures in order to assure a good release by HF etching, which was done together with DRIE etching of the MEMS structures. Some difficulties have been encountered with unequal etching depth. The resulting problem consists in the fact that there may be unsufficient SiO_2 thickness for protection of the nano-gauges, so that they can be destroyed during DRIE. However, this problem could be solved by deposition of thicker photoresist in order to protect the gauges.

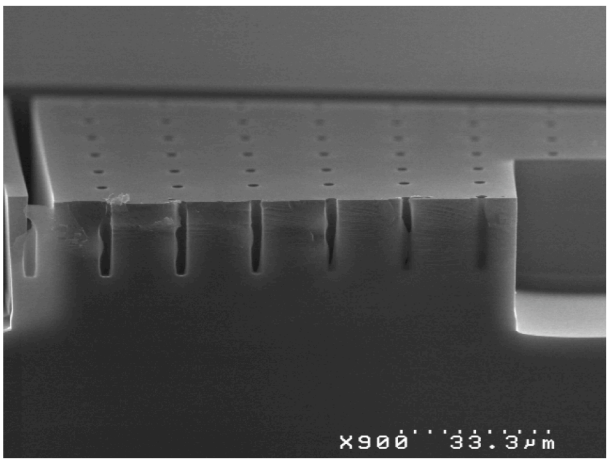

Fig. 4.1: Different etch depths are obtained depending on trench- or hole width.

Another difficulty related to DRIE was to obtain vertical sidewalls. This is crucial, as deviations from beam geometry change mechanical properties of MEMS structures and thus impact sensing performances. The DRIE process was optimized on test structures by etching a cluster of beams. For the non-optimized process, beam width decreases with etching depth (fig. 4.2(a)). The process could be optimized, leading to uniform beams thickness (fig. 4.2(b)).

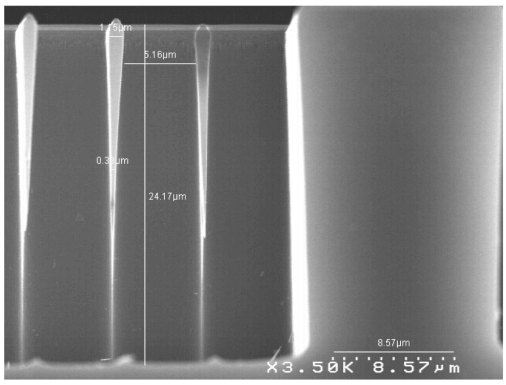

(a)

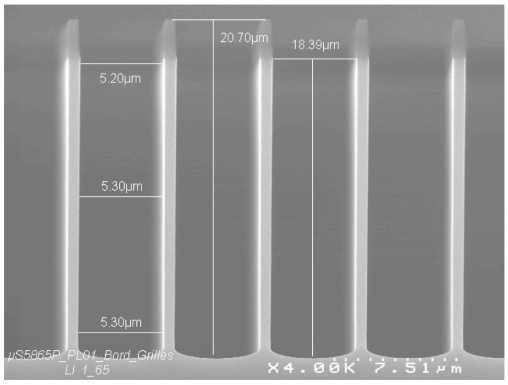

(b)

Fig. 4.2: Etched beam clusters before and after optimization of the DRIE process: (a) beam width decreases with etching depth; (b) uniform beam width after optimized DRIE process.

For the MEMS release step, it is important that deposited magnetic materials withstand exposure to HF during several hours, that all the oxide beneath the MEMS structure is removed, and that stitching of the MEMS structure to the ground does not occur.

4.1.1 MEMS structures without integrated magnetic material

Following images show essential technological results for structures without deposition of magnetic material[2] which validate both critical process steps (DRIE and release of the MEMS structure by vapor HF etching): fig. 4.3 presents magnetometer structures designed for detection of in-plane field components; fig. 4.4 shows magnetometer structures designed for detection of the out-of-plane field component.

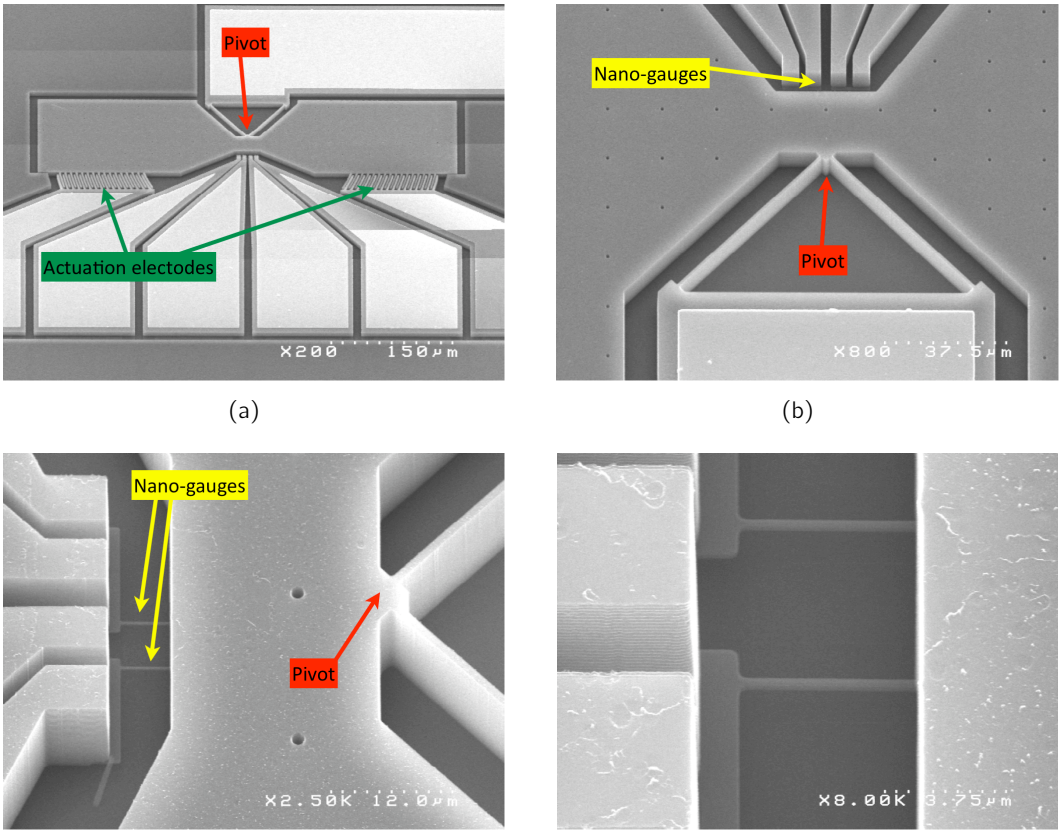

Fig. 4.3: Technology results for magnetometer structures designed for detection of in-plane field components: (a) The complete structure with integrated electrical contacts and actuation electrodes; (b) Bending beams build the pivot, the nano-gauges are placed on the opposite side; (c) 250nm thin nano-gauges compared to the 10µm thick Silicon structure; (d) Close view of the nano-gauges.

Even though the structures did not yet integrate magnetic material, their functional reliability could be verified by electrostatic actuation. By application of a voltage between

[2]MEMS structures without integrated magnetic material are representative for the M&NEMS accelerometer.

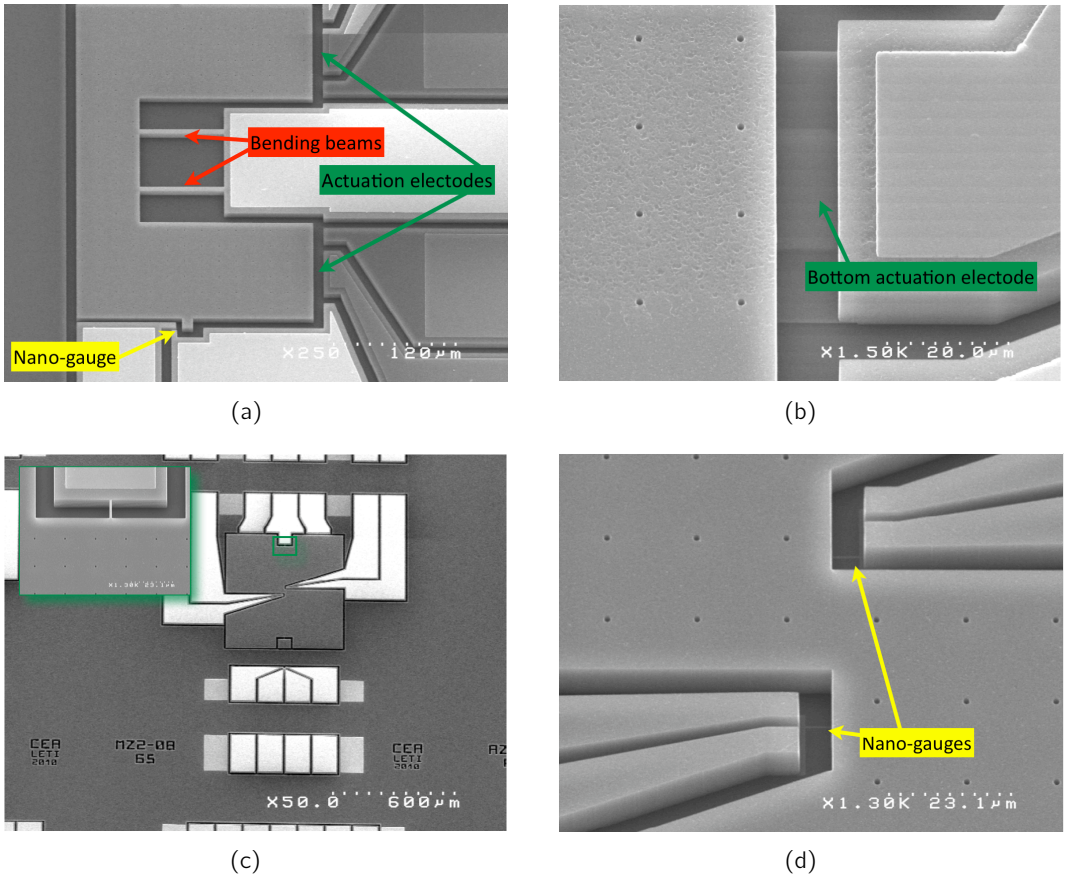

Fig. 4.4: Technological results for Z magnetometer structures: (a) Magnetometer structure using bending beams for rotation; (b) Actuation electrodes are situated under the silicon structure; (c) Magnetometer structure using torsion beams; (d) Position of the nano-gauges for a magnetometer using torsion beams.

electrodes and structures, a corresponding output voltage was measured at the bridge which was buildt by two nano-gauges. For the tested wafer, a yield of 93% well-functioning structures was obtained.

4.1.2 Magnetometers with integrated magnetic material

Magnetometers with integrated AF/F multilayers

All critical process steps could also be validated for magnetometers with integrated AF/F multilayers. Magnetic material is preserved after HF etching and nano-gauges are visible with an optical microscope. Figure 4.5(a) shows this for a z-magnetometer using a combined torsion-bending beam hinge, and fig. 4.5(b) for a torsion beam hinge z-magnetometer, respectively. Fig. 4.6 gives an overview over the achieved technological results obtained for the first magnetometer demonstrator[3].

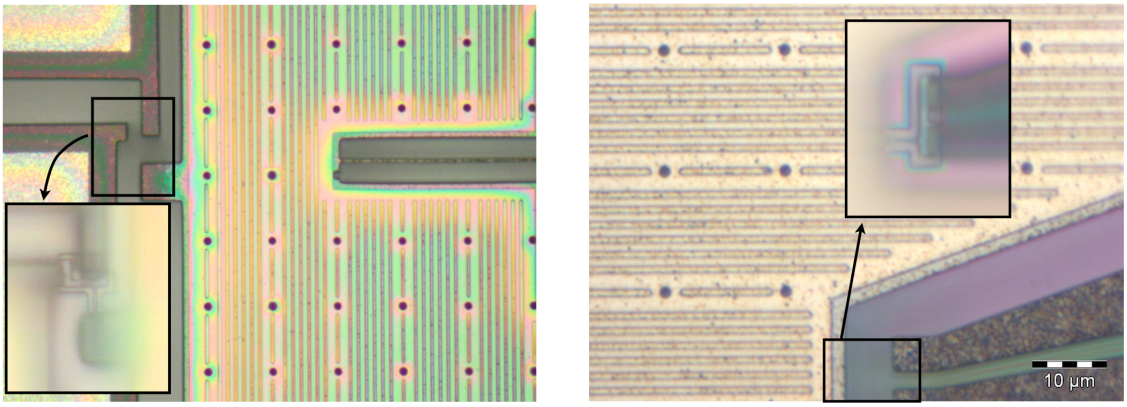

(a) (b)

Fig. 4.5: Validation of critical process steps for magnetometers using integrated AF/F multilayers: (a) outer left border of a z-magnetometer using a combination of torsion- and bending beams. The small picture shows a focus on the nano-gauge. (b) Z-magnetometer using torsion beams for suspension.

[3]Images refer to batch µS3408D, wafer 8.

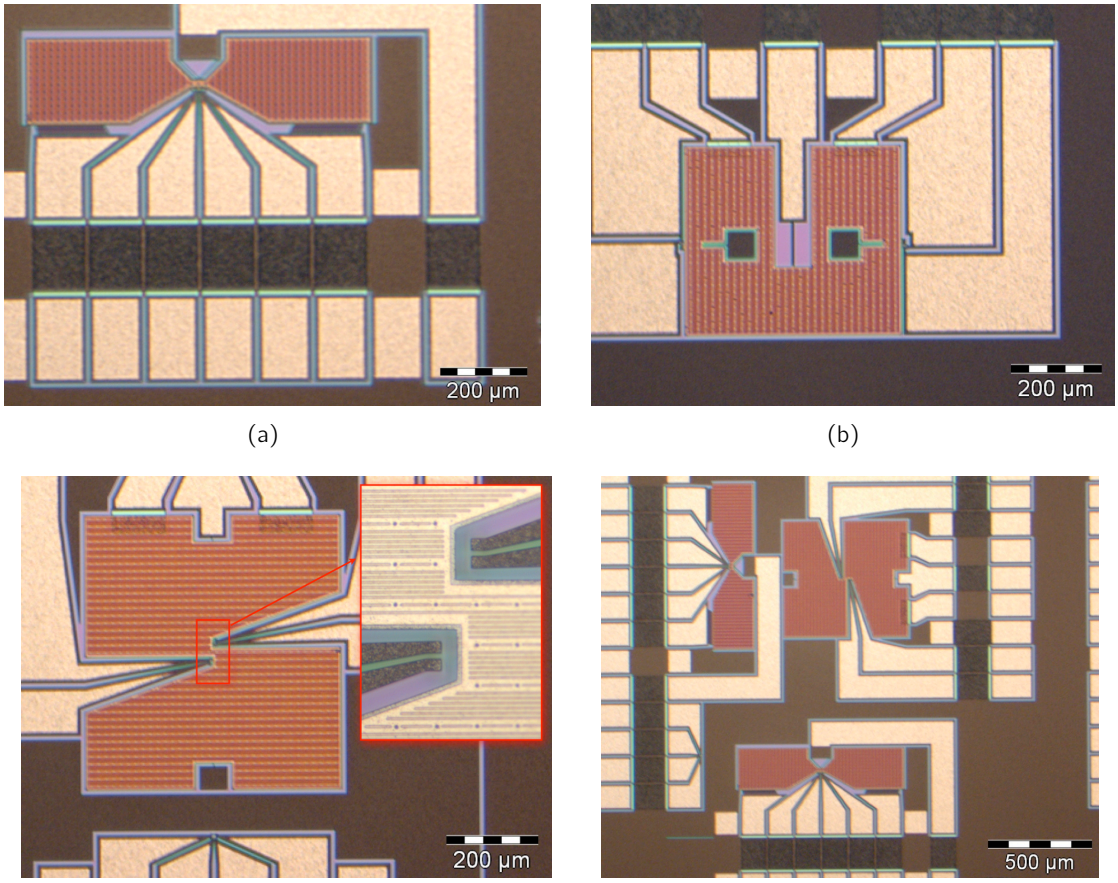

(a) (b)

(c) (d)

Fig. 4.6: Technological realization of magnetometers with integrated magnetic material (coupled antiferromagnetic and ferromagnetic multilayers): (a) Magnetometer for detection of the field components in the plane of the chip; (b) Magnetometer for out-of-plane field detection using a combination of bending- and torsion beams; (c) Magnetometer for out-of-plane field detection using torsion beams; (d) Fully integrated 3 axis magnetometer.

Magnetometers with integrated NdFeB

Contrary to the integration of AF/F multilayers, significant difficulties were encountered for integration of NdFeB into the magnetometers. Initial deposition and patterning of the NdFeB layer was not problematic. However, first defects could be observed after deposition of the W_2N capping layer, which finally led to local peel-of, as shown in fig. 4.7. The brittle W_2N capping layer as well as peel-off can be explained by the high residual stress inside these layers after the annealing step for crystallization. Stress issues are discussed in the following section.

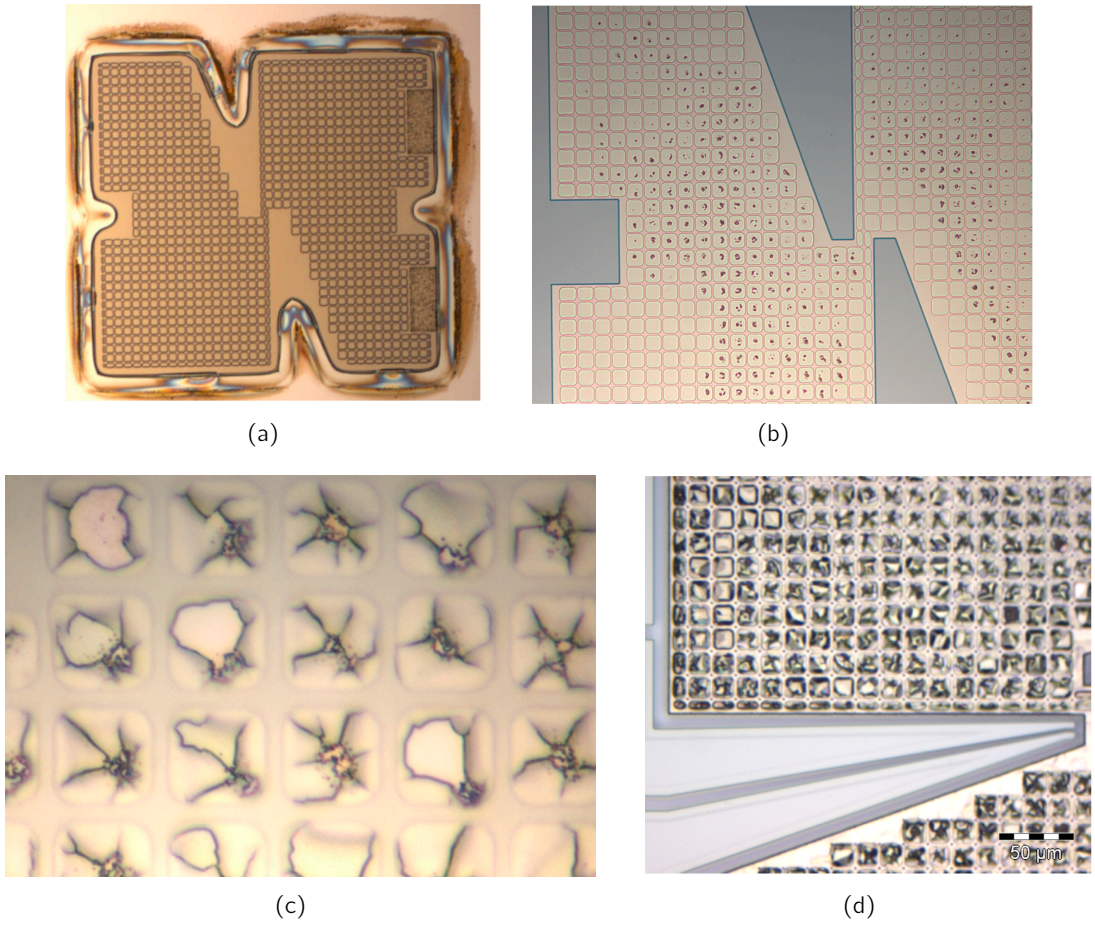

(a) (b)

(c) (d)

Fig. 4.7: Problems with integration of NdFeB in the magnetometer demonstrator: (a) No visible defects after patterning of the NdFeB layer; (b) brittle W_2N capping layer; (c) after deposition and stripping of an AlSi layer for electrical contacts; (d) after HF vapor release.

4.1.3 Summary

Following essential points summarize the main outcome of the sensor fabrication:

- The M&NEMS microfabrication process for magnetometers has been shown to be feasible and critical fabrication steps such as DRIE etching and release of MEMS structures were stabilized.

- PtMn/CoFe multilayers show good adhesion after release of the MEMS structures
- Integration of NdFeB could not be validated in the context of this work due to the presence of high residual stress in the W_2N protection layer. However, it was validated on independent samples (cf. chapter 3).

4.2 Stress in thin films

4.2.1 Introduction

Microfabricated devices subjected to stress may show defects, reduced performances and even complete failure. Also the reproducibility of performances on a wafer may be deteriorated by the influence of stress, so the compensation of its impact on microfabricated devices is an important issue. In our particular case presented in chapter 2, mobile structures are supposed to perform in-plane and out-of-plane motion. For any kind of residual stress (compressive or tensile), the detection gauges may be pre-stressed or even overstressed due to bowing of the mobile structures. In case of compressive stress, where the MEMS structure is bent towards the substrate, its mobility range for out-of-plane motion may be heavily limited. Hence, there are several consequences generated by residual stress, such as complete malfunction of the device, limited sensitivity due to stress-induced modification of mechanical stiffness, limited full scale range, significant offsets etc.

Residual stress can also result in peel-off of the magnetic material from the MEMS structure. This problem has partially been encountered during the magnetometer fabrication process for AF/F multilayers (fig. 4.8).

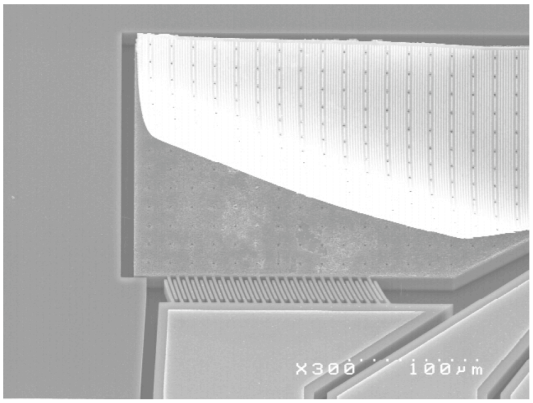

Fig. 4.8: Example for peel-of for a stack of AF/F multilayers after a HF etching step to release the MEMS structure.

Residual stress in these devices mainly occurs for:

- *mechanical* reasons: in this case, stresses appear as result to a specific manufacturing/deposition process, they may also appear naturally or due to intended treatment.
- *thermal* reasons: stresses appear due to thermal treatment (heating/cooling) or mismatches in coefficients of thermal expansion between different phases or materials.

- *chemical* reasons: stresses appear due to volume changes induced by chemical reactions and phase transformations.

In the devices presented in this work, different materials are used to form several individual layers. Different specific mechanical properties of these layers are the leading cause of stress generation. Deposition conditions of the layers play an important role for residual stress, which can often be adjusted by matched conditions of thermal treatment and/or layer thicknesses. Thermal stresses are less influenceable, as they depend on a layer's specific coefficient of thermal expansion. For our technology used to integrate magnetic material in Silicon, we encounter these problems. As mentioned before, two different methods are used to integrate magnetic material in the devices:

- NdFeB as hard magnetic material is deposited in cavities *inside* the silicon substrate
- A stack of thin alternating exchange-bias coupled PtMn- and CoFe layers is deposited *on top of* the silicon substrate.

Both magnetic materials are enclosed by different thin layers, which requires compensation of the effects of stress. This can be achieved by the adjustment of annealing conditions, by adjustment of layer thicknesses and by the choice of an appropriate fabrication process or technological treatment. First, the characterization of stress in thin films is crucial in order to compensate stress-induced effects. We are interested in the characterization of thermally induced stress and the influence of layer thicknesses. As the microstructure inside a thin layer may change depending on its thickness, no standard values can be used for mechanical properties, but dedicated measurements have to be carried out for any particular case. In our work, we will concentrate on residual stresses, but not on thermally generated stress. In principle, it is possible to achieve a configuration of a multilayer stack, in which stress is not affected by temperature variation, but as fabrication technology often imposes limiting edge conditions for a stack, it is difficult to optimize any arbitrary layer configuration with the purpose to solve the problem of thermally induced stress.
In this work, residual stresses were characterized for

- thin NdFeB films,
- multilayer stacks of PtMn/CoFe, and
- layers to be used in the microfabrication process (e.g. materials used for adhesion- and capping layers).

Four different characterization methods were used for measurement of residual stresses in thin films:

- Stoney method
- X-ray diffraction
- Bending measurement of single-clamped microfabricated beams
- Measurement of buckling amplitudes of clamped-clamped beams.

After a brief description of the four measurement techniques, stress measurements are presented and discussed for NdFeB films, AF/F multilayers and other materials used in the technological process.

4.2.2 Theory of used measurement methods

Stress evaluation by Stoney method

A common method used to characterize stress in thin films is the Stoney method, which is based on the work of Stoney in the early 20th century [93]. In this method, a thin film of the thickness t_f is deposited on a substrate of thickness t_s (figure 4.9). Stress in the deposited film induces a curvature of the subtrate-film system, which can be measured. Curvature may be determined without destruction using optical measurement equipment. The model assumes amongst others that $t_f \ll t_s$ and that deformations are only small, which are limiting factors for the application range of the Stoney method. In 1999, Freund *et al.* [94] proposed extensions for the Stoney formula to enlarge its application range to the case of thin substrates and large deformations. Another limiting factor is that the model is valid for a bilayer system, but is does not include the option to estimate stresses in a multilayer system. In 1987, Townsend *et al.* [95] studied the case of elastic relationships in a layered composite media and made an approximation for the case of multiple thin films on a thick substrate. Later, a multilayer-modified Stoney formula was suggested in 1999 by Kim *et al.* [96], but their proposed model was shown to be disconnected from the Stoney formula by A. Klein in 2000 [97]. However, in our model, the simple Stoney formula is sufficient to evaluate the residual stress of a specific thin layer. Stoney's model does not consider the mechanical

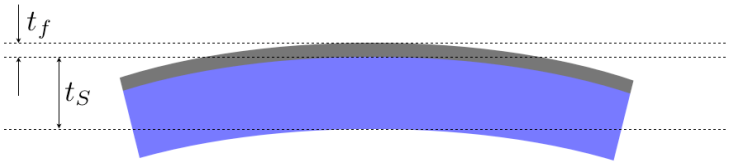

Fig. 4.9: Layer configuration considered for application of the Stoney formula

properties of the thin film, so its stress σ_f can directly be calculated by measurement of the radius of curvature R, using the most basic form of Stoney's model

$$\sigma_f = \frac{E_s t_s^2}{6 R t_f}, \tag{4.1}$$

where E_s is the Young's modulus of the substrate. To extend this model to plates, the biaxial modulus has to be used instead of the Young's modulus, which modifies Stoney's formula to

$$\sigma_f = \frac{E_s}{1-\nu_s} \frac{t_s^2}{6 R t_f}, \tag{4.2}$$

where ν_s is the poisson ratio of the substrate's material.

Stress evaluation by X-ray diffraction

A further non-destructive method for stress-evaluation is based on X-ray diffraction. The principle was discovered 1912 by Max von Laue, who obtained the Nobel prize in physics in 1914. It has first been used for engineering applications in the early 1950's. Until today,

XRD is used as standard method to characterize crystalline structures. XRD is based on the discovery of Willian Lawrence Bragg in 1912 for diffracted X-rays at a crystal lattice:

$$2d_0 \sin\Theta = n\lambda \tag{4.3}$$

where d_0 is the distance between to layers of the crystal lattice, Θ the incidence angle, n the order of the diffraction peak, and λ the wavelength of the X-rays (see fig. 4.10(a)). The generated diffraction pattern is shifted if the interplanar distance is different from the initial state d_0, hence shifting of the diffraction peak is a reference for strain. Consider a sample

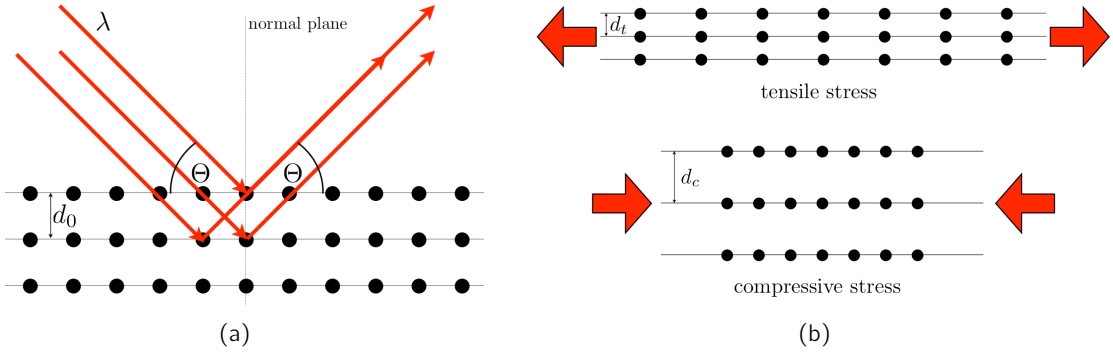

Fig. 4.10: Spacing between planes of a crystal lattice: (a) Principle of diffracted X-rays at a crystal lattice. Constructive interference of diffracted beams occurs for an optical path difference of $n\lambda$; (b) strain due to tensile or compressive stress in crystals

with in-plane stress as presented in fig. 4.11, where the stress σ_{33} perpendicular to the plane is assumed to be negligible. Planar stress in the sample deforms the crystalline grains inside it, so the interplanar distance d_0 of a crystalline element for an unstressed state changes into $d_{\Phi\Psi} = d_t < d_0$ for tensile stress and $d_{\Phi\Psi} = d_c > d_0$ for compressive stress, as illustrated in fig. 4.10(b).

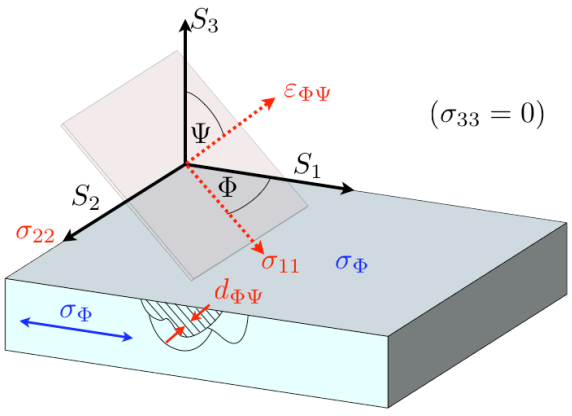

Fig. 4.11: Illustration of the planar stress σ_Φ which can be determined by the $d_{\Phi\Psi}(\sin^2\Psi)$ relation

The general solution [98, 99] for strain of an arbitrary grain normal to the plane defined by

the angles Φ and Ψ relative to a reference coordinate system S_i is given by

$$\begin{aligned}\varepsilon_{\Phi\Psi} &= \frac{d_{\Phi\Psi} - d_0}{d_0} \\ &= \left[\varepsilon_{11}\cos^2\Phi + \varepsilon_{12}\sin 2\Phi + \varepsilon_{22}\sin^2\Phi\right]\sin^2\Psi \\ &\quad + \varepsilon_{33}\cos^2\Psi + \left[\varepsilon_{13}\cos\Phi + \varepsilon_{23}\sin^2\Phi\right]\sin 2\Psi.\end{aligned} \tag{4.4}$$

As stress is related to strain by Hooke's law, neglection of shear stresses $\sigma_{13} = \sigma_{31}$, $\sigma_{23} = \sigma_{32}$ and of σ_{33} finally leads to the relation between planar stress σ_Φ and the angle Ψ as described by [100]:

$$\sigma_\Phi = \left(\frac{E}{1+\nu}\right)_{(hkl)} \frac{1}{d_0}\frac{\partial d_{\Phi\Psi}}{\partial \sin^2\Psi}, \tag{4.5}$$

where

$$\left(\frac{E}{1+\nu}\right)_{(hkl)}$$

is an expression for the elastic constants normal to the considered crystallographic (hkl) plane and

$$\frac{\partial d_{\Phi\Psi}}{\partial \sin^2\Psi}$$

is the slope of the measured $d(\sin^2\Psi)$ curve. The resulting $\varepsilon(\sin^2\Psi)$ curve is a straight line in the case where stress is normal to the plane (fig. 4.12(a)). Presence of other stress components changes its appearance (see fig. 4.12) and may lead to the invalidity of the measurement method.

Stress evaluation from bent single-clamped beams

Bending of beams as a result of an acting force or bending moment is well understood by the Euler-Bernoulli beam theory. Analytical models for bending of substrates with thin films can be used to evaluate thin film stress. We can consider a cantilever, clamped at one end, with one or even a stack of multiple stressed thin layers upon it. Stressed thin films upon a substrate will induce a bending moment and thus a characteristic deformation of the beam. In 2002, C.H. Hsueh presented an analytical model for bending of single-clamped cantilevers with multiple layers on a substrate [102]. His model considers residual stresses in thin films as well as thermally induced stress. A stack as presented in figure 4.13 is considered. The deflection z at any position x along the beam can be predicted by

$$\frac{\mathrm{d}^2 z}{\mathrm{d}x^2} = \frac{1}{r} \Longrightarrow z = \frac{x^2}{2r}. \tag{4.6}$$

By knowledge of the Young's modulus, layer thickness and residual stress for each layer and the substrate in a multilayer stack with n layers, the radius of curvature is known by

$$\frac{1}{r} = \frac{3\left[E_s(c-\alpha_s\Delta T)t_s^2 - \sum_{i=1}^{n} E_i t_i (c-\alpha_i\Delta T)(2h_{i-1}+t_i)\right] + 6M}{E_s t_s^2(2t_s+3t_b) + \sum_{i=1}^{n} E_i t_i \left[6h_{i-1}^2 + 6h_{i-1}t_i + 2t_i^2 - 3t_b(2h_{i-1}+t_i)\right]}, \tag{4.7}$$

where c is the uniform strain component of the strain distribution $\varepsilon = c + \frac{z-t_b}{r}$, given by

$$c = \frac{(E_s t_s \alpha_s + \sum_{i=1}^{n} E_i t_i \alpha_i)\Delta T}{E_s t_s + \sum_{i=1}^{n} E_i t_i}, \tag{4.8}$$

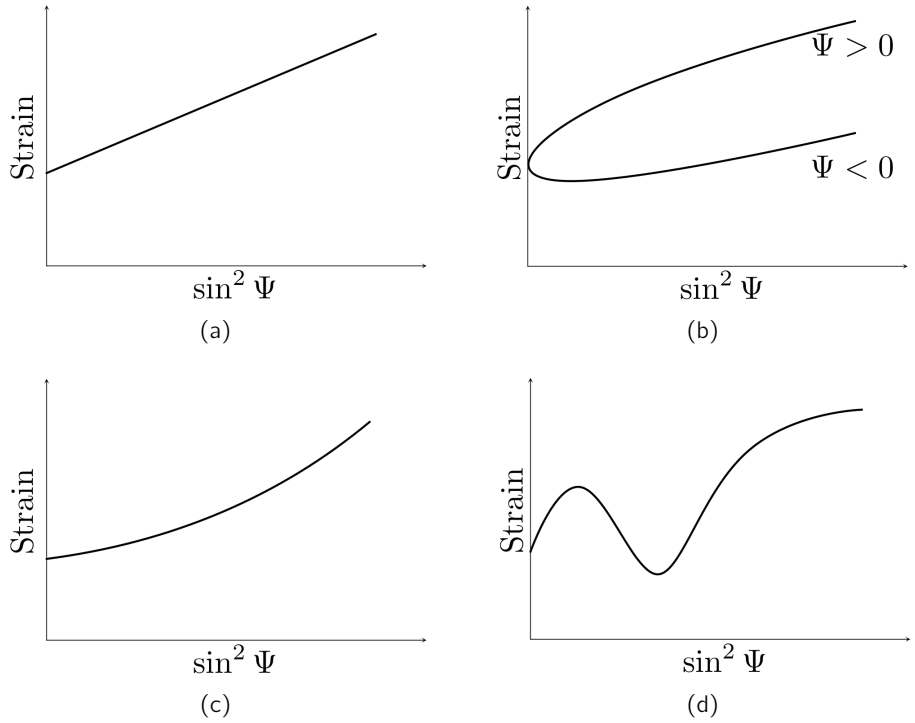

Fig. 4.12: Dependencies of strain on $\sin^2\Psi$: (a) linear dependence for stress perpendicular to the plane; (b) splitting of the curve for the case of shear stresses; (c) presence of a stress gradient perpendicular to the surface; (d) large stress variations; equation 4.4 is not applicable in this case [101].

t_b the position of the bending axis, given by

$$t_b = \frac{-E_s t_s^2 + \sum_{i=1}^{n} E_i t_i (2h_{i-1} + t_i)}{2(E_s t_s + \sum_{i=1}^{n} E_i t_i)} \tag{4.9}$$

and M the bending moment which can be calculated by

$$M = \int_{-t_s}^{0} \sigma_s (z - t_b) \mathrm{d}z + \sum_{i=1}^{n} \int_{h_{i-1}}^{h_i} \sigma_i (z - t_b) \mathrm{d}z. \tag{4.10}$$

The parameters E_i are the Young's modulus, α_i the coefficients of thermal expansion for any layer i and ΔT is the temperature variation. E_i has to be replaced by the biaxial modulus

$$\frac{E_i}{1 - \nu_i},$$

if a two-dimensional geometry is considered, where ν_i is the poisson ratio.

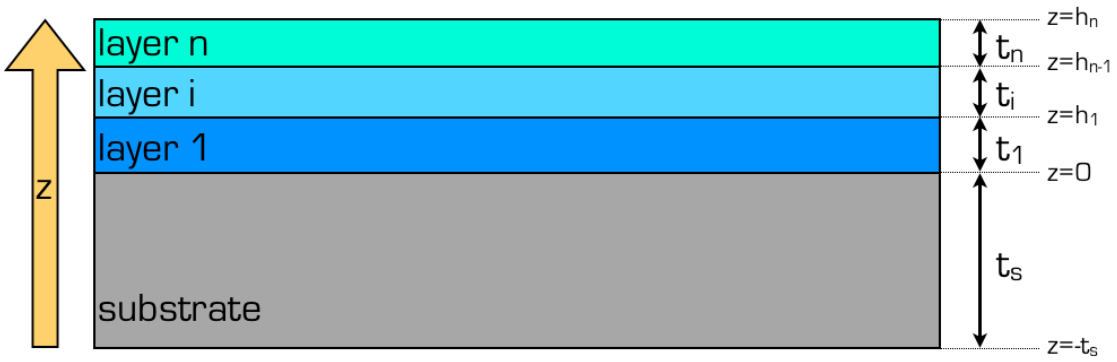

Fig. 4.13: Nomenclature for a multilayer stack for the model of Hsueh

Stress evaluation from buckled clamped-clamped beams

Another method to evaluate stress in thin layers uses buckling of double-clamped beams instead of single-clamped cantilevers. This method may seem more complicated, but double-clamped beams provide a better clamping quality in contrast to cantilevers which are fixed at only one side. A basic process flow for fabrication of SiO_2 beams which were used for stress measurements is presented in fig. 4.14.

Fig. 4.14: Process for fabrication of SiO_2 beams (single-clamped cantilevers or clamped-clamped beams): a) an amorphous silicon layer is deposited on a silicon substrate; b) growth of a low-stress SiO_2 layer using PECVD; c) lithography and etching of beams; d) release of the beams by isotropic XeF_2 etching.

Due to isotropic etching for beam release, the clamping region is overetched; this might modify the beam's boundary conditions and the model might become inaccurate. The influence

of this problem is lower for clamped-clamped beams.

In principle, the measurement procedure remains the same as single-clamped beams. Thin layers are deposited on clamped-clamped beams and the deformation is measured. In classical buckling analysis, only a qualitative prediction about buckling is made by consideration of the critical strain ε_c, where buckling appears:

$$\varepsilon_c = \frac{\pi^2 t^2}{3L^2}, \tag{4.11}$$

where t is the beam thickness and L the beam length. By this expression, the quantitiative deformation of the beam is not considered. To evaluate the amplitude of beam deflections, a non-linear model has to be used. In 1994, W. Fang and J.A. Wickert published a study about post-buckling of micromachined beams [103], where they presented four models to use buckling of beams for stress evaluation. In their work, they used beams made of thermally grown SiO_2. They presented two linear and two non-linear models for beam buckling. Their non-linear model considering imperfections in the material permits to use the transition region between the pre-buckled and post-buckled state of the beam to evaluate the stress. If only the post-buckled state of the beams is considered, a simpler non-linear model which does not consider imperfections in the material can be used for the same purpose, because it fits well with the more complicated model in the post-buckling region. This model predicts the maximum buckling amplitude w_{max} by

$$w_{max} = \pm\sqrt{\frac{4\varepsilon L^2}{\pi^2} - \frac{16I}{A}}, \tag{4.12}$$

where $\varepsilon = \frac{\Delta L}{L}$ is the strain, I the geometrical moment of inertia of the beam and A its section. In contrast to the model of Fang and Wickert who used exclusively SiO_2 as material for their beams, we have to consider a bilayer system as presented in figure 4.15, in which any layer has its own mechanical properties. As the SiO_2 substrate was deposited by PECVD,

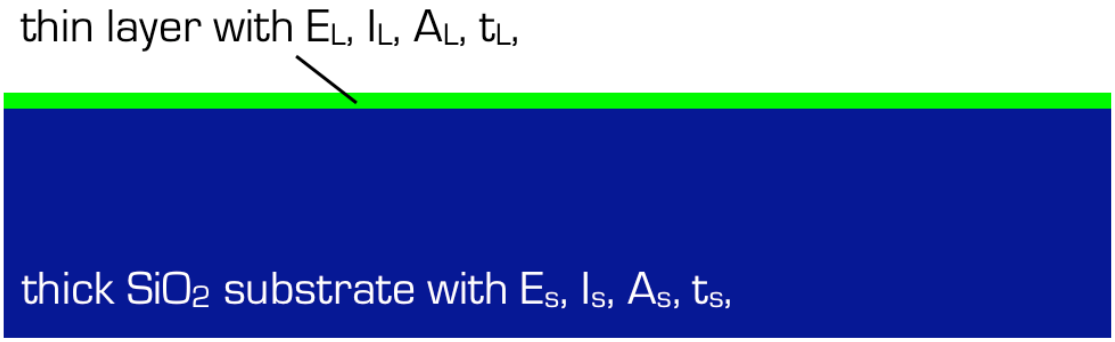

Fig. 4.15: Bilayer system used in this work. The top layer is very thin compared to the SiO_2 substrate.

its residual stress is neglected and the strain in the beam is considered to be induced by the thin top layer only. If the thickness t_L of the top layer is much thinner than the thickness t_s of the substrate, equation 4.12 can also be applied to a bilayer system, because the buckling amplitude is mainly determined by the flexural rigidity EI, and in our case, the geometrical

moment of inertia of the top layer becomes negligible. To combine the mechanical parameters of both layers in the model, we define the beam's geometrical moment of inertia as

$$I = \frac{w(t_s + t_L)^3}{12}, \tag{4.13}$$

where w is th beam width. The beam section is defined as

$$A = w(t_s + t_L). \tag{4.14}$$

The strain value can be obtained by fitting the model to the measured buckling amplitudes. With the given strain value, the mean stress σ_{beam} in the beam can be extracted by considering both layers as two parallel axial stiffnesses:

$$\sigma_{beam} = \varepsilon \frac{E_s A_s + E_L A_L}{A_s + A_L}, \tag{4.15}$$

where E_s, E_L, A_s and A_L are the respective Young's moduli and layer sections. The stress in the deposited thin films can finally be evaluated by consideration of the stiffness ratio between the entire beam and the thin layer, given by

$$\frac{E_s A_s + E_L A_L}{E_L A_L},$$

so the stress σ_L in the thin film is calculated by

$$\sigma_L = \varepsilon \frac{(E_s A_s + E_L A_L)^2}{E_L A_L (A_s + A_L)}. \tag{4.16}$$

4.2.3 Measurement results

Stress measurements for thin NdFeB films

Residual stress of thin NdFeB layers was measured by Stoney method with equipment of the Néel laboratory, and by the method of single-clamped bending beams at Leti.

For Stoney method, wafers of 200mm diameter were used in a triode sputtering equipment which was designed for deposition on 100mm wafers, therefore the NdFeB layer could only be deposited at the wafer's center. Layer thickness at the wafer's center was 1µm, which is representative for the thickness used in the magnetometer application. A difficulty was to obtain a homogeneous layer thickness. Due to a stress gradient in the wafer, nonobservance of these problems would lead to false results in measurement of residual stresses in the thin layer. In order to achieve appropriate measurement conditions using a probe with homogeneous layer thickness of 1µm and complete surface coverage, only a small square of the size $2\times2\text{cm}^2$ was cut from the wafer's center instead of using the entire wafer. This leads inescapably to a reduced measurement accuracy for the radius of curvature. Given that residual stress in a thin layer depends on the annealing temperature, the radius of curvature was measured before and after annealing. A focal point here is the crystallization temperature of the magnetic material, because it has necessarily to be attained during the fabrication process. To perform the measurement, the bending of the square substrate was measured first as a reference for further measurements. After deposition of the layer, the bending was re-measured, so the effective bending could be obtained by subtraction of both measured

curves, and the residual stress in the as-deposited state could be calculated using equation 4.2. The same procedure is used to evaluate the residual stress after annealing. To measure the bending profile, a mechanical stylus profiler was used. Figure 4.16 shows the measured curvature before and after annealing. The corresponding stresses are listed in table 4.2.

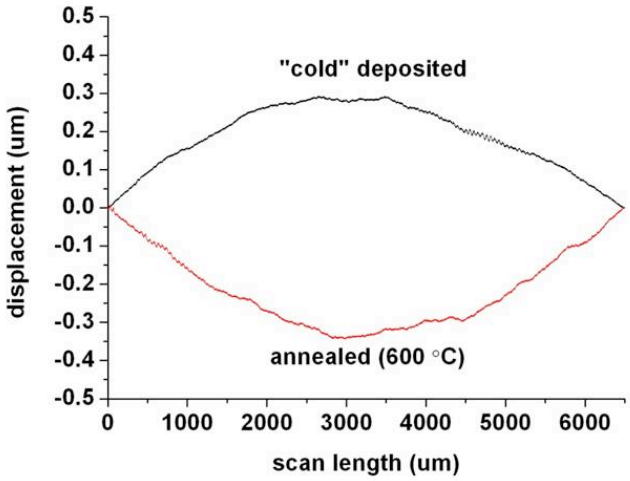

Fig. 4.16: Stress measurements for a 1µm thick NdFeB layer before and after annealing. Downward bending indicates compressive residual stress, upward bending indicates tensile residual stress.

	as-deposited	**annealed (at 600°C)**
Mean stress [MPa]	-120	150

Table 4.2: Residual stresses in a 1µm thick NdFeB layer before and after annealing

For the method of single-clamped bending beams, 2µm and 3µm thick and 50µm large SiO_2 cantilevers have been fabricated to act as substrate for thin film deposition. Different cantilever lengths (50µm to 500µm) have been used for each experiment. By deposition of a layer with unknown stress, the deflection curve predicted by the model can be fitted to the measured curve, which permits to evaluate the unknown residual stress. However, this technique requires knowledge of the elasticity modulus and the thickness of any layer in the stack. Also the residual stresses of the other layers must be known.

100nm thick NdFeB layers were deposited on a single-clamped SiO_2 cantilever. A thickness of 3µm was used for the SiO_2 cantilevers, which were fabricated by PECVD deposition of SiO_2, followed by isotropic XeF_2 etching (cf. process flow shown in fig. 4.14). As the deflection measurements are performed by optical profilometry and the SiO_2 substrate is transparent, a 10nm thin Ta layer was initially deposited to obtain the reflectivity required for measurement of the initial beam deflection. Deposition conditions were a base pressure of 10^{-6}mbar, Ar pressure of 10^{-3}mbar and a deposition rate of 3.4nm/s at room temperature. In order to simulate the thermal process conditions for crystallization, the sample has been annealed for 10min at 600°C, with a heating and cooling rate of 250°C/h. After annealing, all shorter cantilevers (50µm to 250µm, see figure 4.17(a)) were equally deformed, which was

also the case for longer cantilevers (up to 500µm, see figure 4.17(b)). After measurement of the initial beam deformation, the 100nm thick NdFeB layer was deposited by sputtering, using a substrate-to-target distance of 10cm, a deposition rate of 4nm/s at room temperature and the same pressure conditions as used for deposition of the initial Ta layer. The NdFeB layer was compressively stressed in its as-deposited state, so the cantilevers were bent downwards (shown in figure 4.17(c)). Only shorter cantilevers could be used for stress evaluation, because longer ones touched the ground and did not show a homogeneous deflection curve. After annealing at 600°C for 10min with the same heating and cooling rate of 250°C/h, compressive stress passed over to tensile stress which causes an upward deflection of the cantilevers (presented in figure 4.17(d)). To extract values for stress, the beam bending

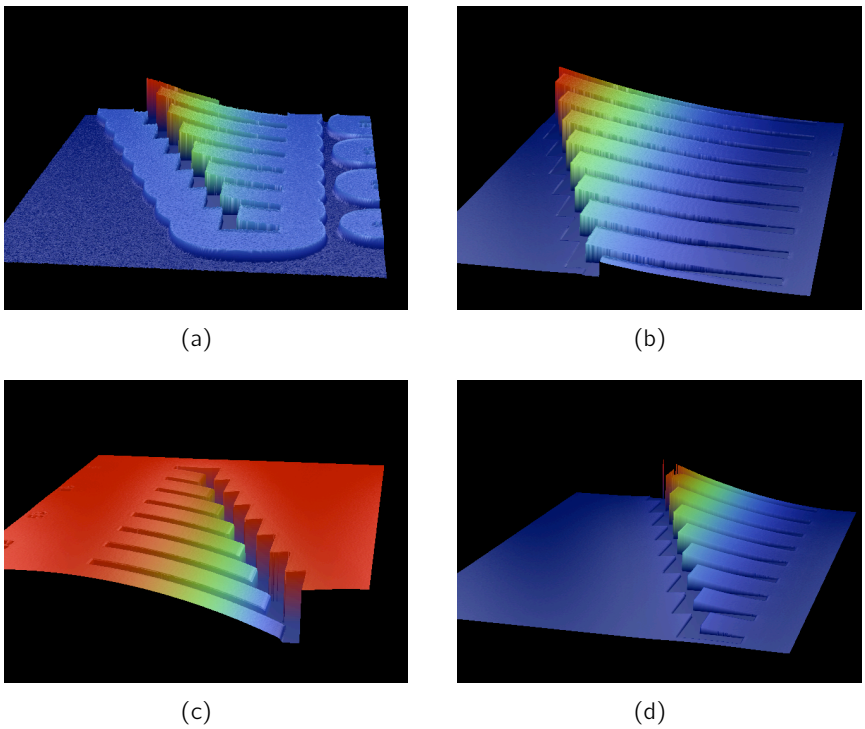

Fig. 4.17: Stress measurements of thin films with bent cantilevers: (a) Initial Ta layer on shorter cantilevers; (b) Initial Ta layer on longer cantilevers; (c) Downward-bent cantilevers with a 100nm thin NdFeB layer in their as-deposited state; (d) Upward-bent cantilevers with a 100nm thin NdFeB layer after annealing at 600°C. Note that deflections are not scaled.

model model was fitted to the measured deformation. Note that before fitting, the initially measured beam deflection has been subtracted from the deflection which was measured after annealing. Figure 4.18 shows that the model fits well to the measurements.

Similar measurements have been performed on several samples. For some of them, a 10nm thin Ta capping layer was used to seal the NdFeB layer during the annealing process. To take into account the influence of the Ta capping layer on the beam deformation, the residual stress in Ta was considered in the model. Former stress measurements on the same can-

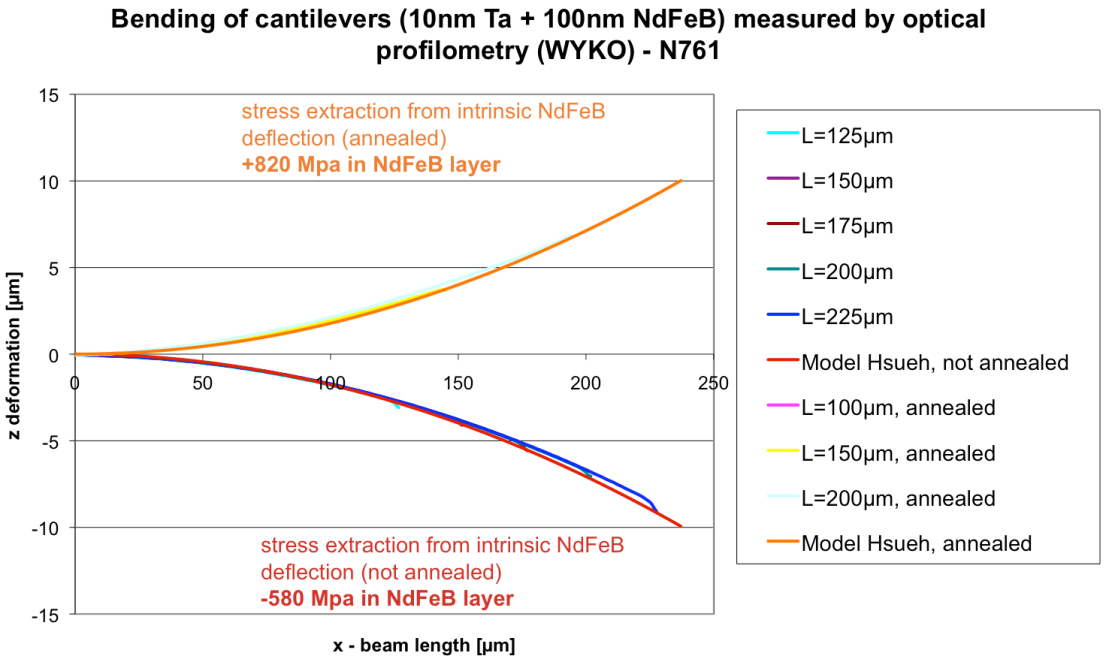

Fig. 4.18: Fit of the model to measurements

tilevers with 100nm thin Ta layers in their as-deposited state provided a value for compressive stress of -1.3GPa. This value could be confirmed by FEM analysis and was used in the model (see fig. 4.19). However, the precise stress value for annealed Ta layers is unknown. Measurement results are resumed in table 4.3. The difference between stresses measured for

Sample name	Layer configuration	Annealing state	Stress [MPa]
N761	Ta 10nm/NdFeB 100nm	as deposited annealed at 600°C	-580 +820
N763	Ta 10nm/NdFeB 100nm	as deposited annealed at 600°C	-450 +810
N764	Ta 10nm/NdFeB 100nm/Ta 10nm	as deposited annealed at 600°C	-440 +1260
N769	Ta 10nm/NdFeB 100nm/Ta 10nm	as deposited annealed at 600°C	-430 +1250
N806	Ta 10nm/NdFeB 200nm	as deposited annealed at 600°C	-460 +1110

Table 4.3: Recapitulation of stress results in thin NdFeB layers

1µm and 100nm thick NdFeB films can be explained by the microstructure and the influence of the Tantalum bottom/capping layer. For 1µm thick NdFeB layers, grains are free to form (fig. 4.20), while layer thickness is below NdFeB grain size in case of 100nm thin layers.

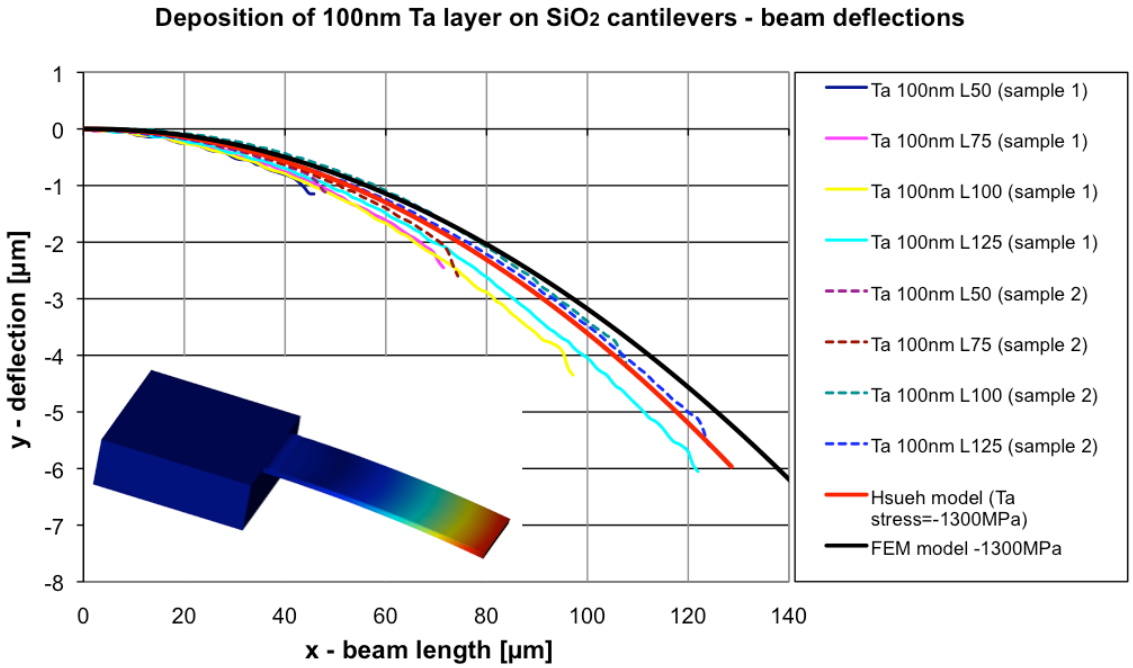

Fig. 4.19: Evaluation of stress in a 100nm thin Ta layer, based on the bending of cantilevers. Measurements were taken from 2 different samples which are represented by continuous and dashed lines. They show good conformity. The stress value extracted from the model is -1.3GPa, which is confirmed by FEM simulation of this cantilever.

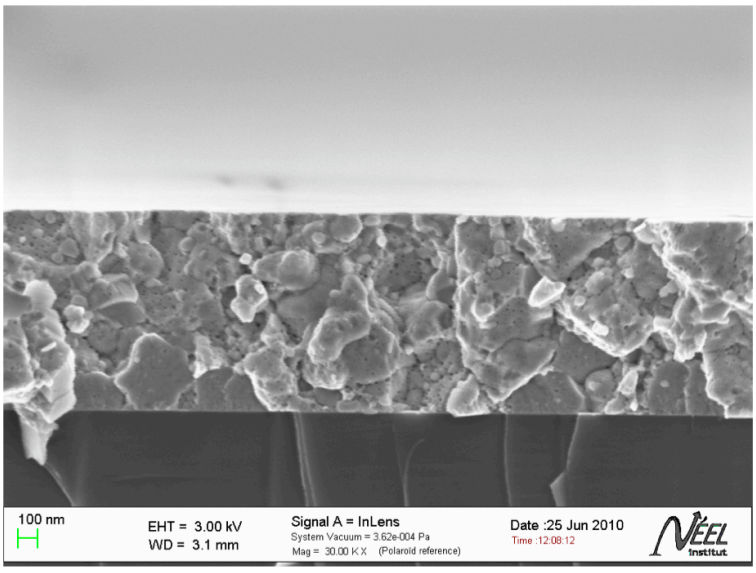

Fig. 4.20: Microstructure of a 1µm thick NdFeB layer as reason for stress-dependency on layer thickness: Grains are free to form in a thick layer, as grain size is of the order of 100nm.

Stress measurements for PtMn/CoFe coupled multilayers

For evaluation of residual stress in PtMn/CoFe multilayers, Stoney method and bending beam method were used. For Stoney method, a representative AF/F-stack was deposited on a silicon wafer to simulate the actual layer configuration used for the intended application (Ta 5nm + [PtMn 20nm + CoFe 10nm]$_{10}$ + PtMn 20nm + Ta 50nm). Here, the 5nm thin Ta bottom layer strengthens adhesion of the subsequently deposited PtMn layer and also serves as diffusion barrier between magnetic material and the substrate, and the 50nm thick Ta capping layer protects the AF/F-stack against oxidation. Stress in the entire stack was determined by curvature measurement of entire wafers, firstly in the as-deposited state and secondly in the annealed state (T_{an} = 265°C, as required for magnetization of the multilayer stack). Table 4.4 shows that the initial compressive stress turns over into tensile stress after annealing.

	as-deposited	**annealed (1h at 265°C)**
Stress in AF/F stack [MPa]	-1100	340

Table 4.4: Comparison of residual stress in a AF/F stack (Ta 5nm + [PtMn 20nm + CoFe 10nm]$_{10}$ + PtMn 20nm +Ta 50nm) in the as-deposited state and after annealing

For stress evaluation using bending cantilevers, 2µm thick SiO_2 cantilevers were used. The initial deformation was measured after deposition of a 5nm thin Ta layer. The deposited stack of alterning antiferromagnetic and ferromagnetic (AF/F) thin layers was [PtMn 20nm/CoFe 10nm]$_{10}$ + PtMn 20nm. A 5µm thin Ta layer was added on top of the stack, so the entire layer thickness was 330nm which approximately corresponds to the layer thickness being used for magnetometer fabrication. As it can be seen from figure 4.21, the layer was highly compressively stressed. Figure 4.21(a) indicates that the gap height under the cantilevers was not sufficiently deep to allow free bending of the beams, so that they touch the gap bottom. Even short beams are all deformed in a different way, so that no quantitative information about the stress could be obtained from these measurements.

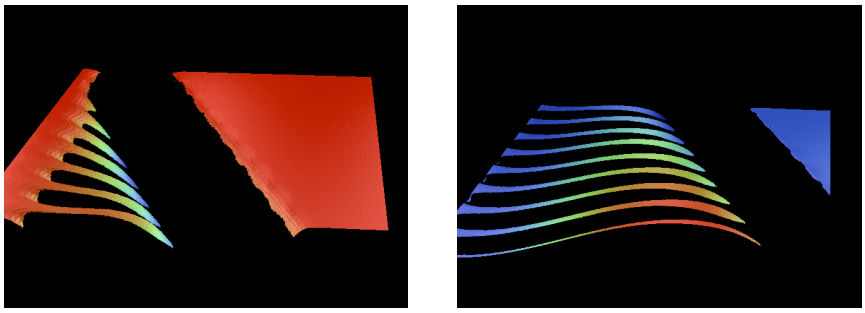

(a) (b)

Fig. 4.21: Deformation of cantilevers due to high compressive stress in a 330nm thick AF/F stack on 2µm thick SiO_2: (a) short cantilevers after deposition of AF/F stack; (b) long cantilevers after deposition of AF/F stack. From a qualitative point of view, the deformation indicates high residual stress in the layer; finally, inhomogeneous cantliever deformations did not lead to a quantitative evaluation of stress.

Stress measurements for adhesion- and capping layers

For the magnetometer fabrication process, different materials were studied as possible encapsulating layers for magnetic material. These materials can serve as diffusion barrier between the substrate and magnetic material, as adhesion layer for the magnetic material, and as protection against oxidation and corrosion during the later magnetometer fabrication process. In this context, Tungsten (W), Tungsten Nitride (W_2N), Tantalum (Ta) and Ruthenium (Ru) were studied. All the four presented characterization methods were used for stress measurement, depending on the specific case (for example, as Ruthenium is an expensive material, the deposited layer was limited to 10nm. Therefore, Stoney method is less appropriate for stress measurements, because a 10nm thin layer on an entire silicon wafer with 725µm substrate thickness might lead to poor measurement precision).

Residual stresses were studied for different annealing temperatures in case of Stoney and XRD method. These temperatures were representative for thermal conditions during the fabrication process. For bending- and buckling beams, only the as-deposited state was investigated. The results are resumed in fig. 4.22

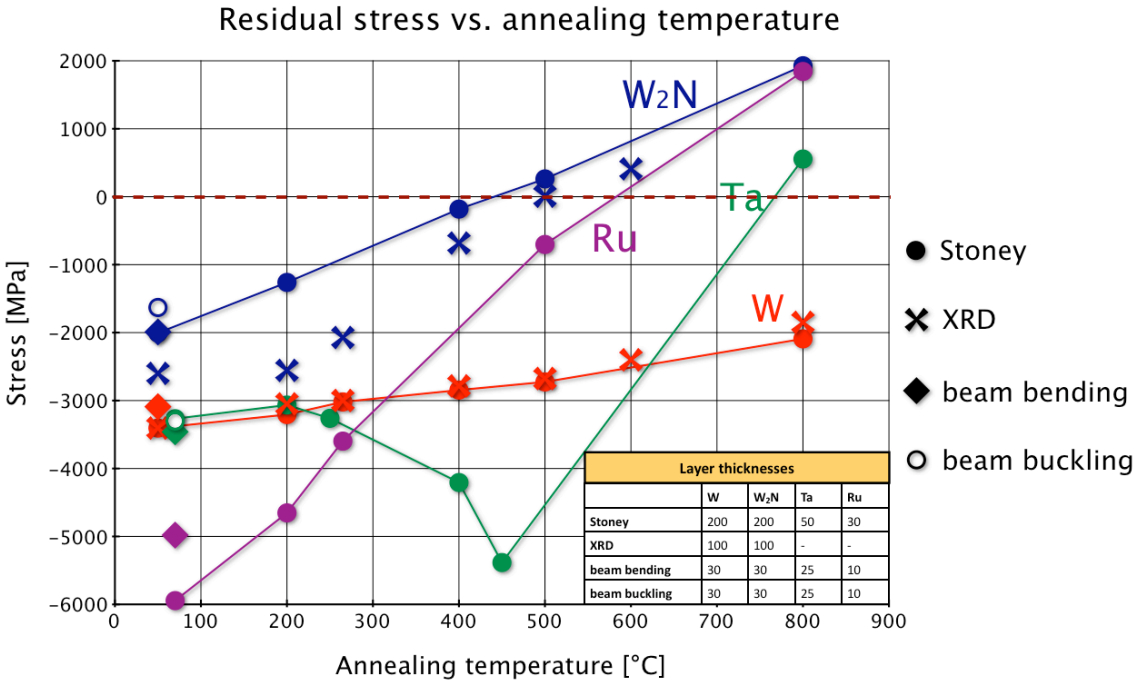

Fig. 4.22: Evolution of residual stresses for different potential sub- and capping layers with different annealing temperatures. Individual measurement points were obtained from all four characterization methods.

The Stoney characterization principle was applied to all four materials. For any material, a layer thickness of 200nm was deposited on a silicon wafer with a diameter of 200mm. As shown in fig. 4.22, stress turns over from compressive stress to tensile stress for all materials, if the annealing temperature is increased. Except from Ta, the relation between residual stress and annealing temperature can be considered as linear in the given range. The nonlinear curve for the Tantalum layer can be ascribed to temperature-dependent changes

and defects in the microstructure of the material.

XRD method was only used for W and W_2N layers of 100nm thickness. Residual stresses were determined by use of the $\sin^2\Psi$-method for different annealing states (as-deposited, 200°C, 265°C, 400°C, 500°C and 800°C). For any annealing state, the interplanar spacing $d = d(\Psi)$ of the lattice was measured for three different angles ($\Psi_1 = 0$, $\Psi_2 = 45$, $\Psi_3 = 90$). Residual stress was then determined from the $\varepsilon(\sin^2\Psi)$ curve, presuming the linear case presented in fig. 4.12(a). Measurement results are in good agreement with those obtained by Stoney method in the case of Tungsten. However, measurement shows fluctuations and deviations from results obtained from Stoney method for W_2N. This can be ascribed to a desorption of N, which leads to modification of lattice parameters and consequently causes variations of residual stress within the layer.

The bending beam method was applied to all four materials in their as-deposited state. However, measurements on samples with the W layer could not be used to determine the stress, because the beam deflection was very inhomogeneous, as shown by figure 4.23. A possible explanation for this problem might be an inhomogeneous stress distribution in the W layer, or stitching of the cantilevers to the gap bottom. Measurement results are listed in table 4.5.

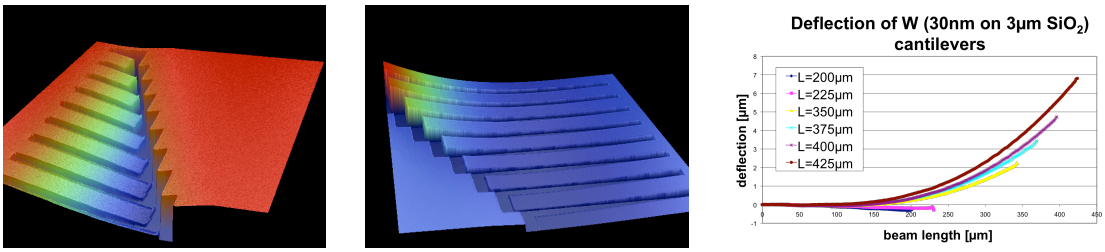

(a) (b) (c)

Fig. 4.23: Deflection of cantilevers with W layer: (a) short cantilevers are slightly bent downwards; (b) long cantilevers are bent upwards; (c) the measured deformation curves of cantilevers with different lengths are not superposed.

The double-clamped beam buckling model was also used for calculation of residual stresses in the layers for all four materials. Beams of different lengths were used, so different buckling amplitudes for different beam lengths could be measured as shown in figure 4.24. The curve was fitted to the model only in the post-buckling region, as shown in figure 4.25. Table 4.5 lists measurement results for the respective material and layer thickness and compares them to the values obtained from bending measurements on single-clamped cantilevers.

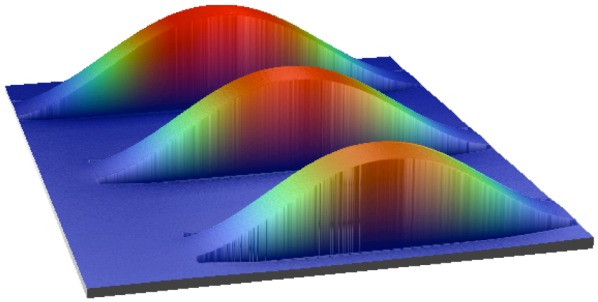

Fig. 4.24: Buckling for beams of different lengths (350µm, 400µm and 450µm) as measured for 3µm thick SiO_2 substrates with a 30µm thin Tungsten layer.

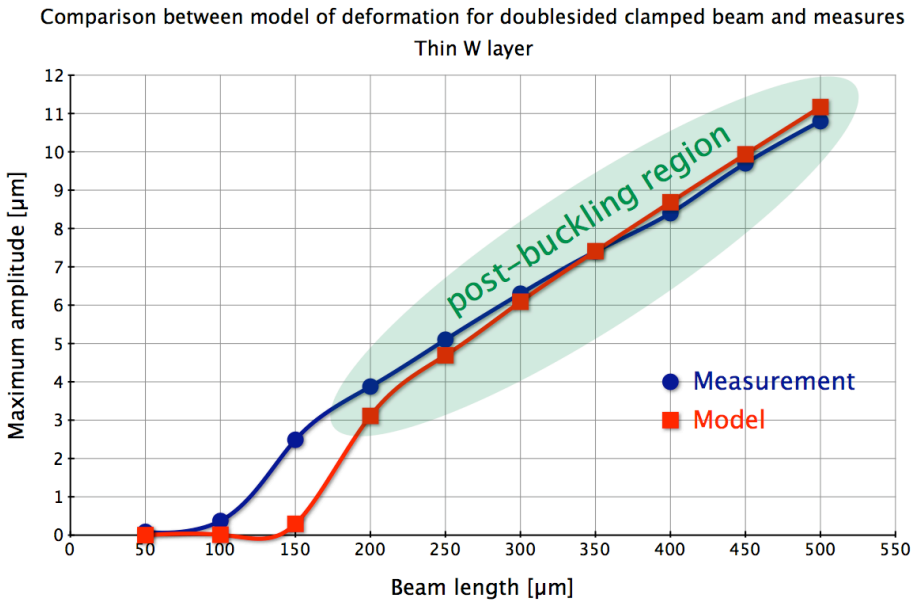

Fig. 4.25: Fitting of the measurements to the model shown by the example of a thin W layer. The fit was applied exclusively in the post-buckling region.

Thin layer	Layer configuration	Stress (buckling)	Stress (bending)
W	SiO_2 3µm/W 30nm	-3090 MPa	-
W_2N	SiO_2 3µm/W_2N 30nm	-1990 MPa	-1630 MPa
Ta	SiO_2 2µm/Ta 25nm	-3460 MPa	-3300 MPa
Ru	SiO_2 2µm/Ru 10nm	-4980 MPa	-3510 MPa

Table 4.5: Measurement results obtained from application to the model of post-buckled beams and comparison to values obtained from the model of single-clamped bending cantilevers. To extract the stress value for Ruthenium (Ru), only three measurement data points were available, which might be able to explain the deviation from the single-clamped cantilever model.

4.2.4 Relevance of residual stress for bending of MEMS structures

Based on results obtained from stress measurements, the deformation of MEMS structures can be estimated. For simplification, we consider the "worst-case" scenario, where the MEMS structure is uniformly covered with the stack required for integration of magnetic material. The stacks listed in tables 4.6 and 4.7 are representative for the layer configurations which are used in the magnetometer application. Further, we consider maximum dimensions of the designed Z-magnetometers, which are 500µm for the magnetometer using integrated NdFeB and 800µm for an integrated AF/F multilayer stack, respectively. If these assumptions are used in the multilayer bending model (section 4.2.2), a $\sim$ 7.1µm upward deformation is calculated for a magnetometer using NdFeB, and a $\sim$ 13.4µm upward deformation for the magnetometer using an AF/F multilayer stack. This deformation can be very disturbing for a later packaging process and modify the sensor's mechanical properties. However, the deformation can principally be compensated by deposition of a compressively stressed layer. For example, a not annealed W_2N layer (residual stress of -2GPa) of $\sim$ 156nm thickness would be needed to compensate the deformation of the magnetometer using NdFeB, and a thickness of $\sim$ 93nm could compensate the deformation of magnetometer using an AF/F multilayer stack.

Layer	Thickness [nm]	Residual stress (annealed at 600°C, [MPa])
W_2N	50	800
NdFeB	600	150
W_2N	50	800
SiN	200	500
Si (bottom layer)	10000	20

Table 4.6: Layer configuration for integration of NdFeB and residual stresses for annealing at 600°C. Values for residual stress in SiN and Si are based on former experience at Leti.

Layer	Thickness [nm]	Residual stress (annealed at 265°C, [MPa])
Ta	5	800
AF/F stack	320	340
Ta	5	800
SiN	200	500
Si (bottom layer)	10000	20

Table 4.7: Layer configuration for integration of a [PtMn 20nm/CoFe 10nm]$_{10}$/PtMn 20nm multilayer stack and residual stresses for annealing at 265°C.

4.2.5 Influence of discontinuously patterned layers on residual stress

Compensation of bending by means of process parameters like annealing conditions or deposited layer thicknesses may be limited in some cases by technological constraints (e.g. limited layer thickness). Patterning of layers was investigated using FEM analysis as another possibility for bending compensation.

The main idea consists of splitting the deposited layer into several individual features, so that relaxation zones for the stress are created between the features. This would lead to a reduction of stress relative to the reduction of layer volume. For this reason, a single-clamped, 10µm thick Silicon beam with differently patterned layers of 1µm thick Iron upon it was built by simulation using COMSOL software. By a first simulation, the maximum deflection of the beam with a homogeneously stressed Fe layer was determined, from which the radius of curvature could be calculated by equation 4.6. This radius served as reference for the layer stress at 100% substrate coverage. Afterwards, the Fe layer was divided into individual, geometrically equal stripes, which where orientated either lengthwise or transverse to the beam. The stripes were seperated by the distance parameter *a* one from each other, while the stripe width varied in each case. The two different cases of integrating the material *inside* and *on top* of the substrate were simulated.

Figure 4.27 shows the results obtained by simulation. The distance *a* between the features was varied by 1µm, 2µm and 3µm for different stripe widths. So the effective layer volume was reduced by the equivalent filling factor of the layer. In both graphs, the red dotted line represents the assumption that stress would decrease proportionally with the effective layer volume. Simulation results show that residual stress of a layer can be regarded as being directly proportional to the layer's volume in the considered range, except the case of a laterally structured layer on top of the beam. This generally means that no significant stress reduction can be achieved by patterning of the layer. Only if the stripes are disposed in lateral orientation *onto* the beam (fig. 4.26(b)), a stress reduction with respect to the volume can be obtained in strong dependence of the seperation parameter *a*.

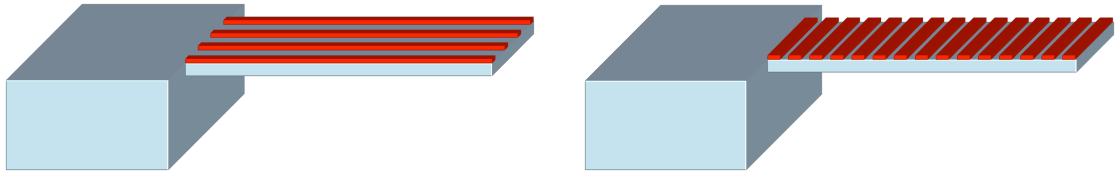

(a) (b)

Fig. 4.26: Two different layer patterns: (a) lengthwise split; (b) lateral split. The drawing shows the case where the stressed layer is situated on top of the substrate. The integration of the stressed layer into the substrate was studied in the same way.

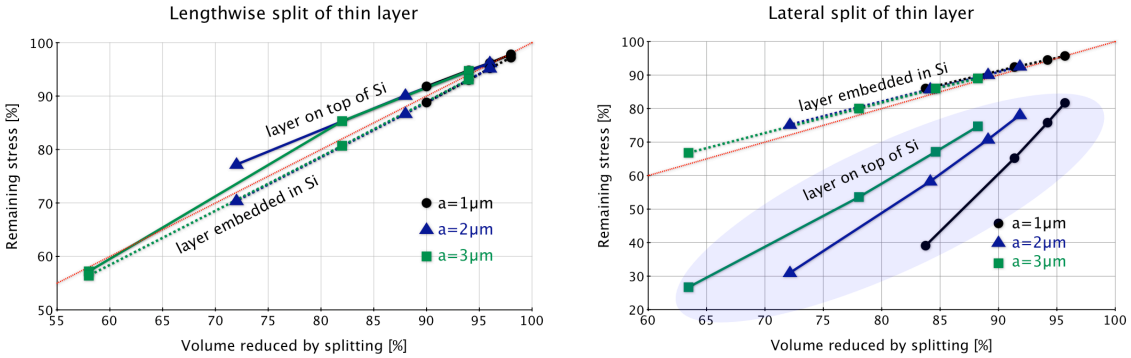

(a) (b)

Fig. 4.27: Influence of patterned layers on residual stress: (a) normalized residual stress for a striped layer, orientated lengthwise to the beam; (b) normalized residual stress for a striped layer, oriented lateral to the beam. The dotted red line indicates the residual stress which would remain in case of a simple reduction of the layer's volume without patterning.

4.2.6 Bending of MEMS structures without magnetic material

A problem encountered after fabrication of MEMS structures consists in downward bending of the structures, even though no magnetic material was integrated. Deformation profiles were measured using interferometry and are shown in figures 4.28 and 4.29. Depending on the structure's suspension, maximum downward deformations are in the range between 100nm - 250nm.

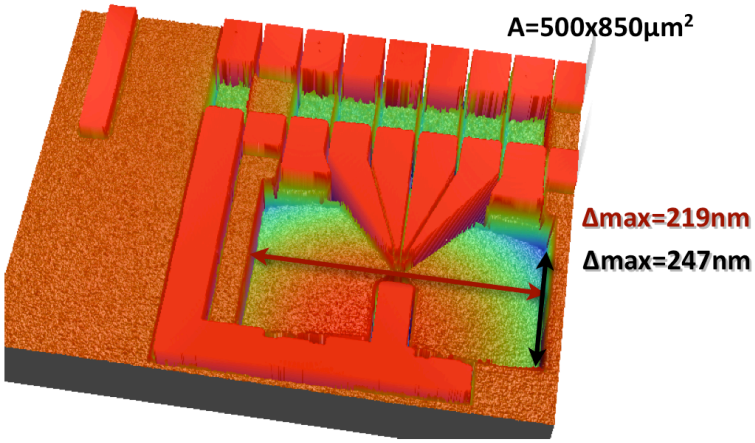

Fig. 4.28: Bending of a x-y-magnetometer MEMS structure without integrated magnetic material. The structure size is 500×850µm^2.

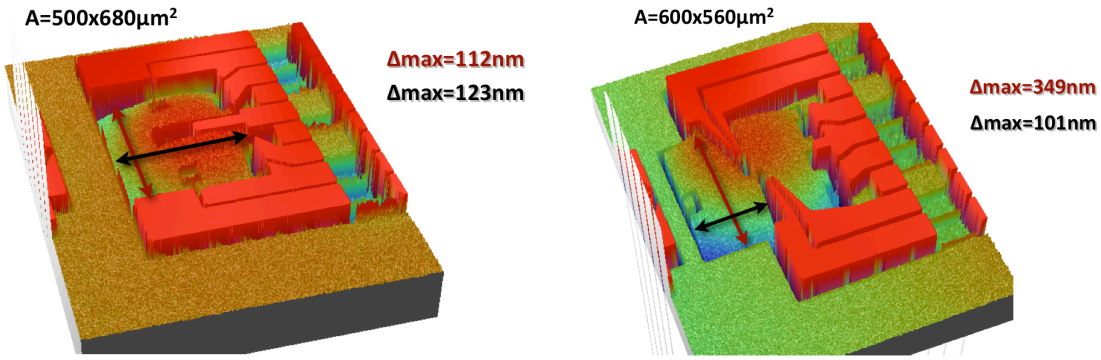

(a) (b)

Fig. 4.29: Downward bending of z-magnetometer structures without integrated magnetic material: (a) z-magnetometer with a size of 500×680µm^2, using a combination of torsion- and bending beam hinges; (b) z-magnetometer with a size of 600×560µm^2, using torsion beams as hinge.

An explanation for the bending of MEMS structures could be a stress gradient in the silicon layer which was grown by epitaxy. A stress gradient may occur in case of defects in the crystal lattice and/or poor temperature control during layer deposition. A dedicated experience was carried out in order to verify the presence of a stress gradient. For this purpose, 14µm thick silicon layers were deposited by epitaxy on SOI wafer with a diameter of 200mm. Deposition conditions were the same as in case of the magnetometer fabrication process. The silicon layer was dry etched in steps of 1µm, and the curvature was measured after each etching step using a mechanical stylus profiler. According to the measurement results shown in fig. 4.30, there is no stress gradient in the considered thickness range of the silicon layer (4µm to 14µm), as the bending amplitude goes linear with the film thickness, which indicates constant stress, even in the very first deposited thicknesses at the deposition interface.

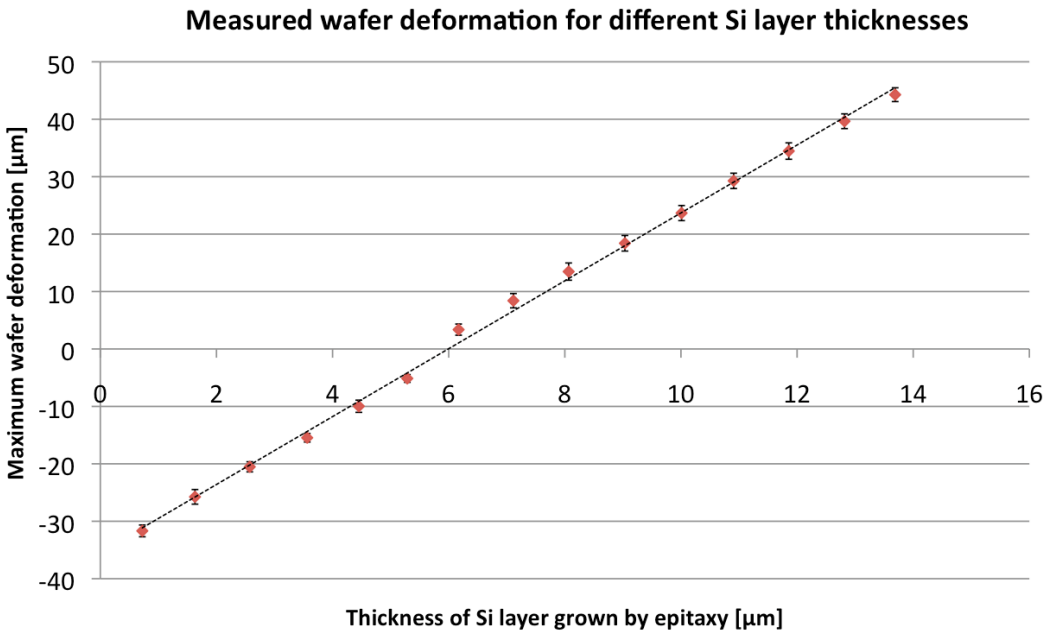

Fig. 4.30: Measured bending amplitudes for different thicknesses of the silicon layer. The linear dependency of bending amplitude on the layer thickness indicates constant stress.

A further experience was carried out to investigate the evolution of stress for Si layers with low thickness. In total, 3µm were deposited by epitaxy in steps of 1µm, and stress was measured after each deposition step by means of wafer curvature measurement using a stylus profiler. Results in table 4.8 show that stress is higher for layers close to the deposition interface and confirm the presence of a stress gradient. However, it should be noted that this last experience is less meaningful, as deposition conditions for the 3µm thick silicon layer were not similar to those used for the magnetometer. According to measurements presented in

Layer thickness [µm]	Stress [MPa]
1	68
2	64
3	57

Table 4.8: Evolution of stress in a silicon layer deposited by epitaxy.

fig. 4.30, a stress gradient as cause for the downward bending of individual released MEMS structures could not be confirmed. The problem of bent structures remains thus an issue for further investigation within the development of the technological process.

4.2.7 Discussion

Four different measurement methods were used for evaluation of residual stresses in NdFeB, PtMn/CoFe multilayers and different potential adhesion- and capping layers for the magnetic material to be integrated. It has been shown that for all studied materials, residual stress turns over from compressive stress into tensile stress for growing annealing temperature.

Depending on annealing conditions, the studied materials for adhesion- and capping layers can exhibit very high stresses in the range of several GPa.

It has also been shown that it is principally possible to compensate the stress-related curvature of the MEMS structure by deposition of a not-annealed, highly stressed W_2N layer. FEM simulations showed that the influence of layer patterning on curvature is in most cases similar to a stress reduction achieved by a simple reduction in volume of the magnetic material.

Downward bending of MEMS structures even without deposited magnetic material was observed. The presumption that this would be caused by a gradient of mechanical stress in the silicon layer grown by epitaxy could not be confirmed by measurement.

Chapter 5

Sensor characterization

This chapter presents measurement results of mechanical characteristics and essential sensor performances and validates the 3D magnetometer concept. The basic magnetometer fabrication process was successfully applied to 4 of 5 initially processed wafers[1]. One wafer was used for SEM[2] observations. Thus, three wafers with functional magnetometers remained and could be used for first measurements. After initial measurements, two wafers were broken during preparation of the wafers for a packaging process which was intended to be finished in the framwork of the Capucine project.

5.1 Mechanical characterization

Initially, the response of MEMS structures to electrostatic actuation was tested. Based on these tests, a number of potentially functional structures was selected for mechanical tests. These tests consisted in measurement of resonance frequencies of different MEMS structures using a Lock-In amplifier with synchronous excitation of the MEMS and signal detection. Only x/y-magnetometers designed for integration of AF/F multilayers were tested. Modeling of resonance frequencies was achieved through a combination of mechanical stiffnesses[3] from the nano-gauges (k_g) and the suspension of the MEMS structure (k_h), leading to

$$f_{res} = \frac{1}{2\pi}\sqrt{\frac{k_g + k_h}{I}}, \tag{5.1}$$

where I is the structure's mass moment of inertia. The stiffness contribution from the gauges is calculated by

$$k_g = \frac{2EA_g}{l_g} d_g^2 \tag{5.2}$$

with elasticity modulus E, gauge section A_g, gauge length l_g and d_g, the distance between nano-gauge and fulcrum of the MEMS structure. Hinge stiffness k_h was obtained through FEM analysis. Fig. 5.1 shows measured resonance frequencies for different geometrical

[1] Leti batch identification: µS3708D

[2] Scanning Electron Microscope

[3] Note that k_g is the stiffness component of the MEMS structure against rotation which is induced by the nano-gauges. It is expressed in units of a moment and not as a stiffness against translation. The same case applies to k_h.

designs (the distance between gauges and fulcrum was varied). Measured resonance frequencies are in good agreement with theory and validate the mechanical part of the concept. However, actually measured resonance frequencies are slightly below theoretically expected values, which is due to minor technological imprecision, where the actual bending beam width was smaller than specified by design. For growing values of d_g, measurements match theory better because stiffness of the gauges becomes predominant.

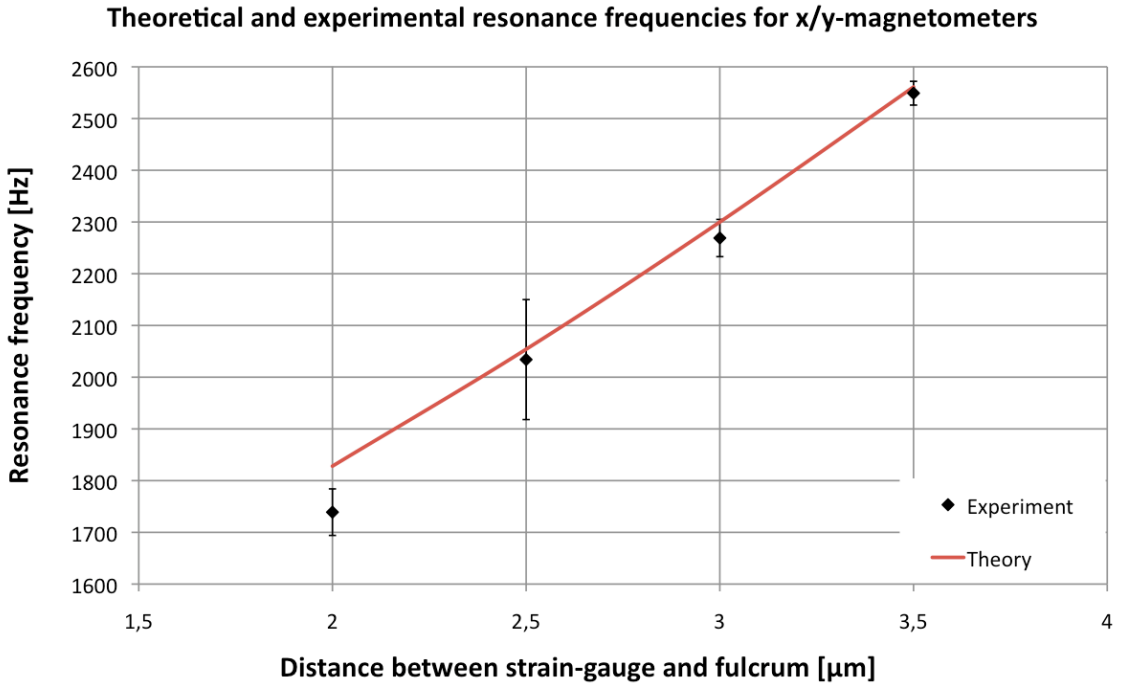

Fig. 5.1: Theoretical and measured resonance frequencies for x/y-magnetometers for validation of the mechanical part of the magnetometer concept

5.2 Sensitivity measurements

5.2.1 Sensitivity measurements using permanent magnets

A first quantitative evaluation of the magnetometer sensitivity was achieved using permanent magnets which were situated at specific distances away from the magnetometer. U-shaped permanent magnets were used for characterization of in-plane magnetometers and bar magnets were used for characterization of out-of-plane magnetometers (fig. 5.2). Initially, the magnetic field magnitude as a function from the magnet's distance was measured to obtain the dependence between magnet distance and strength of the respective magnetic field component. By vertical displacement of the magnets relative to the sensors, the magnetic field's magnitude was then varied, which led to a change in the bridge voltage over the two nano-gauges.

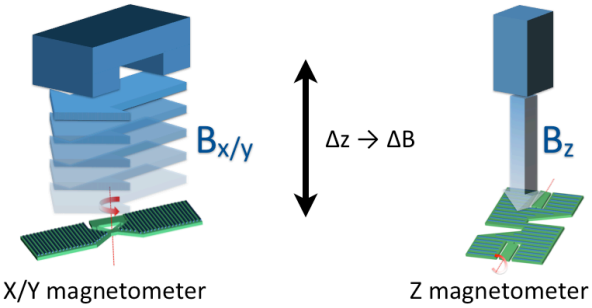

Fig. 5.2: Method for a first quantitative characterization of the magnetometers: U-shaped magnets were used for in-plane magnetometers, bar magnets for out-of-plane magnetometers. The magnets were vertically displaced above the sensors, which led to a change in magnetic field.

A scheme of the measurement setup is presented in fig. 5.3. For measurements, a polarization current of 100µA was applied[4]. Measurement results are presented in fig. 5.4. It is shown that any kind of structure is functional and that they show all a linear dependency on magnetic field. Coarser measurement deviations can be explained by a limited precision of the magnetic field due to the magnet's distance, its measured field value and the non-characterized influence of other field components coming from the permanent magnet. For each different magnetometer design, at least two similar structures on the entire wafer were characterized and showed similar sensitivity.

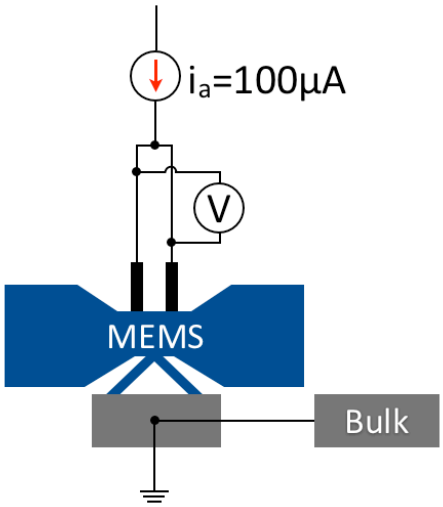

Fig. 5.3: Scheme of the used measurement configuration

In the case of in-plane magnetometers, the estimated sensitivity of 700mV/T was only slightly below the range predicted by design (∼ 930mV/T) and showed encouraging results such as a primary validation of the magnetometer functional principle and a linear sensor response. For out-of-plane magnetometers with a combined bending/torsion beam hinge (MZ1 type), the estimated sensitivity of 90mV/T (for MZ1-08 magnetometers) was below the predicted value of ∼ 370mV/T. As the same result was obtained from a second similar structure, this

[4]This is the polarization current for the readout bridge. The actual gauge current is therefore 50µA.

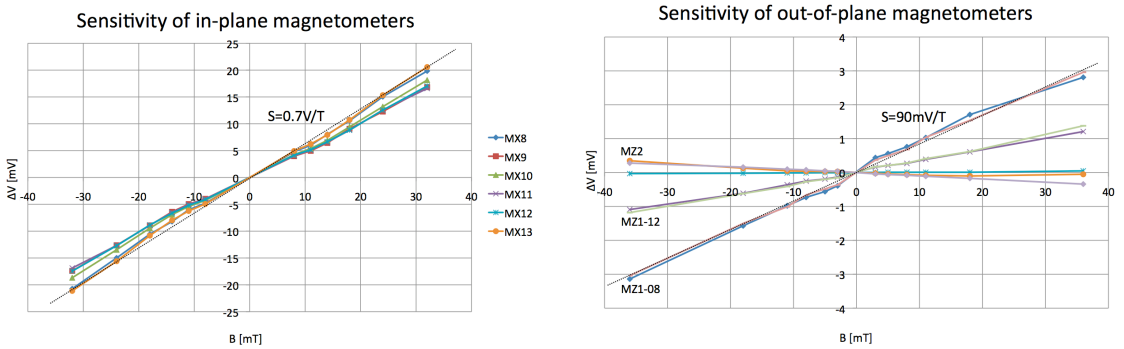

(a) (b)

Fig. 5.4: First characterization results with the application of a magnetic field using permanent magnets and a gauge polarization current of 50µA: (a) Measured sensitivity of in-plane-magnetometers. The measured sensitivity matches well the sensitivity predicted by design; (b) Measured sensitivity of out-of-plane magnetometers. The actual sensitivity is below the predicted value.

is unlikely to be matter of a statistical error. An explanation for the reduced sensitvity could be technological imprecision, including width and thickness of bending- and torsion beams.

The number of functional z-magnetometers with torsion beams (MZ2 type) was very restricted, and measurements showed even less sensitivity than for z-magnetometers of the MZ1 type. Possible reasons therefore are stitching of the relatively large MEMS structures to the ground after tests with electrostatic actuaction.

5.2.2 Sensitivity measurements using coils

In order to improve the precision of measurements and to be able to automatize the tests for characterizations on the full wafer, the former used permant magnets are replaced by coils which were mounted on measurement cards.

For on x/y-magnetometers, a toroidal coil was used, and a planar spiral coil for z-magnetometers as shown in fig. 5.5. An air gap was cut into the flux concentrator (a ferrite core) of the toroid coil, so that in-plane magnetic field components could be generated at the magnetometer position. Vertical magnetic field components are generated at the center of the planar spiral coil. First, the coils had to be calibrated for precise control of the applied magnetic field at the specified sensor position. As the toroid was made of a ferrite core, hysteresis had to be taken into account by simultaneous measurement of the magnetic field at the position of the toroid slot and at the designated sensor position. For the spiral coil, it was sufficient to measure the relation between coil current and the magnetic field at the sensor position.

All measurements were carried out by application of a polarization current of 100µA. Coil current was varied between ±1A over three sequenced cycles; hysteresis was not observed. Fig. 5.6(a) represents the sensitivity curve measured for x/y-magnetometers with a distance of 2.5µm between gauges and the fulcrum. Sensitivity represented in the graph was 1.09V/T with a low non-linearity of 0.02% in the measured range. Even higher sensitivities up to 1.82V/T could be measured for other designs with different geometric parameters (not presented here). A comparison between the measured sensitivity (1.09V/T) and the

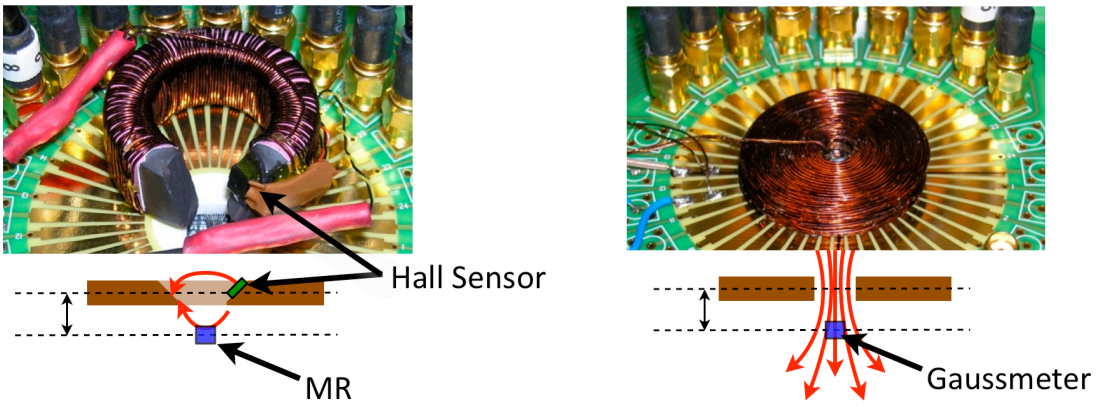

Fig. 5.5: Coils mounted on measurement cards for enhanced measurement precision: (a) toroidal coil for generation of in-plane field components; (b) planar spiral coil for generation of out-of-plane field components.

sensitivity according to design (0.93V/T) shows good agreement between both. The gain in sensitivity relative to the expected value can be explained by the fact that bending beam width after fabrication was actually 0.9 times smaller than specified by design.

Fig. 5.6(b) shows results obtained from z-magnetometers with a combined bending/torsion beam hinge (MZ1 type), where bending beam length was 150µm. Characterizations of MZ2 type magnetometers (torsion beam hinge) are not shown here because the number of functional sensors was very restricted and measured sensitivities were not coherent with design. The sensitivity obtained from the presented graph was 124mV/T with a non-linearity of 0.09% in the measurement range. For z-magnetometers with different geometric parameters, highest sensitivities of 164mV/T could be measured. Measured sensitivity is almost three times smaller than design target (370mV/T). As the measured characteristics for x/y-magnetometers fit well with design predictions, it is unlikely that this loss in sensitivity is caused by technological imprecision, although variations in bending beam thickness may have an impact on sensitivity, because flexural rigidity is proportional to the third power of beam thickness. The problem is more likely related to stitching effects appearing at the level of planar electrodes beneath the MEMS structures[5].

5.2.3 Validation of the 3D magnetometer concept

After experimental validation of the functional principle of magnetometer, it was also important to validate the concept of the fully integrated 3D magnetometer. This is particularly important in order to verify the presence of two integrated magnetic easy axes (cf. fig. 5.7(a)) and to evaluate the correlation between sensitivites to x- and y components of the magnetic field. For this purpose, sensitivities of the x- and y-magnetometers on the same chip were measured using the same measurement technique as mentioned above. The correlation between both sensitivities was measured to be 99.7%, which proves the presence of two equally

[5]Similar problems have also been observed in case of M&NEMS accelerometers and gyrocopes (e.g. immobile mass in case of MEMS structures designed for out-of-plane motion)

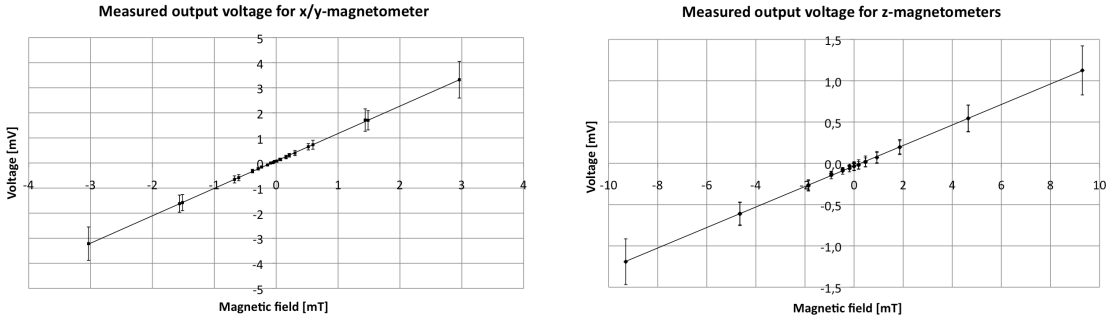

(a) (b)

Fig. 5.6: Results for sensitivity measurements using coils. The error bars represent the technological dispersion over the wafer. (a) x/y-magnetometer with a distance of 2.5µm between gauges and the fulcrum; (b) z-magnetometer (type MZ1) with a bending beam length of 150µm.

aligned magnetic easy axes and validates simultanously the 3D magnetometer concept (fig. 5.7(b)).

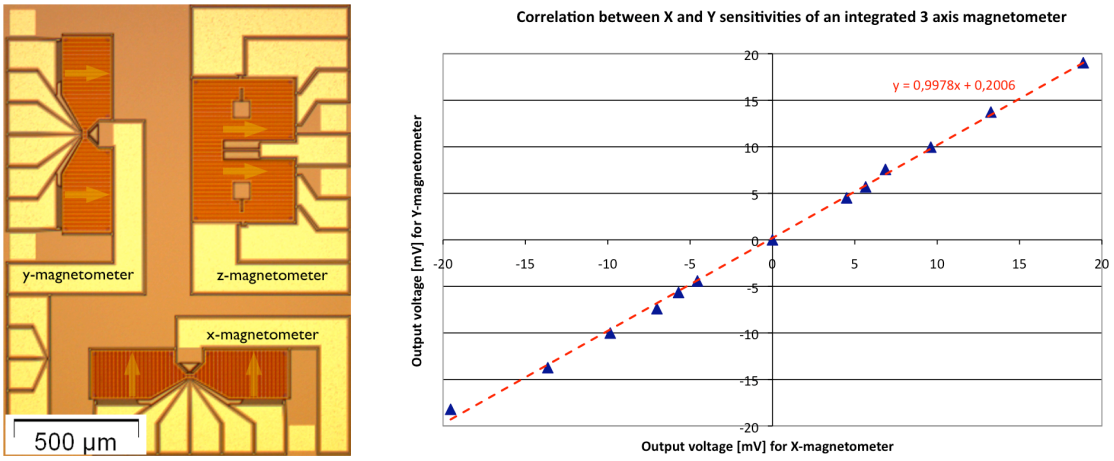

(a) (b)

Fig. 5.7: Validation of the 3D magnetometer concept: (a) Ideal alignement of two magnetization directions in the integrated 3D magnetometer; (b) Measured correlation of 99.7% between x- and y sensitivity axes.

5.3 Discussion

Characterization results validate the magnetometer concept and are very promising. It has been shown by resonance frequency measurements that the mechanical behaviour of MEMS

structures matches well theoretical predictions made by design. Slight deviations could be explained by minor technological imprecisions. Sensitivity measurements for x- and y-magnetometers are in good agreement with design targets; the deviation from design value was ascribed to a bending beam width which was smaller than specified. However, the difference between theoretical and actually measured sensitivity is more signnificant in case of z-magnetometers, which is most likely due to variations in bending beam thickness. Finally, a

	Measured	**Design target**
x/y magnetometer	1.09 V/T	0.93 V/T
z magnetometer	124 mV/T	370 mV/T

Table 5.1: List of measured sensitivities and design targets

correlation of 99.7% between sensitivities for x- and y-direction of the magnetic field confirm the 3D magnetometer concept to be valid and indicate high measurement preciseness for 3D measurement.

Chapter 6

Conclusion and outlook

In this work, the design, technological fabrication and characterizations of a 3D MEMS magnetometer using integrated magnetic material was presented and the sensor concept was proven to be valid. In the context of MEMS magnetometers, a major target of this work was to demonstrate an alternative 3D MEMS magnetometer concept, which, compared to state-of-the-art MEMS magnetometers, allows a significant reduction of power consumption, high sensing performances and small size. For example, power consumption of the complete 3D MEMS magnetometer (without electronics) with a bridge polarization current of 100µA is $\sim$ 30µW, while it is 300µW for state-of-the-art Lorentz force 3D MEMS magnetometers [19]. It has been shown that the MEMS scale is very advantageous for the magnetometer application, as higher electromagnetic interactions forces are obtained in case of integrated permanent magnets than at a macroscopic scale. A second great advantage of MEMS scale is related to the cointegration of inertial sensors together with magnetometers for applications such as navigation and motion tracking, as the sensor output is of the same order of magnitude for magnetometers, accelerometers and gyroscopes. This is particularly interesting for the conception and fabrication of inertial measurement units (IMUs).

The design concept for the sensor is very promising, as permanent magnets allow significant reduction in power consumption contrary to Lorentz force MEMS magnetometers, which require current biasing. Piezoresistive gauges with nanometric section lead to high sensitivity without increase of sensor size, as high mechanical stresses are achieved in the gauges. In particular a resolution of 500nT in a 15Hz bandwidth was required, which corresponds to $\sim$ 130nT/$\sqrt{\text{Hz}}$. In order to achieve this resolution, a noise model was established for the sensor, including thermo-mechanical noise, thermo-electrical noise, 1/f noise and electronic noise. Sensor noise was found to be predominated by 1/f noise in the given bandwidth of 15Hz. In case of x/y-magnetometers with 10µm MEMS thickness, the resolution according to design was $\sim$ 30nT/$\sqrt{\text{Hz}}$ for magnetometers with integrated NdFeB and $\sim$ 100nT/$\sqrt{\text{Hz}}$ for magnetometers with PtMn/CoFe multilayers, respectively and satisfies thus the required target resolution. In case of z-magnetometers, the target resolution could not be achieved with a MEMS thickness of 10µm. An approach to improve the resolution for z-magnetometers consists in reduction of the MEMS thickness in order to decrease mechanical rigidity against rotation of the MEMS structure. Further design considerations were self-heating of nano-gauges during polarization and euler buckling due to compressive mechanical stress. MEMS structures were inertially balanced for minimization of sensitivity to inertial effects and were designed for a resistance against inertial shocks of 10000g.

Integration of magnetic material into the microfabrication process was very challenging. An important sensor specification was resistance to magnetic shocks of 1T. This implies for the magnetic material, that its coercive field must be greater than 1T, or that an exchange-bias based multilayer system must exhibit an exchange field which is greater than the coercive field. Technological integration of two different types of magnetic material was studied. A first option was integration of NdFeB- and SmCo-type rare earth magnets, based on former experience at the Néel laboratory in Grenoble. A second option consists in integration of exchange bias coupled antiferromagnetic-ferromagnetic materials. NdFeB was chosen as rare earth magnet because of its good technological integrability and its excellent magnetic properties (remanence of $\mu_0 M_r = 0.7$T for in-plane magnetization and a coercive field of $\mu_0 H_C = 1.6$T), whereas technological integration of SmCo could not be achieved because it did not withstand the required technological step of chemical-mechanical polishing (CMP). However, the coercive field was reduced below 0.5T after patterning of the magnetic material, which does not satisfy the required resistance against magnetic shocks of 1T. Decreased magnetic properties were explained by defects of grain boundaries at the surface after CMP which generate a magnetic soft phase and by grain defects at the interface between the W_2N adhesion layer and the magnetic layer. Nevertheless, the integration of rare earth magnets into a MEMS magnetometer is a very promising approach to achieve high magnetometer sensitivity. Exchange-bias coupled PtMn/CoFe multilayers were studied for integration into the MEMS magnetometer. For unpatterned multilayer stacks, completely shifted hysteresis loops were found ($H_{ex}/H_C > 1$). The magnetic stacks had to be patterned as narrow stripes in order to enable integration of two different magnetic easy axes, by taking benefit of magnetic shape anisotropy. After patterning of the stacks, a significant decrease in H_{ex}/H_C was found. However, a completely shifted hysteresis loop was found for a stack configuration of [PtMn 50nm/CoFe 20nm]$_{10}$/PtMn 50nm with a stripe width of 2µm. However, a stripe width of 0.5µm was used in the actual magnetometer application in order to minimize the potential loss in sensitivity which is due to the disalignment angle between magnetization and the stripe's long direction. The disalignment angle was estimated to be $\sim 7°$. Further, the integration of two magnetic easy axes within a single fabrication step was successfully demonstrated.

Magnetometer fabrication could only be achieved with integrated PtMn/CoFe multilayers, as serious stress-related problems occured for integration of NdFeB, leading to destruction of the W_2N capping layer after crystallization annealing. Most critical fabrication steps for the MEMS process were a DRIE etching step to define the MEMS structures, and the HF release etching step.

Resonance frequency measurements of the MEMS structures confirmed the mechanical sensor concept and showed good correlation with theoretical expectations. Sensitivity measurements also showed good agreement with design targets in case of x/y-magnetometers, while sensitivity was reduced by a factor 3 for z-magnetometers. This was explained by a deviation from the nominal MEMS thickness of 10µm. The 3D MEMS magnetometer concept could be validated by measurement of sensitivities for x- and y-magnetometers on the same chip with a measured correlation of 99.7% between both sensitivity axes.

The demonstrated 3D MEMS magnetometer was shown to be a very promising alternative to state-of-the-art Lorentz force 3D MEMS magnetometers. A great advantage of the used M&NEMS technological concept consists in the possibility to cointegrate magnetometers together with inertial sensors within a single microfabrication process. Target applications

are amongst others the electronic compass (e.g. motion tracking and navigation), healthcare, contactless current measurement in automobile and further industrial applications, and more.

Perspectives for deepening of the subject consist in broader sensor characterization, including noise measurements, offset stability, and thermal drifts. These aspects could not be studied in the context of this work for lack of functioning magnetometer demonstrators (the wafer has broken during the packaging process after the essential characterizations presented in chapter 5). Another perspective is related to the development of magnetic materials for use in the magnetometer application. Mainly, exchange-bias coupled antiferromagnetic and ferromagnetic multilayers should exhibit a stronger hysteresis loop shift, and patterned rare earth magnets should exhibit higher coercivity in order to make the sensor robust against magnetic shocks. Finally, further design optimizations could lead to higher sensitivities, in particular for the case of z-magnetometers.

Bibliography

[1] i. R. Dixon, "Magnetic sensors head for the big time." Special Report Magnetic sensors H2 2009, 2009.

[2] i. R. Dixon, "isuppli special report - magnetic sensors," 2011.

[3] J. E. Lenz, "A review of magnetic sensors," *Proceedings of the IEEE*, vol. 78, no. 6, 1990.

[4] M. J. Caruso, "A new perspective on magnetic field sensing," *Honeywell Inc.*, vol. 5/98, 1998.

[5] B. D. Josephson, "Possible new effects in superconductive tunelling," *Physics Letters*, vol. 1, pp. 251–253, July 1962.

[6] P. Ripka, "Advances in fluxgate sensors," *Sensors and Actuators*, vol. A, no. 106, pp. 8–14, 2003.

[7] Honeywell, *3-Axis Magnetic Sensor HMC1043*. Honeywell, 2007.

[8] F. da Silva, S. Halloran, L. Yuan, and D. Pappas, "A z-component magnetoresistive sensor," *Applied Physics Letters*, 2008.

[9] M. Baibich, J. Broto, A. Fert, F. N. V. Dau, and F. Petroff, "Giant magnetoresistance of (001)fe/(001)cr magnetic superlattices," *Physical Review Letters*, vol. 21, pp. 2472–2475, November 1988.

[10] C. Roumenin, "Integrated vector sensor and magnetic compass using a novel 3d hall structure," *Sensors and Actuators*, vol. A, no. 92, pp. 119–122, 2001.

[11] C. Schott and R. Popovic, "Integrated 3-d hall magnetic field sensor," 1999.

[12] Z. Kadar, "Magnetic-field measurements using an integrated resonant magnetic-field sensor," *Sensors and Actuators*, pp. 225–232, February 1998.

[13] H. Emmerich, "Magnetic field measurements with a novel surface micromachined magnetic-field sensor," *IEEE TRANSACTIONS ON ELECTRON DEVICES*, vol. 47, May 2000.

[14] B. Eyre, "Resonant mechanical magnetic sensor in standard cmos," *IEEE ELECTRON DEVICE LETTERS*, vol. 19, December 1998.

[15] Z. Izham, "Development of a resonant magnetometer," *Nanotech*, vol. 1, 2003.

[16] V. Beroulle, "Monolithic piezoresistive cmos magnetic field sensors," *Sensors and Actuators A 103*, 2003.

[17] N. Dumas, "Design of a micromachined cmos compass," 2005.

[18] J. Kyynäräinen, "A 3d micromechanical compass," *Sensors and Actuators*, pp. 561–568, August 2008.

[19] M. Thompson, M. Li, and D. Horsley, "Low-power 3-axis lorentz force navigation magnetometer," *MEMS 2011*, January, 23-27 2011.

[20] S. Baglio, S. Castorina, and N. Savalli, *Scaling Issues and Design of MEMS*. John Wiley & Sons Ltd., 2007.

[21] O. Cugat, J. Delamare, and G. Reyne, "Magnetic micro-actuators and systems (magmas)," *IEEE TRANSACTIONS ON MAGNETICS*, vol. 39, pp. 3607–3612, November 2003.

[22] H. Rostaing, *Conception, modelisation et fabrication d'un micro-actionneur bistable, hors plan et magnétique*. PhD thesis, Institut National Polytechnique de Grenoble, 2004.

[23] P. Robert, S. Hentz, L. Durrafourg, G. Jourdan, J. Arcamone, and S. Harrisson, "M&nems: A new approach for ultra-low cost 3d inertial sensor," IEEE SENSORS, 2009.

[24] D. P. Arnold, "Permanent magnets for mems," *Journal of Microelectromechanical Systems*, vol. 18, pp. 1255–1266, December 2009.

[25] L. Bilhaut, *Actionnement magnétique à l'échelle nanométrique*. PhD thesis, Université Joseph Fourier, 2009.

[26] A. Walther, "Micro-patterning of ndfeb and smco magnet films for integration into micro-electro-mechanical-systems," *Journal of Magnetism and Magnetic Materials*, vol. 321, pp. 590–594, 2009.

[27] A. Walther, "Structural, magnetic, and mechanical properties of 5µm thick smco films suitable for use in microelectromechanical systems," *Journal of Applied Physics*, vol. 103, February 2008.

[28] N. Dempsey, "High performance hard magnetic ndfeb thick films for integration into micro-electro-mechanical systems," *Applied Physics Letters*, vol. 90, March 2007.

[29] B. Craig, S. McVitie, J. Chapman, A. Johnston, and D. O'Donnell, "Transmission electron microscopy study of cofe films with high saturation magnetization," *Journal of Applied Physics*, vol. 100, no. 053915, 2006.

[30] W. Thompson *Trans.Roy.Soc. (UK)*, vol. 146, p. 649, 1856.

[31] C. S. Smith, "Piezoresistance effect in germanium and silicon," *Physical Review*, vol. 94, pp. 42–49, April 1954.

[32] J. Richter, O. Hansen, A. N. Larsen, J. L. Hansen, G. F. Eriksen, and E. V. Thomsen, "Piezoresistance of silicon and strained sige," *Sensors and Actuators A 123-124*, pp. 388–396, 2005.

[33] J. Richter, M. B. Arnoldus, O. Hansen, and E. V. Thomsen, "Four point bending setup for characterization of semiconductor piezoresistance," *Review of scientific instruments*, vol. 79, April 2008.

[34] K. Reck, "Piezoresistance in silicon nanowires for sensor applications," Master's thesis, Technical University of Denmark, 2008.

[35] R. Hull, ed., *Properties of Crystalline Silicon*. INSPEC, The Institution of Electrical Engineers, 1999.

[36] Y. Kanda, "A graphical representation of the piezoresistance coefficients in silicon," *IEEE TRANSACTIONS ON ELECTRON DEVICES*, vol. ED-29, no. 1, 1982.

[37] J.M.Chen, "Measuring of the nonlinearity of a silicon piezoresistance by tensile loading of a submicron diameter fiber using a microinstrument," *Review of scientific instruments*, vol. 75, pp. 276–278, January 2004.

[38] K. Matsuda, K. Suzuki, K. Yamamura, and Y. Kanda, "Nonlinear piezoresistance effetcs in silicon," *Journal of Applied Physics*, vol. 73, pp. 1838–1847, February 1993.

[39] S. Hu, "Critical stress in silicon brittle fracture and effect of ion implantation and other surface treatments," *Journal of Applied Physics*, vol. 53, pp. 3576–3580, May 1982.

[40] S. Senturia, *Microsystem Design*. Kluwer Academic Publishers, 2002.

[41] B. Bae, "Design optimization of a piezoresistive pressure sensor considering the output signal-to-noise ratio," *Journal of Micromechanics and Microengineering*, vol. 14, pp. 1597–1607, June 2004.

[42] J. A. Harley, "1/f noise considerations for the design and process optimization of piezoresistive cantilevers," *Journal of Microelectromechanical Systems*, vol. 9, pp. 226–235, June 2000.

[43] R. R. Spencer, "A theoretical study of transducer noise in piezoresistive and capacitive silicon pressure sensors," *IEEE Transactions on Electron Devices*, vol. 35, pp. 1289–1297, August 1988.

[44] T. B. Gabrielson, "Mechanical-thermal noise in micromachined acoustic and vibration sensors," *IEEE TRANSACTIONS ON ELECTRON DEVICES*, vol. 40, pp. 903–909, May 1993.

[45] M. Bao, "Squeeze film air damping in mems," *Sensors and Actuators*, vol. A 136, pp. 3–27, January 2007.

[46] A. Dmitriev, "On the hooge relation in semiconductors and metals," *Journal of Applied Physics*, vol. 106, July 2009.

[47] L. Vandamme, "Annealing of ion-implanted resistors reduces the 1/f noise," *Journal of Applied Physics*, vol. 59, May 1986.

[48] A. Ben Amar, "Rapport de stage," Master's thesis, Université de Provence, 2009.

[49] G. K. Fedder, *Simulation of Microelectromechanical Devices*. PhD thesis, Massachusetts Institute of Technology, 1994.

[50] D. Li, Y. Wu, P. Kim, L. Shi, P. Yang, and A. Majumdar, "Thermal conductivity of individual silicon nanowires," *Applied Physics Letters*, vol. 83, pp. 2934–2936, October 2003.

[51] Y. B. Gianchandani, O. Tabata, and H. Zappe, *Comprehensive Microsystems*, vol. 2. Elsevier, 2008.

[52] S. Kim and C. Doose, "Temperature compensation of ndfeb permanent magnets," in *Proceedings of the 1997 Particle Accelerator Conference*, vol. 3, pp. 3227–3229, 1998.

[53] P. Mohn, *Magnetism in the Solid State - An Introduction*. Springer, 2006.

[54] D. Morris, D. Tennant, S. Grigera, B. Klemke, C. Castelnovo, R. Moessner, C. Czternasty, M. Meissner, K. Rule, J.-U. Hoffmann, K. Kiefer, S. Gerischer, D. Slobinsky, and R. Perry, "Dirac strings and magnetic monopoles in the spin ice $dy_2ti_2o_7$," *SCIENCE*, vol. 326, October 2009.

[55] R. Matzdorf, "Materie im magnetfeld." Lecture notes, Universität Kassel, Germany, 2008.

[56] *Magnétisme II - Matériaux et applications*. Collection Grenoble Sciences, 1999.

[57] A. Walther, *Développement de couches magnétiques dures pour MEMS: application à un microswitch magnétique bistable*. PhD thesis, Ecole Doctorale Electronique, Electronique, Automatique et Traitement du Signal, 2007.

[58] J. S. Becker, *Atomic Layer Deposition of Metal Oxide and Nitride Thin Films*. PhD thesis, Havard University, Cambridge, Massachusetts, December 2002.

[59] F. Dumas-Bouchiat, L. Zanini, M. Kustov, N. Dempsey, R. Grechishkin, K. Hasselbach, J. Orlianges, C. Champeaux, A. Catherinot, and D. Givord, "Thermomagnetically patterned micromagnets," *APPLIED PHYSICS LETTERS*, vol. 96, March 2010.

[60] K. Strnat and A. Tauber, "Internal temperature compensation of rare earth-cobalt permanent magnets for microwave devices by adding heavy lanthanides," *Journal of the Less-Commom Metals*, vol. 93, pp. 269–274, 1983.

[61] A. Zern, M. Seeger, J. Bauer, and H. Kronmüller, "Microstructural investigations of exchange coupled and decoupled nanocrystalline ndfeb permanent magnets," *Journal of Magnetism and Magnetic Materials*, vol. 184, pp. 89–94, 1998.

[62] Y. Zhang, D. Givord, and N. M. Dempsey, "Influence of buffer and capping layers on the mechanical and magnetic properties of nd-fe-b films," in *EUROMAT 2011*, (Montpellier, France), 12-15 September 2011.

[63] J. Allen and C. Young, "Magnetic anisotropy due to spin-orbit and dipole-dipole interactions in spin-density-wave antiferromagnets," *Physical Review B*, vol. 16, no. 3, 1977.

[64] H. Jansen, "Magnetic anisotropy in density-functional theory," *Physical Review B*, vol. 38, no. 12, 1988.

[65] P. Bruno, "Tight-binding approach to the orbital magnetic moment and magnetocrystalline anisotropy of transitition-metal monolayers," *Physical Review B*, vol. 39, no. 1, 1989.

[66] H. Boschker, M. Mathews, E. Houwman, H. Hishikawa, A. Vailionis, G. Koster, G. Rijnders, and D. Blank, "Strong uniaxial in-plane magnetic anisotropy of (001)- and (011)-oriented $La_{0.67}Sr_{0.33}MnO_3$ thin films on ndgao substrates," *Physical Review B*, vol. 79, no. 214425, 2009.

[67] C.-V. Tiusan, *Magnétisme et transport polarisé en spin dans des jonctions tunnel magnétiques. Utilisation du transport tunnel comme une sonde micromagnétique*. PhD thesis, Université Louis Pasteur de Strasbourg, 2000.

[68] B. Viala, "Af-biased cofe multilayer films with fmr frequency at 5ghz and beyond," *IEEE TRANSACTIONS ON MAGNETICS*, vol. 40, no. 4, 2004.

[69] Y. Lamy, *Matériaux magnétiques doux hétérogènes à combinaison d'aimantation élevée et de grande anisotropie utilisant le couplage d'échange, pour applications microondes*. PhD thesis, Université de Limoges, 2006.

[70] W. Meiklejohn and C. Bean, "New magnetic anisotropy," *Physical Review*, vol. 105, pp. 904–913, February 1956.

[71] P. van der Zaag, L. Feiner, R. Wolf, J. Borchers, Y. Ijiri, and R. Erwin, "The blocking and néel temperature in exchange-biased Fe_3O_4/coo multilayers," *Physica B*, no. 276-278, pp. 638–639, 2000.

[72] T. Blachowitz and A. Tillmans, "Exchange bias in epitaxial coo/co bilayers with different crystallographic symmetries," *Physical Review B*, 2007.

[73] J. Nogués, J. Sort, V. Langlais, V. Skumryev, S. Surinach, J. Munoz, and M. Báro, "Exchange bias in nanostructures," *Physics Reports*, vol. 422, pp. 65–117, 2005.

[74] M. Lund, W. Macedo, K. Liu, J. Nogués, I. K. Schuller, and C-Leighton, "Effect of anisotropy on the critical antiferromagnetic thickness in exchange-biased bilayers," *Physical Review B*, vol. 66, no. 054422, 2002.

[75] T. Ambrose and C. Chien, "Dependence of exchange field and coercivity on cooling field in nife/coo bilayers," *Journal of Applied Physics*, vol. 83, no. 11, pp. 7222–7224, 1998.

[76] C. Leighton, J. Nogués, H. Suhl, and I. K. Schuller, "Competing interfacial exchange and zeeman energies in exchange biased bilayers," *Physical Review B*, vol. 60, no. 18, pp. 12837–12840, 1999.

[77] P. Miltényi, *Mikroskopischer Ursprung der Austauschkopplung in ferromagnetischen/antiferromagnetischen Schichten*. PhD thesis, Rheinisch-Westfälisch Technische Hochschule Aachen, 2000.

[78] A. P. Malozemoff, "Mechanisms of exchange anisotropy (invited)," *Journal of Applied Physics*, vol. 63, no. 3874, 1988.

[79] A. Malozemoff, "Heisenberg-to.ising crossover in a random-field model with uniaxial anisotropy," *Physical Review B*, vol. 37, pp. 7673–7679, May 1988.

[80] D. Mauri, H. Siegmann, P. Bagus, and E. Kay, "Simple model for thin ferromagnetic films exchange coupled to an antiferromagnetic substrate," *Journal of Applied Physics*, vol. 62, no. 3047, 1987.

[81] T. Schulthess and W. Butler, "Coupling mechanisms in exchange biased films (invited)," *Journal of Applied Physics*, vol. 85, no. 5510, 1999.

[82] M. Stiles and R. McMichael, "Model for exchange bias in polycrystalline ferromagnet-antiferromagnet bilayers," *Physical Review B*, vol. 59, no. 5, 1999.

[83] J. Keller, P. Miltényi, B. Beschoten, and G. Güntherodt, "Domain state model for exchange bias. ii. experiments," *Physical Review B*, vol. 66, no. 014431, 2002.

[84] D. Lederman, R. Ramírez, and M. Kiwi, "Monte carlo simulations of exchange bias of ferromagnetic thin films on $FeF_2(110)$," *Physical Review B*, vol. 70, no. 184422, 2004.

[85] C. Bilzer, T. Devolder, J.-V. Kim, G. Counil, and C. Chappert, "Study of the dynamic magnetic properties of soft cofeb films," *Journal of Applied Physics*, vol. 100, no. 053903, 2006.

[86] J. Nozières, S. Jaren, Y. Zhang, A. Zeltser, and K. Pentec, "Blocking temperature distribution and long-term stability of spin-valve structures with mn-based antiferromagnets," *Journal of Applied Physics*, vol. 87, no. 8, 2000.

[87] K. ichi Imakita, M. Tsunoda, and M. Takahashi, "Giant exchange anisotropy observed in mn-ir/co-fe bilayers containing ordered mn3ir phase," *Applied Physics Letters*, vol. 85, no. 3812, 2004.

[88] A. Berkowitz and K. Takano, "Exchange anisotropy - a review," *Journal of Magnetism and Magnetic Materials*, vol. 200, pp. 522–570, 1999.

[89] O. Redon, "Patent no. ep 2 341 358 a1," 2010.

[90] G. Herzer, "Grain size dependence of coercivitiy and permeability in nanocrystalline ferromagnets," *IEEE TRANSACTIONS ON MAGNETICS*, vol. 26, no. 5, pp. 1397–1402, 1990.

[91] S. Ladak, L. Fernández-Outón, and K. O'Grady, "Influence of seed layer on magnetic properties of laminated $Co_{65}Fe_{35}$ films," *Journal of Applied Physics*, vol. 103, no. 07B514, 2008.

[92] R. McMichael, T. Watanabe, J. Dura, and J. Borchers, "Origins of coercivity increase in annealed symmetric spin valves," *IEEE TRANSACTIONS ON MAGNETICS*, vol. 32, no. 5, pp. 4636–4638, 1996.

[93] G. Stoney, "The tension of metallic films deposited by electrolysis," *Proc. R. Soc. Lond.*, vol. 82, pp. 172–175, May 1909.

[94] L. Freund, J. Floro, and E. Chason, "Extensions of the stoney formula for substrate curvature to configurations with thin substrates or large deformations," *Applied Physics Letters*, vol. 74, April 1999.

[95] P. Townsend, D. Barnett, and T. Brunner, "Elastic relationships in layered composite media with approximation for the case of thin films on a thick substrate," *Journal of Applied Physics*, vol. 62, December 1987.

[96] J. S. Kim and K. W. Paik, "The multilayer-modified stoney's formula for laminated polymer composites on a silicon substrate," *Journal of Applied Physics*, vol. 86, November 1999.

[97] C. A. Klein, "Comment on "the multilayer-modified stoney's formula for laminated polymer composites on a silicon substrate"," *Journal of Applied Physics*, vol. 88, November 2000.

[98] I. Noyan and J. Cohen, *Residual Stress Measurements by Diffraction and Interpretation*. Springer-Verlag, 1987.

[99] D. Ping, C. Yuze, and Z. Juesheng, "Effect of stress gradients in the surface layer of beryllium on x-ray stress measurement," *Materials Characterization*, vol. 49, pp. 381–386, 2003.

[100] P. S. Prevey, "Current applications of x-ray diffraction residual stress measurement," *Lambda Technologies*, 1996.

[101] O. Anderoglu, "Residual stress measurement using x-ray diffraction," Master's thesis, Texas A&M University, 2004.

[102] C.-H. Hsueh, "Modeling of elastic deformation of multilayers due to residual stresses and external bending," *Journal of Applied Physics*, vol. 91, June 2002.

[103] W. Fang and J. Wickert, "Post buckling of micromachined beams," *Journal of Micromechanics and Microengineering*, vol. 4, pp. 116–122, 1994.

[104] X.-F. Gou, "Analytic expression of magnetic field distribution of rectangular permanent magnets," *Applied Mathematics and Mechanics*, vol. 25, March 2004.

Appendix A

Calculating the magnetic field of a permanent magnet

The magnetic field generated by a magnet can be calculated using a current loop model (Ampère approach) or a magnetic potential model (Coulomb approach). The calculation in this manuscript is based on the current loop model published by X. Gou [104].

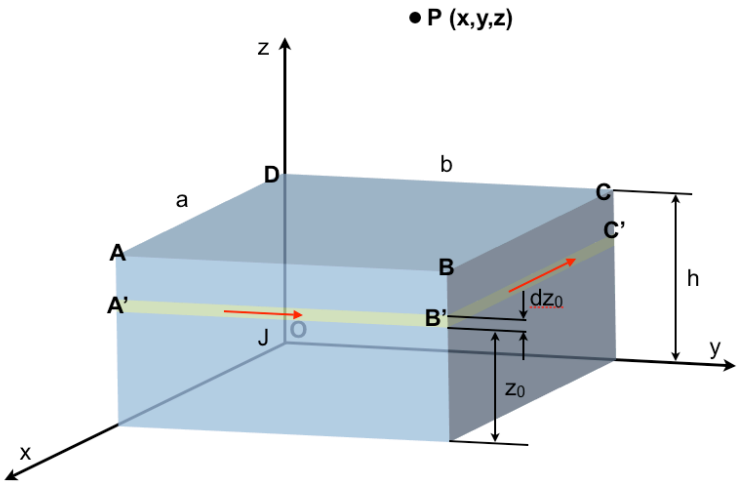

Fig. A.1: Modeling of a permanent magnet with a current loop model

We consider a block with surface ABCD as shown in figure A.1, where the current density caused by the current i is $J = i/h$. We will calculate the components B_x, B_y and B_z of the magnetic field in point P. This is done by considering an infinitesimal thin layer A'B'C'D' of the block and by summing up over the block's height all contributions to the magnetic field components:

$$\vec{B} = \int_0^h (dB_x\vec{e}_x + dB_y\vec{e}_y + dB_z\vec{e}_z) \tag{A.1}$$

According to Biot-Savart's law, the magnetic field generated by a current is

$$d\vec{B} = \frac{\mu_0}{4\pi}\frac{i d\vec{l} \wedge \vec{r}}{r^2}. \tag{A.2}$$

The resulting magnetic field components in point P are calculated as

$$B_x = \int_0^h dB_x = -\frac{K}{2}\left[\Gamma(a-x,y,z) + \Gamma(a-x,b-y,z) - \Gamma(x,y,z) - \Gamma(x,b-y,z)\right]|_0^h \tag{A.3}$$

$$B_y = \int_0^h dB_y = -\frac{K}{2}\left[\Gamma(b-y,x,z) + \Gamma(b-y,a-x,z) - \Gamma(y,x,z) - \Gamma(y,a-x,z)\right]|_0^h \tag{A.4}$$

$$B_z = \int_0^h dB_z = -K\left[\phi(y,a-x,z) + \phi(b-y,a-x,z) + \phi(x,b-y,z) + \phi(a-x,b-y,z) + \phi(b-y,x,z) + \phi(y,x,z) + \phi(a-x,y,z) + \phi(x,y,z)\right]|_0^h, \tag{A.5}$$

where K is defined as

$$K = \frac{\mu_0}{4\pi} J \qquad \text{with } \mu_0 = 4\pi \times 10^{-7}\,\frac{\mathrm{Vs}}{\mathrm{Am}}. \tag{A.6}$$

Γ is defined as

$$\Gamma(\gamma_1,\gamma_2,\gamma_3) = \ln \frac{\sqrt{\gamma_1^2+\gamma_2^2+(\gamma_3-z_0)^2}-\gamma_2}{\sqrt{\gamma_1^2+\gamma_2^2+(\gamma_3-z_0)^2}+\gamma_2} \tag{A.7}$$

and ϕ as

$$\phi(\varphi_1,\varphi_2,\varphi_3) = \begin{cases} \arctan\left[\frac{\varphi_1}{\varphi_2}\frac{\varphi_3-z_0}{\sqrt{\varphi_1^2+\varphi_2^2+(\varphi_3-z_0)^2}}\right] & \text{if } y \neq 0 \\ 0 & \text{if } y = 0 \end{cases}. \tag{A.8}$$